Interrogation of Active Drum Waste

Thesis submitted in accordance with the requirements of the
University of Liverpool for the degree of
Doctor in Philosophy

by

David Ikenna Igwesi

Oliver Lodge Laboratory

March 2021

Acknowledgements

I would like to express my sincere thanks to those who have contributed to the success of this work over the last four years. My thoughts and gratitude go first to my supervisor, Dr Helen Boston who constantly helped to make this work a reality. Thanks for your advice, guidance and support without which this work would have been difficult to complete. A huge thank you goes to Prof Dave Joss for helpful discussions regarding the scope of this work.

Thanks are also due to Prof Paul Nolan for useful advice and suggestions in the early stages of this work. Special thanks to Prof Andy Boston for continuous assistance on MCNP code and valuable discussions. Thanks to Prof Pete Cole for providing the 500 litre standard waste drum used for this work. I acknowledge the valuable help provided by Drs. Carl Unsworth and Dan Judson.

Thanks to Drs. Adam Caffrey and Ellis Rintoul for helping out during the Compton camera measurements and the Compton reconstruction code. To the rest of the nuclear physics group, past and present, thanks for making the journey so great. Special thanks to all my friends Otobong, Emma, Celestine, Maduka, Onemah, Ahmed, Ezekiel, Hamed, Muneerah, Hannah, Bro Ben and many others not mentioned, your words of encouragements and interactions provided the necessary ingredients.

A huge thank goes out to the Petroleum Technology Development Fund (PTDF), Nigeria, for sponsorship of this work, and to Nnamdi Azikiwe University, Awka, Nigeria, for the support extended to me while on study.

I want to thank my family and especially my mum, Catherine, for her effort and unconditional support. She had always believed and supported my dreams and ambitions. We were happily looking forward to this success, but sadly, she passed away on 8th December, 2020. I wish you have been there to celebrate this success. To my siblings, I appreciate your prayers and encouragements. Saving the best for last, a very special thanks to my wife, Oluchukwu, for always standing beside me through thick and thin. To my wonderful children, Chikamso, Ifeanyichukwu and Ifechukwu, thank you so much for those playful and happy moments after exhausting studies.

Abstract

The characterisation and evaluation of a mechanically cooled, broad energy germanium (BEGe) detector has been investigated, with potential application in spectrometric interrogation of a 500 litre standard radioactive waste drum. The BEGe detector is of cylindrical shape with a detection area of 6500 mm^2, and utilises a 0.6 mm thin carbon epoxy window to protect the crystal as well as limiting the attenuation of low energy gamma rays. The detector was first calibrated using standard calibration sources of various energies at a standoff of 25 cm and measurements were taken for 600 seconds each to estimate the efficiency and Full Width at Half Maximum (FWHM being the resolution) of the detector. The detector is thereafter slit-collimated with lead slabs of 10 mm apertures to narrow the angle of acceptance from the position of emittance of the gamma ray hitting the detector and essentially gives spatial location of the emitting radionuclide. The measurement procedure for the interrogation of the waste drum involves segmenting the waste drum axis into 24 vertical segments of 5 cm step. The collimated detector then applied to scan the waste drum from top to bottom on each of the segments for each of the point sources used. Thereafter, radial and angular scanning of the waste drum were performed at the segment with the highest count rates. Image reconstruction for the localisation of the hotspots was performed by combining the vertical count rate obtained with either the angular or radial count rates, and the combined data were implemented using a filtered back projection (FBP) algorithm developed using a MATLAB code. The total activity of the sources within the waste was calculated by taking the average of all the activities from each radial segment of the drum. The measurement procedures were repeated for an extended ^{137}Cs source 15 cm long and 1.5 cm diameter. The results indicated that a well collimated BEGe detector is suitable for the localisation of hotspots and quantification of activity of the source inside the drum. Remarkably, a reconstructed image of length 14.9 ± 1.7 cm for the extended source shows the effectiveness of the BEGe detector for imaging of the different forms of hotspot. Furthermore, Monte Carlo simulations performed to validate the activity of the sources and estimate the attenuation effects of some attenuating materials on the

activity of the sources clearly showed that an accurate utilisation of the MCNP simulations technique can obviously be applied to improve the quantification of the activity of the source, and estimation of the attenuation effects of matrices on the activity of the radioactive waste drum.

Additionally, the feasibility of improving the localisation of hotspots with Compton camera is presented. The Gamma-Ray Imager plus (GRI+), a three-tiered Compton camera imaging system, designed at the Precisions Radiometrics Instrumentation Development and Education (PRIDE) Laboratory comprised of a circular orthogonal-strip lithium-drifted silicon Si(li) detector as scatterer, a cuboid orthogonal-strip HPGe detector as absorber and a coaxial HPGe detector. Data were acquired for two ^{137}Cs point sources positioned 30 cm apart inside the waste drum. Using the analytical image reconstruction algorithm developed at the University of Liverpool, an intensity location on the surface of the cone, known as a Compton cone, was back projected into an imaging slice for each event. A multiple number of reconstructed cone projections onto a two-dimensional imaging slice produces an intensity map which represents the location of the hotspot. FWHM of 69.47 ± 1.50 mm and 74.98 ± 2.77 mm were obtained for the two ^{137}Cs point sources. The results from this novel technique that has not been used to image 500 litre standard waste drum show that the FWHM values for the GRI+ are lower than those obtained from the BEGe detector system indicating a good image resolution. The Compton camera is a reliable alternative for hotspot localisation as it distinctively resolved two ^{137}Cs point sources of different activity and source positions. This technique is therefore recommended for radiological characterisation of waste drum used for low and intermediate level waste (LILW).

Contents

List of Figures

List of Tables

Chapter 1

Introduction & Background

1.1 Introduction

One of the most remarkable events of the late 1950s in the nuclear industry was the commercialisation, and an increased dependance on nuclear power for electricity generation by many countries of the world. This, notably, came during the world oil crises that saw many countries adding nuclear energy to augment their electricity generation. This not only increased the number of nuclear reactors operating worldwide but more importantly and worryingly, increased the quantity of radioactive waste being generated worldwide. Many years down the line, there has been large amount of nuclear/radioactive wastes generated from these nuclear reactors that are on temporary storage waiting for either permanent storage or final disposal. However, the limited number of storage facilities is delaying the permanent storage of these accumulated wastes. Apart from the operation of nuclear reactors, there is an increased in the amount of low level waste on temporary storage as a result of increased in the use of radioactive sources or materials in hospitals, agriculture, industries (such as oil and gas) and research institutes. The health risk associated with these radioactive wastes is that the unstable radionuclides found in the waste streams attain nuclear stability through one or a combination of radioactive decay processes by emitting gamma-rays, neutrons and charged particles. These emitted radiations constitute a health risk to both humans and the environment. Therefore, it becomes imperative to employ best practice for waste management processes in order to minimise the adverse effects of these radiations coming from the accumulated wastes. The fundamental procedure of achieving this is by characterisation of the waste containers/drums to generate information that will aid in handling and proper management of the waste.

According to the data published by the International Atomic Energy Agency

(IAEA) and shown in Table 1.1, the combined global solid radioactive waste in storage for low level waste (LLW) and intermediate level waste (ILW) as at 31 December 2013 stood at 3,939,000 m^3, representing 62.3 % of the total global storage volume. Similarly, the combined global solid waste in disposal for LLW and ILW is estimated at 20,558,000 m^3, representing 72.2 % of the total global packaged volume [91]. The UK radioactive waste inventory as at 1st April 2019 shown in Table 1.1 indicates that about 38 % of the total waste in storage are in the LLW and ILW categories, and about 40 % of the total packaged wastes are classed as LLW and ILW. Remarkably, 97.6 % of the number of packages are for the LLW and ILW category. The data clearly showed that a significant amount of the solid wastes are in temporary storage waiting for permanent or final disposal. Disposal of these stored radioactive wastes requires proper characterisation programme (as illustrated in Figure 1.1) to produce parameters related to the individual waste

Table 1.1: Comparison of global and UK solid radioactive waste inventory. The Global data are as at 31 December 2013, [91], while UK data are as at 1 April 2019 [2].

Waste Category	**Reported Volume**		**Packaged Volume**		**Number of Packages**
	Global (m^3)	**UK** (m^3)	**Global** (m^3)	**UK** (m^3)	**(UK)**
HLW	22,000	1,390	0	1,500	7,660
ILW	460,000	247,000	107,000	499,000	292,000
LLW	3,479,000	1,480,000	20,451,000	1,280,000	22,300
VLLW	2,356,000	2,830,000	7,906,000	2,690,000	0
Total	**6,317,000**	**4,560,000**	**28,464,000**	**4,470,500**	**321,960**

*HLW represents high level waste, and VLLW stands for very low level waste.

package. The information obtained from the waste characterisation helps in providing more insight into the waste streams, ensure that the waste management processes comply with statutory and regulatory requirements relevant to waste acceptance criteria (WAC) and finally, ensure quality assurance during the waste management processes.

The key elements of specific waste properties on which data are collected during waste characterisation are the radiological, chemical, biological, thermal, physical and mechanical properties of the waste. The development of waste characterisation procedures requires the knowledge of the waste acceptance criteria (WAC) for disposal and final storage of radioactive waste. Typically, the WAC specifies

- Limits on the concentration of radionuclides in wastes.
- Limits on the activity of radionuclides to be disposed of at a given time.

- Physics and chemical properties such as leachability, limits on free liquids, limits on chemical and biological hazards, limits on incinerable and pyrophoric substances.

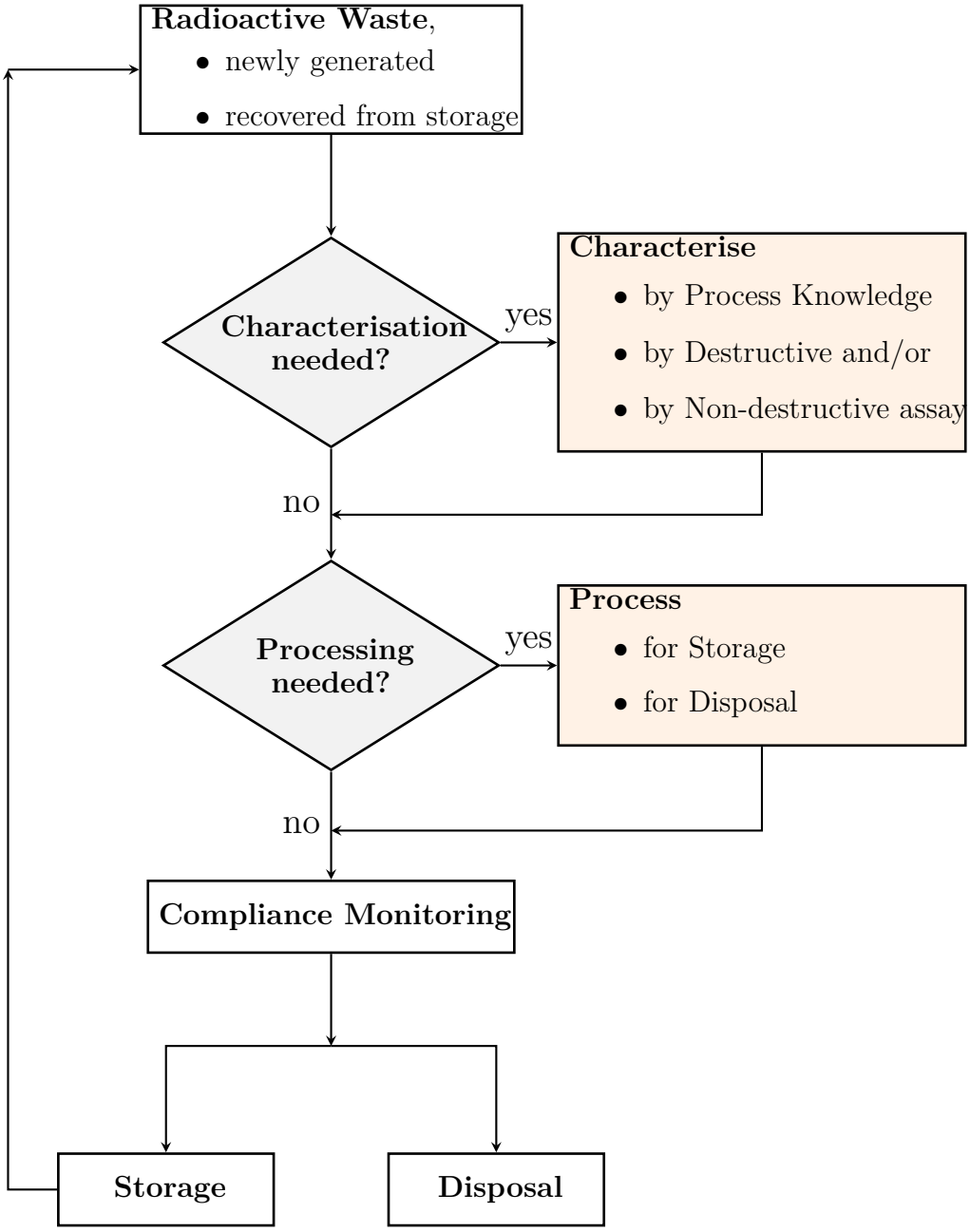

Figure 1.1: General procedure for the characterisation of radioactive waste modified from [82].

1.2 Motivation

It has been projected that the majority of the radioactive waste will come from decommissioning of nuclear facilities. This projection is on the basis that most

reactors built in the 1970s and early 1980s are now nearing their end of lifetime and as such are either due for decommissioning or will be due in the near future. Early characterisation is highly recommended as it helps to appropriately segregate and control the waste streams early in the decommissioning life cycle. This approach will ensure that the greater proportion of the waste is classified appropriately. The most critical part of the waste properties that requires continuous characterisation is the radiological property as it directly impacts on humans and the environment. The main focus of the work presented in this thesis is to evaluate the responses of the Broad Energy Germanium (BEGe) detector, a high purity germanium detector, on radiometric interrogation of a 500 litre standard waste drum and the objectives are outlined in the following:

- To effectively evaluate the use of slit collimated BEGe detector in source activity quantification and localisation of hotspots in a 500 litre standard waste drum.
- To utilise MCNP simulations to model the BEGe detector responses to a 500 litre standard waste drum with a view of improving the computation of the source activity.
- To investigate the effects of matrices on the attenuation of gamma-rays in a waste drum
- To evaluate the feasibility of using the Gamma-Ray Imager plus (GRI+) to localise hotspots in a 500 litre standard waste drum.

The main contributions made by this research work are outlined as follows:

- Improving, through MCNP simulation, the activity computation for both axial and non-axial positions of the source.
- Computation of the gamma-ray transmission factor and % attenuation for four matrices.
- Identification of the variation in intensities for two sources despite small percentage difference in activity.
- Novel imaging of a 500 litre standard waste drum using Gamma Ray Imager plus (GRI+) for the localisation of source(s).

1.3 Commercial Techniques

The increased in decommissioning activities for nuclear facilities had resulted in the availability of several commercial techniques for gamma-ray measurements for Nondestructive Assay. The first ever SGS was developed by the Los Alamos Nuclear Safeguards programme used to estimate the radionuclide content of low-density scrap and waste containers [61]. There are currently different types of radioactive waste assay system utilised commercially for waste characterisation. These instruments are designed to identify the location of the hotspots as well as provision of the spectroscopic information of the radionuclides.

The ANTECH G3200-340 SGS Model

The ANTECH G3200-340 SGS model comprises a shielded and collimated HPGe coaxial detector of 20 % efficiency, a transmission source positioned on the opposite side of the drum and mechanism to rotate and elevate waste drum as shown in Figure 1.2a. This technique was developed for non-destructive assay of radioactive waste containers, involving low-level and intermediate level waste (LILW), utilised emission and transmission source to determine the attenuation correction on a segment by segment basis for the entire drum. The system is designed for measuring up to 200 litre drums containing gamma-ray emitting radioactive waste. SGS is suitable for accurate measurement of low-density waste samples as well as high density waste samples known to be uniform and homogeneous. The system, however, introduces substantial bias/uncertainty when assaying heterogeneous waste samples.

The ANTECH G3850-34 TGS Model

The ANTECH G3850-340 TGS model composed of the basic components as the G3200-340, including a collimated HPGe detector of about 50 % efficiency, a transmission source, and mechanical system for rotating and elevating the waste samples (Figure 1.2b). However, for the measurement of dense heterogenous waste samples, a mechanical motion was included to enable the detector move in the direction transverse to the waste sample axis. This extra motion allows the TGS to determine the spatial distribution whilst quantifying the radionuclides contents of the drum, and produce in a colour map the emission and transmission plot for the drum.

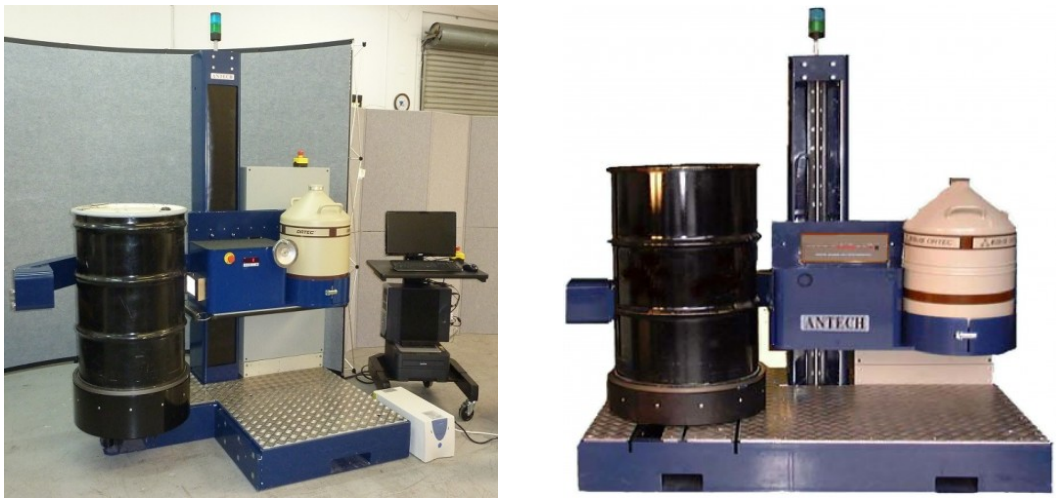

(a) (b)

Figure 1.2: Typical ANTECH Designed Nondestructive Assay System (a) G3200-340 Segmented Gamma-ray Scanner (b) G3850-340 Tomographic Gamma-ray Scanner. Obtained from [74].

The Mirion WW2200 Standard SGS

The Mirion WM2200 is modular designed comprising detector vertical drive module (used to raise and lower the HPGe detector), turntable rotation module as illustrated in Figure 1.3a, transmission vertical drive module and single transmission source shield and shutter. The transmission source is housed in a lead shield providing 101.6 mm of lead shielding around the source to minimise worker radiation exposures. A collimated p-type high purity germanium detector of 30 % efficiency and resolution of 1.9 keV at 1332 keV was utilised for the measurement of the gamma emitting radionuclides from the drum. The detector is electrically cooled by Mirion Cryo-Pulse® Plus cooling technology. The efficiency of the system can be improved by using large coaxial or broad energy germanium detector. Data acquisition is achieved using the Mirion Genie 2000 based NDA Software run on windows platform. The system is designed to accurately assay the gamma-ray emitting radionuclides in a waste drum with volumes up to 200 litre and weights up to 900 kg.

The Mirion WW2900 TGS

Similar to the Mirion WW2200 system, the WW2900 uses high purity germanium detector but with relative efficiency of 45 %, and a resolution of 2.0 keV at 1332 keV and 0.75 keV at 122 keV as shown in Figure 1.3b. Depending on the actual measurement conditions, the sensitivity of the detection system can be modified

over a wide range by altering the detector size, assay time and geometry of the assay system of the technique. The spatial resolution can be improved by varying the horizontal and vertical segments.. The system is designed to quantitatively assay gamma-ray emitting radionuclides from fission/activation product or trans.

(a) (b)

Figure 1.3: Typical MIRION Designed Nondestructive Assay System (a) WW-2200 Segmented Gamma-ray Scanner (b) WW-2900 Tomographic Gamma-ray Scanner. Obtained from [64].

The Cavendish DrumScan® SGS Plus

The Cavendish DrumScan® SGS Plus is a high resolution segmented gamma-ray scanner designed to reliably and accurately measure contaminated waste packed in drums or other containers. The system provides an inventory of the radionuclides present in the waste and can be utilised for measuring both homogeneous and heterogeneous waste samples. The DrumScan® SGS Plus is composed of a detector lift, turntable, a transmission source lift and an operator interface, and is capable of carrying drum sizes ranging from 100 litre to 500 litre as shown in Figure 1.4. It uses a collimated HPGe coaxial detector with an option of electrically or liquid nitrogen cooled. The energy resolution of the detector is 1.9 keV at 1332 keV. The system continuously performs vertical scanning of the drum by the detector while the transmission source move up and down the drum height as is being rotated. The vertical scanning and the drum rotation results in helical scanning of the drum. This form of drum scanning produces uniform gamma detection, good efficiency over the whole drum when compared to the conventional segmented gamma scanner. The DrumScan® SGS Plus produce a visual output of vertical distribution of the waste density as well as the. activity of all measured radionuclides

Figure 1.4: A typical Cavendish DrumScan® Plus Segmented Gamma-ray Scanner for Nondestructive Assay. Obtained from [69].

1.3.1 Comparison of the existing Commercial techniques to GRI+

It is apparent that all the existing techniques mentioned above are designed for the quantification of radionuclides present in the waste and localisation of hotspot. However, the techniques requires a balance between the accurate determination of the quantity of radionuclides and precise determination of the distribution of the radionuclides.

Unlike all the available techniques, the sensitivity of GRI+ is not limited by mechanical collimators. The GRI+ utilises the kinematics of Compton scattering to determine the direction of the incident gamma-ray. For gamma-ray undergoing multiple interactions, the GRI+ determine the source distribution from the information from the position and energy of the gamma-ray interacting in the detectors.

The current SGS and TGS techniques utilise mechanically operated turntable and vertical drive module for up and down movement of the detector. This scanning mechanism can add mechanical complexity that requires occasional maintenance. This effect is very minimal in GRI+ as it does not need mechanical turntable.

The resolution of the techniques discussed in Section 1.3 is affected by the movement of the detector-scanning platform. This movement induces vibration that generate microphonic interference (conversion of mechanical vibration to electrical signal (noise)) inform of noise to the data [93]. The GRI+ system is free of

this interference and has superior resolution.

1.4 Thesis Overview

This research project presents detailed experimental and computational work carried out to improve the responses of the Broad Energy Germanium (BEGe) detector for radioactive waste drum characterisation. An image reconstruction algorithm will be used to obtain the position of the hotspots in the drum. A numerical simulation method based on Monte Carlo will be utilised to calculate the activity of the sources which is to be validated by the source activity obtained through experimental measurements. The work also investigates the feasibility of using the GRI+ to localise radioactive sources in a standard waste drum. Chapter two describes an overview of the radioactive waste characterisation process and its usefulness to waste classifications. Radioactive waste management techniques adopted in safe handling of low and intermediate level wastes (LILW) are also explained. In Chapter three, a brief description of the fundamental physics principles underlying gamma-ray spectroscopy are presented. Chapter four deals with the imaging techniques applied in data analysis. The characterisation of a Broad Energy Germanium (BEGe) detector to investigate its radiometric response to a waste drum together with the comparison of the pinhole and slit aperture collimator are discussed in Chapter five. Chapter six presents the detailed experimental measurement procedures and MCNP simulation models, while Chapter seven discusses experimental and MCNP results. Measurement details and the results of the Gamma-Ray Imager plus (GRI+) system utilised for the localisation of the source in a standard waste drum are presented in Chapter eight, while Chapter nine outlines the conclusions and recommendations derived from the research work.

Chapter 2

Characterisation and Classification of Radioactive Waste

According to the IAEA, "radioactive waste is regarded as any material that contains or is contaminated by radionuclides at concentrations or radioactivity rates higher than the exempted amount established by the component authorities" [18]. Radioactive waste is thus classified based on the physical, chemical and radiological properties which obviously are relevant to particular facilities or circumstances in which radioactive waste is managed. These wastes are mostly generated during operations, maintenance and in some cases decommissioning of nuclear power plants; mining, milling and processing of uranium or thorium ores; agricultural, industrial, medical and research facilities using radionuclides. The management of these radioactive wastes requires proper characterisation to ensure safety and protection of humans and the environment. Effective and efficient management entails treatment and supervision of the waste from generation to final disposal. This involves frequently taking radiological, chemical and physical measurements to find the activity and radionuclide content of the waste in order to establish the best means of treatment, handling, processing, storage or disposal of the waste materials [108].

Radiological characterisation involves localisation and quantifying the presence of radionuclides in the waste. Physical characterisation provides information about the form and strength of the waste. In chemical characterisation, elemental and chemical components of the waste are established.

2.1 Classification of Radioactive Waste

The aim of radioactive waste classification is to ensure proper handling, storage and disposal of the waste materials. The main classification is based on the level of radioactivity emitted by wastes. Another form of classification is either short-lived or long-lived radioactivity which is based on the half-life and how long it takes to drop below the threshold to the next classification. The six radioactive waste classifications as defined by IAEA [18] and based on the level of activity are exempt waste (EW), very short lived waste (VSLW), very low level waste (VLLW), low level waste (LLW), intermediate level waste (ILW) and high level waste (HLW) as illustrated in Figure 2.1. A brief description of each category is presented below.

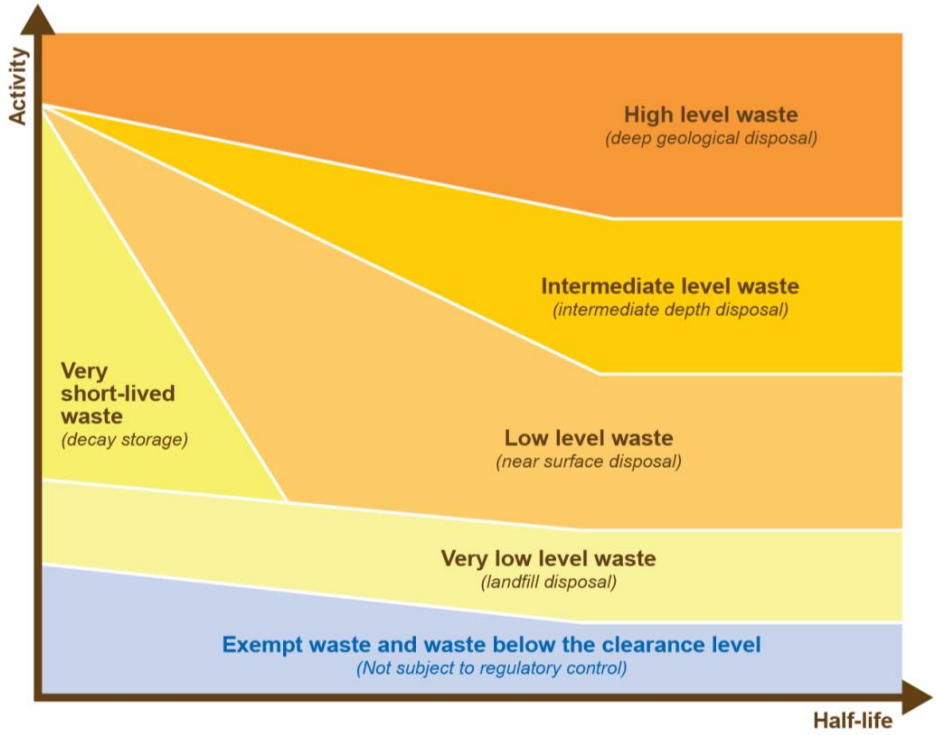

Figure 2.1: An illustration of IAEA's recommended radioactive waste classification with disposal routes from [18].

2.1.1 Exempt Waste (EW)

This classification applies to all radioactive waste whose activity concentrations are very low such that the waste does not require provisions for radiation protection from the regulatory authority. This category of waste is normally disposed in a conventional landfills or recycled.

2.1.2 Very Short Lived Waste (VSLW)

These are waste from radionuclides whose half-lives are of the order not more than a hundred days. The wastes being slightly above clearance level, are predominately stored until their activities have decayed to a level that no longer constitutes a hazard to the environment.

2.1.3 Very Low Level Waste (VLLW)

The activity concentrations of this waste are a little higher than the VSLW but they do not require a high level of containment and isolation. This waste constitutes low level activity from soil and rubble that have previously been contaminated during decommissioning of the radioactive facilities. The near surface landfill facilities are a suitable disposal point for VLLW.

2.1.4 Low Level Waste (LLW)

This classification comprise of radioactive waste containing radioactive content not more than 4 GBq per tonne of alpha activity or 12 GBq per tonne of beta-gamma activity. Low level waste could be short-lived radionuclides of higher activity concentrations or long-lived radionuclides of low level activity concentrations. Low level wastes are unavoidable byproducts of industries such as electricity generation, new pharmaceutical product testing and medical research. These include non destructive testing of airplanes and bridges. These waste streams are normally disposed of using near surface facilities. Specifically, low level wastes range from radioactive waste with an activity concentration not requiring shielding to radioactive wastes with a level of activity concentration requiring shielding and isolation for few hundreds of years.

2.1.5 Intermediate Level Waste (ILW)

The intermediate level waste has activity greater than the upper limit of low level waste and mostly contains long-lived radionuclides in quantities that require a greater degree of containment and isolation. It is important to note that there is no precise boundary between LLW and ILW as limits on the acceptable level of activity concentration differ between individual radionuclides or groups of radionuclides [18]. Intermediate level waste contains significant amounts of long-lived radionuclides that take a considerable period of time to decay, therefore, greater depths ranging from tens of metres to hundreds of metres are required for proper disposal. These radioactive wastes are generated from the reprocessing of

spent fuel and from general operations and maintenance of nuclear power sites. They can be stored in steel drums filled with high density materials such as sand, concrete and bitumen.

2.1.6 High Level Waste (HLW)

The activity concentration in high level waste is significantly high that a great amount of heat is generated in the process of radioactive decay. Due to the high amount of heat generated, deep and stable geological disposal of several hundred of metres or more is appropriate for the disposal of HLW. Two major sources of HLW are spent fuels and wastes from reprocessed spent fuel. HLW are generally disposed in deep, stable geological repositories of several hundreds of metres or more below the surface. Some HLW (such as spent fuels) are stored in ponds for many years to contain the amount of radioactive decay heat.

2.2 Methods of Radioactive Waste Characterisation

The first step in the management of radioactive waste requires that the waste be characterised at various stages before disposal in order to provide information on its properties and waste package [80]. This according to the regulatory requirements will facilitate the subsequent steps for safely processing, transportation and final disposal of the radioactive waste. There are three main methods of radioactive waste characterisation: (a) Process Knowledge (b) Non-destructive Assay (NDA) and (c) Destructive Assay. The most important step of the characterisation, establishing and estimating radionuclides content, is often achieved by non-destructive assay.

2.2.1 Process Knowledge

To effectively enhance waste characterisation, knowledge and proper documentation of all processes involved in radioactive waste generation are extremely important. Process knowledge provides a suitable road map for cost effective techniques to be adopted in waste characterisation.

2.2.2 Destructive Assay

Destructive assay is a measurement technique where the isotopic composition of the difficult (due to chemical and radiological interferences of the radionuclides in the measurement) to measure radionuclides present in the radioactive wastes are determined. This measurement technique transforms the physical form of

the wastes. The basic steps in destructive assay includes the dissolution of the sample followed by a particular chemical separation process and finally, laboratory radiometric analysis depending on the radioactive and chemical properties of the radionuclides present in the sample.

2.2.3 Non-Destructive Assay

In this method, the activity concentrations of the key radionuclides present in the waste packages are determined. Three modes of non-destructive measurements use gamma-ray, neutrons and calorimetry. The laboratory analysis of the waste sample is relatively accurate compared to the destructive assay. However, the NDA measures the entire waste system (such as waste drum).

2.2.3.1 Gamma Methods

This is the most common and widely used NDA method for radioactive waste measurements. Often, during radioactive decay a gamma ray will be emitted which is specific to the decaying nucleus. The emitted gamma rays can be used in NDA to characterise waste. This characterisation measurement can be active or passive. In an active measurement, gamma rays produced by an external source(s) is applied to interrogate the radioactive waste package and the attenuation of the gamma rays is subsequently measured. This method is very useful when determining the rate of transmission and degree of attenuation of gamma-rays through waste containers (such as waste drum) and its matrix; the results are useful in estimating the effect of waste container and matrix on the gamma-rays produced. While in passive measurements, the gamma-rays emitted naturally during radioactive decay process are measured. Passive measurements are commonly used given the fact that gamma-rays are naturally produced by the radionuclides of interest.

In gamma ray measurement, gamma ray scanning provides a non-destructive method to measure the inventory of gamma emitting radionuclides inside a waste package where the specific nature of the matrix and the relationship between the radioactive nuclides and the matrix may be unknown. This measurement is achieved by scanning the waste container where either the detector or waste sample are moved relative to one another in order to take stage by stage measurements of the entire waste sample. There are three types of scan mode used in gamma ray scanning: integral gamma scanning, segmented gamma scanning and tomographic gamma scanning. These scanning modes use either Low Resolution Gamma Spectrometry (LRGS) or High Resolution Gamma Spectrometry (HRGS) techniques to measure the energy of each gamma-ray present in the radioactive waste sample

which helps in the determination of the activity of the radionuclides [92, 93].

Integral Gamma Scanning (IGS)

This is like a one shot mechanical measurement used to acquire the entire spectral volume of the radioactive waste sample and it is effective in measuring waste samples with a known matrix and activity distributions within the detector field of view as shown in Fig 2.2a. For large sample volumes, two or more detectors could be used and the integral spectrum reconstructed.

Segmented Gamma Scanning (SGS)

SGS is the commonly used scanning mode [6, 21, 25, 29, 90, 96]. SGS uses collimated semiconductor or scintillation detectors to measure gamma emissions from specific segments of a radioactive waste package as seen in Fig 2.2b. The matrix and activity in the segments are assumed to be homogeneous and uniformly distributed [92]. In SGS, the external transmission source and the detector are positioned diametrically on opposite sides of the radioactive waste, such that during the measurements, the detector and the transmission source move simultaneously along the vertical, horizontal or radial axes of the waste sample depending on the orientation being scanned. The radioactive waste sample is normally rotating while being scanned so as to minimise the non-homogeneous effect typically associated with measurements of waste. In most cases, SGS requires only a single detector, it therefore takes a longer time for the entire waste system to be assayed.

Tomographic Gamma Scanning (TGS)

The assumption in SGS that the activity in each segment of the radioactive waste is homogenous is not a good representation of the actual activity composition of the waste sample. This assumption in SGS can be corrected by using tomographic gamma scanning. The operational principles of SGS and TGS are very similar except that there is an addition of a translation axis in TGS which allows the detector to view the radioactive waste sample along all lines that pass through the detector rather than only the radial centre line as obtained in SGS. This extra technique enables the TGS to acquire 3-dimensional transmission and emission tomographic measurements from which spatial emission and spatial attenuation plots of the waste assay are determined. To achieve a good detection limit with this method, the time for data acquisition is reasonably extended.

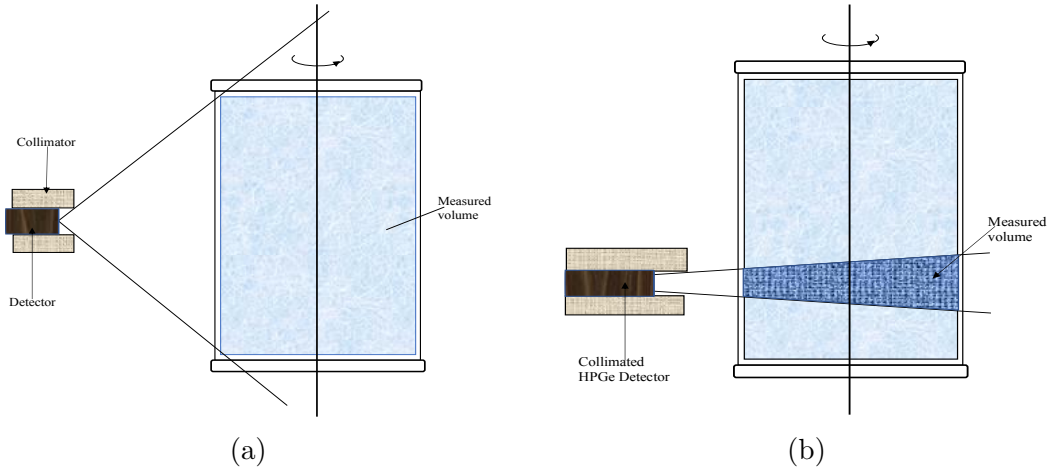

Figure 2.2: A schematic diagram of gamma-ray scanning methods, (a) Open geometry where all parts of the drum contribute to the detector response, (b) Segmented geometry where the drum is divided into segments

2.2.3.2 Neutron Methods

The radioactive decay of Special Nuclear Materials (SNM) emit neutrons through reactions such as spontaneous fission (SF), induced fission and other forms of reactions. Neutron measurement techniques estimate the amount of neutrons emitted through these special reactions. It is a passive or active sensitive technique used in the estimation of large and small quantities of uranium and plutonium. Passive measurement involves direct measurement of a neutron emitted by the radioactive waste materials while the active measurement is employed when the radioactive materials do not sufficiently emit spontaneous neutrons to allow for direct measurements, thus, an external neutron source is used to interrogate the radioactive materials through one of the neutron induced reactions. Therefore, the two types of neutron measurements are passive neutron counting techniques and active neutron counting techniques.

2.2.3.3 Calorimetry

A great quantity of thermal energy is generated during radioactive decay. The measurement of this energy by calorimetry methods and, by extension, the amount of radioactivity provides information about the radioactive materials that produced the heat. Two different types of calorimeter employed are single chamber true isothermal calorimeters and heat flow calorimeters. The calorimetry method is mostly applied in the measurement of plutonium in large quantities where thermal energy is generated through alpha particle decay and measurement of tritium in large quantities in which thermal energy is produced through beta particle de-

cay. The process is not used for any waste classifications that do not generate heat.

2.3 Radioactive Waste Management

The fundamental objective of radioactive waste management is principally to control and account for radioactive waste in order to protect human health and the environment and future generations [80]. The basic means of achieving this, where reasonably practicable, is to concentrate, contain and isolate the radioactive waste from the environment.

The first step in management of radioactive waste is its characterisation to document information about the radioactivity content and form of the waste. Each of the waste classifications is managed differently, as this work is basically for Low and Intermediate Level Wastes (LILW), processes employed for management of these classes of wastes as seen in Figure 2.3 are segregation, treatment, conditioning, storage and disposal.

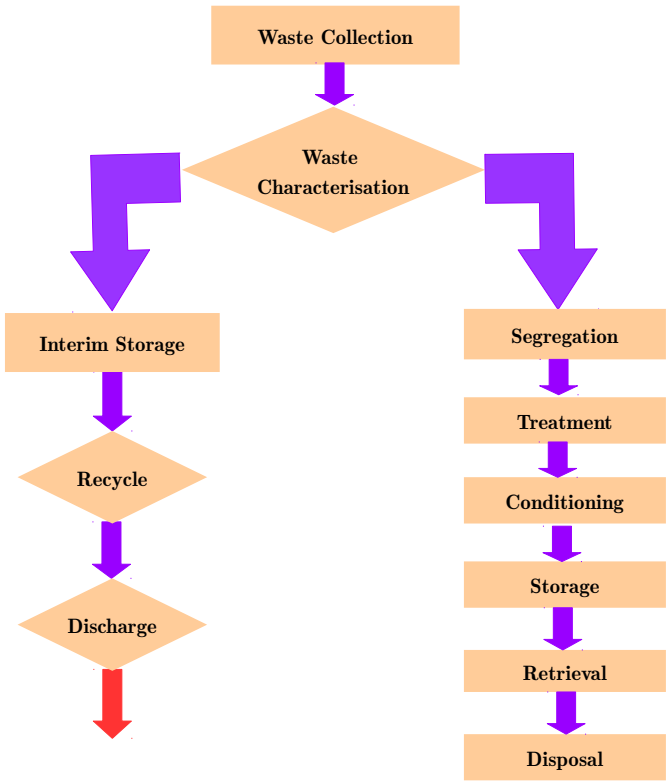

Figure 2.3: The fundamental steps of radioactive waste management.

Waste segregation entails separating waste or radioactive materials based on radiological, chemical and/or physical properties which will facilitate waste handling and processing. In waste treatment, certain operations are carried out to

change the characteristics of the waste for safety. Waste treatment intends to achieve volume reduction, reduction or total removal of radionuclides from the waste and transformation of the waste composition. Typical volume reduction includes mechanical compaction, incineration and evaporation. While these methods reduce the volume of the waste, the radioactivity concentration remains the same. Conditioning of LILW as defined in [70] comprises operations that produce a waste package suitable for handling, transport, storage and disposal.

In conditioning processes, liquid wastes are converted to a solid waste form and stored in a waste containers. Systematic steps in waste conditioning involve the identification of a suitable matrix material (such as cement, bitumen, polymers or borosilicate glass), that will guarantee stability of the radioactive materials within the storage period. Matrix choice depends on the waste classification. The waste is then immobilised through mixing with the matrix material and then packaged in waste drums or containers. Liquid LILW are typically solidified in cement, bitumen or polymers. Storage of radioactive waste is to avoid any risk of radiation exposure to people or environment. LLWs are disposed directly to a land-based disposal while ILW that contains long-lived radioisotopes is stored in temporary storage pending the final disposal in a geological repository.

2.4 Matrix for Radioactive Waste Management

A wide range of potential matrix materials are available for waste immobilisation in radioactive waste management. Waste immobilisation is a process of passively stabilising waste form in a manner that reduces risks to human health and the environment for the time during the decaying of the waste radioactivity. The choice of any material matrix depends not only on the criteria stipulated by the regulatory bodies, but also by the chemical composition, and the waste acceptance criteria (WAC) for storage and disposal. It has been established that immobilisation of radioactive waste in suitable matrices significantly reduces the potential for the release of radionuclides into the environment [72]. These matrices obviously provide shielding to personnel and the environment through radioactivity reduction in any waste. The matrices to be considered in the work are concrete, bitumen and polymer (plastic). The usefulness of these matrices in radioactive waste immobilisation has extensively been documented [66, 22, 71, 56]. The properties of concrete, bitumen, polymer and polymer concrete composites are presented in Table 2.1.

Table 2.1: Comparative properties of immobilising matrices for radioactive waste management [49].

Descriptions	**Concrete**	**Bitumen**	**Polymer**
Resistance to leaching	Poor to excellent	Excellent for most radionuclides	Good to excellent for most radionuclides
Waste Loading	10-25 wt% ion exchangers	25 - 50 wt% ion exchangers	25 - 50 wt% ion exchangers
Compressive strength	Excellent	Poor to moderate	Moderate to good
Radiation stability	Excellent	Moderate	Moderate
Thermal stability	Good	Poor; can melt and ignite	Moderate; some will melt
Resistance to biodegradation	Stable	Moderate	Moderate to stable
Gas generation	Low	Moderate to high	Moderate
Chemical Compatibility	Good for most materials	Good but worst for solvents and oils	Good for most materials

The properties from the table showed that the matrices performed well in solidification of liquid or sludge radioactive wastes and therefore, have been used for many years in radioactive waste immobilisation. However, the focus in this work is to investigate the effects of these matrices in reducing radioactivity concentration in radioactive waste.

Polymer offer moderate radiation stability as seen in the Table 2.1. However, a composite material involving polymer and concrete will greatly improve the radiation stability of radionuclides.

Chapter 3

Principles of Gamma-ray Spectroscopy and Imaging Technique

3.1 Gamma-ray Interactions

The interaction of a gamma-ray with the surrounding materials affects the energy spectrum collected by the detector. Within the energy regime of interest there are three main processes of gamma-ray interaction with matter. These are photoelectric absorption, Compton scattering and pair production. Each of these interaction modes has an effect on the gamma-ray energy as it traverses through matters such as the matrix of radioactive waste. The predominant mode of interaction strictly depends on the atomic number (Z) of interacting material and the gamma-ray energy. Photoelectric absorption is the dominant interaction at low gamma-ray energy (approximately 10 keV to 500 keV) and with high Z materials. Compton scattering dominates at intermediate energies (ranging from 100 keV to $\leq$ 10 MeV, creating an energy overlap with the photoelectric absorption) and low Z while pair production is the dominant process at energy $>$ the threshold of 1022 keV. The relative importance of the three processes as a function of Z and gamma-ray energy is shown in Figure 3.1. The significance of photoelectric absorption at energies below 400 keV and the strong Z dependence of this interaction are evidence in explaining the discrepancies observed at lower energies in the simulations result described later in this thesis.

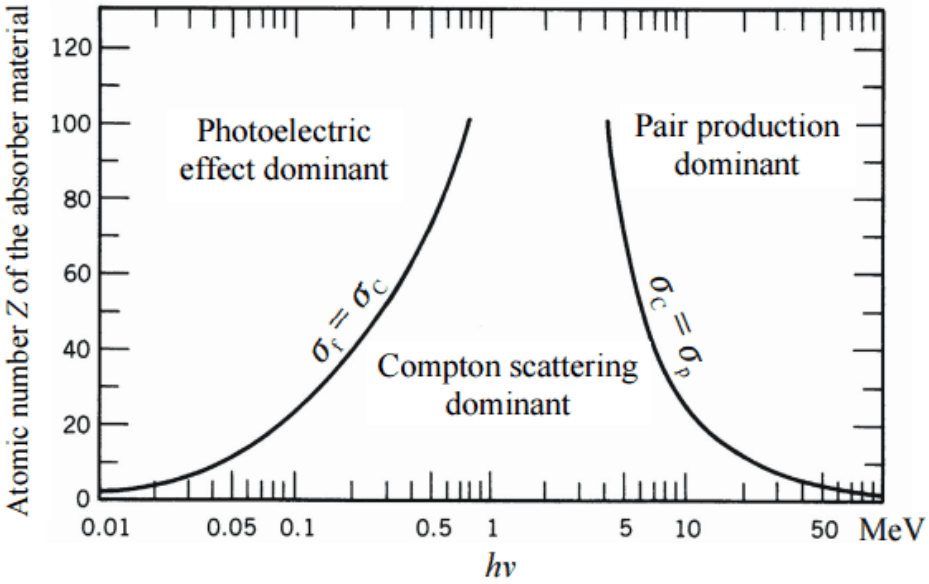

Figure 3.1: Importance of the three principal interactions of photons in matter as a function of absorber atomic number, Z, and gamma-ray energy. Obtained from [52].

3.1.1 Photoelectric Absorption

Photoelectric absorption is an interaction mechanism where an incident gamma-ray transfers all of its energy to a bound atomic electron as shown in Fig. 3.2a. This is a dominant process for low energy gamma-rays incident on materials with high atomic number, Z, as seen in Fig. 3.1. The electron, known as the photoelectron, is subsequently knocked out of its orbit with a kinetic energy equal to the difference between the gamma-ray energy, E_γ, and the binding energy , E_b, of the electron (energy required to remove the bound electron from the atom).

$$E_e = E_\gamma - E_b. \tag{3.1}$$

where E_e is the kinetic energy of the electron.
The photoelectron is usually ejected from the K-shell creating a vacancy. The vacancy is filled from a higher lying orbital state and a characteristic x-ray is emitted. The probability that photoelectric absorption (τ) occurs in a given interaction depends upon the energy of the incident gamma-ray and the atomic number of the material medium. This probability is given as

$$\tau \propto \frac{Z^n}{E_\gamma^{3.5}} \tag{3.2}$$

with n being a variable depending upon the energy of the incident gamma-ray and its value is usually between 4 and 5. The significance of Equation 3.2 is the primary reason why high atomic number materials such as lead are predominantly utilised in gamma-ray shields [35].

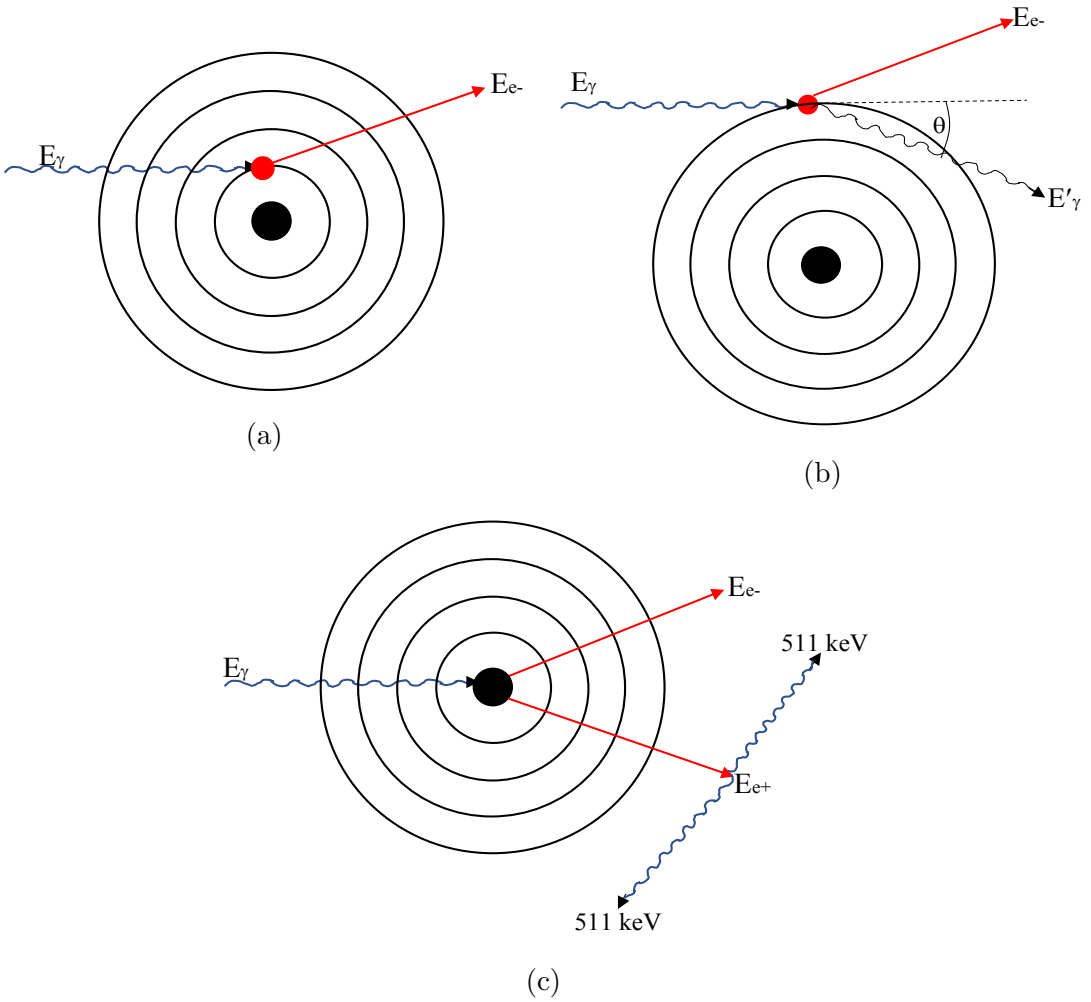

Figure 3.2: Schematic illustration of the three main gamma-ray interaction mechanisms with matter (a) Photoelectric Absorption (Also Photoelectric Effect), (b) Compton Scattering and (c) Pair Production.

3.1.2 Compton Scattering

In Compton scattering, the gamma ray interacts with a loosely bound electron transferring a fraction of its energy to the recoil electron as seen in Fig. 3.2b. The incident gamma ray deflected through an angle, θ, resulting in the reduction in energy of the gamma-ray. The most important consequence of Compton scattering is the energy transferred to the recoiling electron, E_e, which depends upon the scattering angle of the gamma-ray. The Compton scattering coefficient decreases

with increasing energy and it is almost independent of the atomic number. The energy of the recoil electron is given as:

$$E_e = E_\gamma - E'_b. \tag{3.3}$$

where E'_b is the binding energy of the electron.
If the electron is initially at rest and unbound with a rest mass of $m_e c^2 = 511$ keV, the expression relating the energy transferred and the scattering angle for a given interaction is derived as;

$$E'_\gamma = \frac{E_\gamma}{1 + \frac{E_\gamma}{m_e c^2}(1 - \cos\,\theta)}. \tag{3.4}$$

where E'_γ is the final energy of the gamma-ray, E_e is the energy transferred to the electron and E_γ is the incident gamma-ray energy.
The energy transferred depends upon the scattering angle; a small scattering angle transfers little energy. θ varies from 0° (where minimum energy transferred occurs) to 180° (where the maximum energy transfer occurs). In reality, the recoil electron, bound to the atom, is not at rest, rather moving within an atomic orbital. The result of this motion is the further spread of energies called Doppler broadening. This effect is more noticeable in high Z absorbing materials and lower energy incident gamma-rays [73].
The angular distribution for scattering gamma-rays can be predicted by a differential scattering cross section, $\frac{d\sigma}{d\Omega}$ known as the Klein-Nishina distribution as shown in Equation 3.5

$$\frac{d\sigma}{d\Omega} = Zr_e^2 \left(\frac{1}{1 + \alpha(1 - \cos\theta)}\right)^2 \left(\frac{1 + \cos^2\theta}{2}\right) \left(1 + \frac{\alpha^2(1 - \cos\theta)^2}{(1 + \cos^2\theta)[1 + \alpha(1 - \cos\theta)]}\right). \tag{3.5}$$

where $\alpha = \frac{E_\gamma}{m_e c^2}$ and r_e is the classical electron radius.
The graphical representation of the Klein-Nishina distribution describes a strong tendency for forward scattering at high values of the gamma-ray energy, while lower energy gamma-rays are scattered in a more symmetrical distribution about 90° as seen in Fig. 3.3.

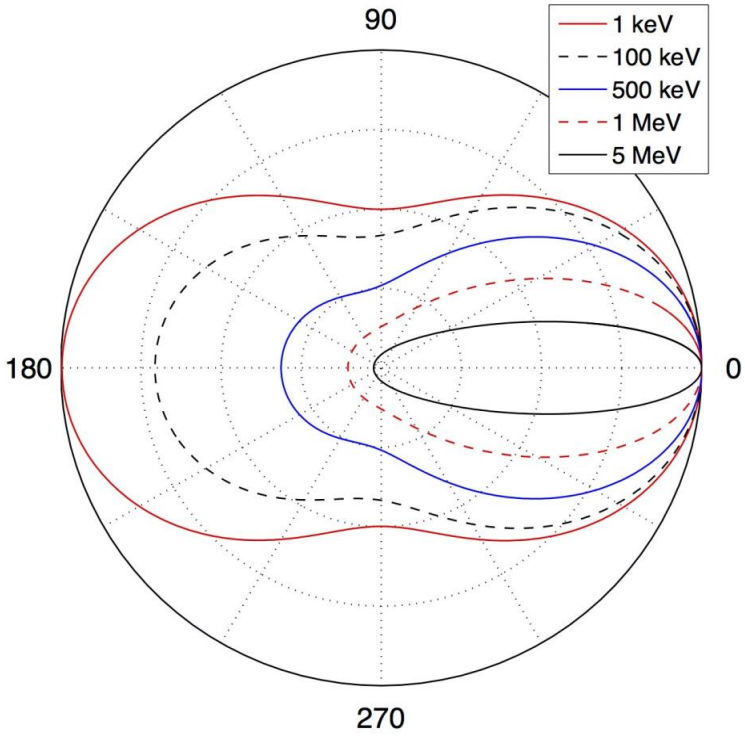

Figure 3.3: The Klein-Nishina distribution shows that Compton scatter in higher energy gamma-rays are in the forward direction [52, 67].

3.1.3 Pair Production

In pair production, gamma-ray interacts with the strong electromagnetic field surrounding the nucleus as shown in Fig. 3.2c, converting its energy into two electrons, one of which is positively charged (the positron) and the other negatively charged (the electron). The incident gamma-ray is required to possess an energy not less than twice the rest-mass energy of an electron (1.022 MeV) before the process of pair production can occur. Any energy in excess of double the electron mass goes into kinetic energy that is shared by the positron and electron. The positron then travels through the material dissipating its kinetic energy and eventually getting annihilated by a free electron to produce two 511 keV annihilation gamma-ray peaks at 180° from each other. These two annihilation gamma-rays can be partially or fully absorbed within the material, although one or both may escape resulting in escape peaks visible in gamma-ray spectra of most radionuclides [52].

3.2 Gamma-Ray Attenuation

The attenuation of gamma-rays results from a combination of absorption and scattering in materials. Gamma-ray penetration in material is statistically controlled

by the probability per unit distance travelled when a gamma ray interacts by one or two physical processes. If an incident gamma-ray beam of intensity, I_o, collides perpendicularly with an absorber of thickness x, the intensity I_x traversing through the absorber is given as;

$$I_x = I_o e^{-\mu_l x}. \tag{3.6}$$

where μ_l is the probability per unit distance of the interaction known as the linear attenuation coefficient. Equation 3.6 suggests that theoretically complete absorption of a beam of gamma-rays never really occurs, but in a practical sense exponential attenuation and/or absorption can be used to reduce most of the beam intensities to an imperceptible level.

The linear attenuation coefficient (LAC) describes the fraction of a beam of gamma-rays that is either absorbed or scattered per unit thickness of the absorber at a particular energy. μ_l depends on the absorber's atomic number, thickness and density as well as the energy of the gamma-rays. The linear attenuation coefficient increases as the atomic number of the absorber increases. It decreases as the gamma-ray energy increases. Similarly, the higher the density of the absorber, the lower the linear attenuation coefficient and the thicker the absorber, the greater the attenuation. Since the linear attenuation coefficient varies with the density of the absorber, the mass attenuation coefficient, which does not change with the physical state of the absorber, is widely used. The relationship between the linear and mass attenuation coefficients is given as;

$$\text{Mass Attenuation Coefficient}, \mu_m = \frac{\text{LAC}}{\text{Density}} = \frac{\mu_l}{\rho}, \tag{3.7}$$

where, ρ represents the density of the material measured in gcm^{-3}. A plot of the mass attenuation coefficient as a function of the gamma-ray energy for germanium is shown in Figure 3.4. This mass attenuation coefficient, μ_m, represents the measure of the average number of interactions between incident gamma-rays and matter per unit area thickness of the material.

For the mass attenuation coefficient, equation 3.6 could be written as

$$I_x = I_o e^{-\frac{\mu_l}{\rho}(\rho x)}, \tag{3.8}$$

where ρ is the density of the absorber and ρx is the mass thickness of the absorber. From Equation 3.7, the linear attenuation coefficient can be seen as the product

of the mass attenuation coefficient and the density of the material.

$$\mu = \left(\frac{\mu_l}{\rho}\right) \times \rho. \tag{3.9}$$

Since the linear attenuation coefficient is connected to the probability that an interaction will occur in a given distance, the reciprocal of this defines the average distance travelled by a gamma-ray before interacting with material. This is known as the mean free path, λ, of the gamma-ray and is defined as

$$\lambda = \frac{1}{\mu_l}, \tag{3.10}$$

with typical values of λ varying from a few mm to cm. The mean free path for a gamma-ray energy of 661.67 keV will be approximately 2.5 cm in germanium.

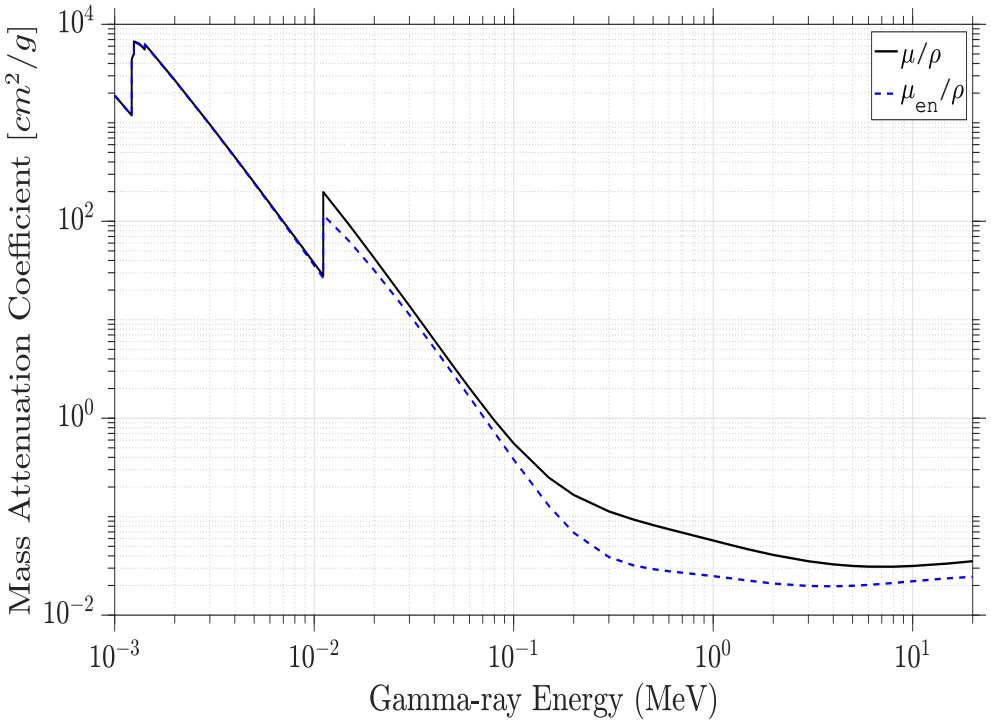

Figure 3.4: Plot of mass attenuation coefficient, μ_l/ρ, and mass energy absorption coefficient, μ_{en}/ρ, as a function of gamma-ray energy for germanium (Z = 32). Data reproduced from [48].

The mass energy-absorption coefficient, μ_{en}/ρ, on the other hand, is the measure of the average fractional amount of incident gamma-ray energy translated into the kinetic energy of charged particles as a result of interactions between gamma-rays and atoms in materials. It is essentially important in estimating the absorbed dose in medical and health physics, industrial and agricultural irradi-

ation technology and other practical situation involving gamma-ray effects and metrology [47].

3.3 Basic Properties of Gamma-ray Detectors

Once the gamma-rays have been attenuated by the absorbing materials, they interact with the detector. This section deals with the basic properties for any suitable detector for effective interactions with gamma-rays.

3.3.1 Detector Efficiency

The probability that an emitted gamma-ray interacts within the volume of a detector and produces a pulse or signal is regarded as the efficiency of that detector. All radiations emitted from a radioactive source are not incident on the detector as some will get scattered while others are absorbed by the surrounding materials. This is an indication that a radiation detector cannot record all the radiations impinging on it from the radioactive source. The interaction of the radiation incident on the active volume of a typical semiconductor detector induces ionisation or excitation which produces ion pairs. The collection of the ion pair generates a pulse (or signal) that is recorded by the detector. Ideally, the detector efficiency will be 100 % if all the radiations incident on it generate a pulse, in reality however, the detector efficiency is always less than 100 % as all the radiations do not generate a pulse or unable to record a pulse generated. The efficiency of such a detector will therefore be measured either by the absolute efficiency, ε_{abs}, or/and intrinsic efficiency, ε_{int}, and are defined as

$$\varepsilon_{\text{abs}} = \frac{\text{Number of } \gamma \text{ rays detected}}{\text{Number of } \gamma \text{ rays emitted by the radioactive sources}} \tag{3.11}$$

and

$$\varepsilon_{\text{int}} = \frac{\text{Number of } \gamma \text{ rays detected}}{\text{Number of } \gamma \text{ rays incident on the detector}}. \tag{3.12}$$

The number of gamma rays detected represent the number of counts contained within the photopeak. The absolute efficiency depends not only on the properties of the detector but also on the distance of the detector from the source. The intrinsic efficiency, unlike the absolute efficiency, is independent of the solid angle subtended by the detector as it is the basic parameter of the detector but depends primarily on the radiation energy and the detector material. Absolute and intrinsic efficiencies can as well be expressed as the full-energy peak efficiency which takes

into account only the photons which result in the full-energy peaks. The relative efficiency of a detector usually compares the absolute efficiency of a detector to a 76 x 76 mm NaI(Tl) detector, irradiated by 1332.5 keV γ ray from a ^{60}Co source at a distance of 25 cm from the centre of the endcap of the detector. The absolute peak efficiency of this 76 x 76 mm NaI(Tl) is 1.2×10^{-3}. In applications involving radioactivity quantification in radioactive waste characterisation, a highly efficient detector is usually required for the calculation of the activity concentration in a waste drum.

3.3.2 Detector Resolution

Energy resolution is the measure of the ability of the detector to distinctively resolve gamma-rays with close energies. It involves measuring the width of the peaks in a gamma-ray spectrum. The smaller the width of the photopeak, the higher the resolution and the better the resolving power of the detector. In gamma-ray spectroscopy, the differential pulse height distribution produced by a detector can exhibit fluctuation in width for gamma-ray peaks. These fluctuations reflect the fact that a variation in pulse to pulse was recorded even when the same energy was deposited in the detector for each event. Making the amount of these fluctuations smaller, reduces correspondingly the width and the peak approaches a sharp spike. This width becoming smaller enhances the ability of the detector to resolve a complex spectrum of closely related peaks. The parameter utilised for the measurement of the peaks width is the full width at half maximum (FWHM) of the photopeak, defined as the width of the distribution at a level which is just half the maximum ordinate of the peak. Then, the ratio of the FWHM to the energy value of the peak centroid is the energy resolution. The potential sources of the width fluctuation that result in poor energy resolution are the statistical spread in the number of charge carriers, variations in the charge collection efficiency and the contributions of electronic noise within the detector and instrumentation system. These are represented by the quadrature of the FWHM values of the individual sources as:

$$(\mathrm{FWHM})^2_{\mathrm{overall}} = (\mathrm{FWHM})^2_{\mathrm{statistical}} + (\mathrm{FWHM})^2_{\mathrm{noise}} + (\mathrm{FWHM})^2_{\mathrm{collection}} \tag{3.13}$$

The $(\mathrm{FWHM})^2_{\mathrm{statistical}}$ is due to the statistics associated with the charge production process in the detector which arises because of the discrete number of charge carriers generated within the detector, and is mathematically given as;

$$(\mathrm{FWHM})^2_{\mathrm{statistical}} = (2.35)^2(\mathrm{F}.\mathrm{E}_\gamma.\varepsilon) \tag{3.14}$$

where F is the Fano factor, E_γ is the gamma-ray energy and ε is the energy required to create an electron-hole pair. It can be seen that, $(\text{FWHM})^2_{\text{statistical}}$ is proportional to the gamma-ray energy, E_γ, meaning that the predicted uncertainty at higher energies (such as 1332.5 keV) is significantly large compared to the overall statistical uncertainty in Equation 3.13. This indicates that the processes that give rise to the formation of each individual charge carriers are not independent, and thus the overall number of charge carriers cannot be described strictly by Poisson statistics. The Fano factor, F, is then introduced to bridge the discrepancy between the observed statistical uncertainty in the number of charge carriers from that predicted by Poisson statistics, and can be defined as

$$\text{F} = \frac{\text{observed variance in the number of charge carriers}}{\text{the variance predicted by the Poisson statistics}} \tag{3.15}$$

The Fano factor for germanium detectors varies from 0.057 to 0.12 [35]. A Fano factor of 0.099 has been used for all modelling in this work (details in Section 5.2.1.3). The high energy resolution of germanium detector makes them suitable for complex spectroscopic applications such as hotspot localisation within the radioactive waste drum/containers.

3.4 Semiconductor Detectors

The choice of semiconductor detectors in gamma-ray spectroscopy over gas-filled detectors is due to its dense active medium and ionisation potential which is about 10 times smaller in solid state than in gaseous state. Additionally, it provides better statistics regarding the number of signal carriers generated by a radiation interaction than either gas-filled detectors or scintillation detectors. While it takes between 25 and 40 eV to produce an electron-ion pair in a gas-filled detector, and between 0.1 to 1 keV to eject a photoelectron from the photomultiplier tube of a scintillation detector, it takes on average, 3-5 eV to produce an electron-hole pair in a semiconductor [39]. Therefore, more charge carriers are produced by a semiconductor from a primary ionisation event thereby reducing the statistical fluctuations in the energy resolution. Semiconductors have limited number of electrons because their atoms are closely packed together in a crystalline form known as crystal lattice, such that the various potentials of each of the atoms affects the surrounding neighbours and those electrons associated with them. As the field of semiconductor detectors is too vast to cover, this sections offers basic operation and characteristics of semiconductor detectors, while a detailed description can be found [39, 89].

3.4.1 Band Structure

Electrons in a free atom are confined to determined energy levels. These energy levels are broadened into energy bands with a fixed number of electrons by the aggregation of atoms into a solid structure. The energy regions between these bands are forbidden to electrons. The two most common bands of interest in semiconductor materials are the valence band and the conduction band. The valence band which is responsible for chemical reactions corresponds to outer-shell electrons that are bound to specific lattice sites within the crystal. The conduction band, on the contrary, represents electrons which can move freely throughout the crystal and as such directly contribute to the electrical conductivity of the semiconductor. The gap between these bands is referred to as the band gap or energy gap. Classification of materials into insulators, semiconductors and conductors depends hugely on the size of the energy gap as illustrated in Figure 3.5.

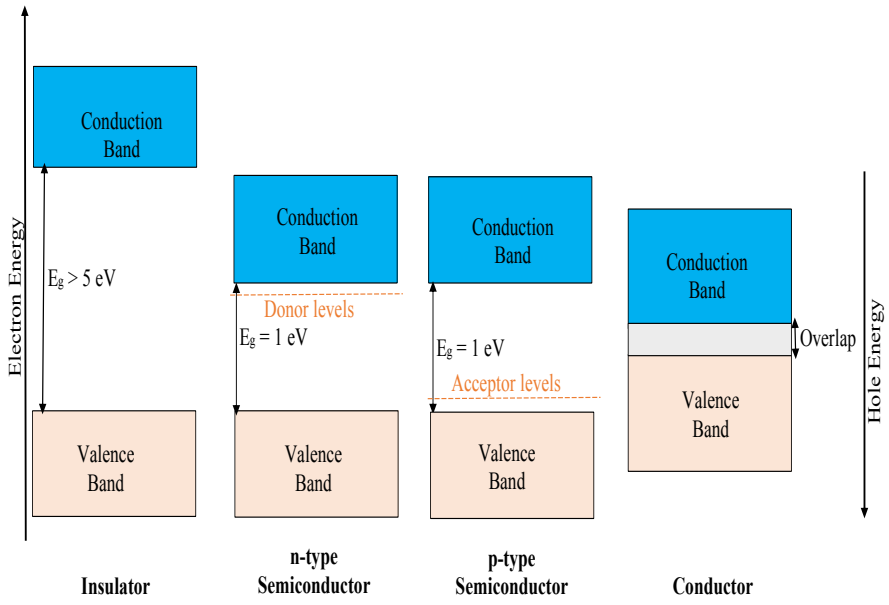

Figure 3.5: Schematic illustration of energy bang gap for semiconductors, conductors and insulators.

The valence band in an insulator is completely full and the available energy states in the conduction band is separated by a band gap with a minimum value of 5 eV. The energy produced by thermal excitation is insufficient to promote electrons. Therefore, for an electron to migrate through the insulator material, it must gain sufficient energy to jump from the valence band across the wide band gap into the conduction band. For conductors, the conduction and valence bands are either overlapped or the valence band is not full occupied which means there

are always electrons free to move through the material. Semiconductors have a valence band full like insulators, except that the band gap of about 1 eV between the bottom of the conduction band and the top of the valence band permits thermal excitation of electrons. The thermal excitation of electrons leaves a positively charged vacancy known as a hole in the valence band. The excited electron and the hole are referred to as electron-hole pairs and are the charge carriers in semiconductor materials. The probability per unit time that an electron-hole pair is thermally generated is given by

$$p(T) = CT^{3/2}exp\left(-\frac{E_g}{2kT}\right) \tag{3.16}$$

where T is the absolute temperature, E_g is the energy gap, C is the material dependent constant and k is the Boltzmann constant. It can be seen from Equation 3.16 that the probability of thermal excitations for semiconductors with small band gaps, strongly depends on the temperature of the detector. So operating a semiconductor detector such as a germanium detector at room temperature is practically impossible due to its small band gap energy which generates unbearable leakage current. Because of this, germanium detectors need to be cooled and maintained at 77 K either with liquid nitrogen or with a mechanical cooling system before use in gamma-ray spectroscopy. Creation of electron-hole pairs is the main technique by which the semiconductor detects gamma-rays. Electron-hole pairs are created along the path of the charged particle when it passes through a semiconductor.

3.4.2 Intrinsic and Extrinsic Semiconductors

Intrinsic semiconductors are pure forms of semiconductor materials without any impurity atoms. In the intrinsic semiconductor, the valence band is completely filled while the conduction band is empty at room temperatures. However, electrons can be made to migrate if there is an increase in temperature. The conductivity of an intrinsic semiconductor is so low at room temperature that it cannot be effectively utilised in fabricating important electronics devices.

Improving the conductivity of intrinsic semiconductors by the addition of impurities to the pure semiconductor materials constitutes the extrinsic semiconductors. The impurity atoms, known as dopants could be either group III or group V elements, and the deliberate addition of an impurity to a semiconductor is referred to as doping. The impurity will be added such that there is no distortion on the original lattice structure of the intrinsic semiconductor, rather, the impurity

occupies few of the original semiconductor atom sites in the crystal.

3.4.3 p-n Junction

The electronic properties of semiconductors can be changed by introducing impurities, a process known as doping. Silicon or germanium atoms contain four valence electrons which bind covalently to another four additional atoms. However, on introduction of impurities by adding a control amount of either pentavalent or trivalent, the lattice will possess an excess of holes or electrons. The new semiconductor materials are known as n-type (pentavalent doped) and p-type (trivalent doped).

When a p-type semiconductor material is treated with n-type semiconductor material to form a p-n junction, there is a tendency for the free electrons to diffuse over to the p-side and holes to the n-side at the boundary, which result in a region empty of charge carriers in the vicinity of the interface of the two materials. This region, over which free charge carriers have been diffused away, is known as the *depletion region*. The depletion region is the active volume of the detector but very thin. If reverse bias is applied to the detector, in which the p-type receives a negative bias and n-type receives a positive bias, the depletion region can be increased. The bias causes the remaining electrons and holes to migrate towards their respective contacts, thus increasing the active volume of the detector. The thickness of the depletion region, d, and the net impurity concentration, N, within the semiconductor material are related by [52],

$$\mathrm{d} \cong \left(\frac{2\epsilon \mathrm{V}}{\mathrm{eN}}\right)^{\frac{1}{2}} \tag{3.17}$$

where ϵ is the dielectric constant, e is the electronic charge, and V is the applied voltage.

3.4.4 High Purity Germanium Detector

Germanium remains the semiconductor material of choice for several detector applications. It has a much larger linear attenuation coefficient due to its higher atomic number, and as a result, shorter mean free path when compared to other semiconductor devices like silicon. It can be seen from Equation 3.17 that the depletion depth is inversely proportional to the net impurity concentration, the lower the net impurity concentration, the higher the depletion depth. Germanium, of typical semiconductor purity, can only achieve a maximum depletion depth of

a few mm even when a bias voltage close to breakdown level is applied. Therefore, the net impurity concentration should be reduced down to 10^{10} $atoms/cm^3$ in order to achieved the depletion depths of cm that is required. One existing way to improve the net impurity concentration is by compensating the residual impurity with an opposite type impurity material. Since the material with highest available impurity in Ge is the p-type, an addition of donor atoms from the alkalis metals like Li, form interstitial donors. The donor atoms when introduced into Ge under the influence of a strong electric field get ionised and become mobile enough to drift at high temperature, a process known as *Lithium ion drifting*. The process has been utilised to developed Ge(Li) and Si(Li) detectors. Another way of improving the net impurity concentration is by the addition of refining processes to achieve required purity of the crystal. This leads to the development of *High Purity Germanium* (HPGe) detectors. HPGe detectors are semiconductor detectors that are produced from refined ultrapure germanium with net impurity concentration tending as low as 10^{12} atoms/cm^3, in order to achieve a depletion depth of several centimeters with a reverse bias voltage less than 1 kV [52]. Table 3.1 illustrate the relevant properties of germanium.

Table 3.1: Properties of Intrinsic Germanium [35].

Properties of Intrinsic Germanium	Ge
Atomic Number	32
Atomic weight	72.60
Density (300K); g/cm^3	5.32
Atoms/cm^3	4.41×10^{22}
Dielectric constant (relative to vacuum)	16
Intrinsic carrier density (300K); cm^{-3}	2.4×10^{13}
Intrinsic resistivity (300K); $\Omega.cm$	47
Electron mobility (300K); $cm^2/V.s$	3900
Hole mobility (300K); $cm^2/V.s$	1900
Electron mobility (77K); $cm^2/V.s$	3.6×10^4
Hole mobility (77K); $cm^2/V.s$	4.2×10^4
Energy per electron-hole pair (77K); eV	2.96

This work utilises a broad energy germanium (BEGe) planar geometry made from germanium with an impurity profile capable of improving charge collection at high energies. The detector has a fat but short shape which greatly improves the efficiency below 1 MeV. We can see from Table 3.1, 2.96 eV is required to produce an electron-hole pair enabling a large number of charge carriers to be generated for a given initial gamma-ray, placing germanium at higher advantage to silicon (which require 3.76 eV), scintillator or gas detectors in terms of energy resolution. As the energy resolution is a function of statistical fluctuations, the increase in charge

carrier explicitly minimises the influence of large fluctuations thereby, essentially, improving the overall resolving power of the germanium detectors.

3.5 Compton Camera

A Compton camera is a gamma-ray detector with the capacity to image point or extended radiation sources by using the Compton scattering process. The system is capable of detecting gamma-rays of a very wide range of energies from 100 keV to over 1 MeV. The camera system produces voltage pulses which are proportional to the energy deposited in the detector crystal by the gamma-ray. It offers a potential gain to other forms of camera such as pinhole type, [99, 31, 30, 111], or coded aperture type [110] in that the Compton camera does not require any collimation to define spatial position [36].

Typically, the Compton camera system consist of two or more detectors separated by a defined distance. The requirement for two or more detectors is based on the ease of separating the two interactions of a gamma-ray. However, one detector could be utilised if it is possible to isolate the interactions within the single volume. The first detector known as the scatterer detector is used in detecting Compton interactions. The recommended materials for this component of the Compton camera are silicon, germanium or argon. Silicon is considered a very good material for the scatterer detector because the Doppler broadening effect is observed to be smaller in silicon devices than other semiconductors.

The second detector which is used to absorb the scattered gamma-ray is called the absorber detector. Typical materials of high photo-absorption cross sections such as NaI, CdZnTe, BGO and xenon are preferred choices for the detector. Gamma-ray imaging with Compton camera was proposed by [85] for astronomical applications and later it was used in medical applications [95]. In homeland security, the goal of the Compton camera is to provide improved capabilities to detect, localise, and characterise nuclear materials by passive means without compromising the environment [114, 68]. Theoretically, gamma-ray emissions from nuclear materials could be passively detected at a distances greater than 100 metres. However, detection at this range has long been thought to be impractical due to spatially fluctuating levels of natural background radiation. These fluctuations are the major sources of uncertainty in detection which indicate that sensitivity cannot be increased simply by increasing detector size. Recent work has shown that this problem can be overcome through the use of imaging techniques [114]. With the Compton imaging, the estimation of the local background is achievable, making it possible to detect spatially localised radioactive sources from consid-

erable distances [46]. In radioactive waste, the huge volumes of wastes have to be characterised as low, intermediate or high level radiation prior to disposal or final storage. The Compton camera can be utilised to identify hotspots in waste drums/barrels of largely low level materials but with few localised intermediate radioactive spots, which can be safely removed if possible, allowing the remaining material to be disposed as low level waste. This will significantly reduced cost and volume of high radioactive wastes. The ability of the Compton camera to obtain a localised image of hotspots in waste containers from a fixed viewpoint is a significant advantage over other imaging techniques that require scanning of the container.

3.5.1 Principle of Operation

A gamma-ray incident on the Compton camera system undergoes Compton scattering in the scatterer detector depositing a fraction of its energy where the position and energy of interaction are measured, and then interact via photoelectric absorption depositing its remaining energy in the absorber detector where the position and the energy of absorption are similarly measured [79]. For useful events to be recorded, the gamma-ray signatures measured by both detectors have to satisfy coincidence requirements to ensure that those events are from the same sources. By measuring the energies and positions of the two interactions, the Compton scattering angle θ, could then be calculated by rearranging the Compton kinematics equations 3.3 and 3.4.

$$\cos\,\theta = 1 - \frac{\mathrm{E}_1}{\alpha(\mathrm{E}_0 - \mathrm{E}_1)} \tag{3.18}$$

Where E_1 is the energy deposited in the scatter detector, $\mathrm{E}_0 = \mathrm{E}_1 + \mathrm{E}_2$ is the initial gamma-ray energy, E_2 is the energy deposited in the absorber detector and $\alpha = \frac{\mathrm{m_e c^2}}{\mathrm{E}_0}$ with $\mathrm{m_e c^2}$ being the rest mass of an electron. The scattering angle is used to form a cone where its apex angle is given by 2θ for each incident gamma-ray. The axis of the cone is the vector difference between the interaction positions in the scatter and absorber detectors and the radioactive source is a point on the surface of the cone produced as shown in Fig. 3.6. The source of radiation can be found at a point of maximum interactions of the generated cones by reconstructing many of these events.

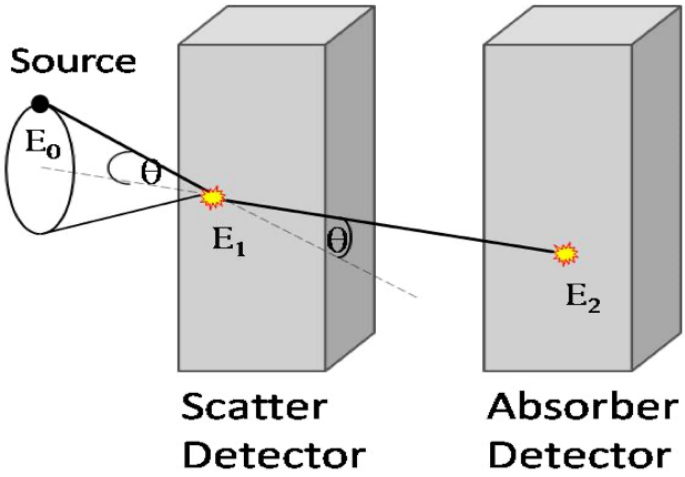

Figure 3.6: A schematic diagram of a dual planar detector Compton camera system showing the cone produced for one incident gamma-ray.

Chapter 4

Image Reconstruction Techniques

In a segmented gamma-ray scanning system, rotating a mechanically collimated detector around a radioactive waste container provides 2D images of a 3D distribution at various angles, known as projections. These projections are typically formed on a grid of pixels, each of which contains the number of gamma-rays absorbed by the detector that have successfully traversed through the radioactive waste drum wall and matrices. Thus, the relative number of photons in each pixel provides information about the location of the radioactive source within the drum. Image reconstruction is the procedure for putting these projections together to obtain a clear image of the object. The two most commonly used image reconstruction algorithms are the iterative reconstruction and analytical reconstruction [10, 101]. One main example of iterative reconstruction is the maximum likelihood expectation maximization (MLEM) method, while that of analytical reconstruction is filtered back projection (FBP). The reconstructed tomographic image quality depends on the attenuation and scattering of the gamma-ray within the materials or matrices, the detection efficiency and the spatial resolution of the collimator-detector system [15]. The resultant effects of these factors are poor spatial resolution, low contrast and high noise level observed on the image. These effects are reduced using image filters during reconstruction to improve the image resolution and limit the degradation of the image.

4.1 Iterative Reconstruction

Iterative reconstruction algorithms are a form of image reconstruction that involve successive approximations, or estimates to obtain the true image of objects. It starts with an initial estimate which may be simple. Then, using a mathematical process known as forward projection, a set of projection data is estimated from the initial estimate. The difference between the resulting and recorded projections

is used to make further estimates. The basic process of iterative reconstruction is the discretisation of the image into pixels, then generating a system of linear equations from the discretised pixels according to the imaging geometry and underlying physics. The final process is solving the generated linear equations by an iterative algorithm [113]. The whole process of iteration is repeated until the difference between the calculated and measured data is smaller than a preselected value. One of the examples of iterative reconstruction is the maximum likelihood expectation maximization (MLEM). MLEM provides solutions to a set of linear equations by incorporating the Poisson nature of the acquired data into the reconstruction algorithm. The main advantages of MLEM reconstruction algorithm over an FBP is that the projection data are not required to be equally spaced, it can utilise incomplete sets of projection data, and produces fewer artefacts in the reconstructed images [17].

4.2 Analytical Reconstruction

The limitation of the iterative reconstruction methods is that they are based on a more complex mathematical solution which requires multiple steps before a reconstructed image is obtained. The alternative is to use analytical reconstruction methods that employ a direct mathematical solution to obtain a reconstructed image.

4.2.1 Filtered Back Projection

The filtered back projection (FBP) technique remains a widely applied method of image reconstruction. In FBP, the values of attenuation coefficients are computed using sets of equations of gamma-ray sums taken at different angles of a sine wave. The measurement data for these equations are obtained through *projections*, which represent the recorded counts (line integral) by detection of gamma-rays emitted from radioactive sources. A graphical display of all of the different projections for a given slice stacked together shown in Figure 4.1b, is known as the *sinogram*. Since image reconstruction intends to reproduce the original image of a low level waste drum represented as Figure 4.1a, these projections are redistributed at each particular point back along a line from which they were originally detected, a technique known as *back projection* as seen in Figure 4.1c. The back projection process is repeated for all angles and all pixels to obtain a clear reconstructed image of the object. It therefore means that as the projection gets data from an image, back projection produces an image from the data that has been calculated during the projection process.

Apparently, one problem associating with back projection is that counts are unavoidably projected outside the true location of the object, resulting in blurring (star-like artefacts) of its image as clearly shown in Figure 4.1c. Although, the quality of the image can be improved by increasing the number of projections, still that will not totally correct the blurred image. Filtered back projection as a form of analytic reconstruction algorithm is developed to overcome this particular limitation of the back projection. It applies a convolution filter to remove blurring as illustrated in Figure 4.1d. Two steps involved in FBP are filtering of data and subsequently back projecting the filtered data [38].

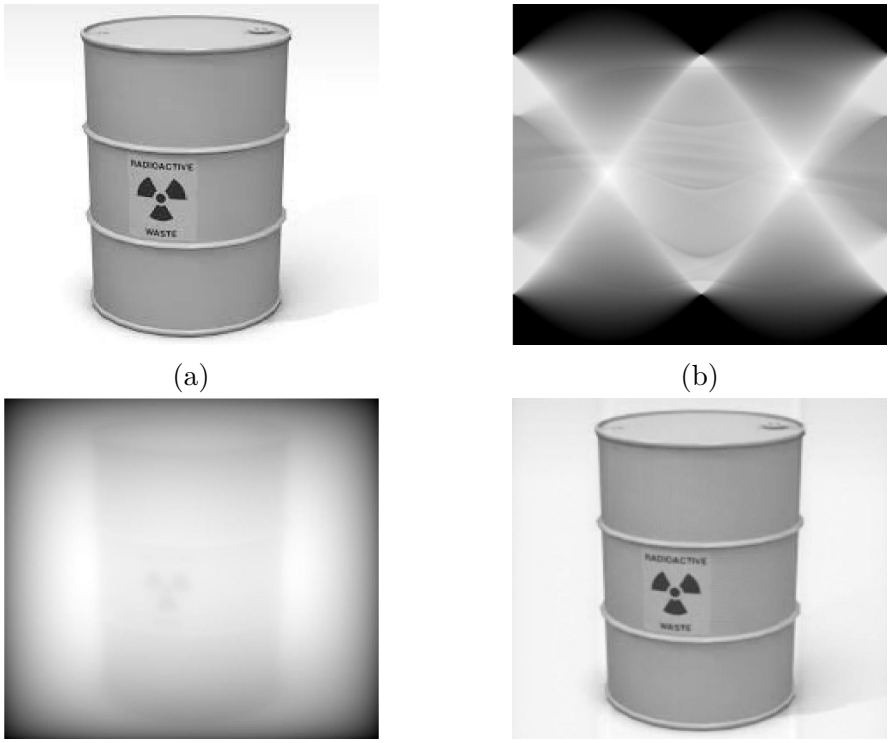

Figure 4.1: Density plot of a low level waste drum (a) Original waste drum, (b) The sinogram of the waste drum, (c) back projection of the waste drum, (d) filtered back projection of the waste drum.

4.2.2 Basic Concepts

The Lambert-Beer law [28] of attenuation states that a gamma-ray passing through a homogeneous material of length x and with constant attenuation coefficient, μ_0, will produce an intensity of magnitude

$$\mathrm{I} = \mathrm{I}_0 \exp^{-\mu_0 \mathrm{x}}. \tag{4.1}$$

where I_0 is the initial intensity of the gamma-ray at the radiation source, I is the final intensity of each gamma-ray beam at the radiation detector. In some materials, the attenuation coefficient $\mu(x)$ is a function along the gamma-ray's path, thus the intensity produced becomes

$$\mathrm{I} = \mathrm{I}_0 \exp^{-\int_{\mathrm{L}} \mu(\mathrm{x})\,\mathrm{dx}}. \tag{4.2}$$

Rearranging Equation 4.2 into line integral form

$$-\log\left(\frac{\mathrm{I}}{\mathrm{I}_0}\right) = \log\left(\frac{\mathrm{I}_0}{\mathrm{I}}\right) = \int_{\mathrm{L}} \mu(\mathrm{x})\mathrm{dx}. \tag{4.3}$$

Changing the orientation of the source and detector, and measuring the corresponding intensity change, and solving the attenuation coefficient, provides further information about the internal density of the material. In a two dimensional plane (x, y), Equation 4.3 becomes;

$$-\log\left(\frac{\mathrm{I}}{\mathrm{I}_0}\right) = \log\left(\frac{\mathrm{I}_0}{\mathrm{I}}\right) = \int_{\mathrm{L}} \mu(\mathrm{x(s)}, \mathrm{y(s)})\mathrm{ds}. \tag{4.4}$$

If (l, θ) defines each projection line which can be measured, and any point on this projection line, (x, y), is specified by either $x(s) = l\ cos\ \theta - s\ sin\ \theta$, and $y(s) = l\ sin\ \theta + s\ cos\ \theta$ or $x\ cos\ \theta + y\ sin\ \theta = l$, then, a transformation from μ(x, y) to projections $g(l, \theta)$ known as a Radon transform [10, 28] could be written as

$$\begin{aligned} g(l,\theta) &= \int_L \mu(x,y)dl. \\ g(l,\theta) &= \int_{-\infty}^{\infty}\int_{-\infty}^{\infty} \mu(x,y)\,\delta(x\cos\theta + y\,sin\,\theta - l)dx\ dy. \end{aligned} \tag{4.5}$$

Therefore, $g(l, \theta)$ is the Radon transform of $\mu(x, y)$. The Radon transform determines the total density of certain function, μ, along a given line l.

$$g(l, \theta) = \mathbf{R}\{\mu(x, y)\}. \tag{4.6}$$

The simplest method of calculating $\mu(x, y)$ from $g(l, \theta)$ is back projection which reconstructs the original object from the summation of all projections. To achieve this, an image is generated for each corresponding value of θ, using

$$b_\theta(x, y) = g(l, \theta) = g(x\ cos\theta + y\ sin\theta, \theta). \tag{4.7}$$

Adding all the back projected images together

$$\mu_b(x,y) = \frac{1}{N}\sum_{i=1}^{N} g(x\,cox\theta_i + y\,sin\theta_i, \theta_i). \tag{4.8}$$

As mentioned before, one inherent problem with back projection is the blurring of the images produced. This simply means that $\mu_b(x,y) \neq \mu(x,y)$. This can be corrected by modifying or filtering the profile [38]. The Radon transform is related to the Fourier transform by the *central slice theorem* [28]. The F_1 and F_2 denoting the 1D and 2D Fourier transforms and the Radon transform, R, are related by

$$F_2\mu(\omega\ cos\theta, \omega\ sin\theta) = F_1(R\mu)(\omega,\theta). \tag{4.9}$$

The first step towards inverting the radon transform and estimation of the gamma-ray attenuation coefficient is through back projection. However, the result obtained depicts a smoothed-out function and not the original one. Filtered back projection is utilised to recover the original function and correct the smoothing effect. So filtering the Fourier transform of $R\mu$ by multiplying by ω, a filtered back projection equation is obtained.

$$\mu(x,y) = \frac{1}{2}B\{F^{-1}[|\omega|]F(R\mu)(\omega,\theta)]\}(x,y). \tag{4.10}$$

Equation 4.10 indicates that multiplying the Fourier transform of $R\mu(\omega,\theta)$ by the absolute filter value, $|\omega|$, before carrying out the inverse Fourier transform is fundamentally the essential step for getting image reconstruction very close to the original image. This therefore means that the original image, μ, can be reconstructed from the sinogram, g, by first applying a filter and then back projection, a procedure that will be utilised in the work to reconstruct the radioactive sources inside a waste drum.

4.3 Image Filtering

We have seen from Figure 4.1d that recovering the original image requires a technique that enhances and modifies the image obtained from back projection. Such technique is known as filtering. This filtering in FBP takes a form of simple mathematical equations of varying frequency. The basic functions of this filter include reduction of star artefacts, noise suppression and signal enhancement. There are various types of filter utilised in reduction of frequency information through an amplitude-adjusting function between 0 and 1 Nyquist as shown in Figure 4.2. Depending on the value of the cut-off frequency, a filter could be classified as a

low-pass frequency or a high-pass frequency. The value of this cut-off frequency determines how the image noise and resolution of a given filter are influenced. Low-pass filters allow low frequency components while cutting off the high frequency components. The cutting off of low frequency increases the smoothing of the reconstructed image while worsening the image contrast. *Hanning* and *Hamming* filters [28, 60] are both examples of low-pass filter that are effective in reducing the image noise. Both only differ in amplitude on the cut-off frequency. Another example of a low-pass filter is the $Shepp - Logan$ filter [28, 60] which produces less smoothing than other low-pass filters but with a resolution far better than others. The low-pass filter mostly used for smoothing in image reconstruction is the *butterworth* filter. Significantly, the butterworth filter is characterised by the critical frequency and the order or power which varies the slope of the filter [51]. The butterworth filter can be utilised for both noise smoothing and image resolution because of its capacity to change both in critical frequency and order [60].

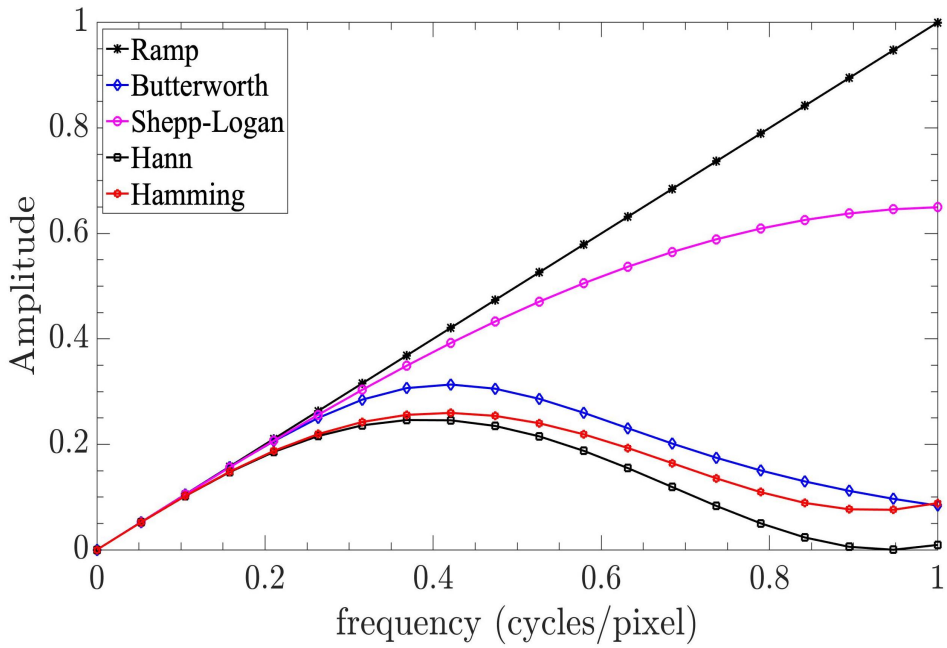

Figure 4.2: Types of filters utilised for high or low frequency components reductions. All filters shown allow low frequency component except ramp filter.

For a high-pass filter, the low-frequency components of the image are either removed entirely or drastically reduced, allowing high-frequency ones to appear on the reconstructed image. A high-pass filter can simply be obtained by subtracting a low-pass filtered image from the original image. An example of a high-pass filter is the *ramp* filter, that does not allow low frequency to pass through to form the image since it causes image blurring. For image sharpening, the ratio of the high-

frequency content to the low-frequency content is increased by adding a high-pass filter version of the image to the original image. The amplification of statistical noise in the measured gamma-ray counts is a serious limitation of a high-pass filter. The effect of this can however, be reduced by combining the ramp filter with a low-pass filter. As defined before, a filter acts either to smooth (reduce noise) image or amplify noise. If the effect of both low-pass and high-pass filters are not noticed after their implementation on an image, it typically indicates that the noise level on the image or data is very minimal.

4.4 Image Interpolation

Image interpolation as a basic tool used for image resizing, is the process of sampling known values at a point to estimate values at other unknown locations. Two broad categories of image interpolation are deterministic and statistical interpolation techniques. While statistical interpolation technique approximate the signal by minimising the estimation error, the deterministic interpolation techniques assumes variability between the sample points. As the statistical technique is computationally inefficient, deterministic techniques will be applied in the work for the smoothing of reconstructed images. Methods of deterministic techniques for image interpolation used in FBP reconstruction include:

Nearest: Being the most basic of all, nearest neighbour interpolation requires the least processing time because it only considers one pixel. This basically takes the pixel of the nearest position. The advantage of the nearest neighbour over others is its fast processing speed. However, it produces very poor quality images.

Linear: Being a first degree interpolation method, linear interpolation passes a straight line through every two consecutive points of the original image. Linear interpolation takes the weighted average of the closest 2×2 neighbourhood of known pixel values to find the surrounding unknown pixel.

Cubic: This is a simple cubic interpolation.

Spline: This is a form of interpolation where the interpolant is a special type of piecewise polynomial that tries to fit each division of the curve.

Pchip: This is a a special form of cubic interpolation which preserves the shape of the image.

V5cubic: This is a simple cubic interpolation from MATLAB 5.

Spline, pchip and v5cubic interpolations are forms of cubic interpolation. Therefore, the investigation of which forms of image interpolation to be adopted in this work will be limited to linear, nearest and cubic interpolation and this will be illustrated in chapter five.

Chapter 5

Detector Characterisation and Collimator Optimisation

The characterisation of broad energy germanium detectors employed in radioactive waste assay and other gamma-ray spectroscopy is being actively researched in the field of nuclear instrumentation. The purpose of the characterisation is to provide an in-depth understanding of the detector response to a range of gamma-ray energies. This is achieved through detailed experimental measurements and complete simulations of the detectors' response. This chapter is dedicated to reporting on the detailed characterisation and Monte Carlo simulations of the spectroscopic response of the broad energy Germanium (BEGe) detector and collimator optimisation used in this work.

5.1 Detector Specification

The detector used for this work is an electro-mechanically cooled broad energy germanium (BEGe) detector (Model BE6530) produced by MIRION formerly Canberra and situated at the Nuclear Physics Research Laboratory, (Precision Radiometrics Instrumentation Development and Education (PRIDE) laboratory) within the Department of Physics at the University of Liverpool. The temperature of the detector is maintained at 77 K by a Cryo-pulse 5® Plus cryostat. The dimensions of the detector crystal are 3.15 cm high and 9.15 cm in diameter as shown in Fig. 5.1b. It has a small boron-implanted p+ electrode of 1.35 cm in diameter which serves as the signal contact. The lithium-diffused n+ electrode covering most of the residual surface of the crystal, serves as the high voltage contact and is separated from the p+ electrode by an annular groove. The detector crystal is held by a copper cup in a 0.16 cm thick aluminium endcap and placed 0.8 cm from the front window as shown in Fig. 5.1a. The front window is made of 0.06

cm thick carbon epoxy producing a window to enhance the efficiency for detecting low-energy gamma rays that penetrate from the front. A bias voltage of +4000 V is recommended for the detector. Other major descriptions and specifications of the detector used are presented in Table 5.1 [8].

The data acquisition system used in this work is a charge-sensitive pre-amplifier, an integrated digital signal analyser and Maestro software. The pre-amplifier is integrated with the detector and pre-amplifies the charge signal from the p+ electrode. The digital signal analyser (DSA) integrates functions of the high voltage module, main amplifier module and multi-channel analyser module in an analogue electronics chain. The DSA records the signal pulse shapes from the pre-amplifier with a fast sampling ADC, extracts their energy information through firmware with the trapezoidal shaping algorithm and finally sends the information to the Maestro software, which addresses the production and storage of energy spectra.

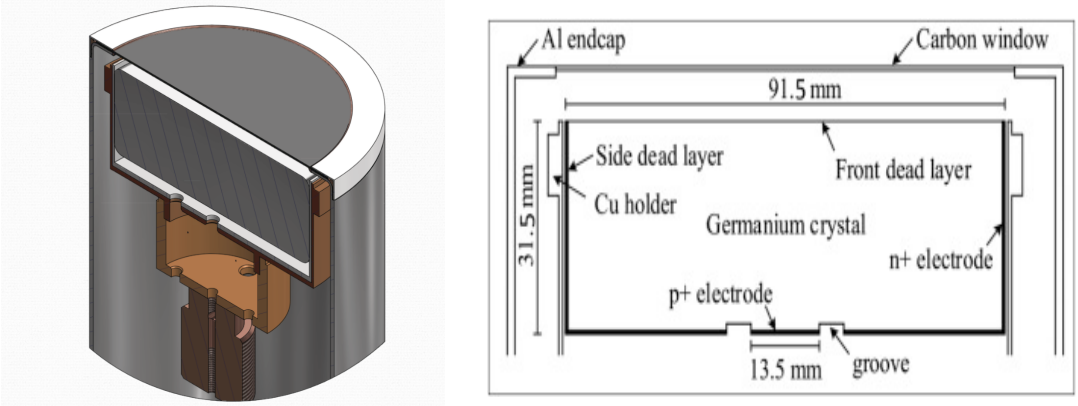

(a) BEGe Detector

(b) BE6530 Model

Figure 5.1: A schematic diagram of a BE6530 Detector (a) Ge detector with the dark top representing carbon epoxy from [8] (b) View of BEGe detector with dimensions and labels from [40].

Table 5.1: Specifications of BEGe detector used in the experimental measurements.

Descriptions	**Detector**
Detector type (Mirion)	BE6530
Detector geometry	Plane
Detector active area facing window (mm^2)	6500
Active crystal diameter (mm)	91.5
Thickness of crystal (mm)	31.5
Distance from window (outside) (mm)	5.0
Window thickness (mm)	0.6
Aluminum endcap distance from window (mm)	8.0
Window material	Carbon Epoxy
Relative efficiency at 1332.5 of ^{60}Co	60
Full Width Half Maximum (FWHM) Resolution (keV) at 5.9 keV	0.478
Full Width Half Maximum (FWHM) Resolution (keV)at 122 keV	0.695
Full Width Half Maximum (FWHM) Resolution (keV) at 1332.5 keV	1.785
Depletion voltage	(+)4000
Recommended bias voltage	(+)4000
Time constant (μs)	4
Cryostat description	Vertical Dipstick
Peak shape (FWTM/FWHM) for ^{60}Co	1.88
Cooling system	Electric

5.2 Measurement Techniques

The measurement techniques employed in this detector characterisation are experimental measurement and simulations. The simulations will be used to validated the experimental measurement.

5.2.1 Experimental Methods

The detection system set-up for the high resolution gamma-ray spectroscopic measurement consists of a BEGe detector (BE6530 model), an amplifier, mulit-channel analyser and a desktop computer as shown in Figure 5.2.

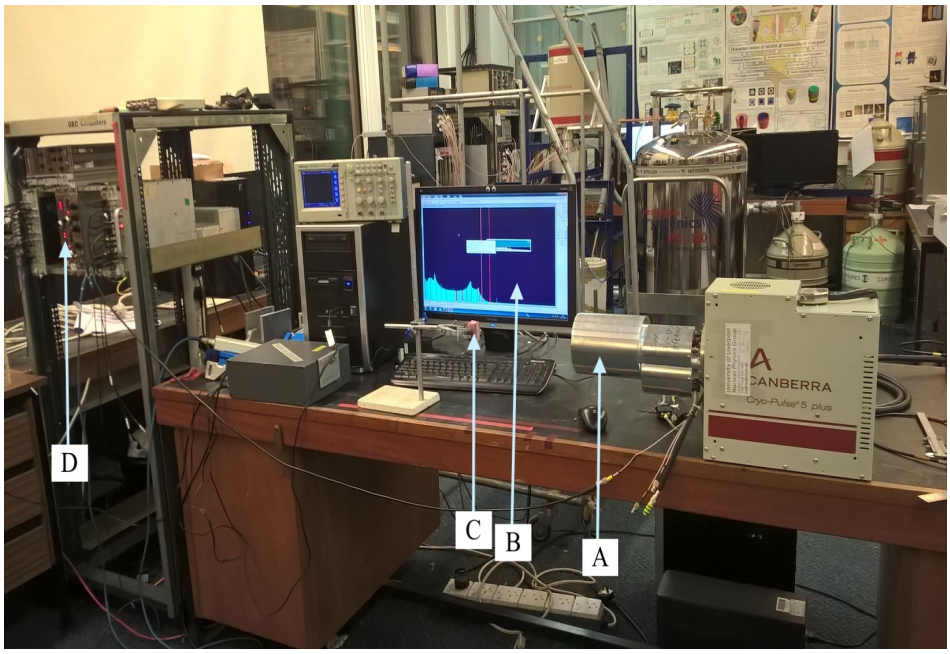

Figure 5.2: The setup for high resolution gamma-ray spectroscopy system. A is the BEGe detector, B is the desktop computer, C is a point radioactive source and D represents the Amplifier and MCA housed in a rack.

This system was connected to a desktop computer, which uses MAESTRO spectrometry software [75] for spectrum acquisition.

5.2.1.1 Energy Calibration

The detection system was calibrated for energy using ^{241}Am and ^{152}Eu sources with respective activities of 179 kBq and 310 kBq at a horizontal standoff of 25 cm using any gamma rays with peaks of emission probability above 2% [100, 44]. The calibration was over the energy range of 59.54 keV to 2.56 MeV for a 8K Multi Channel Analyser (MCA) (that is 8192 channels) for a good peak resolution. The energy calibration process was done by setting regions of interest (ROI) around a number of peaks of interest in an acquired spectrum shown in Figure 5.3. The selected peaks were then manually calibrated by entering the known energies corresponding to the ROI centroids. The energy calibration parameters were afterwards calculated by fitting a linear regression model as indicated in Figure 5.4.

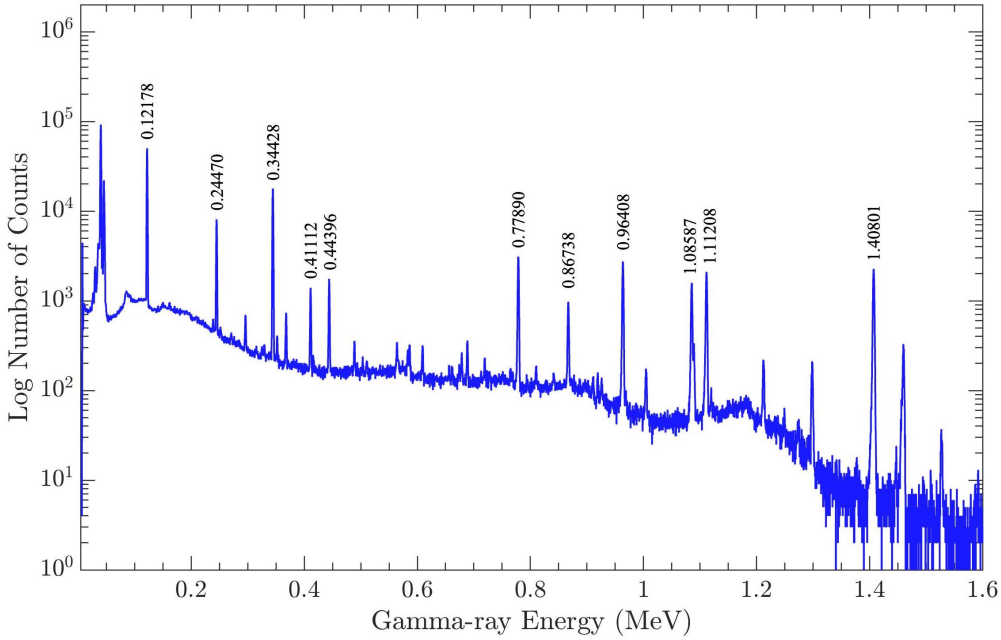

Figure 5.3: Experimental energy calibration spectrum of a ^{152}Eu source acquired over 3600 seconds at 25 cm distance from the detector.

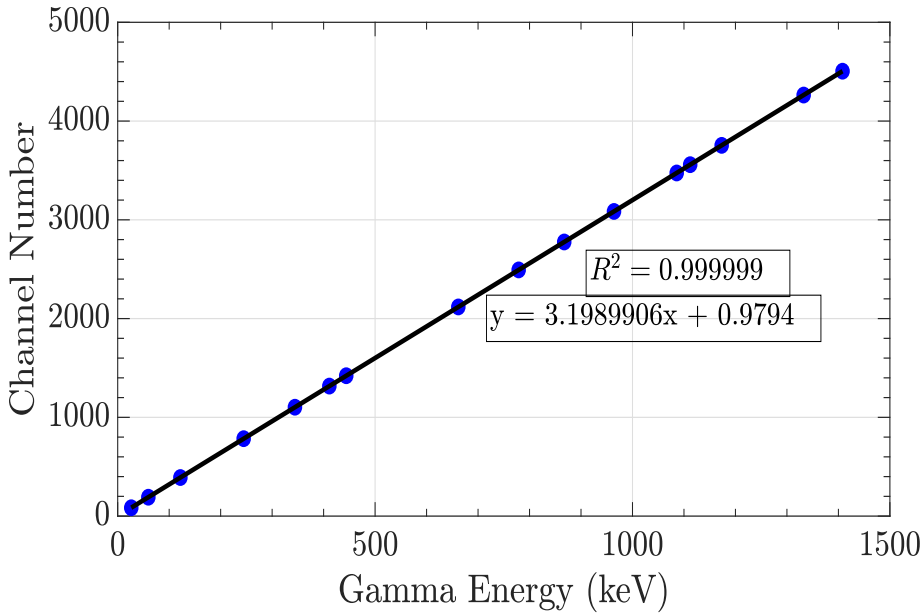

Figure 5.4: Energy calibration as a function of channel number for the BE6530 detector. A curve fitting package in MATLAB was used to fit the data.

After calibration, uncollimated ^{137}Cs, ^{241}Am and ^{60}Co point-like sources with activities of 200 kBq, 179 kBq and 281 kBq respectively were independently placed at the same horizontal standoff [52, 35]. The choice of 25 cm standoff being a standard detector-source measurement was such that the dead time and count

loss due to pile-up were not significant and thus considered negligible. A live time of 3600 seconds was found to be enough time to obtain reasonable counts and keep the average uncertainty below 2 %.

5.2.1.2 Detector Efficiency

The efficiency of a detector can be described as the ratio of the detected gamma-rays to the overall number of gamma-rays emitted by the radioactive source. It is a function of the source-detector distance, material density and the gamma-ray energy [52]. The absolute detector efficiency was calculated by extracting the net peak area from the Gaussian fit of each of the gamma-ray peaks from the ^{152}Eu, ^{241}Am, ^{60}Co and ^{137}Cs spectra using the region of interest (ROI) feature in Maestro software and implementing the values obtained in Equation 5.1 [35]:

$$\varepsilon(\mathrm{E}) = \frac{\mathrm{N_{peak}}}{\mathrm{L_T} \times \mathrm{A} \times \mathrm{P}_\gamma} \tag{5.1}$$

where

ε (E) = absolute peak efficiency

$\mathrm{N_{peak}}$ = net counts in the peak after background correction

$\mathrm{L_T}$ = live time, during which the system processes a pulse

A = activity concentration of the radionuclides in Bq/kg

P_γ = gamma branching ratio i.e. emission probability

In estimating the absolute efficiency of the detector, gamma-ray peaks with good quality nuclear data and precision are conventionally considered [35]. The gamma-ray peaks chosen for absolute efficiency calculation in this work were those with emission probability above 2 % and are shown in Table 5.3. The activities (A) of the radionuclides for the sources used in the efficiency calculation were corrected for using Equation 5.2:

$$\mathrm{A} = \mathrm{A_0 e^{-(\lambda)\times t}} \tag{5.2}$$

where

λ = decay constant

$\mathrm{A_0}$ = the initial activity of the radionuclides

t = the decay time

The absolute efficiency from experimental measurements is shown in Figure 5.5. As noted from the graph, there is improved efficiency at low energies peaking at 59.5 keV of the BEGe detector when compared with typical coaxial detectors. This improvement which is due to high photoelectric absorption of low energy

gamma-rays by the dead layers and detector cap, is a characteristic importance associated with the shape and geometry of BEGe detectors that stand them out for low energy gamma-ray spectroscopy. The relative efficiency, as explained in Section 3.3.1, obtained from experimental measurements at 1332.5 keV of ^{60}Co is 67 % which is about a 12 % deviation from the manufacturer quoted value of 60 %. The decrease in absolute efficiency as the gamma-ray energy increases is largely due to the higher probability of gamma-rays escaping the active detector area through Compton scattering, discussed in Section 3.1.2.

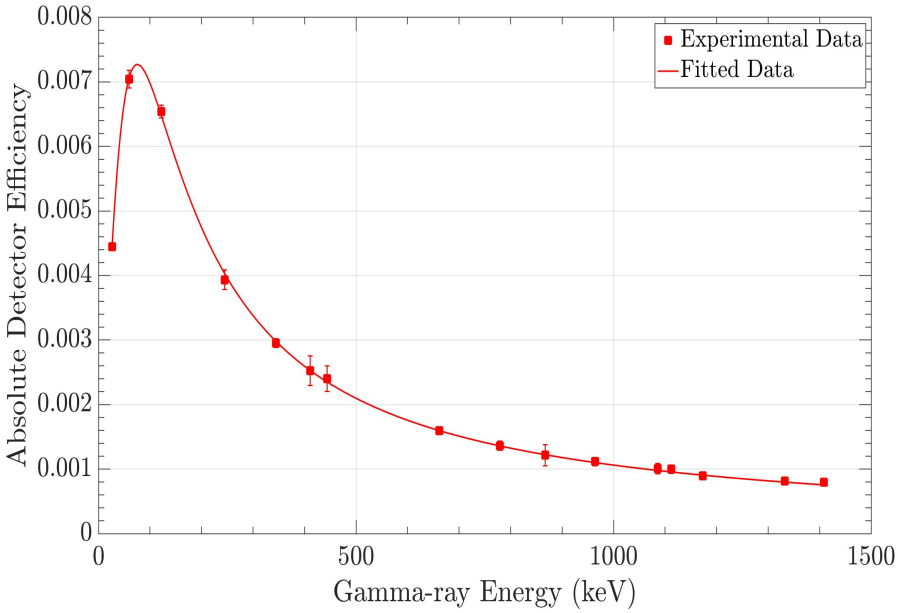

Figure 5.5: Absolute efficiency as a function of gamma energy for experimental measurement. A curve fitting package in MATLAB was used to fit the data.

5.2.1.3 Energy Resolution

The energy resolution of a BEGe detector is a combination of factors such as the inherent statistical spread in the number of charge carriers, variations in the charge collection efficiency, and contributions of electronic noise [52, 35]. In this work, energy resolution was determined by extracting the FWHM (as explained in Section 3.3.2) of the spectra Gaussian fit for each of the gamma energies from the radioactive sources used in the energy calibration. As shown from Table 5.2, the values of FWHM increases as the gamma-ray energy increases. 0.75 keV being the value obtained at 121.78 keV gamma-ray energy is in agreement with the value published by the manufacturer [8], while the deviations for the measured values from the published values are within 8 %.

Table 5.2: Experimental measured values of FWHM of BEGe detector using radioactive sources.

Source Reference	**Radionuclide**	**Gamma energy (keV)**	**FWHM ± Error (keV)**	**FWHM (%)**
NPRL 464	^{241}Am	26.34	0.58 ± 0.01	2.20
		59.54	0.65 ± 0.01	1.09
NPRl 471	^{137}Cs	661.66	1.45 ± 0.02	0.22
NPRl 462	^{60}Co	1173.23	2.03 ± 0.01	0.17
		1332.5	2.19 ± 0.01	0.16
NPRL 618	^{152}Eu	121.78	0.75 ± 0.01	0.61
		244.70	0.90 ± 0.02	0.37
		344.28	1.06 ± 0.02	0.31
		443.96	1.17 ± 0.04	0.26
		778.90	1.60 ± 0.01	0.21
		867.38	1.66 ± 0.03	0.19
		964.08	1.80 ±0.03	0.21
		1085.87	1.85 ± 0.01	0.17
		1112.08	1.95 ± 0.02	0.17
		1408.01	2.26 ± 0.01	0.16

The energy resolution, as measured by FWHM, is the combination of major uncertainties as shown in Equation 5.3 [Knoll, 2010],

$$W_T^2 = W_P^2 + W_C^2 + W_N^2 \tag{5.3}$$

where W_T is the total uncertainty in the energy, W_P is the uncertainty in the electron-hole pair production in the detector, W_C is the uncertainty in charge collection by the detector, and W_N is the uncertainty from the electronic noise arising from the pulse processing.

The variation of the FWHM as a function of gamma-ray energy in Figure 5.6 clearly shows that the dominant contributions at low energies are from electronic noise and charge collection, while at higher energies, the broadening due to carrier statistics shows significant effect. It is understood that small volume detectors, such as the those widely employed in spectroscopic measurements, have lower capacitance values and by extension lower electronic noise and similarly, large volume detectors have higher capacitance values given that detector capacitance is directly proportional to the electronic noise of the system. The large volume of BE6530 compared to other BEGe detectors limits the fundamental energy resolution performance of the detector. However, the electronic noise of 0.56 keV obtained from the experimental measurements is still reasonably good for low energies such as 26.34 keV and 59.54 keV from the ^{241}Am nuclide. A second order

polynomial fit of the square of the FWHM as a function of gamma-ray energy (Figure 5.6) produces Equation 5.4.

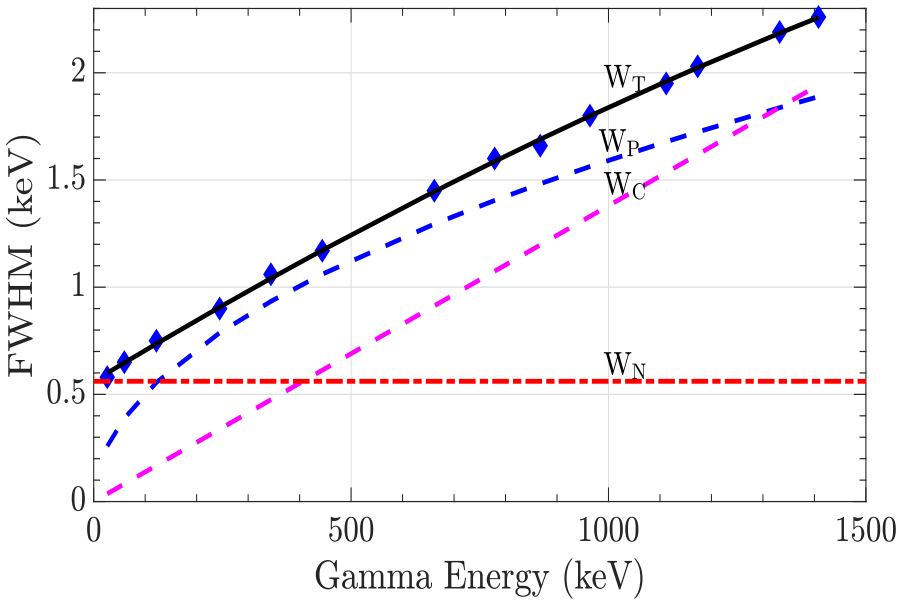

Figure 5.6: Variation of the FWHM as a function of gamma-ray energy for BEGe showing the total uncertainty (W_T), uncertainty from charge collection (W_C), uncertainty from electronic noise (W_N), and uncertainty from electron-hole pair production (W_P). The blue points are experimental data, while the lines are from calculations.

$$(\text{FWHM})^2 = 0.31472 + (1.6269 \times 10^{-3}\text{E}) + (1.9039 \times 10^{-6}\text{E}^2) \tag{5.4}$$

the uncertainties obtained from the Equation 5.4 are given as;

$$\text{W}_\text{P}^2 = \text{P}^2\text{E} = 1.6269 \times 10^{-3}\text{E}$$
$$\text{W}_\text{C}^2 = \text{C}^2\text{E}^2 = 1.9039 \times 10^{-6}\text{E}^2$$
$$\text{W}_\text{N}^2 = \text{N}^2 = 0.31472$$

where

$$\text{P} = 0.04033$$
$$\text{C} = 1.3798 \times 10^{-3}$$
$$\text{N} = 0.561$$

The Fano factor which is the ratio of observed variance in the number of electron-hole pairs created to the variance predicted by Poisson statistics [52] was calculated from;

$$F = \frac{W_P^2}{(2.35)^2} E = \frac{1.6269 \times 10^{-3}}{(2.35)^2 (2.96 \times 10^{-3})} \approx 0.099.$$

The Fano factor obtained is within the range of reported values for germanium detectors which is from 0.057 to 0.12 [35].

Table 5.3: Gamma ray energies and emission probabilities for the radionuclides used in the calibrations (from [100, 44]).

Source Reference	**Radionuclide**	**Gamma Energy (keV)**	**Emission Probability (%)**	**Uncertainty (%)**
NPRL 464	^{241}Am	26.34	2.40	0.030
		59.54	35.78	0.090
NPRl 471	^{137}Cs	661.66	84.99	0.200
NPRl 462	^{60}Co	1173.23	99.85	0.030
		1332.5	99.98	0.001
NPRL 618	^{152}Eu	121.78	28.40	0.130
		244.70	7.55	0.040
		344.28	26.58	0.120
		411.12	2.24	0.010
		443.96	3.13	0.014
		778.90	12.96	0.060
		867.38	4.24	0.023
		964.08	14.62	0.060
		1085.87	10.13	0.060
		1112.08	13.40	0.060
		1408.01	20.85	0.090

5.2.2 Detector Modelling

A Monte-Carlo based technique and Laboratory Sourceless Object Calibration Software (LabSOCS), [9, 104], were used to calculate the absolute efficiency of the detector. Since the efficiency calculated by the Monte Carlo technique is sensitive to the detector's parameters [58], some parameters such as the dead layer were adjusted to obtain a good agreement with the experimental efficiency.

5.2.2.1 Monte Carlo Methods

The interaction of a gamma-ray with a detector involves many processes whose outcomes are oftentimes very difficult to predict. The Maxwell-Boltzmann distribution which describes these processes may be difficult to explain using analytical methods, and to solve them requires computational statistical tools. Monte Carlo methods becomes suitable statistical tools for estimating the gamma-ray interactions mechanism through detectors. Monte Carlo methods solve numerical

problems through simulation of random variables in order to obtain statistically significant results [7].

MCNP6 utilised in this work is a robust simulation code which merged MCNP5 features with MCNPX making it suitable for applications in wider areas. Similar to older versions, MCNP6 files contains well structured important information such as the geometry of the specified problem, complete description of materials involved and cross section evaluations, location and properties of the particle source, desired tallies and variance reduction techniques for improving efficiency [37, 109]. This information is located in the input file with distinct sections as shown in Figure 5.7.

Message Block (Optional)
Blank Line Delimiter (Optional)
One Line Problem Title Card
Cell Cards
Blank Line Delimiter
Surface Cards
Blank Line Delimiter
Data Cards
Blank Line Terminator (Optional)

Figure 5.7: Typical Structural input file in MCNP6.

Using the interactive graphical terminal, the geometry of the input file is checked by looking at different views with the geometry plotting option. A two dimensional view (see Figure 5.8a) or three dimensional view (see Figure 5.8b) of the geometry could be checked to ensure that it is a representation of the problem.

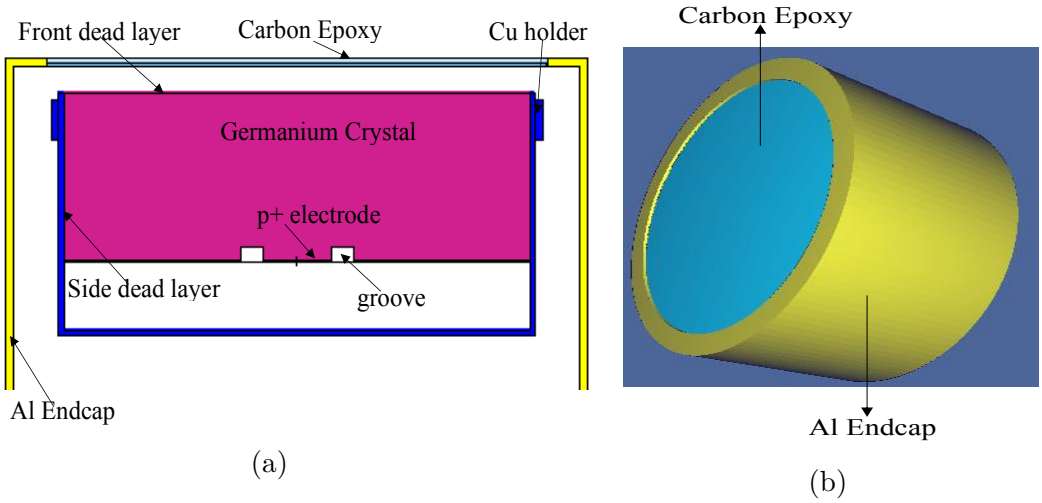

Figure 5.8: Broad Energy Germanium (BEGe) Detector model (a) shown in 2-dimensional view (b) in 3-dimensional view, generated through MCNP Visual Editor.

The Monte Carlo technique relies on tracking the probabilistic interactions of an emitted gamma-ray from a radioactive source. It generates a history of all interactions of the gamma-ray from creation to possible final absorption or escape from the defined world, taking records on the interaction mechanism, and energy deposited through randomly sampled probability distributions. It provides information on the gamma-ray history until it reaches a cut-off energy or escapes from the medium boundaries.
Similar to other areas of gamma-ray spectroscopy, the Monte Carlo technique has been applied in radioactive waste characterisation for the estimation of detector response[42], efficiency calibration, [84, 87, 90, 4, 16], estimation of the detector geometrical response, [11] and activity of point source reconstruction [53, 94, 54]. It has been used to adjust the physical detector parameters, such as the thickness of the dead layer, in order to obtain good simulated results in agreement to the experimental results [84, 45], uncertainty analysis [32, 112], coincidence and non-coincidence summing in gamma-ray spectroscopy [26]. MCNP6 has been utilised in this work to simulate the responses of a BEGe detector to sources in a radioactive waste drum. Upon validation by the experimental results, the simulations will be extended to include attenuation matrices in the drum with a bid to estimate the effect of some selected attenuating materials on the source activity of the waste drum.

MCNP Modelling

The geometrical configuration of the experimental set-up modelled with MCNP includes the source position, detector specifications as contained in Table 5.1, which were obtained from the detector manual supplied by Mirion and shown in Fig 5.1b. MCNP is a general-purpose code applied to the simulation of neutron, photon and electron transport. It uses continuous-energy nuclear and atomic data libraries, [109]. The F8 tally (Pulse Height Distribution) was used to calculate the detector response. 8192 bins corresponding to the number of channels used in the experimental measurements were maintained in the bin description of the input file. The MCNP input file is developed such that the geometry specification, material descriptions, cross sectional selection, source definition and energy range, tally type as well as variance reduction techniques are clearly stated. The point sources (^{152}Eu, ^{137}Cs, ^{241}Am and ^{60}Co) used in the experiment were implemented in the MCNP input file by the use of the SDEF card, that describes the source position, gamma-ray energy emitted by the radioactive source in MeV and the gamma-ray emission probability.

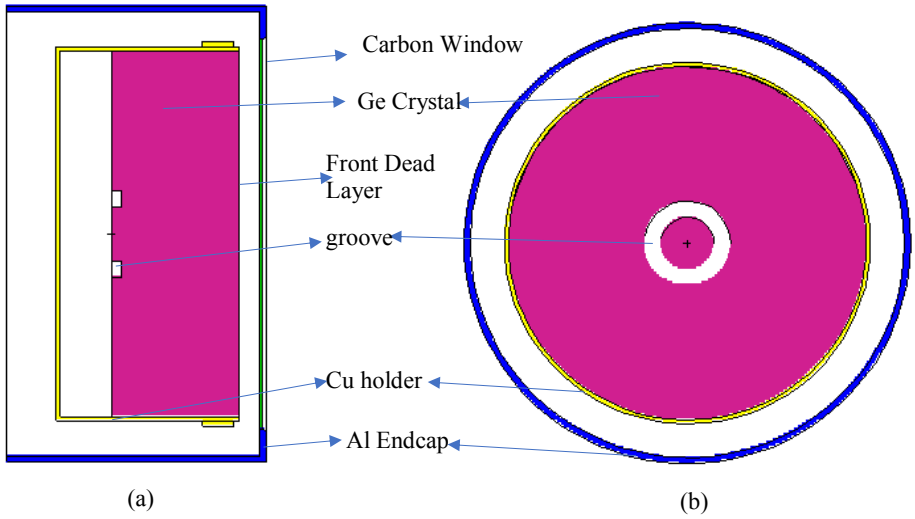

Figure 5.9: MCNP model for BEGe detector. (a) viewing from YX plane (b) viewing from XY plane. The blue colour represents the aluminum cap, yellow being the copper holder, the purple is the detector crystal and the white colour indicates the vacuum. The green colour showing in (a) is the carbon epoxy.

Gamma-ray energies from these sources were used to estimate the absolute efficiency of the detector. The 25 cm source-detector distance is maintained. The Gaussian Energy Broadening (GEB) card provides an essential means of obtaining a spectrum that can be favourably compared with the experimental results in terms of energy resolution (FWHM). Gaussian broadening is a key step to compare MCNP outputs with a real measurement to account for limitation of the resolution of the detector and electronics. The GEB parameters specify the FWHM of the observed energy broadening in a physical radiation detector. The GEB is called by entering FTn card in the input file of MCNP and the tallied energy is broadened by sampling from the Gaussian [78]:

$$F(E) = Ce^{-((E-E_0)/A)^2} \tag{5.5}$$

Where E is the broadened energy, E_0 is the unbroadened energy of the tally, C is a normalisation constant, and A is the Gaussian width. The Gaussian width and the FWHM are related by

$$A = \frac{FWHM}{2\sqrt{\ln 2}} \tag{5.6}$$

and the FWHM is given as

$$FWHM\ (MeV) = a + b\sqrt{E + cE^2}. \tag{5.7}$$

Where E is the energy of the gamma rays in MeV, the fitting parameters a, b

and c were obtained experimentally by taking a quadratic fit for FWHM with the gamma-ray energy as in Figure 5.6. The units of a, b, and c are MeV, $\text{MeV}^{\frac{1}{2}}$, and MeV^{-1}.

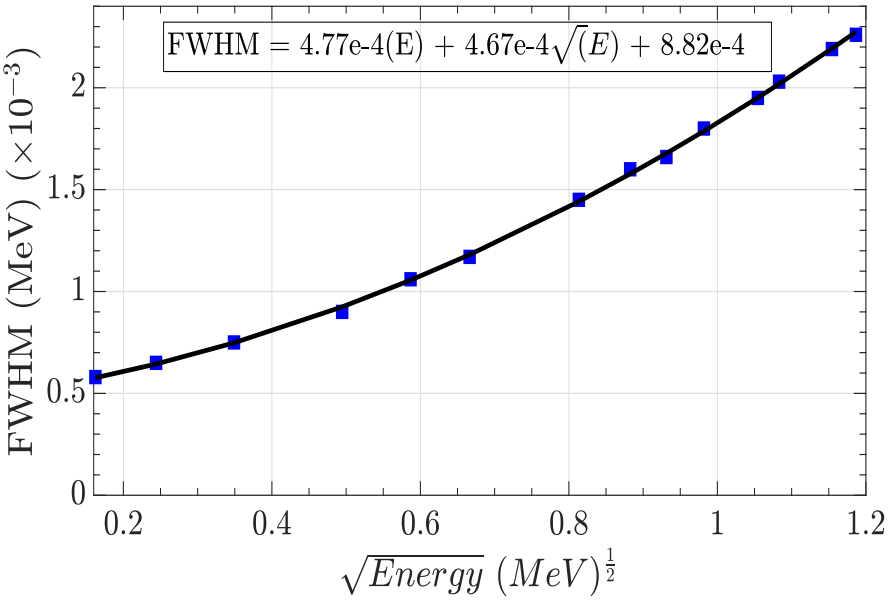

Figure 5.10: Gaussian energy broadening fit to extract the fitting parameters a, b, and c.

The following parameters were extracted from the experimental measurement and fit into FTn card:

$$\begin{aligned} \text{a} &= 4.77 \times 10^{-4}\ \text{MeV}, \\ \text{b} &= 4.68 \times 10^{-4} MeV^{\frac{1}{2}}, \\ \text{c} &= 8.82 \times 10^{-4} MeV^{1}. \end{aligned}$$

In order to validate the detector-source model, the MCNP photon transport codes written were run independently for each of the radioactive sources and the energy distribution of pulses generated as the gamma-rays incident and interact with the detector crystal obtained as Pulse Height Tally denoted as F8 in the code, and normally, the total number scored by this tally represent the histogram of the energy depositions. The energy histogram for this work were binned into equal energy window steps of 0.312 keV covering a range of 2556 keV and corresponding to the MCA channel in the experimental energy distribution. In the MCNP simulations, a cutoff terminates the program when a certain defined number of particle histories is attained. For this work, photon transport interactions were run for 2×10^9 histories such that the estimated uncertainty on the scored values in F8 is within 0.5% at the σ level. The number of particles histories (NPS card) cutoff terminates the program when the number of photon histories is reached. Experimental

configurations involving many variables are in most cases vastly more complex than can be modelled in a simulation, and as a consequence, both simulation and experimental results do not always match. However, data are normally simulated until relative errors of both measurements and simulations come within acceptable values.

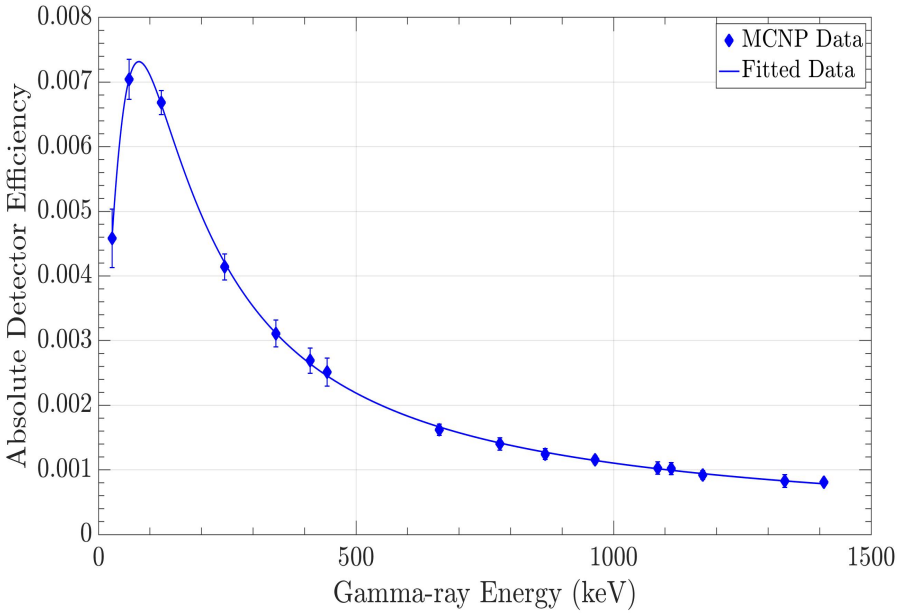

Figure 5.11: Absolute efficiency as a function of gamma energy for MCNP simulations. A curve fitting package in MATLAB was used to fit the data.

Figure 5.11 shows the absolute detector efficiency against gamma-ray energy for MCNP simulations. As can be seen, absolute detector efficiency estimated from MCNP increases to a maximum at gamma-ray energy of 59.5 keV, then decreases for higher gamma-ray energies.

Laboratory Sourceless Object Calibration Software

Laboratory Sourceless Object Calibration Software (LabSOCS) is a computer program used for quick and accurate efficiency calibration of germanium detectors. The code is integrated into the Mirion Genie 2000 gamma-ray spectrometry system. The LabSOCS calibration software algorithm requires an accurate description of the problem geometry. This is done through the Geometry Composer which allows the interactive definition of all geometry-related parameters such as detector properties, sample dimensions, composition and densities. For creating and maintaining the nuclides library used for both quantitative and qualitative radionuclide analysis, the Nuclide Library editor is utilised [104, 55]. An efficiency calibration curve is the final output of LabSOCS which can be analysed using

MATLAB or other programmes. The plot of efficiency against energy shown in Figure 5.12 clearly agrees with the experimental and MCNP simulated efficiencies in such that the maximum efficiency occurred at 59.5 keV which represents great improvement in BEGe technology for lower energy spectroscopy compared to typical coaxial detectors.

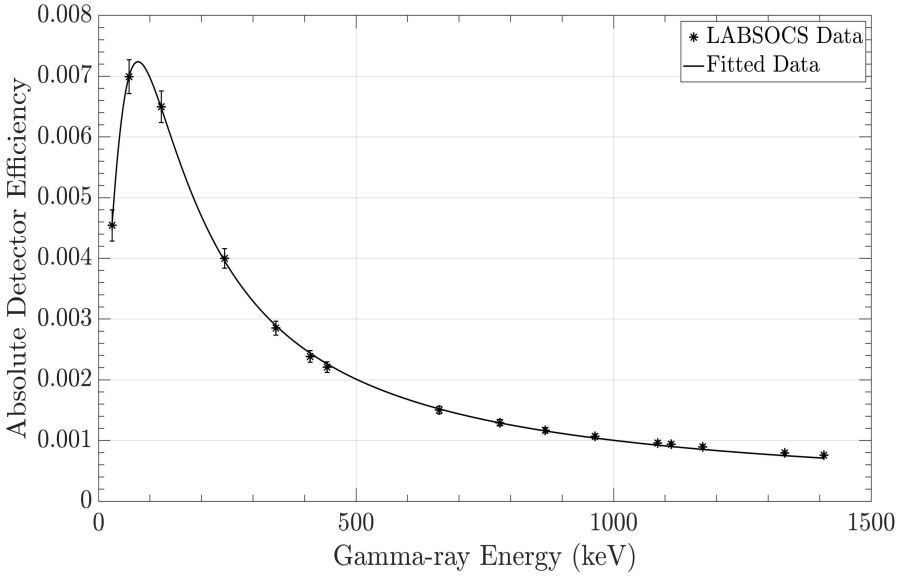

Figure 5.12: Absolute efficiency as a function of gamma energy for LabSOCS simulations. A curve fitting package in MATLAB was used to fit the data.

As illustrated by the ratios of the efficiency computed from MCNP, experiment and LabSOCS (Figure 5.13), it is clear that efficiency calculated from MCNP agrees with experimental efficiency at higher energies but over predicted at lower energies. This could be attributed to the effects of electric field, pile-up and dead time being accounted for in the experimental measurement but not modelled in MCNP simulation. The percentage deviations of MCNP efficiency from experimental efficiency at those lower energies are within 14 % for all energies.

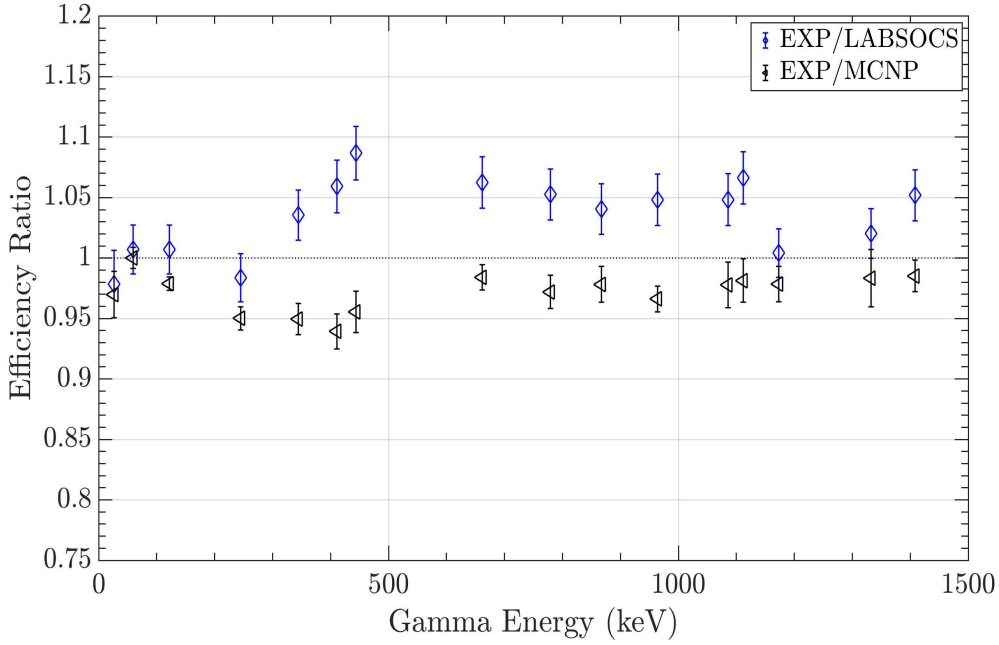

Figure 5.13: The relative variation of the computed efficiencies with gamma-ray energy.

5.3 Optimisation of Detector Collimator System

Gamma-rays from a point radioactive source can hit a detector at any point on it's field of view (FoV) but to ensure directional detection of gamma-rays by a detector, collimation of the gamma-rays is required. However, gamma-rays are emitted isotropically and as a result cannot be easily focused. An absorptive collimator material enables all gamma-rays emerging from the collimator aperture to be absorbed while those in the desired direction get directed onto the detector. Factors such as the size of FoV, the diameter of imaging detector and importantly, the nature of measurements to be taken (which parameter between sensitivity and spatial resolution will be given priority) are to be considered in making decisions on the type of collimator to be used in tomographic scanning. Collimator response is dependent on the shape, length and diameter of collimator holes/slits. In gamma ray imaging, two parameters that describe collimator performance are the collimator resolution and collimator efficiency.

The detail of the gamma-ray image projected onto the detector is the collimator resolution while the fraction of gamma-rays that pass through the collimator aperture and get projected onto the detector is the collimator efficiency. The length and diameter of the collimator significantly affects collimator resolution, while the collimator efficiency is affected by the collimator diameter and septal thickness.

Collimator resolution (R_{coll}) is given as

$$R_{coll} = \frac{d(l_{eff} + b)}{l_{eff}}, \tag{5.8}$$

and the effective length (l_{eff}) is given as;

$$l_{eff} = l - 2\mu_l{}^{-1}.$$

where d is the collimator diameter, b is the distance of the collimator from the radiation source, l is the length of the collimator and μ_l is the linear attenuation coefficient of the collimator material at a particular gamma-ray energy.

The higher the values of R_{coll}, the poorer the resolution and vice versa. To improve the collimator resolution, the ratio of the collimator diameter to effective length (d/l_{eff}) is made smaller. This can be achieved by reducing the values of the collimator aperture.

Collimator efficiency (E_{coll}) is given as

$$E_{coll} = \frac{k^2 d^4 (d + t)}{l_{eff}^2}. \tag{5.9}$$

where t is the septal thickness and k is a constant which depends on the shape of the collimator hole. k = 0.24 for a round hole, 0.26 for a hexagonal hole and 0.28 for a square hole.

A relationship between the collimator resolution and collimator efficiency can be developed from Equations 5.8 and 5.9 to obtain

$$E_{coll} \propto R_{coll}^2. \tag{5.10}$$

Thus, equation 5.10 shows that collimator resolution improves at the expense of collimator efficiency.

5.3.1 Experimental Collimator Setup

The experimental setup for collimator optimisation for waste drum tomography involves setting up of a slit-collimator of aperture 10 mm with lead slabs of dimensions 150 mm x 75 mm x 75mm such that one side of the collimator lies just in front of the detector window while the other side is 155 mm from the radioactive source. The radioactive source is placed such that its axis passes through the centre of the collimator aperture to the centre of the detector crystal. Four uncollimated radioactive point sources described in Section 5.2.1.1 were counted

for an hour each to acquire spectrum for the estimation of the detector's response. The peak area was extracted and fitted in Equation 5.1 for the estimation of the collimated detector efficiency. The whole process was repeated for collimator apertures of 20 mm and peak area extracted for the calculation of collimated detector efficiency. The slit collimator was then replaced with a lead slab pinhole collimator of aperture 10 mm and the peak area extracted from the spectrum obtained after counting the same radioactive sources for an hour. The detector efficiency was calculated.

From the absolute detector efficiency against gamma-ray energy, shown in Figure 5.14, it can be seen that the collimator system for both slit and pinhole demonstrate variations in efficiency for all gamma-rays energies being considered. The results show that slit aperture performs more efficiently than the pinhole aperture. This observation could be attributed to the fact that for pinhole aperture, the detector field of view (FoV) is smaller compared to the slit aperture, limiting the number of gamma-rays hitting the detector crystal for interactions.

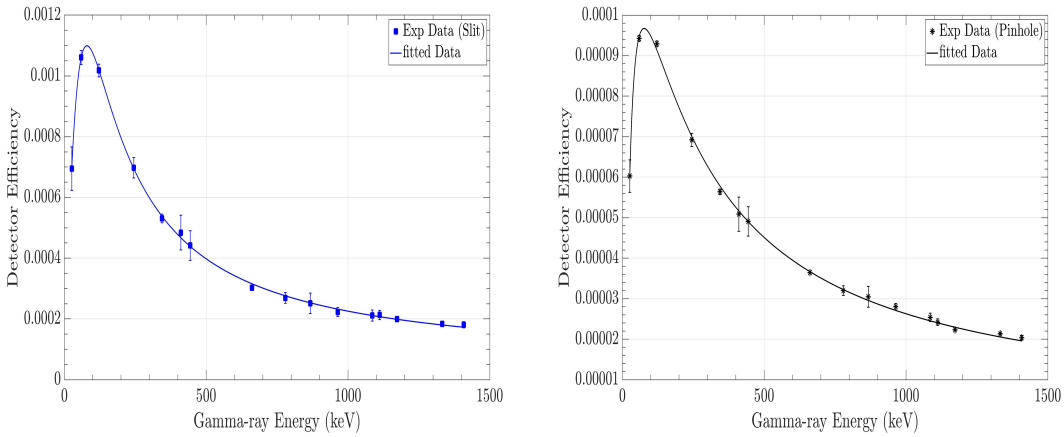

(a) (b)

Figure 5.14: Experimental detector efficiency as a function of gamma-ray energy for BEGe detector for source-detector distance of 25 cm (a) slit-collimated (b) pinhole-collimated. Statistical error bars are included on the plot but in some cases they are smaller than the size of the symbols. A curve fitting package in MATLAB was used to fit the data.

A comparison of the slit collimator to pinhole collimator shows that slit is of high sensitivity compared to pinhole of same aperture as shown in Figure 5.14. This indicates that for sensitive/efficiency or activity calculation, the slit collimated detector is preferred.

5.3.2 MCNP Simulation of Collimator Setup

MCNP was utilised to model the experimental set-up of the detector collimator optimisation. The model takes into account the detector geometry, radioactive source (energy composition and position), collimator geometry (dimensions, elemental compositions and density) as shown in Figure 5.15. Both slit and pinhole collimators were modelled to depict the actual experimental set-up. To aid in comparison, the detector to source distance, dimensions of collimator were maintained as in the experiment. In the model, the dead layer, though, caused by lithium n+ contact was modelled as pure germanium since it consists of impure germanium caused by lithium diffusion into the crystal [35]. With the collimator aperture kept at 10 mm for the slit collimator, a simulation was run for 1 billion histories (to keep the uncertainty below 5 %) for each of the four radioactive sources used for the experimental measurements with the pulse height (F8) tally being the detector response. Similarly, the aperture was increased to 20 mm and a repeat of the simulation run for each of the radioactive sources.

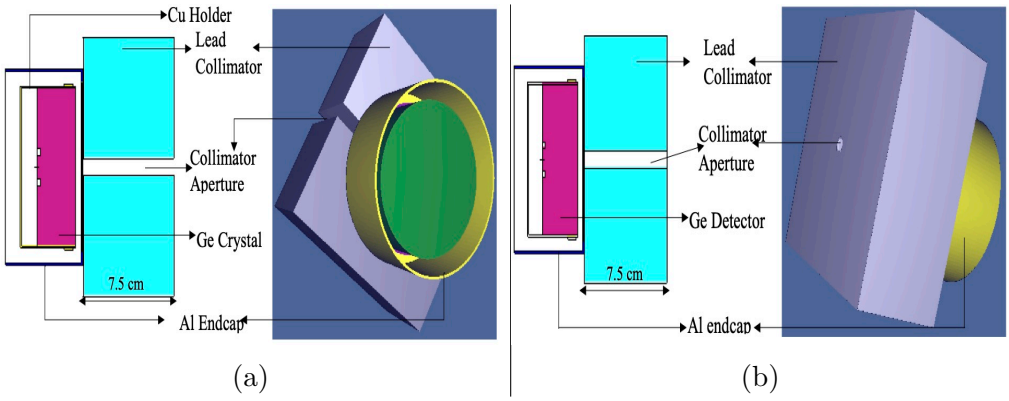

Figure 5.15: MCNP model for the detector collimator showing (a) 2D (XY Plane) and 3D views of slit model (b) 2D (XY Plane) and 3D views of the pinhole model.

The same processes were repeated for a pinhole collimator and the pulse height tally obtained for each of the radioactive sources simulated and efficiency extracted using a MATLAB programme. Figure 5.16 shows the simulated efficiency for both slit and pinhole collimator as a function of gamma-ray energies. As with the experimental efficiencies, the sensitivity of the slit collimator is higher than the pinhole collimator as indicated on the relative ratio of the two efficiencies in Figure 5.16c. The efficiencies showed clear resemblance with the experimental efficiencies and true indication of good comparison.

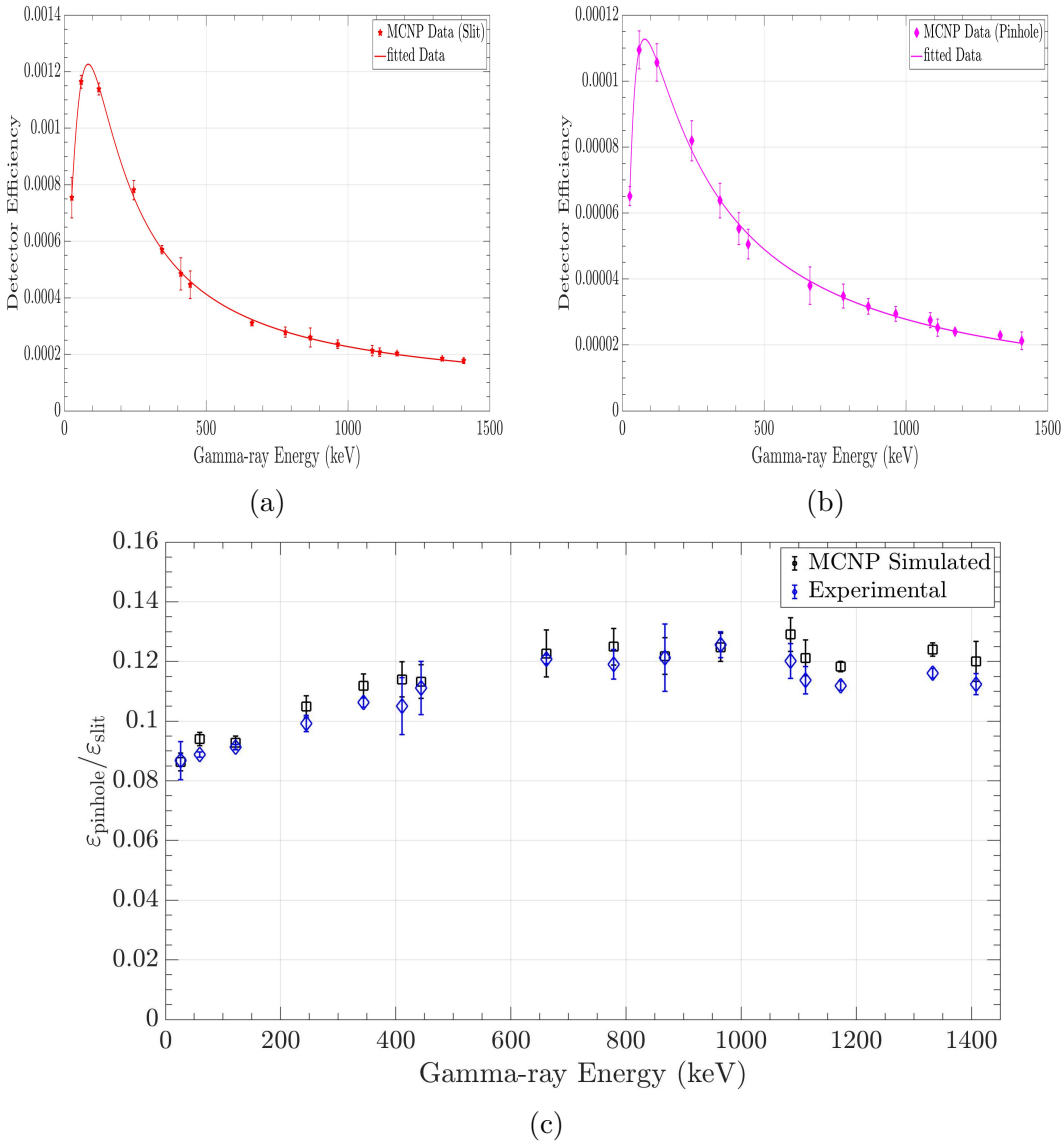

Figure 5.16: Simulated detector efficiency as a function of gamma-ray energy for BEGe detector for source-detector distance of 25 cm (a) slit-collimated, (b) pinhole-collimated, and (c) Relative ratio of pinhole model to slit model for both experimental and simulated efficiencies. A curve fitting package in MATLAB was used to fit the data. Statistical error bars are included on the plot but in some cases they are smaller than the size of the symbols.

5.3.2.1 Horizontal Field of View Simulation

The collimator system reduces the horizontal field of view of a detector, thus enabling a segmented view of an object using collimated detector. This reduction, depending on the aperture of the collimator, helps to shape the detector resolutions. The effect of collimator on detector resolution and point spread function of the detector was investigated by simulating a ^{137}Cs point source at 1 cm steps

along the detector's horizontal field of view. This simulation was carried out for both slit and pinhole models of the collimating system using 10 mm and 20 mm as the apertures. 10 simulation positions were modelled on each side of the axis passing through the centre of the collimator aperture to the centre of the detector crystal. This simulation models maintained the experimental detector to source distance. The result showed a maximum detector response when the radioactive source was at the centre but slowly decreased by the outward movement of the source from the horizontal mid point of the detector. The detector response showed signs of a peak that gradually became flat as the aperture increases as shown in Figure 5.17a, to figure 5.17d.

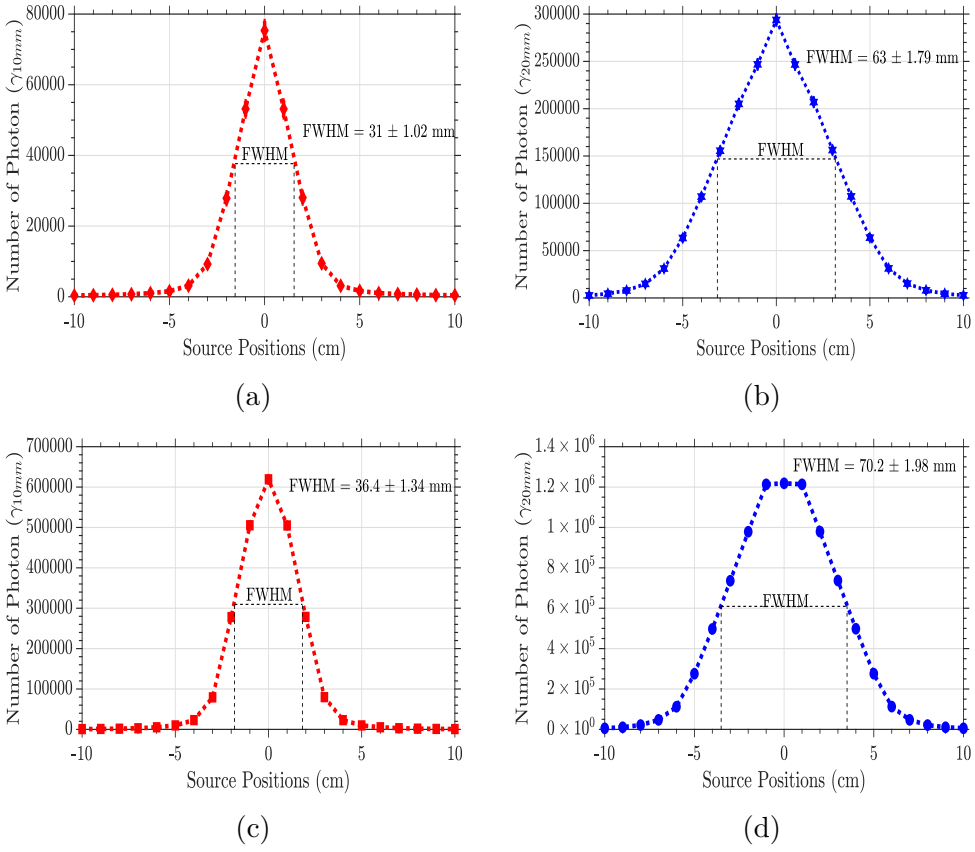

Figure 5.17: Simulated effect of detector collimator on the radioactive sources at different horizontal points (a) pinhole collimator for 10 mm aperture (b) pinhole collimator for 20 mm aperture (c) Slit collimator for 10 mm aperture, and (d) slit collimator for 20 mm aperture.

The computed FWHM for the 10 mm aperture of pinhole model is 31 ± 1 mm, while for 20 mm aperture of the same model is 63 ± 2 mm. The values of the FWHM obtained for both 10 mm and 20 mm apertures of slit model are respectively 36.4 ± 1.3 mm and 70 ± 2 mm. These computed values of the FWHM

suggest that the pinhole collimator model performs better than the slit collimator model in resolution. It also confirms the understanding that the smaller the aperture, the better resolving power of the collimator. However, as illustrated in Figure 5.17, the slit collimator produces relatively higher numbers events than the pinhole collimator, and this indicates that the sensitivity of the slit collimator is much better than the pinhole collimator.

5.4 Summary

Broad Energy Germanium (BEGe) detectors are suitable for a wide range of spectroscopic applications including radioactive waste assay due to their high resolution and good efficiency. The absolute detector efficiency obtained from experimental measurements, MCNP simulation and LabSOCS simulations indicate good efficiency at low energies as a result of the photoelectric absorptions of low energy gamma-rays by the carbon window. A FWHM of 0.75 keV at 122 keV obtained is about an 8 % deviation from the manufacturer's specifications. Similarly, a resolution of 2.19 keV at 1332.5 keV is within the range provided in the manufacturer's specifications as shown in Table 5.1.

For waste drum tomography, it is clearly shown that a compromise between radionuclide identification and hotspot location is required in making the choice of collimator for drum scanning. Identification of radionuclides in a radioactive waste drum depends upon the sensitivity of the detector system, and by extension high collimator aperture. On the other hand, hotspot localisation needs collimators of very good resolution to be able to resolve any interesting features or spots right inside the waste drum or to separate gamma-rays of close energies. So, a trade-off is required to get the optimum result from the detector collimating system by maintaining a balance between radionuclides identification and hotspots localisation when choosing the aperture of the detector collimator.

From the modelled results of the collimated detector efficiency and the collimated detector resolution, a slit collimator of 10 mm aperture is suitable to effectively provide better sensitivity and relatively good resolution for the tomographic interrogation of the waste drum, and therefore will be utilised in the vertical, radial and angular scanning of the waste drum as will be explained in the next chapter. The percentage difference for the resolution of 10 mm aperture for slit collimator to the same aperture for pinhole collimator is about 14.8 %, showing that the resolution of the 10 mm slit collimator is about 85.2 % of the pinhole collimator.

Chapter 6

BEGe Measurement and MCNP Simulations

Over the years, we have had stockpiles of radioactive waste in drums/containers with little or no process knowledge and inadequate documented information about the radiological properties of the waste form. In many situations, these stocked radioactive wastes are concentrated in liquid forms using resins or other forms of chemical. As they have decayed over the years with likely changes in radioactivity concentration and hotspots, there is a regulatory requirement [80] that these radioactive wastes be characterised before either transportation, interim or final storage. This characterisation helps to provide detailed information on the radioactivity, chemical and physical form of the waste.

In this chapter, the experimental details of the segmented gamma scanning (SGS) for a 500 litre standard stainless steel waste drum using a slit-collimated HPGe detector are presented. The methodology adopted in this work involved having radioactive source(s) at different positions inside the drum and the detector response (sensitivity) measured. The acquired detector responses are then reconstructed to obtain the image(s) of the radioactive sources used in the form of a hotspot. Finally, MCNP simulations will be utilised to compute the efficiency of the counting system as well as the matrices' effect on the activity of the sources.

6.1 Scanning System Setup

A slit-collimated HPGe detector (BE6530 model) described in Section 5.3.1 was mounted on a stainless steel trolley and was positioned such that the collimator surface was 9.5 cm from the wall of 500 litre standard stainless steel waste drum that is described in Appendix A.1. The drum stood on a turntable as shown in Figure 6.1. This standard waste drum of wall thickness 7 mm is recommended

for the storage of long-lived low level and intermediate level wastes [33]. The data acquisition system consisted of an inbuilt preamplifier connected to an ORTEC amplifier, with the output fed into an ORTEC multi channel analyser. The gamma-ray spectra were acquired and displayed using MAESTRO software [75] running on a laptop computer. In the coordinate geometry of the scanning system, the source distance from the detector is represented by x, the height of the drum represented by y and the horizontal distance of the drum from left to right and perpendicular to the x-axis is represented by z.

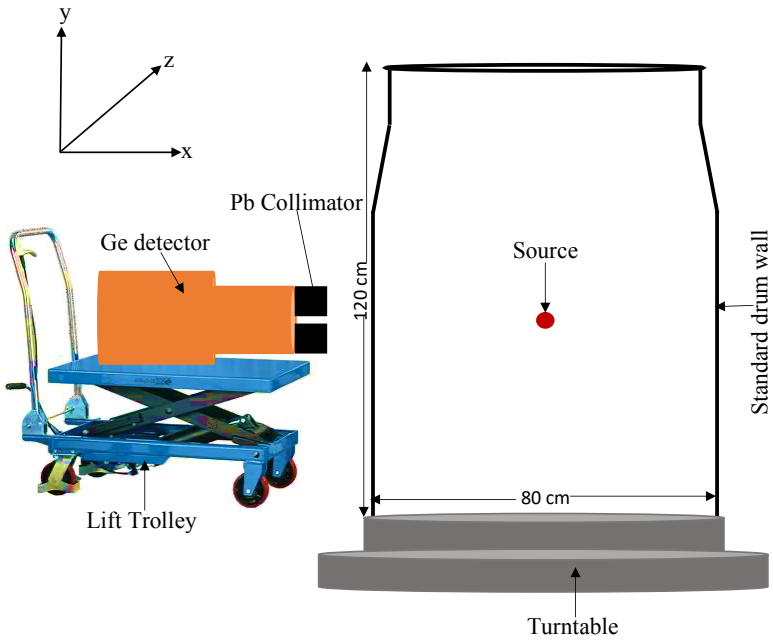

Figure 6.1: A schematic representation of standard waste drum measurement geometry. Top left is the coordinate system for the measurement.

6.2 Efficiency Calibration of the Counting System

The most desirable method of efficiency calibration is to replicate a representative sample of the radioactive waste being measured using collected radioactive waste samples from industry. However, not only does this approach require provisions for the storage and disposal of the radioactive materials used, there is also a regulatory requirement for radioactive materials licenses. Therefore, an alternative approach for the efficiency calibration of the system was adopted in this work. This approach entailed having radioactive source(s) inside the drum and measuring the number of gamma-rays reaching the detector. From this the intrinsic efficiency of the detector was calculated. Thereafter, by applying a series of mathematical correction factors, such as the drum wall attenuation corrections and geometry corrections, the efficiency of the counting system was computed. It showed that

the counting system efficiency depends on the intrinsic efficiency of the BEGe detector, the source-detector geometry and the gamma-ray attenuation property of the drum wall material. Experimentally, the efficiency, ϵ_γ, of the counting system was calibrated using ^{241}Am, ^{152}Eu, ^{60}Co and ^{137}Cs point sources, with a range of gamma-ray energies between 59.54 keV to 1408.02 keV. Two approaches were adopted for this counting efficiency calibration. The first approach was having each source positioned right at the centre of the drum (that is 55 cm from the detector surface) and at a drum height of 60 cm from the bottom, with detector collimator to drum wall distance set at 9.5 cm. The absolute detection system efficiency, ϵ_m, for this configuration was estimated for each of the gamma-ray energies generated by the point sources utilising Equation 6.1 and the drum wall attenuation corrections.

$$\epsilon_\gamma = \frac{\mathrm{N_c}}{\mathrm{A\ T\ P_\gamma}}\mathrm{K_i} \tag{6.1}$$

where $\mathrm{N_c}$ is the net area of the peak, A is the activity of the radionuclide, T is the live time, $\mathrm{P_\gamma}$ is the gamma-ray emission yield and $\mathrm{K_i}$ represents the geometry and drum wall attenuation correction factors and its effect was not considered for the experimental efficiency calculation. The value for $\mathrm{K_i}$ will be computed using the MCNP simulation code.

The second approach was having the radioactive sources positioned at 17 cm from the detector surface and maintaining the same drum height. The absolute detector efficiency, ϵ_w, for this configuration was also calculated for each of the gamma-ray energies.

6.3 Computation of Source Activity inside the Drum

The activity of the radionuclides inside the waste drum was calculated using Equation 6.2;

$$\mathrm{A_i} = \frac{\mathrm{N(E_i)}}{\epsilon(\mathrm{E_i}).\rho(\mathrm{E_i}).\mathrm{t.CF_{wall}}}. \tag{6.2}$$

where $\mathrm{A_i}$ = the activity of the radionuclide at energy $\mathrm{E_i}$, $\mathrm{N(E_i)}$ is the full energy net peak area after background corrections for each of the segment, $\epsilon(\mathrm{E_i})$ is the drum efficiency at energy $\mathrm{E_i}$ determined segment by segment, $\rho(\mathrm{E_i})$ is the emission probability corresponding to energy $\mathrm{E_i}$, t is the live time and $\mathrm{CF_{wall}}$ is the drum wall correction factor that depends on the material composition of the drum wall. And the measurement uncertainty, μ_A, was calculated using Equation 6.3;

$$\mu_\mathrm{A} = \mathrm{A_i}\sqrt{\left(\frac{\mu_\mathrm{N}}{\mathrm{N(E_i)}}\right)^2 + \left(\frac{\mu_\epsilon}{\epsilon(\mathrm{E_i})}\right)^2 + \left(\frac{\mu_\rho}{\rho(\mathrm{E_i})}\right)^2 + \left(\frac{\mu_\mathrm{t}}{\mathrm{t}}\right)^2 + \left(\frac{\mu_\mathrm{CF}}{\mathrm{CF_{wall}}}\right)^2}. \tag{6.3}$$

where μ_N, μ_ϵ, μ_{rho}, μ_t and μ_K are the net area uncertainty, efficiency uncertainty, emission probability uncertainty, live time uncertainty and uncertainties of the correction factors respectively. The deviation, D_A of the experimental value from the true value was calculated using the Equation 6.4.

$$D_A(\%) = \frac{A_{TR} - A_{CA}}{A_{TR}} \times 100. \tag{6.4}$$

where A_{CA} is the average of the calculated activity, A_{TR} is the true or certified activity which is the source's activity after decay corrections. The activities for the radionuclides calculated using Equation 6.2 are presented in Table 7.1. The total activity of the radioactive sources within the drum was calculated by taking the average of all the activities from each radial segment. For ^{137}Cs, the total activity inside the waste drum was calculated by adding up the individual activities of the two sources, while for the ^{133}Ba and ^{22}Na sources, a gate was applied on one of their gamma-ray energies and the net peak area for the respective gamma-ray energy utilised in activity calculation.

6.4 Waste Drum Scanning

Radioactive waste drum scanning is typically the process of moving the detector and drum relative to one another in order to allow the entire drum to be measured in stages or steps. The measurement procedure for waste drum scanning adopted in this work involves segmenting the drum axis into different segments. The first step is dividing the drum into 24 vertical segments. The segmented gamma scanning was then applied to scan each of the vertical segments from top to bottom as illustrated in Figure 6.2a with a ^{60}Co point source of activity 247 kBq placed on the central axis of the drum, 59 cm from the face of the detector and at a height of 40 cm from the bottom of the drum. The vertical layer with the maximum measured counts represents the segment position where the radioactive point source is located. At this segment of interest, the collimated detector was then moved from right to left with a 5 cm step size, as shown in Figure 6.2b, and the measured counts recorded to determine the actual positional coordinates of the radioactive point source. The next measurement of the segment was the angular scanning where the collimated detector was used to scan the drum at a positional angle of $\theta = 0°$ and thereafter rotated at an angular step of 12°, as seen in Figure 6.2b. The rotation of the drum during the measurement was to acquire several data at multiple angular locations of the drum. These measurements were then averaged to reduce the measurement uncertainty due to non-homogeneity. Each of the multiple data acquired were regarded as a projection for the corresponding

angular position. A set of projections was obtained after turning the standard

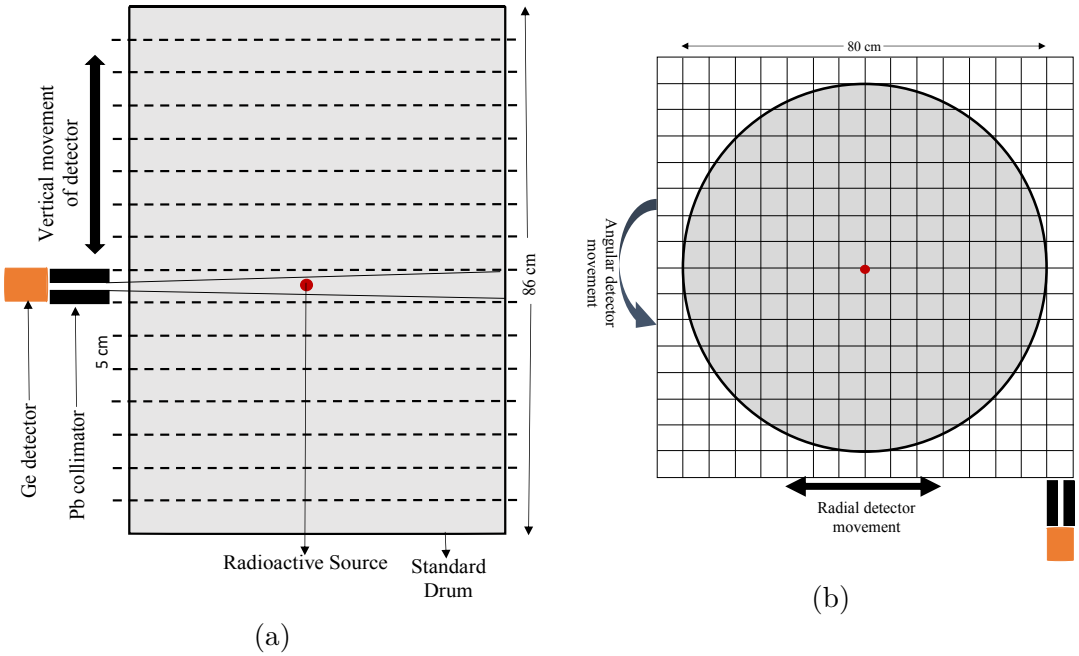

Figure 6.2: Segmented gamma scanning system of the standard drum (a) Vertical movement of the drum (b) radial and angular movement of the drum. This sketch does not include the tapered upper part of the drum. The measurement coordinates follow that shown in Figure 6.1

waste drum around. The time for each scan was 4 hours and this time was enough to acquire sufficient events with low statistical uncertainty given that the drum wall is of stainless steel material of 7 mm thickness which will have significant attenuation effects on the number of low energy gamma-rays measured.

Thereafter, three other measurement configurations were carried out with the following descriptions of the source positions relative to the experimental set-up as illustrated in Figure 6.3. The first used ^{133}Ba and ^{22}Na point sources of activities 748 kBq and 115 kBq respectively offset 10 cm on either side of the midpoint of the drum's central axis. The ^{133}Ba source was at 80 cm and the ^{22}Na source was at 40 cm from the bottom of the drum, while the detector was positioned at a height of 60 cm. Secondly, a 15 cm long and 1.5 cm diameter extended ^{137}Cs source of maximum activity 1.2 MBq and of non-uniform activity distribution was placed horizontally along the z-axis, 59 cm from the detector surface and at a height of 60 cm. The final measurement was two ^{137}Cs point sources of activities 230 kBq

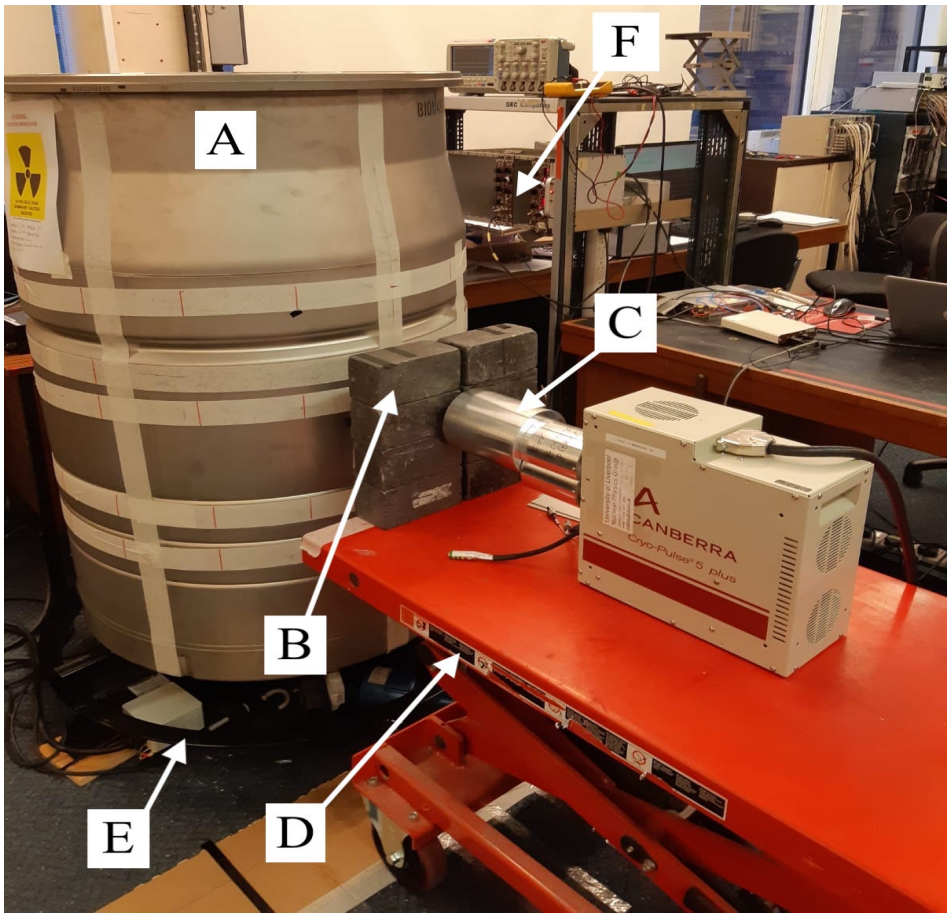

Figure 6.3: Experimental set-up for the counting system. A is the 500 litre standard waste drum, B represents the lead collimator, C is the BEGe detector and D is the lift trolley, E is the turntable and F is the MCA.

and 223 kBq placed 10 cm and 20 cm respectively from the midpoint on opposite sides of the drum's central axis and is 59 cm from the surface of the detector. The source was placed at a height of 60 cm above the bottom of the drum. It is instructive to note that the detector surface to source distance of 59 cm was chosen to minimise the effect of the inverse square law and maintain relatively good counts in order to reduce uncertainty. For each of the measurement configurations, counts for vertical and radial scanning were recorded along with a projection for each angle. The information obtained from the emission tomography was analysed to estimate the location of the radioactive source and activity distributions inside the waste drum. The emission tomography images were reconstructed from the total projections for each of the measurement configurations using a filtered back-projection method discussed in Section 4.2.1 with linear interpolation as a smoothing algorithm.

6.5 Reconstructed Image Quality Metrics

The quality of a reconstructed image depends on the level of uncertainty, the nature of the geometrical setup and the number of measurements available. The statistical uncertainty in the measurement is required to be low to achieve low uncertainties in the reconstructed image. Uncertainties in the reconstructed image can be minimised by filtering or smoothing the reconstructed image. The quality of a reconstructed image can be evaluated using image quality metrics. Three of the most important of these assessment metrics are Mean Square Error (MSE), Peak Signal to Noise Ratio (PSNR) and Structural Similarity (SSIM). The MSE measures the average squared difference between the reconstructed image and the actual image. The higher the MSE, the less similar the reconstructed image is from the original image. PSNR is used to measure the quality of an image after reconstruction in which a higher PSNR value indicates a higher image quality and, hence good reconstruction and enhancement. PSNR is expressed in dB. SSIM is used to measure the similarity between reconstructed and actual images [107]. These metrics are to be utilised in evaluating quality of images obtained from different interpolations, filters and frequency compressions.

The first image processing technique to be considered is interpolation (described in Section 3.6.2.3). The comparison of the reconstructed images using three most commonly used image interpolation methods to the original image is shown in Figure 6.4. The reconstructed image using linear and cubic interpolation show similar features to the original image because they consider more values for the known pixel in calculating the values of the unknown pixel. The artefacts-like seen in Figure 6.4b for the nearest interpolation is because only one nearest pixel to the unknown was considered in finding the value of the unknown pixel. The interpolation results illustrated in Figure 6.4 show that the quality of reconstructed image is not significantly distorted by any of the interpolation forms, an indication of low measurement noise level in the original image.

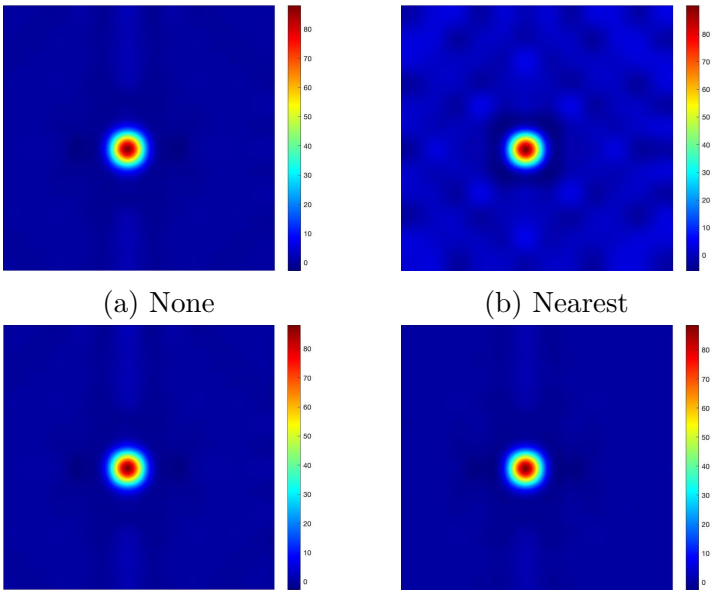

(a) None (b) Nearest

(c) Linear (d) Cubic

Figure 6.4: Image reconstructed using several forms of interpolation.

Since the appearance and quality of the output image is estimated by the amount of error created by any interpolation method, the analysis of the image processing technique in Figure 6.5 shows that linear interpolation and cubic interpolation produce better reconstructed images. The analysis shows variation of MSE, PSNR and SSIM with increasing percentage of image reconstruction. It can be seen that at 100 % reconstruction, the linear interpolation performs well as it produces low MSE, high PSNR and SSIM. Therefore, it is on the basis of the quality of the reconstructed image as well as being, computationally, the simplest form of interpolation that linear interpolation is chosen as a form of image interpolation in the work.

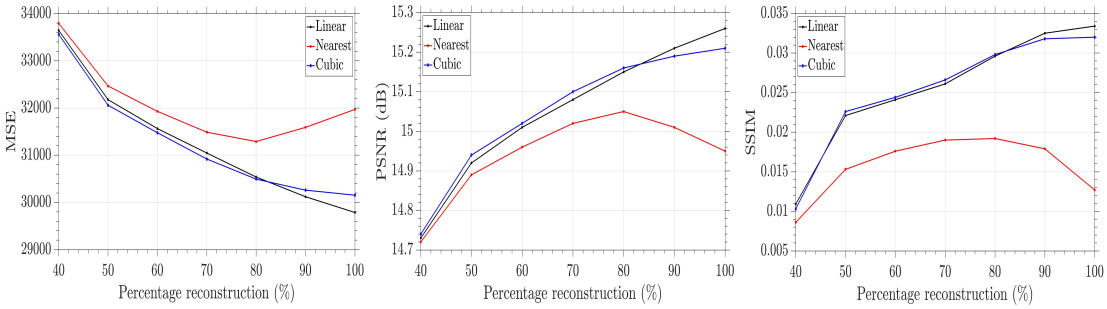

(a) MSE (b) PSNR (c) SSIM

Figure 6.5: Analysis of the image quality as a function of percentage reconstruction (%) for the three forms of image interpolation with respect to Figure 6.5a.

The next step towards image reconstruction is to investigate the effect of the

variation of different filters to the quality of the image. Four filters to be considered are the ramp, Shepp-Logan, Hann and Hamming filters [60, 27]. They are used together with the linear interpolation. The reconstructed images are shown in Figure 6.6.

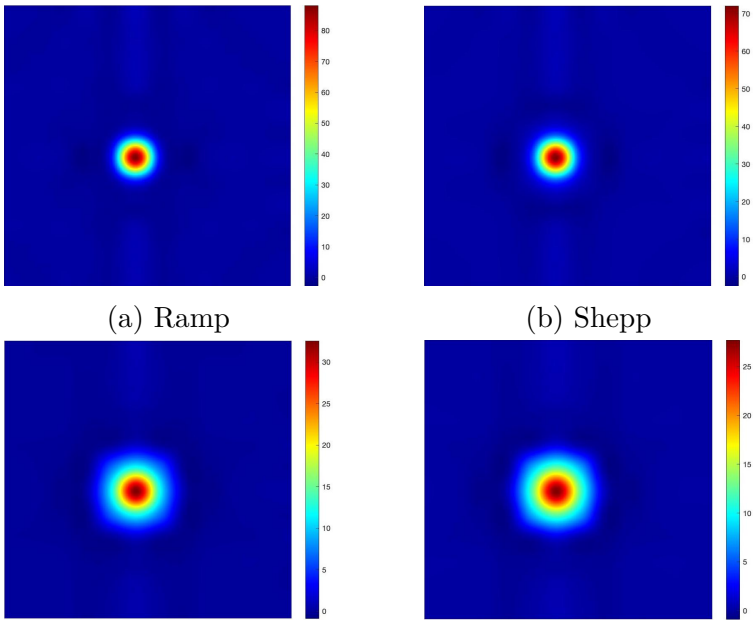

(a) Ramp (b) Shepp

(c) Hamming (d) Hann

Figure 6.6: Image reconstructed by varying different types of filter.

While the ramp and Shepp-Logan produced good quality images as seen in Figure 6.6, the true test of the reconstructed image quality can be established from Figure 6.7. It can clearly be shown that for all three metrics the ramp filter gives the quality image. Therefore, the ramp filter will be utilised in this work as it produces high quality image and reduces image blurring by not allowing the low frequency components to pass.

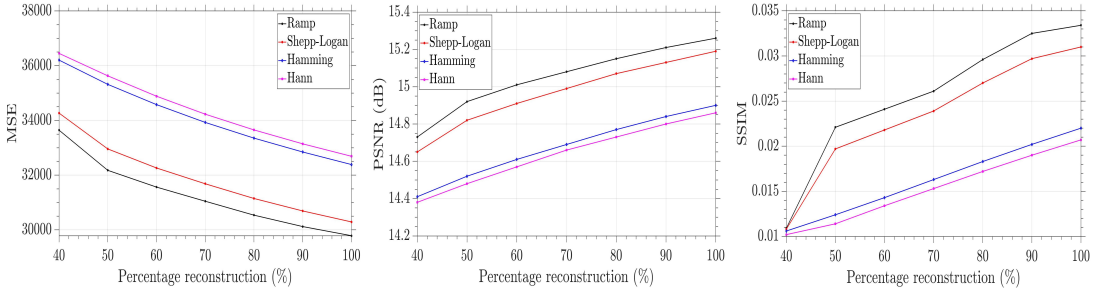

(a) MSE (b) PSNR (c) SSIM

Figure 6.7: Analysis of image quality for different types of filter.

Broadly, the effect of the filters in the performance may not be clearly observed because the image being reconstructed has no noise to filter as seen in the

low values for SSIM. Finally, the effect of frequency compression in the reconstruction is investigated using several values of the frequency compression parameters. Frequency compression is a scalar in the range [0,1] which modifies the filter by rescaling its frequency. The default value is 1 and for the value to be less than 1, denoted by, n_i, means that the filter is compressed to fit into the frequency range [0,n_i], in normalised frequencies. The effect of decreasing the frequency compression parameter is shown in Figure 6.8

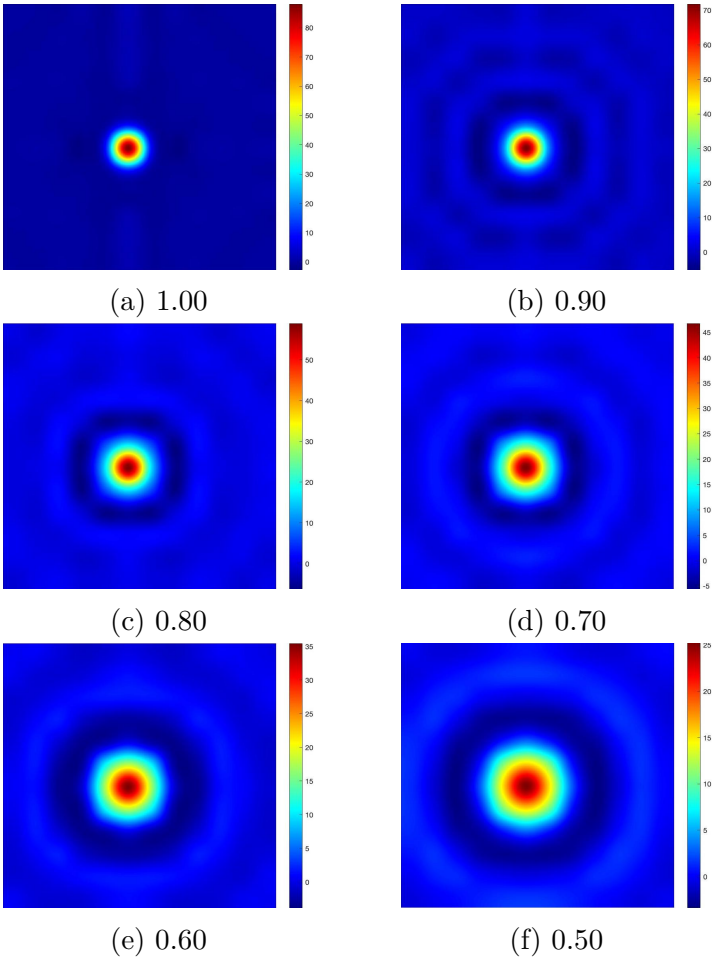

(a) 1.00 (b) 0.90

(c) 0.80 (d) 0.70

(e) 0.60 (f) 0.50

Figure 6.8: Image reconstructed by varying the frequency compression.

There is significant difference in the quality of the reconstructed images as a result of the variation in frequency compression parameters, however, this difference can be clearly established quantitatively by analysing the image quality metrics as shown in Figure 6.9.

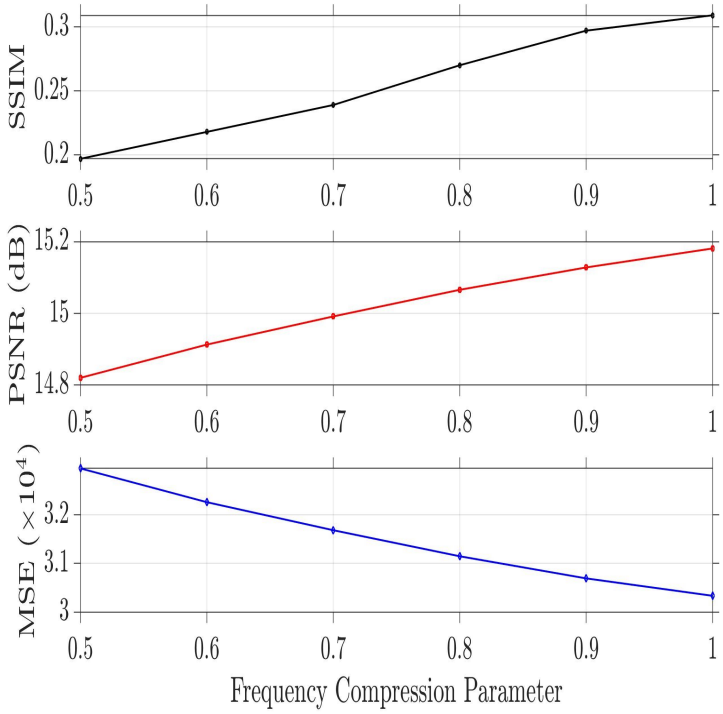

Figure 6.9: Analysis of image quality variation with the frequency compression factor.

There is an improved quality on the images as the frequency compressional parameter is increased. It therefore shows that since the frequency components of the reconstructed image are not being removed, there is less need for frequency compression. Thus, the default value for the frequency compression is to be maintained for all image reconstructions since low values of frequency compression introduce noise into the image as seem in Figures 6.8b to 6.8f.

6.6 Position Reconstruction

Safe disposal of radioactive waste ensuring safety of the environment is an important aspect of radioactive waste management. In most waste container, there is the probability that the activity concentration of the waste is localised. Limiting the radiation effect of the waste to the environment requires proper identification of these localised hotspots inside waste containers. This is why localisation of hotspots is necessary in mitigating the radioactive hazard to the environment and general public and is the objective of this research work. The tomographic reconstruction of radioactive sources inside the waste drum requires knowledge of the gamma-ray attenuation by the matrices in the waste container. However, since the experimental measurement part of this work did not involve active waste, the effect of the matrix on the attenuation is not going to be factored and thus would

be taken as a unity. This will obviously contribute to the uncertainty associated with the measurements when calculating the activity of the radionuclides. The attenuation effect by the matrices will be investigated and modelled into the MCNP code to be discussed later in Section 6.8.

Consider a radioactive source placed at any point inside a waste drum and its response being measured by a collimated detector. The intensity of the radiation detected is a function of the radioactive source activity, position and the surrounding attenuation matrix. The raw data measured by the detector for the angular direction through the waste drum are a set of gamma-ray projections acquired at multiple angles for the full rotation. These raw data for the angular direction represent the full set of line integrals through the waste drum for all paths of the gamma-ray beam at all angles. As discussed in Section 4.2.1 this is known as the Radon Transform. For the localisation of hotspots, the set of angular projections cannot alone be sufficiently reconstructed [1], so it is most commonly combined with projections from either radial scanning or vertical scanning. The two image reconstruction approaches for radioactive source localisation in this work are (a) the radial and vertical segmented dependent count rate distributions where the projections obtained from radial and vertical movements of the detector are combined, (b) the angular and vertical segmented dependent count rate distributions where the projections from the angular and vertical movements of the detector are combined. The final stage in the positional reconstruction is implementation of the resulting projections from the two approaches above into the filtered back projection (FBP) algorithm developed using a MATLAB code for image filtering and smoothing.

6.6.1 Point Source Measurement

To investigate the detector response and hotspot localisation, a ^{60}Co point source of activity 247 kBq given at the time of measurement was placed at a height of 40 cm. The distance of the drum segment centre from the centre of the detector surface was 59 cm and the distance of the ^{60}Co point source from the drum segment centre was 10 cm, meaning that the point source was 69 cm from the detector surface as can be seen in Figure 6.10. The 1332.5 keV gamma-ray was used for the measurements.

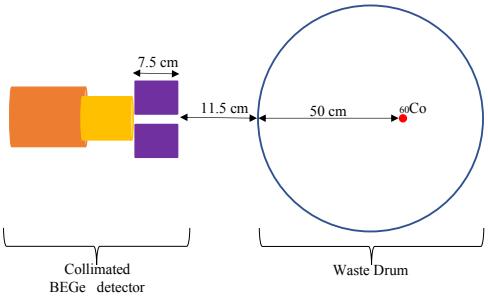

Figure 6.10: Plan view of ^{60}Co source inside a radioactive waste drum relative to the collimated detector.

This ^{60}Co point source at any location inside the waste drum can be described in cylindrical coordinates with respect to the centre of the drum. Therefore, the position of the point source is defined by its radial offset, R_s, its polar angle θ, and its height, H, relative to the drum centre. The signature of each of the gamma-ray energies associated with the point sources inside the drum is generally a peak in the angular, vertical and radial dependent count rate distributions. The cylindrical coordinates can then be estimated through the combination of either the angular and height dependent count rate distributions, or radial and height dependent count rates distributions. The vertical height of the waste drum was segmented into 24 sections in steps of 5 cm. As mentioned before, the angular scanning was done at steps of 12° round the waste drum at the segment of interest. A collimated BEGe detector was utilised to scan each segment of the vertical axis from top to bottom and the count rates were recorded. A slice was taken of the segment of interest and scanned for the angular rotation and the radial axis and the count rates for each of the angular and radial projections recorded. It took about 4 hours to acquire enough counts for each projection given the high attenuation by the drum wall which is made of stainless steel and is 7 mm thick.

6.6.2 Measurement of Two Point Sources

The response of the detection system to sources with variable activity distributions was investigated using two point sources at different locations inside the waste drum. The first scenario was having the two sources positioned at same vertical drum height but different positions along the z-axis (radial plane). The second was having both sources positioned at different heights of the vertical drum axis and different z-axis (radial plane). The detailed measurement procedures for the two scenarios are discussed below.

6.6.2.1 Two Point Sources at Same Height inside the Drum

Two ^{137}Cs point sources of relatively equal activities at the time of measurements, 230 kBq (to be denoted SB) and 223 kBq (to be denoted SA), were positioned at 10 cm and 20 cm respectively on opposite sides of the drum centre vertical axis as shown in Figure 6.11. This meant that the distance of separation between the two sources was 30 cm.

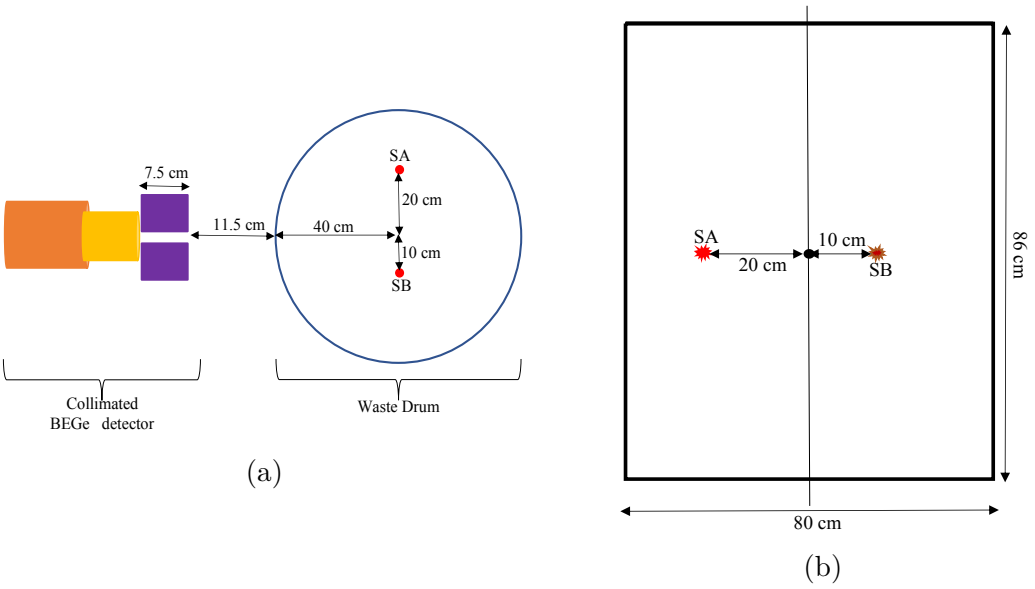

Figure 6.11: Two ^{137}Cs point sources at same height inside a radioactive waste drum. (a) Plan view with collimated detector, (b) Front view of the setup. The tapered end of the drum is not shown.

The activity ratio of SA to SB was estimated to be 0.9695, being 3.05 % in difference between the activities of the sources. Both sources were 60 cm above the bottom of the drum with SA being 52.46 cm from the collimator surface and SB 55.25 cm from the collimator surface. The displacement ratio of SB to SA from the detector collimator surface was calculated as 0.9495, being 5.05 % in difference between the displacement of the two point sources from the detector collimator surface. The drum was scanned by moving the detector along the vertical segments in steps of 5 cm from top to bottom and the projections at each segment were recorded. With the detector height at 60 cm from the bottom of the drum, the radial scanning of the drum was undertaken in 5 cm steps and the projections at each step were recorded. At the same height, the angular scanning of the drum was carried out in 12° steps, and the projections for each angular position were recorded.

6.6.2.2 Two Point Sources at Different Height inside the Drum

Two sources of different radionuclides were utilised to evaluate the response of the detecting system to sources of non-uniform height and significant difference in values of activity. A ^{133}Ba point source of activity 748 kBq (given at the time of measurement) positioned at a height of 80 cm above the bottom of the drum. This source was 10 cm away from the drum's central axis towards the drum wall as represented in Figure 6.12.

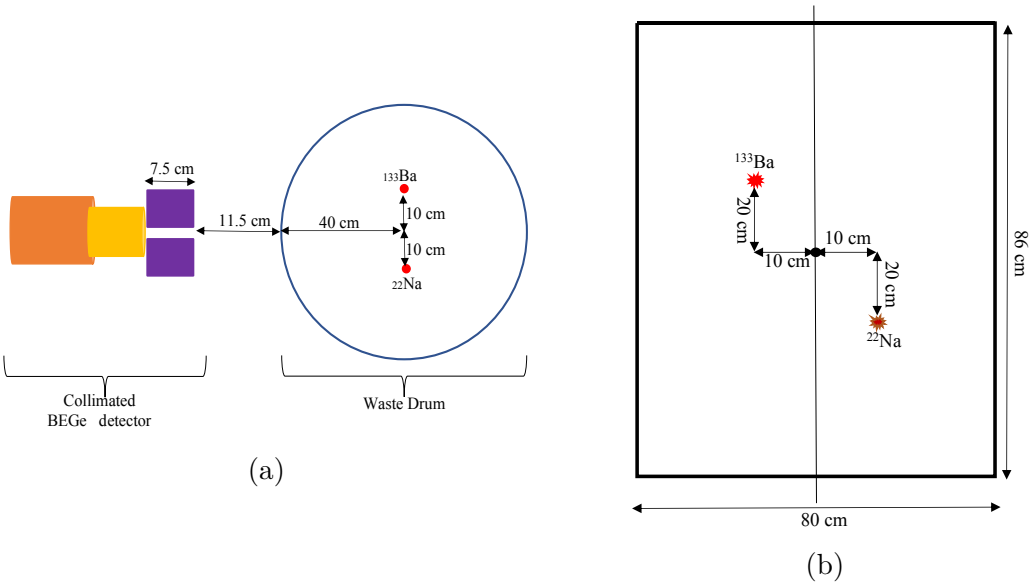

Figure 6.12: ^{133}Ba and ^{22}Na point sources at different height inside a radioactive waste drum. (a) Plan view with collimated detector, (b) Front view of the setup. The tapered end of the drum is not shown.

The notable gamma-ray energies of ^{133}Ba are 80.99 keV of gamma-ray emission probability of 34.2 % and 356.99 keV with gamma-ray emission probability of 62.2 %. The second source is a ^{22}Na point source of activity 115 kBq (given at the time of measurement) placed at a height of 40 cm above the drum bottom but 20 cm distance separation from ^{133}Ba source. This means that the source is 10 cm from the drum mid centre axis towards the other side of the drum wall. The gamma-ray energy considered for ^{22}Na is 1274.5 keV with percentage yield of 99.9 %. The other gamma-ray energy is 511 keV which is an annihilation peak, has percentage yield of about 180 %. The percentage activity ratio for the ^{22}Na source to ^{133}Ba source is 15.37 %. The configuration of the sources inside the drum was such that each is 10 cm away on opposite sides of the drum central axis. The drum was first scanned from bottom to top and the two peaks positions in the axial scan corresponding to the vertical positions of the hotspots noted. The detector was then moved from left to right at a height of 60 cm from the bottom of the

drum, which was the mid point between the vertical positions of the two sources. Afterwards, the drum was scanned at an angle, $\theta = 0^{\circ}$ maintaining the same 60 cm height position of the detector and the corresponding projection recorded. It was then rotated by an angle, $\theta = 12^{\circ}$ and the projection corresponding to the new angle recorded. This was repeated until a set of projections after turning the drum through 360 degrees was obtained. Each of the projections included count rates for each of the gamma-ray energy peaks of the two radioactive sources. For the image reconstruction, the 80.99 keV gamma-ray energy from ^{133}Ba was chosen specifically to check as part of the investigation the detector response to low energy gamma-rays, while the 1274.5 keV gamma-ray energy emitted from ^{22}Na was chosen for the image reconstruction.

6.6.3 Extended Source Measurements

Radioactive wastes are generated from different sources and there is a likelihood of having non point like hotspots inside the drum. The hotspots could be distributed in a volume forming an extended source. Characterisation of such a drum requires an approach capable of estimating the approximate size, intensity and localisation of the distributed source. Interrogating such a waste drum is somewhat complicated due to the fact that the detector responds differently to every point within the source, which in effect contributes to a different degree in the overall gamma-ray intensity unlike the point-like source that is straightforward. For activity quantification of distributed sources, it is evidently important to deduce the efficiency for a given energy for the volumetric source, which can be done from the efficiency of point-like source by using an efficiency transfer technique [58, 102]. This requirement for the deduction of the efficiency from the point source like efficiency will not necessarily impact significant uncertainty in hotspot localisation.

For this measurement, a non-uniform distributed ^{137}Cs source of activity 1.2 MBq, 15 cm long and 1.5 cm in diameter was utilised. The activity concentration at one end of the source is 'hotter' than the activity concentration at the other end. The source is a composition of a ^{137}Cs source prepared in a typical English soil [23] and wrapped in a soft polythene bag as shown in Figure 6.13.

Figure 6.13: A schematic representation of ^{137}Cs extended source wrapped in a polythene bag. The tape indicates the hotter end of the source.

The extended source was positioned at the middle of the drum central axis in such a way that it extended to both sides of the drum half as illustrated in Figure 6.14. It stood 60 cm above the bottom of the drum and 51.5 cm from the detector collimator surface. Given that the aperture of the detector collimator was 10 mm, the source-collimator distance of 51.5 cm is enough for the extended source to be viewed completely by the detector through the collimator aperture. With the collimated BEGe detector, the drum was scanned from top to bottom, and thereafter the detector was moved from left to right with a 5-cm step size at the axial position with the maximum peak counts. The projections (count rates for both radial and vertical scanning were recorded. For the angular scanning, the drum was first scanned at an angle $\theta = 0°$, and the projection

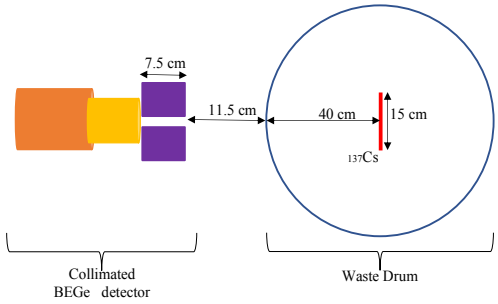

Figure 6.14: Plan view of extended ^{137}Cs source inside a radioactive waste drum relative to the collimated detector.

recorded. The drum was then rotated by angle increments of $\theta = 12°$ and the corresponding angular projections recorded. A set of projections was obtained after turning the drum around. The data acquired in all measurements were then used for tomographic image reconstruction.

6.7 Evaluation of Measurement Uncertainty

Establishing the activity of the radionuclides and hotspot localisation are the major objectives this study set out to achieve. Due to the statistical nature of radioactive decay, the measurement results obtained in this work are an estimation

of those parameters, requiring discussion of the measurement uncertainties which had some effects on the results. It is required that for proper estimation of the measurement uncertainty, an assessment of the effects of all significant sources of uncertainty must first be carried out. The sources of the uncertainty are both statistical and systematic. The uncertainty of statistical errors present in the counting measurement are not very significant as the error can be controlled by the user. On the other hand, the systematic error contributes significant uncertainties in non-destructive techniques as it relates to the properties of the radioactive sample itself. Sources of systematic errors in passive gamma-ray assay include attenuation by the matrix and drum wall, self-absorption in the radioactive material, inhomogeneity of the matrix, calibration factor, and measurement geometry. For reliable results, these measurement uncertainties were corrected for and considered in the computation of the final result values. To correct for the self-absorption within the individual gamma-ray emitting particles, it is always assumed that radioactive material to be assayed and the matrix are reasonably uniform so that self-absorption within the individual gamma-ray emitting particles are negligible. However, these experimental measurements did not involve a matrix and as such, the effects on the activity of the radionuclides are very minimal.

The rotation of radioactive material in segmented gamma scanning while taking measurements helps to minimise the effects of radial inhomogeneities. From the effect of rotation of the radioactive sample on count rate (CR) variation illustrated in Figure 6.15, it can be shown that the ratio of the average count rate of a radioactive

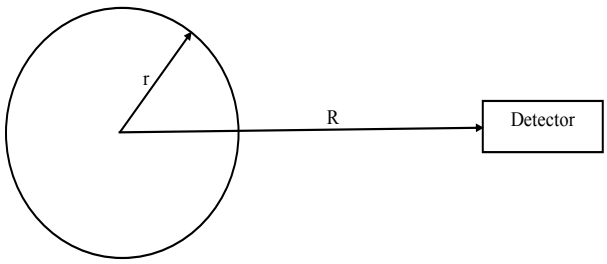

Figure 6.15: Effect of rotation of the radioactive material on count rate variation.

source rotating at a radius, r, to that of a radioactive source located at the centre [24] is given by Equation 6.5

$$\frac{\mathrm{CR(r)}}{\mathrm{CR(0)}} = \frac{1}{1 - \left(\frac{\mathrm{r}}{\mathrm{R}}\right)^2}. \tag{6.5}$$

And for a non-rotating radioactive source, the ratio of the count rate is given by

Equation 6.6 [24];

$$\frac{\mathrm{CR(R-r)}}{\mathrm{CR(R)}} = \frac{1}{\left(\frac{\mathrm{R-r}}{\mathrm{R}}\right)^2}. \tag{6.6}$$

Calculating the effect on the angular scanning using ^{60}Co source with r = 10 cm and R = 59 cm, the ratio of the average count rate, $\frac{\mathrm{CR(r)}}{\mathrm{CR(0)}}$ for a rotating drum was obtained as 1.03 while that of a non-rotating drum, $\frac{\mathrm{CR(R-r)}}{\mathrm{CR(R)}}$ was estimated as 1.45 which is a 29 % improvement when rotating the drum while measuring. Similarly, for the one of the ^{137}Cs sources with r = 20 cm and R still 59 cm, the respective values of $\frac{\mathrm{CR(r)}}{\mathrm{CR(0)}}$ and $\frac{\mathrm{CR(R-r)}}{\mathrm{CR(R)}}$ were 1.13 and 2.29, a 50.6 % improvement by rotating the drum. As clearly shown from the above expression, radioactive material rotation helps in reducing the effects of radial inhomogeneity. The effect of the vertical inhomogeneities was as well minimised by segmenting the height of the drum in stepwise of 5 cm.

The evaluation of the uncertainty of the activity of the radionuclides and hotspot localisation in this work followed international recommended practices [41], by evaluating the contributions of the main uncertainty component. However, a convenient approach to measurement uncertainty computation in non-destructive assay is the use of statistical modelling to simulate the various effects of uncertainties. This will be incorporated into the MCNP simulation to be described in the Section 6.8 below.

6.8 MCNP Simulations

For the validation of the Broad Energy Germanium (BEGe) measurements, simulations for the expected detector performance were performed using the Monte Carlo N-Particle (MCNP) code, a Monte Carlo based particle tracking simulation tool. During this investigation, MCNP modelling was employed for radioactive waste drum interrogation. The performance of the BEGe detector, under a variety of different complex conditions and environments that could not be achieved during laboratory measurement, was investigated with this code once validation of the code for this detector was completed. These conditions included computation of detector responses to radioactive sources at different positions inside the waste drum and estimation of the effect of attenuation matrix on the activity of the radioactive waste.

Monte Carlo simulation has become a very suitable tool for solving these type of complex radiation problems involving a particle's transport because the radiation interactions with matter strictly obey the probability law [98]. The Monte Carlo ability to trace a particle's path from production to absorption or escape

makes the technique useful in radionuclide metrology such as efficiency computation and estimation of detector response function [42, 106].

The main disadvantage of using Monte Carlo modelling to estimate the detector responses to different spectrometric measurements is insufficient reliability in detector parameters provided by the manufacturers. It is therefore required that optimisation of these detector parameters (such as detector crystal dead layers, charge collection and electric field contribution) be carried out first to estimate the values of those parameters that match the experimental measurement. The optimisation of these parameters for the BEGe detector (Model BE6530) utilised in this work had satisfactorily been carried out as discussed in Sections 5.2.1 of this thesis.

The Monte Carlo technique has been applied in this work to simulate the response of a collimated detector to two ^{137}Cs point sources positioned inside a 500 litre standard radioactive waste drum. From the estimated detector response, the efficiency of the modelled detection system geometry was computed. The simulated system efficiency would be utilised to compute the activities of the radionuclides. This simulated activity will then be validated by the experimental activity. MCNP6.2 has been utilised for this simulation. This version of the code is suitable for modelling the collimated detector response due to its pulse height tally (F8) function, which calculates the energy deposition pulses created in the detector. Also, the FMESH tally that creates a file for image visualisation of the source distribution is another feature in this version of the code as shown in Figure 6.19a. This version is very useful in this work due its capacity to model a tapered conical object which formed part of the waste drum as seen in Figure 6.16. The versions of MCNP lower than version 5 do not have this particular feature.

To achieve reliability of the MCNP results, the radioactive source and detector must be accurately modelled and simulated in the computational code environment. The detector responses from the simulation are then validated with experimental data to ensure the physical compatibility of both the simulated and experimental results.

6.9 MCNP Model for Radioactive Waste Measurement

The model for the detector collimator optimisation developed in Section 5.3 was extended by adding the 500 litre standard waste drum whose dimensions are given in Figure A.1 of Appendix A.1. The waste drum wall was modelled as stainless steel of density and elemental compositions listed in Table A.1 of Appendix A.1 [62]. However, no literature was found to categorically provide the type of stain-

less steel as it is required in the choice of material compositions in MCNP code. Therefore, 316L stainless steel was chosen after modelling four types of stainless steel (304, 304L, 316 and 316L) as the material for drum wall that produced closely related detector efficiency with the experimental values. The results for 316L were found to be in good agreement with the experimental efficiency as shown in Figure A.3. The thickness of the drum wall was 7 mm. The MCNP model of the waste characterisation system carefully included all the significant components of the set up used for the experimental measurements as shown in Figure 6.11.

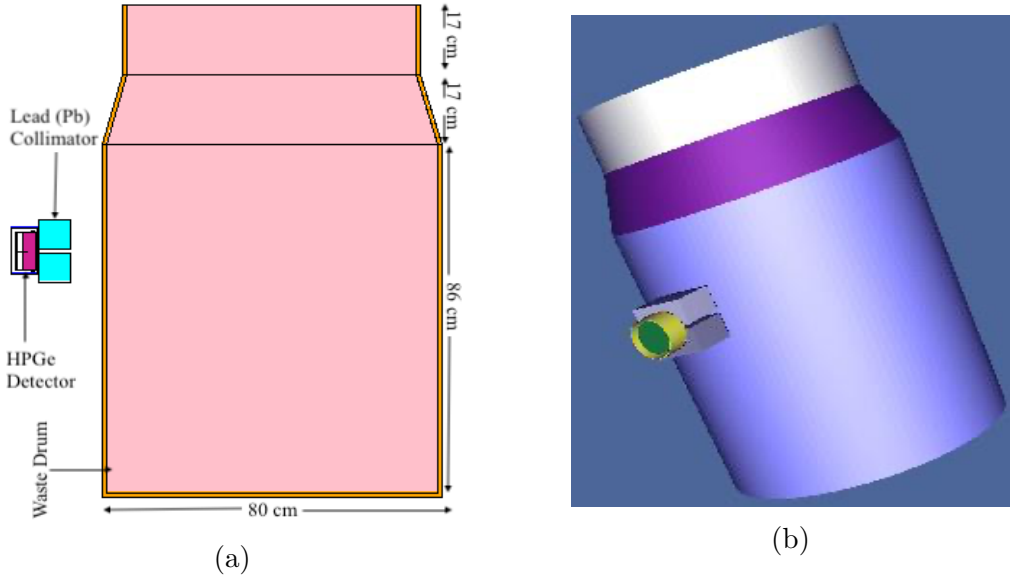

(a) (b)

Figure 6.16: An MCNP model of the radioactive waste drum with BEGe detector (a) 2-dimensional view (3) 3-dimensional view.

6.10 Absolute Efficiency of the Detection System

Similar to the experimental measurements, the efficiency of the system was investigated using ^{241}Am, ^{60}Co, ^{137}Cs and ^{152}Eu modelled as point sources positioned at the geometrical centre of an air filled drum. Generally, the full-energy peak efficiency (ε) of the measurement system is given as the ratio of the number of photons (N_d) detected to the number of photons (N_e) emitted by the source and is represented as;

$$\varepsilon = \frac{N_d}{N_e}. \tag{6.7}$$

The modelled measurement system is simulated using the MCNP code to obtain the number of pulses generated in each channel of the energy spectrum with F8 tally function. The F8 tally simply sums the total energy deposition for each event in a given cell (which in this case is the active volume of germanium detector). The tally result represents the probability per event that a given energy is

deposited in the detector.

The variance (uncertainty) associated with the probability per energy bin is also calculated by MCNP. This uncertainty is based on the sampling statistics and the values can be reduced by running more histories. The estimated uncertainties level for the simulations were maintained at 5 % for a confidence interval of 95 % (k = 2) by running 1×10^9 histories. The simulated result was then normalised to one gamma-ray emitted to obtain pulse height per emitted gamma-ray which represents the full-energy peak efficiency for the modelled measurement system.

6.10.1 Absolute Efficiency of the Detection System for Axial Source Positions

The point of the simulation is to account for variations in detector responses due to source positioning inside the drum. The significance is to develop a model that can improve the quantification of activity of radionuclides present in drum waste. Improving the estimation of the activity of the radioactive samples required correct determination of the solid angle between the source and the detector, and this entails taking into consideration every absorber or attenuating material between the source and detector active medium. Therefore, the MCNP code was written to simulate the detector response for sources located at different points inside the drum and efficiency for each of the source position estimated.

To consider the variations in detector response to sources at different positions inside the drum, four point sources (^{241}Am, ^{60}Co, ^{137}Cs and ^{152}Eu) were simulated with the sources in coaxial and non-axial positions. The first simulation modelled the four sources at three coaxial positions describing (1) source to detector distance of 17 cm (denoted by SR), (2) source to detector distance of 55 cm (represented by SM), and (3) source to detector distance of 92 cm (denoted by SL), all along the detector FoV and on the same horizontal axis with detector midpoint as shown in Figure 6.17.

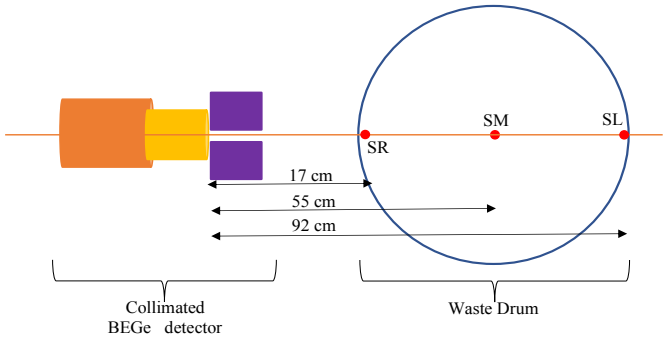

Figure 6.17: Top-down view of ^{60}Co source inside a radioactive waste drum relative to the collimated detector. These sources are all at the same height of 60 cm from the base of the drum.

A history of 1×10^9 particles was simulated to keep the uncertainties low and the efficiency as a function of gamma-ray energy calculated for the three source positions.

6.10.2 Absolute Efficiency of the Detection System for Non-Axial Source Positions

For non-axial positions of radioactive sources, three sources positioned 10 cm, 20 cm and 30 cm away from the drum central midpoint as illustrated in Figure 6.18, and denoted by SN1, SN2 and SN3 respectively were modelled to calculate the detector response and effects of solid angle between the sources and detector active medium on the gamma-ray energies. The detection efficiency for the simulated response was calculated for the gamma-ray energies from 59.54 keV to 1408.01 keV and the results plotted against the gamma-ray energy as illustrated in Figure 7.5.

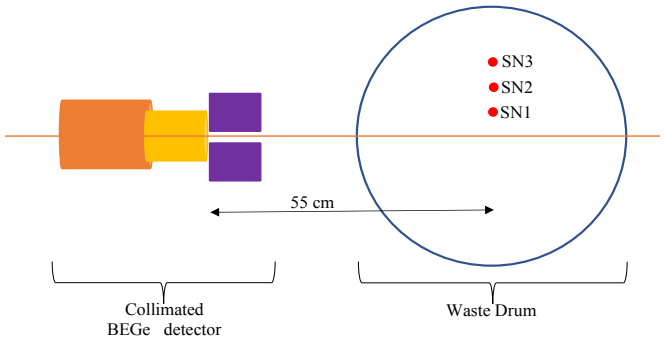

Figure 6.18: Top-down view of ^{60}Co source inside a radioactive waste drum relative to the collimated detector. SN1, SN2 and SN3 are respectively 10, 20 and 30 cm from the centre of the drum.

6.11 Activity Computation Using Simulated Efficiency

The activity of the radioactive sources was computed using Equation 6.8 for the chosen energy lines of ^{60}Co: 1332.5 keV, ^{137}Cs: 661.67 keV, ^{133}Ba: 80.99 keV and ^{22}Na: 1274.47 keV.

$$\mathrm{A} = \frac{\mathrm{N_e}}{\varepsilon \mathrm{T} \rho_\gamma} \mathrm{CF_m CF_w}. \tag{6.8}$$

where N_e is the gamma-ray counts from the experimental measurements, T is the live time and ρ_γ is the emission probability, $\mathrm{CF_m}$ is the matrix attenuation correction factor, $\mathrm{CF_w}$ is the steel wall attenuation correction factor and ε is the detector efficiency. The matrix correction factor, $\mathrm{CF_m}$, was calculated using the Parker formula [77, 103];

$$\mathrm{CF_m} = \frac{-\ln(\mathrm{T^k})}{1 - \mathrm{T^k}}. \tag{6.9}$$

where T is the gamma-ray transmission calculated for each gamma-ray energy and source positions using MCNP, and k is the geometry dependent factor with approximate value of 0.83 [77, 103] for a cylindrical geometry. For the no-matrix model, the matrix correction factor was taken as a unity. Similarly, the drum wall correction factor, $\mathrm{CF_w}$, was calculated using Equation 6.10 [61];

$$\mathrm{CF_w} = \frac{1}{\sqrt{\mathrm{T_w}}}, \tag{6.10}$$

where $\mathrm{T_w}$ is the transmission factor calculated for each gamma-ray energy and source positions using MCNP.

The detection system efficiency, ε, was calculated by averaging the angular efficiency of each segment. To calculate the relevant efficiencies for the gamma-ray peaks, each of the source positions was modelled using MCNP and the individual gamma-ray efficiencies obtained segment by segment using the F8 tally. The FMESH tally feature in the code was used to generate mesh volume for visualisation of the sources inside the radioactive waste drum as shown in Figure 6.19.

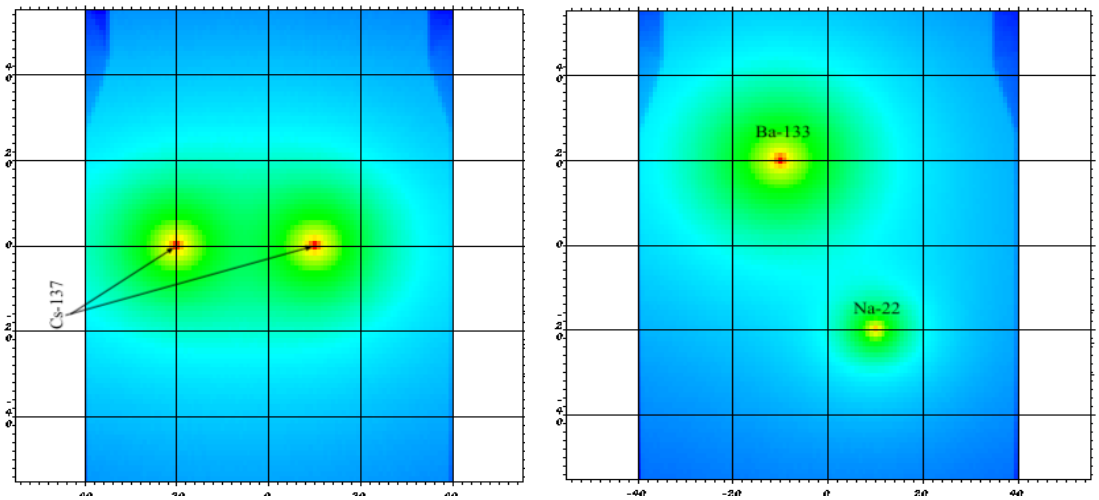

(a) (b)

Figure 6.19: FMESH plots (a). Two ^{137}Cs sources separated by 30 cm (b) A ^{133}Ba and ^{22}Na sources. The blue colour represents the waste drum and the red is the point sources.

The system efficiency obtained for each of the source positions and the corresponding simulated values of CF_m and CF_w were inputed into Equation 6.8 for computation of the activity of the radionuclides. Other parameters in Equation 6.8 such as the values N_e and T were obtained from the experimental measurements.

6.12 Effects of Matrices on the Activity

Apart from waste immobilisation, matrices play significant roles in overall shielding and activity reduction in radioactive waste. Since the fundamental principle for waste packaging entails holding radioactive waste in storage until it has sufficiently decayed to an acceptable level, the amount of time the radioactive waste spent in such storage can be reduced by the introduction of an appropriate shielding matrix. This evidently will help to minimise the amount of time the packaged radioactive waste is stored and thus save time and resources as the activity would have decayed away and the waste can safely be disposed of as clearance level.

The matrices being investigated for their shielding capability of gamma-rays in radioactive waste are concrete, bitumen, polymer and polymer concrete composite. Concrete, bitumen and polymer have regularly been used for waste immobilisation and the possibility of them being used as attenuating materials is explored in this work. Polymer concrete composite is potentially considered a good material that can offer effective attenuation of gamma-rays being a composite material.

Concrete is a compact material formed by the hydration of cement, sand, gravel and water. It has been used as a shielding barrier in nuclear reactors and is one

of the shielding materials for radioactive waste immobilisation [72]. These shielding effects of concrete are dependent on its density and elemental composition. Compared to other shielding materials, concrete is usually preferred because it is a composite-type material in which its constituents can be optimised to meet specific shielding demands. Additionally, concrete is relatively non expensive and its composition relatively in abundant. It is also easy to manufacture.

Bitumen is a typical mixture of high molecular weight hydrocarbons obtained naturally or a residue from petroleum. Bitumen has low radiation stability compared to concrete and could potentially be a useful material for gamma-ray shielding due to its chemical inertness and readily availability. Among all types of bitumen available, asphalt was chosen for this work because like concrete, it is readily available.

Polymer like other materials mentioned above has been used for radioactive waste immobilisation due to its high strength, low permeability, compatible with difficult waste and radiation tolerance. An example of a polymer used in this work is epoxy resin. It is a lightweight, easy to process polymer material, has good radiation stability though not as good as concrete and good mechanical properties utilised as a shielding material for low energy gamma-rays. Epoxy resin is a promising material for shielding low gamma-ray energies due to its lightweight nature.

For the shielding of high gamma-ray energies, a composite material was formed by a mixture of epoxy resin and concrete known in this work as polymer concrete composite (PCC). The PCC is a mixture of concrete and epoxy resin by varying % weight fraction of concrete and epoxy resin. The densities and elemental compositions of these matrices are provided in Table B.2 of Appendix B.1.1. Whilst several studies had been conducted on the effects of epoxy based polymer on gamma-ray shielding, no detailed research has been carried out on the application of epoxy concrete composite matrix in gamma-ray shielding of a radioactive waste drum of LLW or ILW.

The elemental compositions and densities for the concrete and bitumen used in MCNP codes were obtained from the Compendium of Material Composition Data for Radiation Transport Modelling [62], whilst that of epoxy resin was obtained from the Neacrp Comparison of codes for the radiation protection assessment of transport packages [5]. The comprehensive elemental compositions and densities for the materials are listed in Table B.1 of Appendix B.1

The effects of these matrices on the gamma-ray energies in radioactive waste can be investigated by calculating the gamma-ray transmission factor and % attenuation of gamma-rays. The gamma-ray transmission factor represents the frac-

tional number of gamma-rays that are detected after traversing through a matrix compared to that which was detected without a matrix. The fraction of gamma-rays detected depends on the density and elemental compositions of the matrix. The gamma-ray transmission factor can be estimated by computing the ratio of the detected gamma-ray intensity, I, to the incident gamma-ray intensity, I_0, as shown in Equation 6.11.

$$\text{Transmission factor} = \frac{I}{I_0}. \tag{6.11}$$

The incident gamma-ray intensity, I_0, was determined by simulating the counting system with no matrix for source to detector crystal face distances of 17, 27, 37, 47 and 55 cm (for source location at the centre of the drum) in a gamma-ray energy range of 59.54 to 1408.01 keV. The F8 tally was used to obtain the pulse height distribution and this represents the detector response with no matrix.

Thereafter, the waste drum was filled with concrete (Los Alamos) and the detected gamma-ray intensity, I, was determined by simulating the waste drum counting system for a source to detector distance of 17 cm. From the F8 tally, the intensity was estimated. The simulation was repeated for source to detector distances of 27, 37, 47 and 55 cm, and in each case, the detected gamma-ray intensity estimated for all the gamma-ray energies being considered. The whole procedure was then repeated for the remaining matrices (bitumen, polymer and PCC) one after another and their corresponding detected gamma-ray intensities at each of the source to detector distances obtained.

The percentage of the gamma-rays attenuated by the matrices for each of the source to detector distances at four selected gamma-ray energies of 59.54 (^{241}Am), 121.78 (^{152}Eu), 661.67 (^{137}Cs) and 1332.5 (^{60}Co) keV were calculated using Equation 6.12. These gamma-ray energies represent the energy range for the three main interaction mechanisms (photoelectric absorption, Compton scattering and pair production) for gamma-ray.

$$\%\ \text{Attenuation} = \frac{I_0 - I}{I_0} \times 100\ \%. \tag{6.12}$$

Chapter 7

BEGe and MCNP Simulation Results

Results and discussions of experimental measurements at the Precision Radiometrics Instrumentation Development and Education (PRIDE) laboratory and the MCNP simulations are presented in this chapter. The format of the results presentation include the validation of the MCNP simulated efficiencies and activities with the experimental calculated efficiencies and activities.

These are followed by the results of the tomographic reconstruction of radioactive sources from segmented gamma scanning of the drum waste. Finally, the results comparing the gamma-ray transmission factors and % attenuations of some selected matrices on the intensity of the radioactive sources will be presented.

7.1 Validation of the System Efficiency

As mentioned in Chapter six, the two approaches adopted in this work for the calculation of the efficiency of the system include positioning the sources inside the drum at a source to detector crystal face distance of (1) 55 cm, and (2) 17 cm.

The plot of the absolute system efficiencies against the gamma-ray energy for source to detector distance of 55 cm of both experimental and simulated results are shown in Figure 7.1. Similarly, the plot of the absolute efficiencies against the gamma-ray energy for source to detector distance of 17 cm of both experimental and simulated results are shown in Figure 7.2.

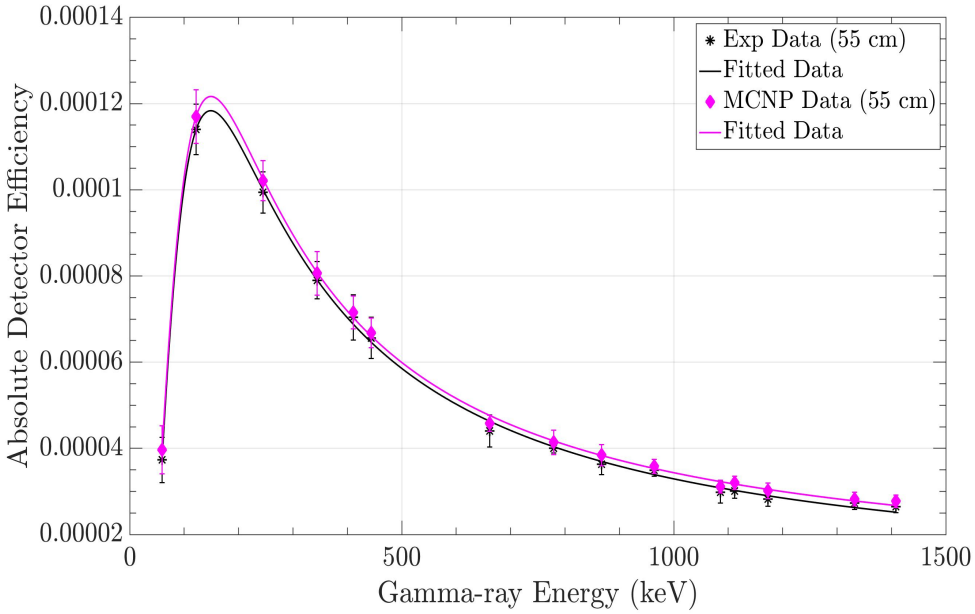

Figure 7.1: Absolute efficiency as a function of gamma-ray energy for the counting system for source to detector distance of 55 cm. A curve fitting package in MATLAB was used to fit the data.

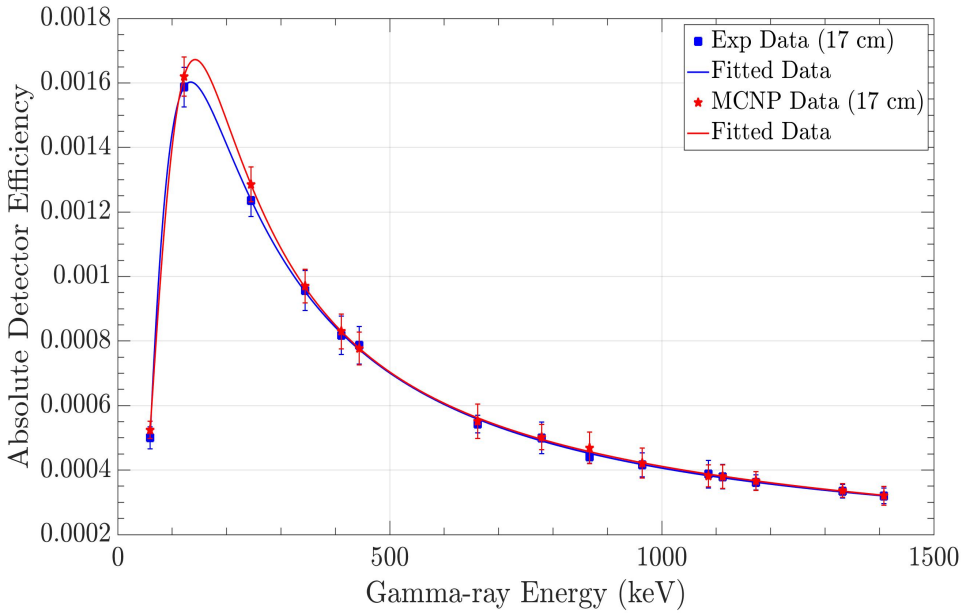

Figure 7.2: Absolute efficiency as a function of gamma-ray energy for the counting system for source to detector distance of 17 cm. A curve fitting package in MATLAB was used to fit the data.

As illustrated in Figures 7.1 and 7.2, the efficiency curves obtained from the two calibration approach follow the same trend, as the maximum efficiency occurred at the gamma-ray energy of 121.78 keV. There is a sudden rise in efficiency

between 59.54 keV and 121.78 keV. This observation is due to higher photoelectric absorption for low energy gamma-rays by the drum wall. The elemental compositions of the drum wall as listed in Appendix A.1 has higher density (8.00 gcm^{-3}) and some high Z elements such as molybdenum. The relative ratio of the simulated efficiency to the experimental efficiency is illustrated in Figure 7.3 to show the agreement between the simulated and experimental efficiencies. The simulated efficiency (though, systematically higher due to reason given in Section 5.2.2.1) and experimental efficiency showed good agreement with the discrepancies for all the energies within 5 %.

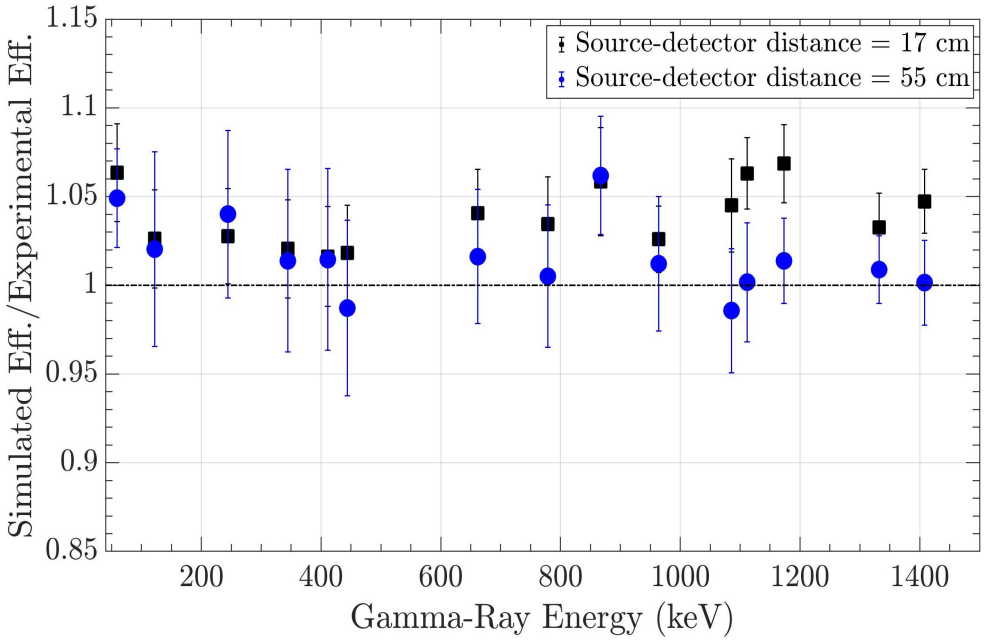

Figure 7.3: Comparison of the simulated to experiment drum efficiencies for both source positions.

7.1.1 Absolute Efficiency for Axial Source Positions

As mentioned in Chapter six, the three axial source positions are denoted by SM (representing source to detector distance of 55 cm), SR (representing source to detector distance of 17 cm, and SL (representing source to detector distance of 92 cm). The efficiency ratios SM/SM, SR/SM and SL/SM were calculated and the results plotted against gamma-ray energy as shown in Figure 7.4. It can clearly be seen that there is a strong dependence of detector response (efficiency) on the positions of radioactive sources. Even on the same axis, the detector to source distance is a function of the solid angle. The response decreases with a reduction in solid angle.

The significance of this result is that localisation of hotspots inside a waste

drum should be aptly considered during waste management proposals. These findings support the usefulness of radial or angular scanning of the drum during waste characterisation. During radial or angular scanning, the detector response varies with changes in detector positions or drum positions, and the rotation or movement of either the drum or detector seek to reduce the detector to source distance thus improving the efficiency of the measurements and the ease of hotspot localisation.

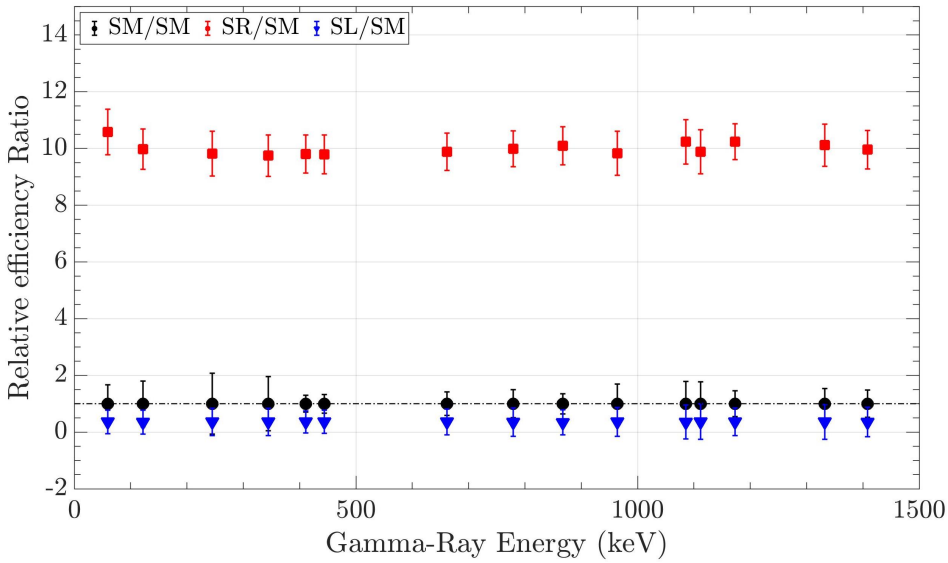

Figure 7.4: Detector response dependence on the sources positions for axial source positions. Source, SM, is 55 cm from detector, Source, SR, is 17 cm from detector and Source, SL, is 92 cm from detector.

7.1.2 Absolute Efficiency for Non-axial Source Positions

The result of the detection efficiency for the simulated response was calculated for the gamma-ray energies from 59.54 keV to 1408.01 keV and plotted against the gamma-ray energy as illustrated in Figure 7.5.

As can be seen from Figure 7.5, the system detection efficiency showed an opposite trend to the efficiency when the sources are in coaxial positions (the black curve). A decrease in gamma-ray energy produces an exponential increase in attenuation effects, limiting the probability of low energy gamma-rays reaching the detector surface. The impact on low energy gamma-rays could be attributed to the high rate of photoelectric absorption by the lead collimator and the drum wall. Further observation showed that an increase in asymmetry (i.e. source farther away from the drum detector axis) reduced the detection efficiency. These results imply that the computation of source's activity by one shot scanning of radioactive drum could significantly be underestimated for non-axial radioactive

sources. We, therefore demonstrate by these results that axial scanning of radioactive waste drums could effectively and efficiently offer better means of estimating the activity of the sources or hotspots. This is potentially recommended for waste drum characterisation for accurate estimation of the activity of hotspots.

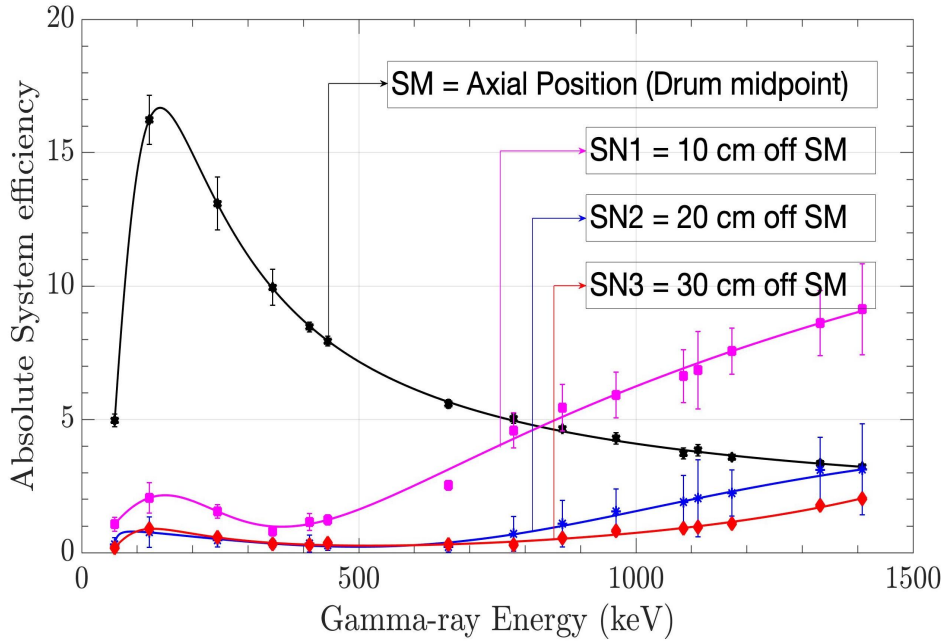

Figure 7.5: Simulated detection efficiency for non-axial radioactive source positions compared to axial source position. SM represents source at the centre of the drum, while SN1, SN2 and SN3 are respectively 10, 20 and 30 cm from the centre of the drum. A curve fitting package in MATLAB was used to fit the data.

The significance of these results for the detection efficiencies for coaxial and non-axial source positions is the need to undertake radial scanning of the drum while performing efficiency calibrations during waste characterisation process so as to achieve reliable detector response for accurate quantification of activity and localisation of the radioactive sources or hotspots. This is to minimise the uncertainty imposed on the efficiency by non-axial position of the sources.

7.2 Validation of Source Activity inside the Drum

It was stated earlier that the total activity of the radioactive sources within the drum was calculated by taking the average of all the activities from each radial segment. The calculated activity is then compared with the true activity (activity of the sources after decay corrections) as illustrated in Table 7.1. The table shows quite some discrepancies on the calculated activities for ^{137}Cs, ^{60}Co, ^{133}Ba and ^{22}Na from the true activities with a minimum percentage deviation of 6.22 % to a maximum percentage deviation of 15.16 %. The estimated activity distribution

Table 7.1: Comparison between the true activity and calculated activity of radionuclides used.

Radionuclides Reference	**Energy (keV)**	**True Activity (kBq)**	**Calculated Activity (kBq)**	**Deviation (%)**
^{133}Ba	80.99	748 ± 27	634.58 ± 39.34	15.16
^{137}Cs	661.67	453 ± 21	408.74 ± 22.98	9.78
^{22}Na	1274.47	115 ± 11	99.26 ± 19.85	13.69
^{60}Co	1173.28	247 ± 16	227.90 ± 29.46	7.73
^{60}Co	1332.50	247 ± 16	231.60 ± 34.57	6.22

for ^{137}Cs is a combination of the activities for the two sources. Specifically, the activity of ^{133}Ba is much more underestimated compared to the other radionuclides due to the higher absorption coefficient of the gamma-rays for 80.99 keV (being the energy considered in the calculation) by the drum wall and lead collimator which significantly reduced the number of gamma-rays being measured by the detector. Furthermore, the activity underestimation for ^{133}Ba and ^{22}Na can also be attributed to non-axial positions of the two sources with the detector. Both sources are not on the same vertical height with the detector and with wider solid angles, will not be fully visible within the detector FoV.

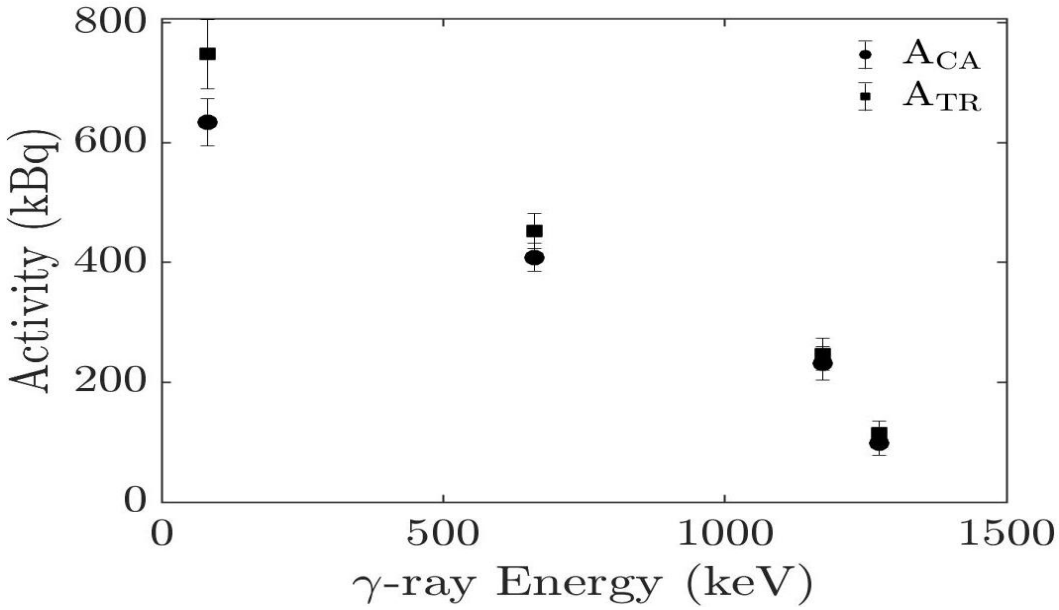

Figure 7.6: Activity ratio for low energy gamma-rays and higher energy gamma-rays. A_{CA} is the average of the calculated activity while A_{TR} is the true activity.

Among the radionuclides, the least deviation was observed in ^{60}Co with 6.22 % difference between the calculated and true activities. This observation could be explained noting the absorption coefficient at the energy is not as high as it is in

low gamma-ray energies.

A comparison of the activity ratio for the low energy gamma-rays and the higher energy gamma-rays is shown in Figure 7.6. As can be seen, the calculated activity for ^{60}Co and ^{22}Na were underestimated from the true activity by a factor of 1.07 and 1.17 respectively, while that of ^{137}Cs and ^{133}Ba were respectively underestimated by 1.11 and 1.17. The figure clearly showed that discrepancy between the calculated and true activities decreases as the gamma-ray energy increases.

Taking a slice through the diameter (radial) of the waste drum at the drum height segment of interest, a normalised activity distributions inside the drum for two ^{137}Cs sources are shown in Figure 7.7. They reflect the angular and radial distributions of the radioactive sources within the drum.

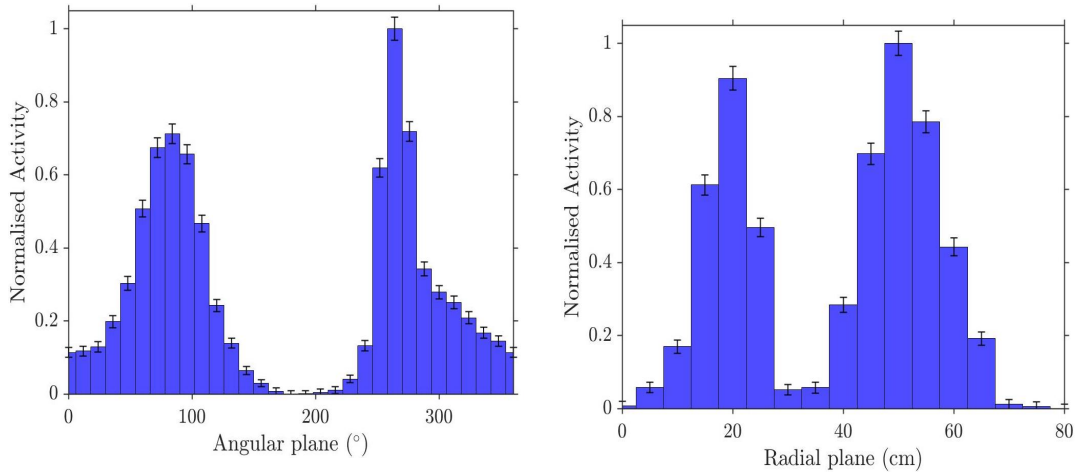

(a) (b)

Figure 7.7: Activity distribution of two ^{137}Cs sources taken from the drum segment of interest. (a) Angular activity distribution on the segment of interest (b) Radial activity distribution on the segment of interest. The sources are positioned 10 cm and 20 cm on both sides of the drum central axis.

The variations in amplitude as seen in Figure 7.7 is a demonstration of the difference in the true activities of the radionuclide.

The simulated activity of the radionuclides is presented in Table 7.2, while the plot of relative activity ratios for the simulated/calculated, true/simulated and true/calculated against the gamma-ray energy is represented in Figure 7.8. As can be seen, the minimum deviation of the simulated activity from the true activity is 5.59 % while the maximum deviation is 14.65 %, indicating an improvement with the simulated results when compared to experimental activity. This improved activity is due to the consideration of the correction factor, CF_{wall}, in Equation 6.2, being the attenuation by the drum wall in the MCNP model and that shows the

capability of modelling in estimating some complex measurement scenarios, and so a suitable technique for the modelling of radioactive waste drum. The highest uncertainties observed in ^{133}Ba and ^{22}Na at 80.99 and 1274.5 keV respectively keV are as a result of non-axial positions of the sources with the detector central axis. Both sources are 20 cm away on either sides of the detector central axis.

Table 7.2: Comparison between the true activity (source activity after decay corrections) and simulated activity of radionuclides used.

Radionuclides Reference	**Energy (keV)**	**True Activity (kBq)**	**Simulated Activity (kBq)**	**Deviation (%)**
^{133}Ba	80.99	748 ± 27	638.39 ± 28.48	14.65
^{137}Cs	661.67	453 ± 21	414.36 ± 18.01	8.53
^{22}Na	1274.47	115 ± 11	100.90 ± 10.67	12.26
^{60}Co	1332.50	247 ± 16	229.13 ± 16.72	7.23
^{60}Co	1332.50	247 ± 16	233.20 ± 19.12	5.59

The result showed that the use of computational technique offered an acceptable alternative method of activity calculation in radioactive waste assay especially for the waste configurations where experimental determination of some parameters such as attenuation correction factor is not readily achievable. A comparison of simulated and calculated to the true activity values shown in Figure 7.8 indicates a good agreement between the simulated/calculated activities as well as between true/simulated and true/calculated activities.

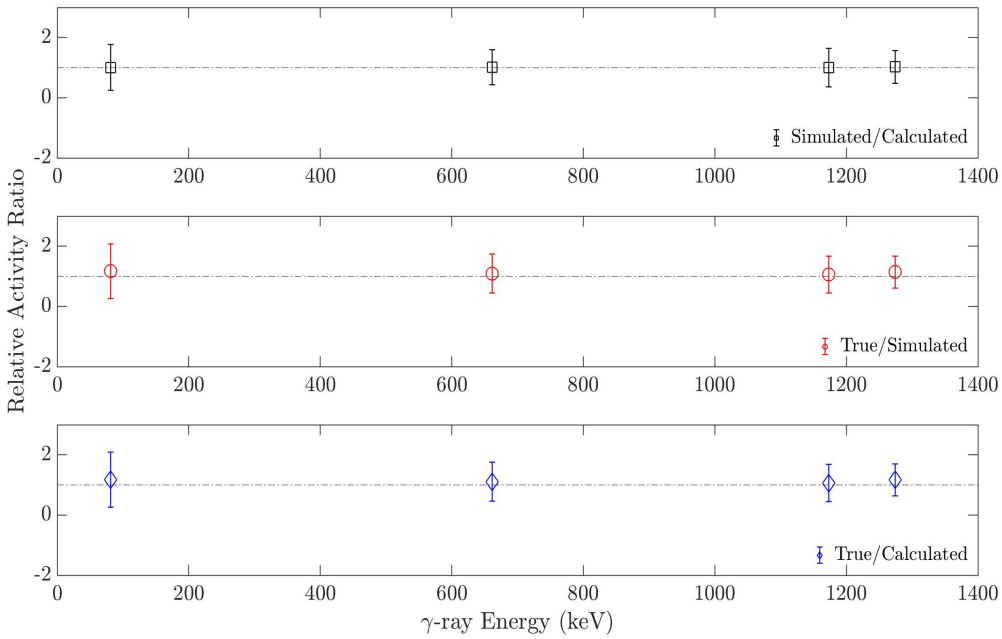

Figure 7.8: Relative activity ratio for the simulated, calculated and true values of source activity used for the measurements.

7.3 Experimental Results of Segmented Gamma Scanning of the Waste Drum

The results of the segmented gamma scanning of the waste drum for (a) a point source, (b) two point sources, and (c) an extended source are presented in this section.

7.3.1 Point Source Reconstruction

By combining both the radial and vertical count rates from the point source measurement, the gamma emission tomography image was reconstructed for the segment of interest using a filtered back-projection technique and smoothed using intensity transformation and linear interpolation as shown in Figure 7.9a.

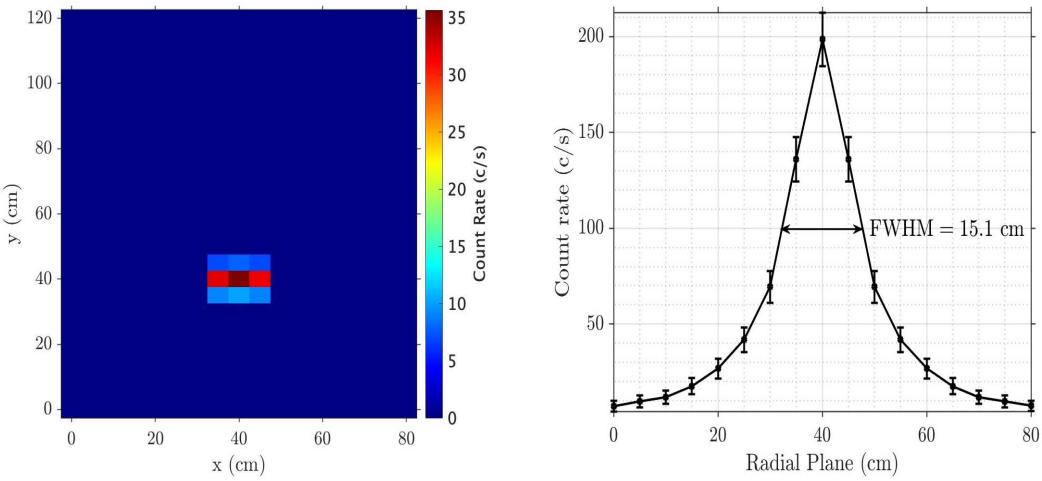

(a) (b)

Figure 7.9: Count rate distributions of a ^{60}Co point source in air from a standard drum. (a) Tomography image reconstruction of the vertical and radial planes (b) Point Spread Function (PSF) for the count rates for radial plane.

The X-Y position of the point source based on the reconstructed image with FBP was calculated. The radial and vertical position (X,Y), of the ^{60}Co point source calculated from the reconstructed image in Figure 7.9a was given as (X,Y) = $(39.9 \pm 1.9, 39.7 \pm 1.9)$ (cm), while the real (X,Y) position of the point source was $(40 \pm 1, 40 \pm 1)$ cm. Figure 7.9b shows the point spread function of the count rate distribution for the radial slice from the segment of interest. The maximum count rate on the point spread function plot occurred at 40 cm.

In a similar way, by combining both the angular and vertical count rates, the gamma emission tomography image was reconstructed at the segment of interest using a filtered back-projection technique and smoothed using intensity transfor-

mation and linear interpolation as illustrated in Figure 7.10a. From the reconstructed image, the θ, Y, position of the point source was estimated. The angular and vertical positions (θ, Y), of the ^{60}Co point source estimated from the reconstructed image in Figure 7.10b is given as $(\theta, \mathrm{Y}) = (179.8 \pm 2.5°, 39.7 \pm 2.1$ cm), while the real (θ, Y) position of the point source is $(180 \pm 2°, 40 \pm 1$ cm). The estimated θ-Y position of the ^{60}Co point source as illustrated in Figure 7.10a represents the location of the 'hotspot' inside the waste drum. Notably, the maximum of the count rate for the 'hotspot' occurred at a drum rotation angle, θ, corresponding to the closest distance between the detector and the radioactive source (hotspot). There is a possibility of a second smaller peak known as the mirror peak when the point source appeared again in the field of view of the collimated detector after a half rotation during the angular scan, however, this reconstruction considers the major full energy peak for the location of the actual hotspot.

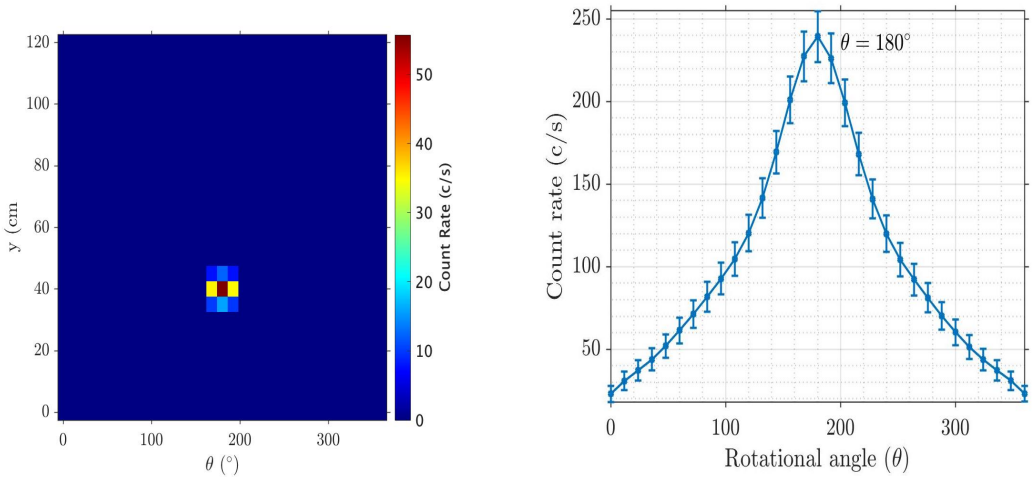

(a) (b)

Figure 7.10: Angular dependent count rate distributions of ^{60}Co point source (a) Image reconstruction of the vertical and angular plane (b) Point Spread Function (PSF) of the angular count rates.

Figure 7.10b shows the angular count rate distribution of the point spread function. The maximum count rate on the point spread function plot occurred at the rotational angle, $\theta = 180°$ being the closest angle to the source with the maximum count rates.

7.3.2 Reconstruction of Two Point Sources

The measurements taken for the two point sources are (a) two point sources at the same height inside the drum but placed opposite sides of drum vertical axis,

and (b) two point sources at different height inside the drum but placed opposite sides of the drum vertical axis..

Two Point Sources at the Same Height inside the Drum

By the combination of the vertical and radial count rates from two point sources on the same drum axis, the projections were reconstructed using filtered back projection and the reconstructed image smoothed as illustrated in Figure 7.11a.

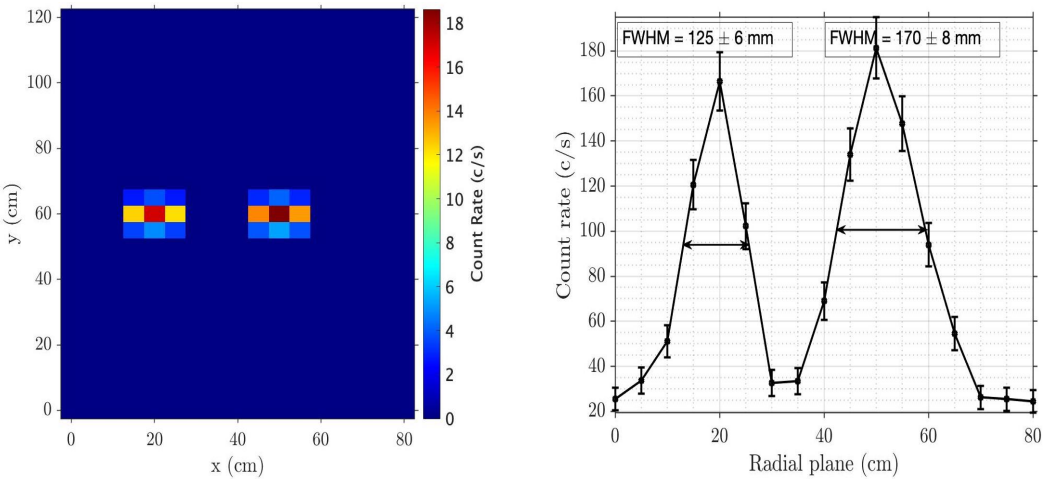

(a) (b)

Figure 7.11: Count rate distributions of two ^{137}Cs point sources in air from a standard drum. (a) Tomography image reconstruction of the vertical and radial planes (b) Count rate distribution on the radial plane of the segments of interest with FWHM of 125 $\pm$ 6 mm and 170 $\pm$ 8 mm for peaks SA and SB respectively.

The radial and vertical positions (X,Y), for SA calculated from the reconstructed image as seen in Figure 7.11a were given as $(X, Y) = (18 \pm 2, 57 \pm 4)$ (cm), while the real position (X,Y) of the point source was $(20 \pm 1, 60 \pm 1)$ cm. The radial and vertical positions (X,Y), for SB calculated from the reconstructed image as shown in Figure 7.11a were given as $(X, Y) = (49.2 \pm 1.8, 57.9 \pm 2.2)$ (cm), while the real position (X,Y) of the point source was $(50 \pm 1, 60 \pm 1)$ cm. The percentage difference in the intensity of the count rate of SA from SB as shown in Figure 7.11a is estimated as 8.26 %. This difference in intensity is largely due to (a) difference in activity, calculated earlier as 3.05 % and (b) displacement difference of the two sources from the detector collimator surface, obtained previously as 5.57 %. The addition of these two percentage values is approximately the same as the percentage difference estimated from the reconstructed images. The count rate distribution demonstrated in Figure 7.11b clearly showed that the radial position of SA is 20 cm while the radial position of SB is 50 cm. The percentage ratio

in count rate amplitude of SA to SB is estimated as 8.27 %, which is closely related to the figure obtained earlier. This percentage ratio in amplitude results from the percentage ratio of both sources activities and displacement of the sources to the detector collimator surface. This observation shows the effectiveness of the system in localisation of hotspots of variable intensities or amplitudes as represented in Figure 7.11.

In a similar manner, by using both the vertical and angular count rates, the gamma emission tomography image was reconstructed at the segment of interest using filtered back-projection techniques and smoothed as illustrated in Figure 7.12a. From the reconstructed image, the θ-Y positions of the point sources were estimated. The angular and vertical positions (θ_A, Y_A), of SA estimated from the reconstructed image in Figure 7.11a were given as $(\theta_A, Y_A) = (83.6 \pm 2.5°, 59.3 \pm 1.9$ cm), while the real (θ_A, Y_A) position of the point source was $(84 \pm 2°, 60 \pm 1$ cm). For the SB, the angular and vertical position (θ_B, Y_B) obtained from the reconstructed image was given as $(\theta_B, Y_B) = (263.9 \pm 5.1°, 59.9 \pm 1.9$ cm), while the actual position of SB was $(264 \pm 5°, 60 \pm 1$ cm). These estimated θ -Y positions of the two ^{137}Cs point sources are representations of the locations of the

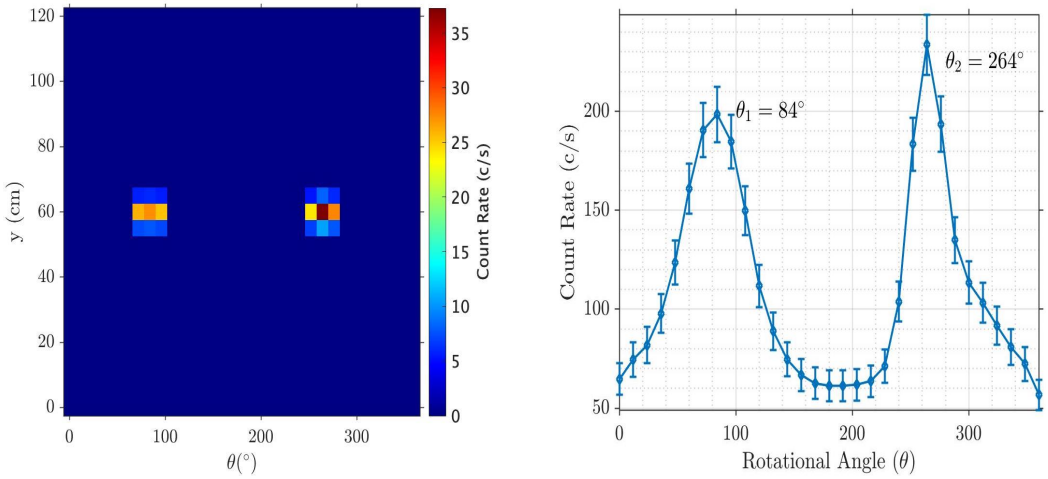

(a) (b)

Figure 7.12: Angular dependent count rates distributions of two ^{137}Cs point sources. (a) Image reconstruction of the vertical and angular count rate distributions. (b) Point Spread Function (PSF) of the angular count rates of the two sources.

'hotspot' inside the waste drum. Remarkably, the maximum of the count rate for the hotspot occurred at a drum rotation angle, θ, corresponding to the closest distance between the detector during drum rotation and the hotspots. This therefore implies that the maximum of the count rate for SA occurs at a rotating angle, θ, of $84 \pm 3°$, while the maximum of the count rate for SB occurred at a rotating

angle, θ, of $264 \pm 5°$ as also shown in Figure 7.12b, which is a plot of the angular count rate distribution.

Two Point Sources at Different Height inside the Drum

The image reconstruction of the two sources requires gating on each of the selected energy and thereafter, combining them to produce a reconstructed image of the locations of the radioactive sources. With a combination of the radial and vertical count rates, a reconstructed image of the gated 80.99 keV using filtered back-projection technique is presented in Figure 7.13a.

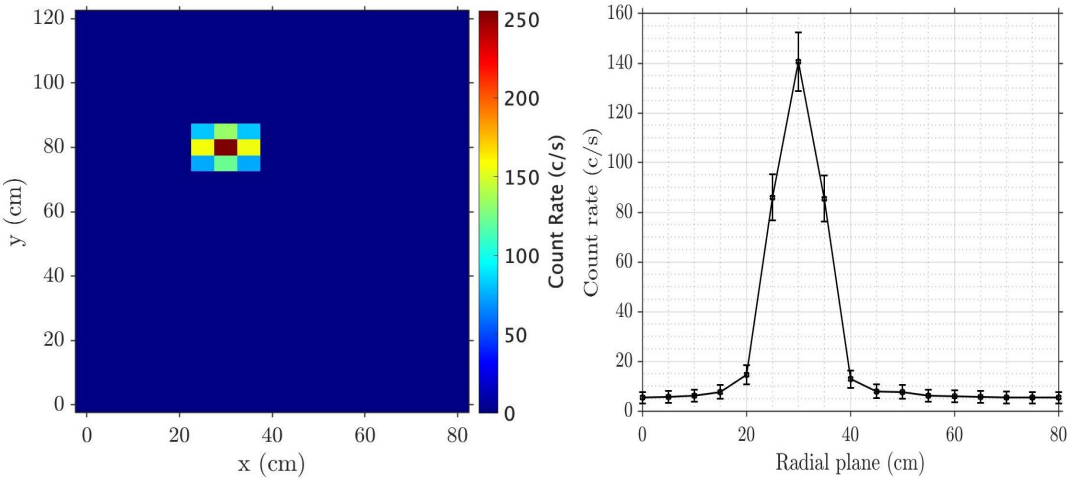

(a) (b)

Figure 7.13: Count rates distributions of 80.99 keV gamma-ray energy of ^{133}Ba point source in air from a standard drum. (a) Tomography image reconstruction of the vertical and radial plane (b) Count rate distribution on the radial plane of the segment of interest.

Implementing the vertical and radial count rates, the X-Y position of the ^{133}Ba source was estimated from the reconstructed image. The estimated position of the ^{133}Ba, (X,Y) = $(29 \pm 2, 79 \pm 2)$ (cm), while the real position is (X_r, Y_r) = $(30 \pm 1, 80 \pm 1)$ (cm). The count rate distribution on the radial plane of the segment of interest as shown in Figure 7.14b clearly showed that the ^{133}Ba source is positioned 30 cm from one radial end of the drum wall and 10 cm off the drum radius.

By combining the vertical and angular count rates, a tomography image using a filtered back-projection technique was reconstructed for the gated 80.99 keV as shown in Figure 7.14a. The vertical and angular position (θ, Y), of the ^{133}Ba point source estimated from the reconstructed image in Figure 7.14a was given as $(\theta, \mathrm{Y}) = (263.9 \pm 1.5°, 79.3 \pm 1.6$ cm), while the real (θ, Y) position of the point

source was $(264 \pm 2°, 80 \pm 3$ cm).

The angular count rate distribution of the ^{133}Ba point source on the horizontal axis is illustrated in Figure 7.14b. The estimated angular position of the sources was given as $263.8 \pm 2.1°$, which lies within 1σ of the actual source position.

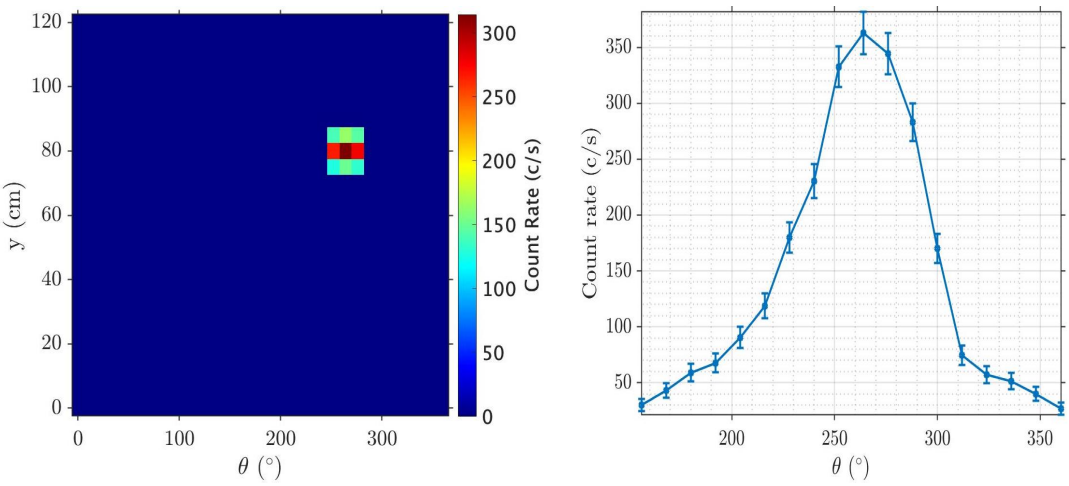

(a) (b)

Figure 7.14: Angular dependent count rate distribution of the 80.99 keV gamma-ray energy of a ^{133}Ba point source (a) Image reconstruction of the vertical and angular count rate distribution (b) Angular count rates of the source plotted against $\theta°$.

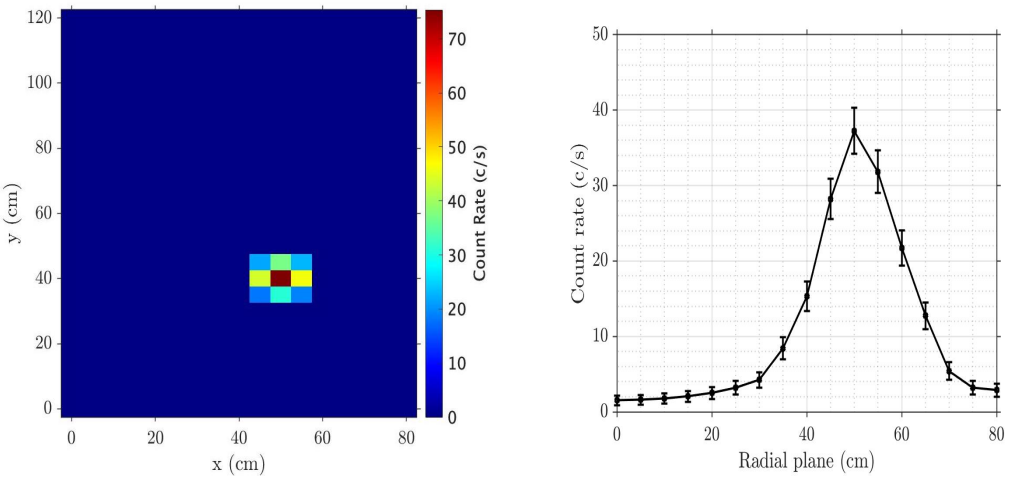

(a) (b)

Figure 7.15: Radial dependent count rate distributions of 1274.5 keV gamma-ray energy of ^{22}Na point source in air from a standard drum. (a) Tomography image reconstruction of the vertical and plane plane (b) Count rate distribution on the radial plane of the segment of interest.

By combining the radial and vertical count rates, a tomography image of the gated 1274.5 keV was reconstructed using filtered back-projection technique as demon-

strated in Figure 7.15a. From the reconstructed image, the X-Y position of the ^{22}Na source was calculated. The calculated position showed the location of the ^{22}Na point source was (X,Y) = (49.9±2.1, 39.4±1.2) (cm), while the actual source position was (X, Y) = (50 ± 1, 40 ± 1) (cm). The count rate distribution plotted on the radial plane of the segment of interest presented in Figure 7.15b clearly shows that the ^{22}Na source is on a radial position of 50 cm.

The count rates for the vertical and angular scans were combined for the reconstruction of the tomography image for the gated 1274.5 keV using filtered back-projection technique. The reconstructed image shown in Figure 7.16a was used to calculate the vertical and angular positions of the ^{22}Na source. The vertical and angular (radial) position (θ, Y), of the ^{22}Na point source estimated from the reconstructed image in Figure 7.16a was given as (θ, Y) = ($71.8 \pm 1.6°, 39.8 \pm 1.5$ cm), while the real (θ, Y) position of the point source was ($72 \pm 2°, 40 \pm 1$ cm).
The angular count rate distribution of the ^{22}Na point source on the radial plane is presented in Figure 7.16b. The estimated angular position of the sources is given as $71.9 \pm 1.1°$, which is within 1σ of the actual source position.

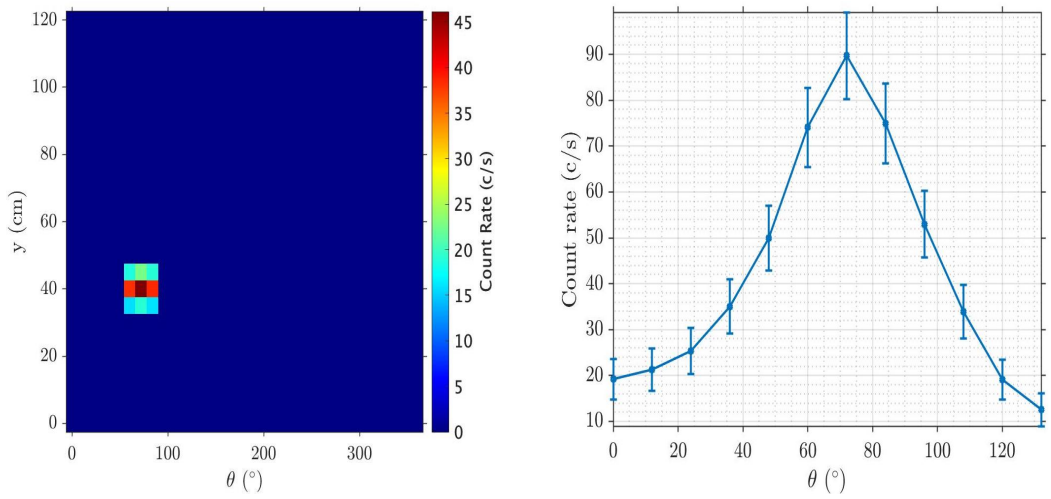

(a) (b)

Figure 7.16: Angular dependent count rate distribution of 1274.5 keV keV gamma-ray energy of ^{22}Na point source (a) Image reconstruction of the vertical and angular count rate distribution (b) Angular count rates of the source plotted against $\theta°$.

The vertical and radial count rates for the 80.99 keV energy peak were respectively combined with the vertical and radial count rates for 1274.5 keV energy. With the combined data, a tomography image for the two gamma sources was reconstructed as illustrated in Figure 7.17a. From the reconstructed image, the vertical and radial positions of the ^{133}Ba and ^{22}Na sources within the

waste drum were estimated. The reconstructed image showed that the radial and vertical coordinates of ^{133}Ba source was $(X_{Ba}, Y_{Ba}) = 29.7 \pm 0.9, 79.8 \pm 1.8$ cm. Similarly, the radial and vertical positions of ^{22}Na source was calculated to be $(X_{Na}, Y_{Na}) = 49.9 \pm 0.6, 39.9 \pm 0.8$ cm. These values are within the 1σ confidence level of the actual position of the sources ($(X_{Ba}, Y_{Ba}) = 30 \pm 1, 80 \pm 1$ cm and $(X_{Na}, Y_{Na}) = 50 \pm 1, 40 \pm 1$ cm) and show the effectiveness of the system in localisation of hotspots inside the drum for sources at different vertical heights. The percentage intensity ratio of the reconstructed image of ^{22}Na to ^{133}Ba was estimated to be 29.54 % which is relatively higher than the activity ratio for the two sources. This high variation compared to the activity could be due to high uncertainty associated with none of the sources on the same vertical height with the detector.

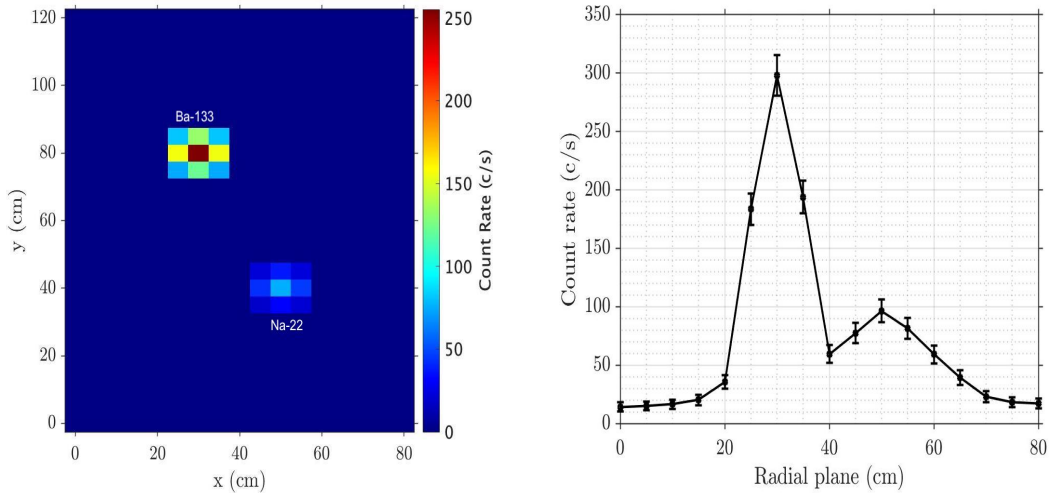

(a) (b)

Figure 7.17: Radial dependent count rate distributions of ^{133}Ba and ^{22}Na point sources in air from a standard drum. (a) Tomography image reconstruction of the vertical and radial plane (b) Count rate distribution on the radial plane of the segment of interest.

As can be seen from Figure 7.17b, the count rate distribution plotted on the radial plane for both sources evidently showed that ^{133}Ba and ^{22}Na are respectively 30 cm and 50 cm from one radial end of the drum wall.

For the angular reconstruction of the two sources, the vertical and angular count rates for the 80.99 keV energy peak were combined with the vertical and angular count rates for 1274.5 keV energy. With the combined data, a tomographic image for the two gamma sources was reconstructed. From the reconstructed image, the angular and vertical positions of the ^{133}Ba and ^{22}Na sources within the waste drum were calculated. The reconstructed image, as seen in Figure 7.18a shows that the angular and vertical coordinates of ^{133}Ba source were

$(\theta_{\mathrm{Ba}}, \mathrm{Y}_{\mathrm{Ba}}) = 263.7 \pm 0.9°, 79.8 \pm 1.2$ cm. Similarly, the angular and vertical coordinates of ^{22}Na source were calculated to be $(\theta_{\mathrm{Na}}, \mathrm{Y}_{\mathrm{Na}}) = 71.9 \pm 0.6°, 39.9 \pm 0.8$ cm. These values are within the 1σ confidence level to the actual position of the sources ($(\theta_{\mathrm{Ba}}, \mathrm{Y}_{\mathrm{Ba}}) = 264°, 80$ cm and $(\theta_{\mathrm{Na}}, \mathrm{Y}_{\mathrm{Na}}) = 72°, 40$ cm) and show the effectiveness of the system in localisation of hotspots of non homogeneous segments of the drum.

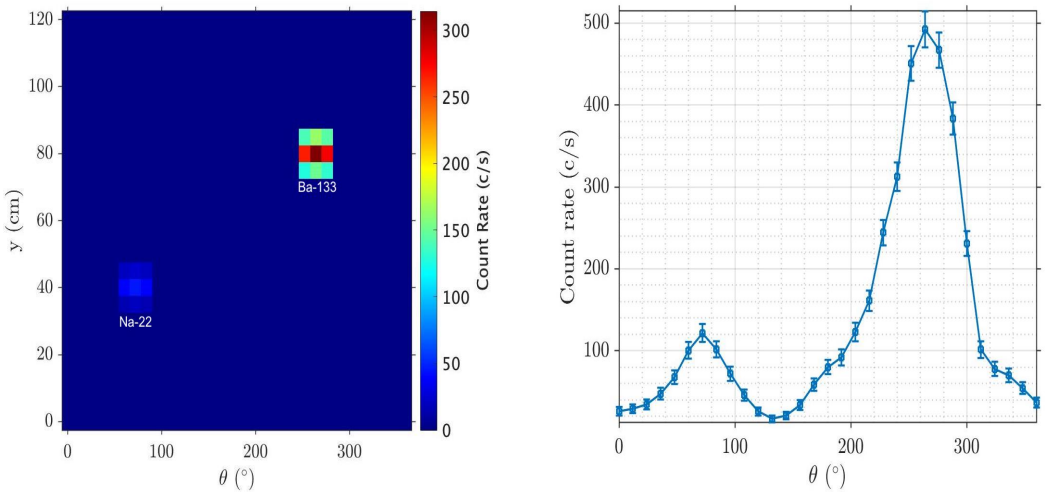

(a) (b)

Figure 7.18: Angular dependent count rate distribution of ^{133}Ba and ^{22}Na point sources (a) Image reconstruction of the vertical and angular count rates distribution (b) Angular count rate of the sources plotted against $\theta°$.

As can be seen from Figure 7.18b, the angular count rate distribution for both sources evidently showed that the angular positions of ^{133}Ba and ^{22}Na are respectively 264° and 72°. These values which are in agreement with initial calculations represent respective angles with maximum count rates for the sources. The percentage intensity ratio of the reconstructed image of ^{22}Na to ^{133}Ba was estimated to be 14.68 % which is within 1σ of the activity ratio for the two sources.

7.3.3 Reconstruction of the Extended ^{137}Cs Source

The extended ^{137}Cs Source was 15 cm long and 1.5 cm in diameter. The activity distribution of the source was non uniform.

With the vertical and radial count rates combined, a tomography image of the source position was reconstructed using filtered back-projection techniques. The reconstructed image was then smoothed as illustrated in Figure 7.19a. The reconstructed image distinctly showed the non-uniform distribution of the source with the intensity at one end being slightly higher than the intensity at the other end. This is also reflected in the linear plot of the count rate against the drum radial

plane seen in Figure 7.19b by the non flat nature of the peak, and demonstrates the effectiveness of the collimated HPGe detector system for the localisation of a non-uniform extended source. The percentage activity difference for the ends of the non-uniform extended ^{137}Cs source is calculated to be 5.65%.

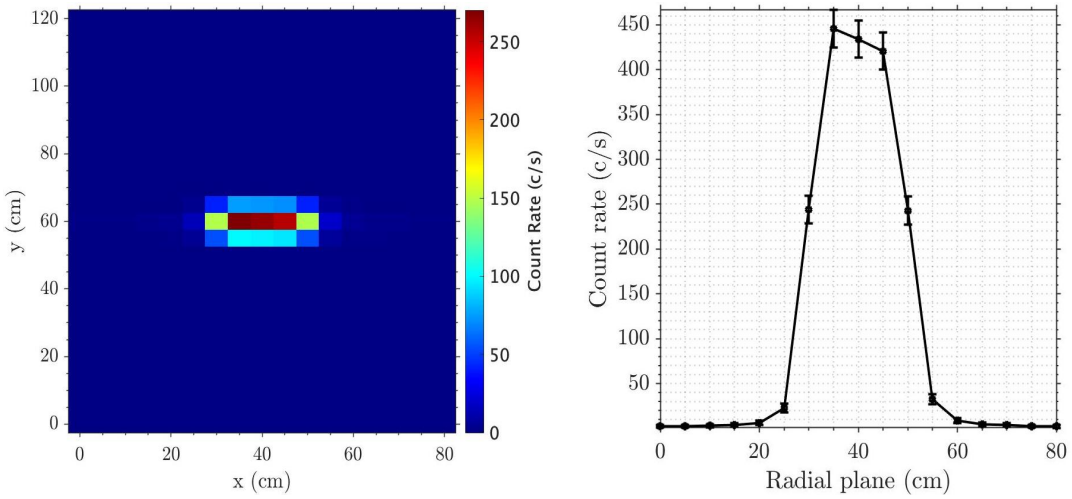

(a) (b)

Figure 7.19: Count rate distribution of ^{137}Cs extended source inside a standard drum. (a) Tomography image reconstruction of the vertical and radial plane. (b) Count rate distribution on the radial plane for the non-uniform extended source.

The calculated position from the reconstructed image showed the location of ^{137}Cs extended source was $(X_h, Y) = (32.7 \pm 1.1, 59.9 \pm 1.2)$ (cm) for the high intensity end of the source, while the low intensity end of the source was positioned at $(X_l, Y) = (47.6 \pm 1.3, 59.9 \pm 1.2)$ (cm). The difference between the two ends of the extended source was estimated to 14.9 ± 1.7 cm, which is within 1σ of the actual length of the extended source.

With the vertical and angular count rates combined, a tomography image of the source position was reconstructed using filtered back-projection techniques illustrated in Figure 7.20a. The reconstructed image clearly showed the non-uniform distribution of the source with two hotspots (denoted by H (high intensity) and L (low intensity)) of variable intensities. The hotspot H represents the end of the extended sources with high intensity, while the hotspot L is the other end of the extended source with low intensity. This is reflected in the plot of the angular count rate against the rotational angle θ, shown in Figure 7.20b in the form of two peaks of different amplitudes. The peak with higher amplitude represents the end of the extended source with high intensity which corresponds to the hotspot, H, while the other peak of low amplitude represent that end of the extended source with low intensity corresponding to the hotspot L.

The calculated position from the reconstructed image showed the location of ^{137}Cs extended source was $(\theta_h, Y) = (83.8 \pm 3°, 60 \pm 2\ cm)$ for the hotspot H,

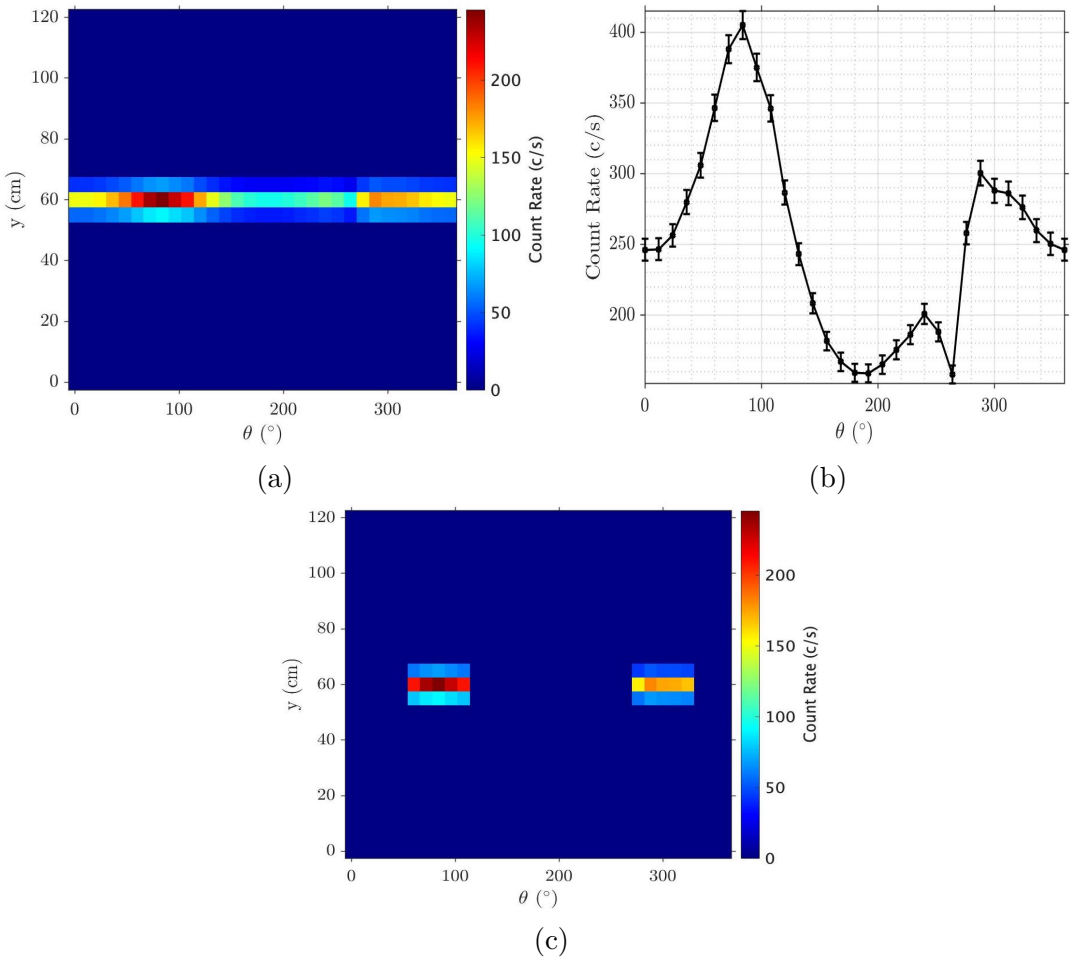

Figure 7.20: Angular count rates distribution of ^{137}Cs extended source inside a standard drum. (a) Tomography image reconstruction of the vertical and horizontal plane (b) Angular count rate distribution against rotational angle θ (c) Smoothed reconstructed image of the extended source.

while the hotspot L was located at $(\theta_l, Y) = (288 \pm 3°, 60 \pm 2\ cm)$. These two angular positions $(83.8 \pm 3°)$ and $(288 \pm 3°)$ are the closest angles with maximum count rates to the higher (H) and lower (L) intensity ends of the extended source. Apart from the two hotspots observed in Figure 7.20a, the entire axial segment of interest is characterised by an extended source distribution with a very low intensity. This could be attributed to the length and intensity of the source. Implementing a smoothing filter on reconstructed image smoothens the lower intensity areas and clearly showed two hotspots of non-uniform intensity, as illustrated in Figure 7.20c, which represent the two ends of the extended source.

7.4 Matrices' Effect on the Source Activity

The gamma-ray transmission factor for each of the matrices was calculated for

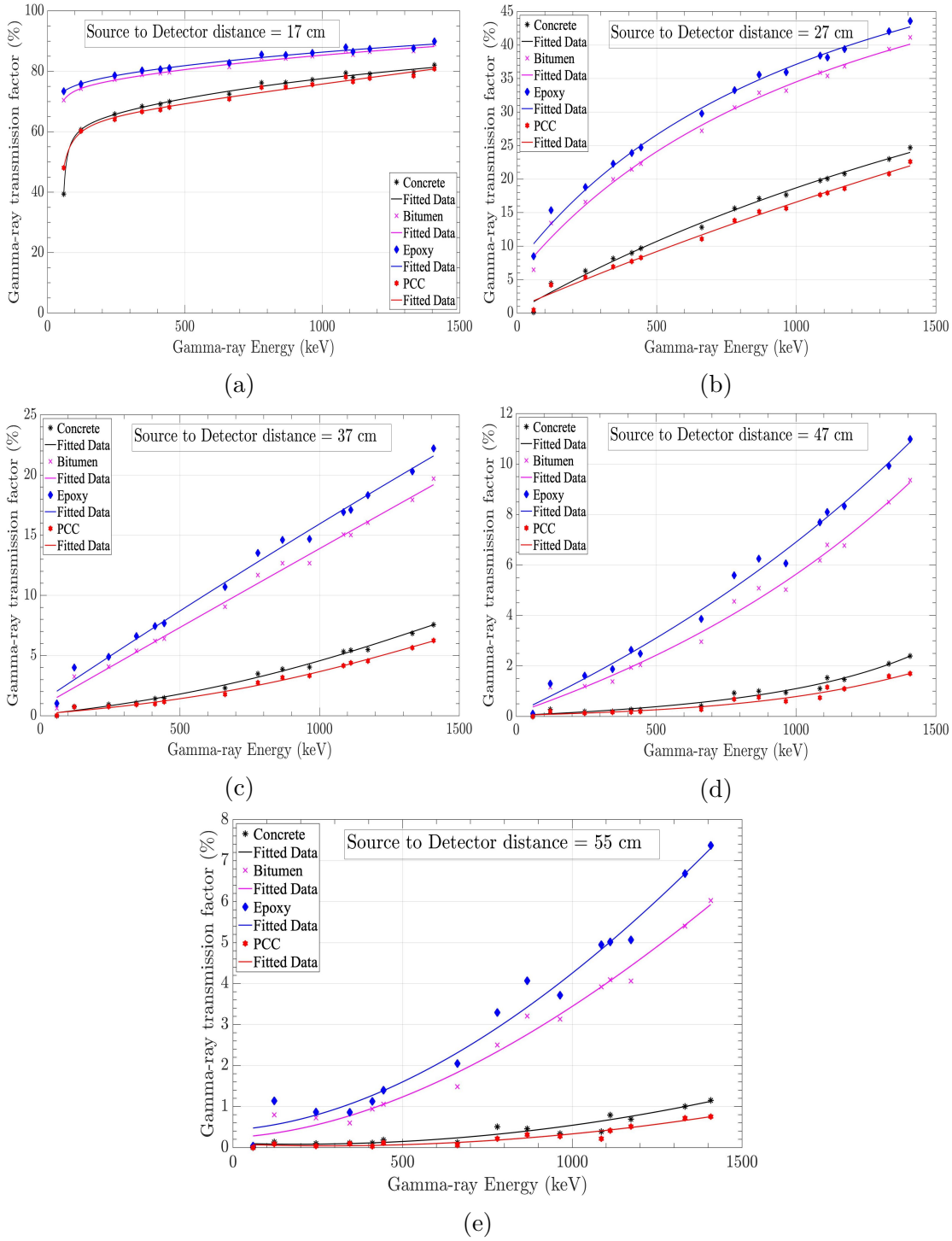

Figure 7.21: Comparison of gamma-ray transmission factor as a function of gamma-ray energy. The fitting was done using polynomial fit function in Matlab code.

each of the source to detector distances using Equation 6.11 and the results plot-

ted against the gamma-ray energy as illustrated in Figures 7.21a to 7.21e.
It can be seen that the gamma-ray transmission factor increases with increasing gamma-ray energy in all the matrices and for all the source to detector distances. The transmission factor for epoxy (having the least density) is the highest among the matrices. However, the case is different for the concrete and PCC with 2.25 gcm^{-3} and 1.75 gcm^{-3} respectively where the transmission factor for the concrete is higher than the PCC. This is due to the variation in elemental composition for both materials. Significantly, for ^{241}Am (59.54 keV), the transmission factor for the concrete matrix is zero at source to detector distances above 27 cm and for PCC at the same energy, the transmission factor is zero for source to detector distance higher than 37 cm.

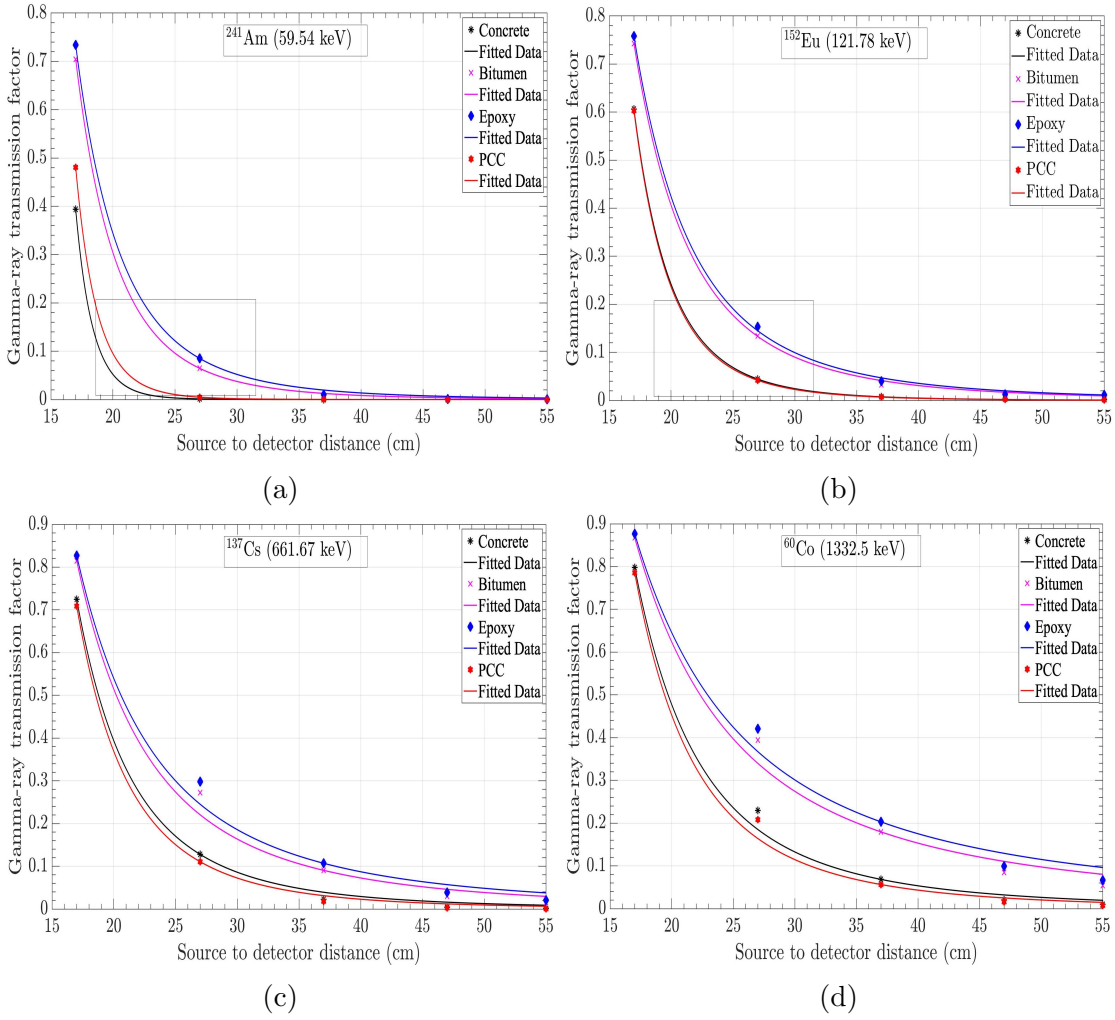

Figure 7.22: Comparison of gamma-ray transmission factor as a function of source to detector distance for (a) ^{241}Am (59.54 keV), (b) ^{152}Eu (121.78 keV), (c) ^{137}Cs (661.67 keV) and (d) ^{60}Co (1332.5 keV).

A comparison of the gamma-ray transmission factor for selected gamma-ray

energy against the source to detector distance is shown in Figure 7.22. It clearly shows, as would be expected, that the gamma-ray transmission factor decreases with increase in source to detector distance.

The results showed that the gamma-ray transmission factor depends on the gamma-ray energy, the elemental composition of the matrix, the density of the matrix and the source to detector distance. Concrete and PCC, having the highest densities of 2.25 gcm^{-3} and 1.75 gcm^{-3} respectively, transmit much lower fractions of incident gamma-rays than bitumen and polymer matrices.
The results of the computed percentage gamma-ray attenuations are presented in Tables 7.3 to 7.6.

Table 7.3: Comparison of gamma-ray % attenuation of the four matrices as a function of source to detector distance for ^{241}Am (59.54 keV).

Source to detector distance (cm)	**Matrix % attenuation**			
	Concrete	**PCC**	**Bitumen**	**Polymer**
17	60.65	51.93	29.55	26.62
27	99.88	99.52	93.55	91.50
37	100.00	100.00	99.39	98.99
47	100.00	100.00	99.94	99.89
55	100.00	100.00	100.00	100.00

Table 7.4: Comparison of gamma-ray % attenuation of the four matrices as a function of source to detector distance for ^{152}Eu (121.78 keV).

Source to detector distance (cm)	**Matrix % attenuation**			
	Concrete	**PCC**	**Bitumen**	**Polymer**
17	39.38	39.77	25.74	24.18
27	95.56	95.81	88.59	84.64
37	99.25	99.27	96.77	96.01
47	99.72	99.80	98.85	98.71
55	99.87	99.92	99.20	98.86

Table 7.5: Comparison of gamma-ray % attenuation of the four matrices as a function of source to detector distance for ^{137}Cs (661.67 keV).

Source to detector distance (cm)	**Matrix % attenuation**			
	Concrete	**PCC**	**Bitumen**	**Polymer**
17	27.54	29.15	18.52	17.28
27	87.20	88.94	72.78	70.22
37	98.23	97.70	90.95	89.30
47	99.54	99.72	97.04	96.14
55	99.88	99.94	98.52	97.95

Table 7.6: Comparison of gamma-ray % attenuation of the four matrices as a function of source to detector distance for ^{60}Co (1332.5 keV).

Source to detector distance (cm)	**Matrix % attenuation**			
	Concrete	**PCC**	**Bitumen**	**Polymer**
17	20.23	21.50	13.27	12.32
27	77.02	79.20	60.60	57.96
37	93.16	94.36	82.05	79.70
47	97.91	98.40	91.51	90.07
55	99.00	99.28	94.60	93.32

As can be seen from the results, there is a strong correlation between % attenuation and source to detector distances in all the matrices. The % attenuation increases as the source to detector distance increases. This is due to the increase in the mean free path (MFP) which the gamma-ray had to traverse, thus increasing the probability of the gamma-ray being absorbed by the matrices. There is 100 % attenuation of ^{241}Am (59.54 keV) at 55 cm from the detector. At this source to detector distance, the gamma-ray traversed through a half of the drum diameter, and this resulted in complete photoelectric absorption of the gamma-ray. The implication of this result is that any of the matrices studied are suitable for attenuation and photoelectric absorption of the ^{241}Am radionuclide located at the centre of the drum, while also significantly attenuating the same radionuclide positioned close to the edge of the drum.

An increase in % attenuation is observed more prominently at lower energies (59.54 and 121.78 keV) due to the dominance of photoelectric absorption at that energy range. A comparison of the two best matrix performers, concrete and PCC (50 % epoxy resin (ER) & 50 % concrete (Con)), showed that concrete is a better matrix for energies below 100 keV. However, increasing the weight fraction of concrete changes the attenuation effect for energies at such range. A variation

in % change in composition of PCC was found to have less significant effect on the attenuation of high gamma-ray energies (> 150 keV), but shows variations in the energy of 59.54 keV as shown in Figure B.1. Evidently, an attenuation plot presented in Figure B.2 showed that the highest % attenuation was observed at weight (wt) fraction 10 wt % ER: 90 wt % Con. This could be attributed to the fact that 90 % of this particular weight fraction is concrete which has higher gamma-ray attenuation factor compared to epoxy resin.

Evidently, the findings showed that PCC exhibits strong gamma-ray attenuation compared to other matrices investigated. This material is therefore recommended for use as matrix for activity reduction in radioactive waste drum/container.

7.5 Summary of the Experimental Measurements and MCNP Simulations Results

One of the main objectives of this research is to investigate the effectiveness of a BEGe detector in interrogation of radioactive waste drum. The results of the system efficiency and image reconstruction from segmented gamma scanning measurements give strong credence to the usefulness of BEGe detector in radioactive waste drum interrogation. The efficiency calibration of the counting system showed that the system efficiency depends among other factors on the source positions inside the drum. The system efficiency for sources on the same axial position as the detector decreases at the distance between the source and the detector increases. The FWHM values obtained for peaks SA (^{137}Cs with activity 223 kBq) and SB (^{137}Cs with activity 230 kBq) are 125 ± 6 mm and 17 ± 8 mm. This poor resolution could be attributed to the vibrations caused by the movement of the detector during the drum scanning.

From the image reconstruction of segmented gamma scanning measurements to estimate the locations of the hotspots, the overall positional image reconstructed as summarised in Tables 7.7 and 7.8 show the comparisons between the true

Table 7.7: Comparison of the true source positions to the calculated source positions for the radial and vertical plane.

Sources	**True Position**		**Calculated Position**	
	x (cm)	**y (cm)**	**x (cm)**	**y (cm)**
^{60}Co	40.0 ± 0.5	40.0 ± 0.5	39.9 ± 2.0	39.7 ± 2.0
^{137}Cs	20.0 ± 0.5	60.0 ± 0.5	18.0 ± 2.2	57.0 ± 3.2
^{137}Cs	50.0 ± 0.5	60.0 ± 0.5	49.2 ± 1.8	57.9 ± 2.2
^{133}Ba	30.0 ± 0.5	80.0 ± 0.5	29.0 ± 1.8	79.0 ± 2.0
^{22}Na	50.0 ± 0.5	40.0 ± 0.5	49.9 ± 2.1	39.4 ± 1.2

positions of radioactive sources used for the measurements and the reconstructed positions. The ability to estimate the positions of radioactive sources at different points inside the drum sources through the reconstructed images clearly indicated that BEGe detector can effectively be utilised in localisation of hotspots in radioactive waste drum through passive interrogation.

Table 7.8: Comparison of the true source positions to the calculated source positions for the angular and vertical plane.

Sources	**True Position**		**Calculated Position**	
	θ (°)	**y (cm)**	**θ (°)**	**y (cm)**
^{60}Co	180.0 ± 2.0	40.0 ± 0.5	179.8 ± 2.5	39.7 ± 0.5
^{137}Cs	84.0 ± 2.0	60.0 ± 0.5	83.6 ± 2.5	59.3 ± 2.0
^{137}Cs	264.0 ± 2.0	60.0 ± 0.5	263.9 ± 5.1	59.9 ± 2.0
^{133}Ba	264.0 ± 2.0	80.0 ± 0.5	263.9 ± 1.5	79.3 ± 1.6
^{22}Na	72.0 ± 2.0	40.0 ± 0.5	71.8 ± 1.6	39.8 ± 1.5

The computation of source activity for the counting system is strongly dependent on whether the source is axially located as the detector or non-axially located. This is because as illustrated earlier, the efficiency of the counting system which is a main component in calculating activity depends of source distribution inside the drum. The measurement uncertainty for sources on the same axial position as the detector is relatively small compared to sources at non axial positions of the detector.

These experimental results indicate that BEGe detector is suitable for measurement and localisation of hotspots during the radioactive waste characterisation process. When compared with existing commercial systems (discussed in Section 1.3), the BEGe used for this work showed superior efficiency and good agreement in terms of FWHM as illustrated in Table 7.9. It can therefore be concluded that the BEGe system used for this research work was able to agree on hotspot locali-

sation and quantification of activities with the existing commercial systems.

Table 7.9: Comparison of the BEGe detector responses for radioactive waste characterisation to existing commercial system.

System	**Detector type**	**Relative Efficiency %**	**FWHM at 1332 keV**
G3200-340	Coaxial HPGe	20	-
G3850-340	Coaxial HPGe	50	-
WW2200	Coaxial HPGe	30	1.9
WW2900	Coaxial HPGe	45	2.0
Cavendish	Coaxial HPGe	-	1.9
This Work	BEGe	60	2.19

*The dash lines mean that the values were not supplied by the manufacturers.

The MCNP based Monte Carlo simulation developed for the radioactive waste system counting, comprising a BEGe detector and radioactive waste drum, was successfully utilised to estimate the absolute system efficiency for axial positions of radioactive sources. The absolute system efficiency calculated for two source positions were in excellent agreement (within 10 %) with the experimental calculated efficiencies.

The MCNP simulation code was further modified for non-axial source positions and ran to compute the absolute system efficiency. The absolute system efficiency calculated showed low efficiency for low gamma-ray energy as compared to the normal efficiency curve. This was basically due to attenuation of low gamma-ray energies caused by non-axial positioning of the sources.

The good agreement (within 15 %) between the activity calculated using MCNP simulation values and true values is due to the ability of MCNP to compute, to a reasonable degree of accuracy, the absolute efficiency of the counting system.

The simulated results presented clearly show that Monte-Carlo simulation is a very useful technique for modelling of the radioactive waste drum counting system, especially some complex measurement scenarios. It was found from the study that MCNP produces very consistent results when compared with the experimental results. This consistency of the simulated and experimental results indicates that MCNP is a reliable numerical technique for efficiency and activity calculations for the radioactive waste drum.

Chapter 8

Compton Camera Measurement and Results

The limitations of collimated passive gamma-ray detection techniques discussed in the previous chapter in providing precise and efficient identification and localisation of radioactive sources in a waste drum requires alternative techniques for identifying and localising radioactive materials. The passive gamma-ray detection technique relies on a mechanical collimator system with a high degree of positional information. However, this introduces complex correction factors (such as geometry correction factor) into the technique. An alternative technique for localisation of hotspots studied in this work is to use a Compton camera. The Compton camera operates on the principle of electronic collimation enabling more gamma-rays to be incident upon the detector, thus increasing the amount of data for analysis due to an increase in detector sensitivity. This increase in the amount of data for analysis increases the quality of the reconstructed image. The Compton camera is designed to identify and track the radioactive material using the kinematics of Compton scattering. The Compton camera has proven to be an effective imaging device for a gamma-ray energy range of 140 keV to 10 MeV and can be utilised to image separately, the energy of mixed gamma-ray sources, [83, 19]. This is due to its large field of view, increased efficiency and good background suppression. For large volume radioactive waste characterisation, a Compton camera can effectively be applied in identifying hotspots in waste drums which can be safely removed [59]. This will allow the remaining waste to be disposed as low level waste.

This chapter will describe the measurements taken with the Compton camera imager along with providing information on image reconstruction and the usefulness of Compton camera for identification and localisation of radioactive materials. Two ^{137}Cs point sources inside the waste drum with the same separation distance as in the BEGe measurement, as described in Section 6.6.2.1, were imaged and

the results presented in this chapter. With known literatures [114, 79], the Compton camera is proven to be a better alternative to mechanical collimated systems for localisation of radioactive materials in three-dimension without the need for a complex rotational system and this is also investigated in this chapter.

8.1 The Gamma-Ray Imager Compton Camera

The Gamma-Ray Imager plus (GRI+) is a three-tiered Compton camera designed at the Nuclear Physics Research Laboratory, (Precision Radiometrics Instrumentation Development and Education (PRIDE) laboratory) within the Department of Physics at the University of Liverpool. The system comprises a circular orthogonal-strip lithium-drifted silicon Si(Li) detector as the scatterer, a cuboid orthogonal-strip HPGe detector as the absorber and a coaxial HPGe detector. All three detectors were manufactured by Mirion Technologies and each held in separate aluminium cryostats. Silicon was the choice for the scatterer because of its high energy resolution (though, not as good as germanium) and small Doppler broadening compared to other detectors. The choice of germanium as absorber was due to its large linear attenuation coefficient at the energy range of interest. The coaxial detector is included to boost the efficiency of the GRI+ system for the imaging of high energy gamma-ray sources at industrial sites.

8.1.1 System Geometry

The scatterer was a cylindrical double-sided silicon detector (DSSD) with diameter of 71 mm and 8 mm thick producing an active area of 3500 mm^2. There was a 2.5 mm guard ring surrounding the circumference of the active volume to uniformly maintain the electric field at the active volume edge. Position-sensitivity of the detector was achieved by electronically segmenting the active volume of the crystal into 13 strips on the AC side (p type) and 13 orthogonal strips on the DC side (n type) producing 169 voxels [43]. The strip layout is shown in Figure 8.1.

As can be seen in Figure 8.1, each strip varied in length due to the circular geometry of the crystal but had a width (pitch) of 5 mm and inter-strip separation of 500 μm that provided position of interaction information. This strip pitch and thickness resulted in a voxel size of $5 \times 5 \times 8$ mm^3 for each interaction position. Each strip was connected to a charge-sensitive preamplifier with a cold FET (Field Effect Transistor) configuration which provided a gain of 300 mV/MeV in the 26 output channels [14].

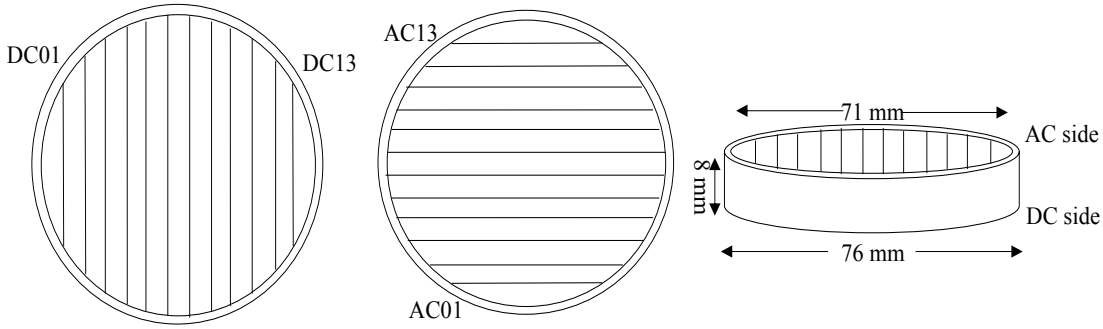

Figure 8.1: Illustration of the Si(Li) detector showing its dimensions.

The Si(Li) detector can be operated at room temperature but a Mirion CryoPulse 5 electrical cooler [20] is used to maintained the temperature at 81 K so as to reduce any leakage currents and thermal excitations. A depletion bias voltage was required for the detector of +150 V but the detector was biased to +430 V applied to the AC face while the DC side is grounded. Electrons migrated to the AC face while holes were collected at the DC face.

The absorber detector was a planar HPGe detector also manufactured by Mirion Technologies and had dimensions of 75 mm × 75 mm × 20 mm with an active volume of 60 mm × 60 mm × 20 mm. A 3.5 mm guard ring surrounded the active volume of the HPGe detector and the entrance windows to the crystal were 0.8 mm thick. The detector was segmented into 12 AC (p-type) and 12 DC (n-type) strips, each with a strip pitch of 5 mm as shown schematically in Figure 8.2, resulting in a voxel size of 5 × 5 × 20 mm^3 for each interaction position. Each strip was connected to a warm FET charge-sensitive preamplifier that processed the energy information provided by the interactions [13]. This preamplifier provided a gain of 200 mV for a 1 MeV energy deposit. The depletion voltage of the detector crystal was -1300 V and was operated at -1800 V applied to the AC face, allowing electrons to be collected at the DC face and holes to be collected at the AC face. The crystal was electrically cooled to a temperature of 81 K by a CryoPulse® CP5 cooler [20].

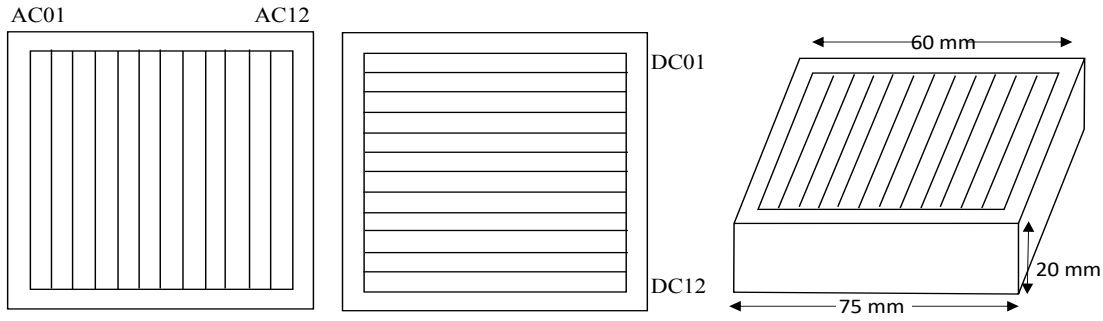

Figure 8.2: Illustration of the HPGe detector showing its dimensions.

The coaxial detector, manufactured by Mirion Technologies, was a standard electrode germanium detector (SEGe) which had a diameter of 66.5 mm and length of 50 mm. This coaxial detector of p-type comprised a germanium cylinder with an n-type contact on the outer surface and a p-type contact on the surface of an axial well [76]. The detector operated with a bias voltage of +3000 V applied to the crystal, which was above the depletion voltage of +2500 V. The detector was cryogenically maintained at 81 K using a CryoPulse CP5 cooler. A custom-built detector frame allowed the distance of the coaxial detector from the back of the absorber cryostat to be varied. The addition of this detector in the GRI+ system was basically for a planned industrial high gamma-ray energy measurement and, was not used during data acquisition for this work.

The HPGe and Si(Li) crystals were housed in an aluminium cryostat of dimensions 330 mm × 330 mm × 50 mm and were 15 mm apart. The coaxial crystal was aligned centrally to the absorber and was positioned very close to the back of the absorber's cryostat with extra care taken to protect the delicate entrance windows. Recording significant events for image reconstruction entailed an interaction in the scatterer detector, and subsequent absorption by the absorber detector. The maximum scattering angle permissible in the Si(Li) detector for such significant events to be achieved largely depended on the separation between the two detector cryostats and the source to absorber detector distance. The Si(Li) cryostat was positioned so that the DC strips were vertical and the AC strips horizontal, while the DC strips for the HPGe were horizontal and the AC strips vertical.

The three detectors together with the associated power, cooling and data acquisition systems were mounted in a mobile cart for flexibility in taking measurements at different points in the laboratory or outside the laboratory. The cryostats were placed in such a position that the three crystals were centrally aligned in accordance with the manufacturer specifications. The Si(Li) and HPGe detectors had their AC sides towards the front of the cart. The coaxial detector was placed 2 mm behind the HPGe cryostat.

8.1.2 Data Acquisition System

The digital electronics for data acquisition used together with the detectors were CAEN V1724 digitiser cards, a gain and offset (GO) box and a V1495 global clock card as shown schematically in Figure 8.3. The digital electronics allowed for the storage of preamplifier pulses from the detectors and which were then processed offline. In the GRI data acquisition system, a gain and offset (GO) box was utilised to amplify voltage signals from the preamplifiers by a factor of

5. This amplification was to exploit the full dynamic range (2.25 V) available on the CAEN V1724 card. CAEN V1724 cards were a set of six bit digitiser cards [12], each with eight channels, providing 48 channels of electronics in total, used for analogue-to-digital conversion (ADC).

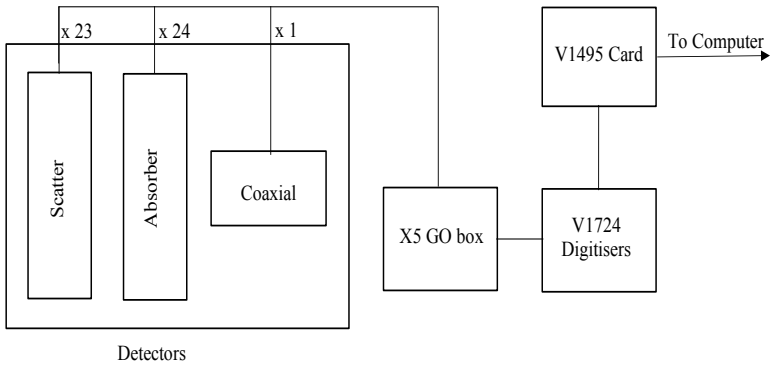

Figure 8.3: Schematic of GRI+ data acquisition system used in this work.

The output signals from the preamplifier of the three detectors were split between the six digitisers, with the first three taking up signals from the scatterer and coaxial detectors whilst signals from the absorber detector went into the remaining three. Each channel was processed and controlled individually, with moving window deconvolution (MWD) [34], trigger levels and other settings programmed into the V1724 digitisers.

The system was triggered when the CAEN V1724 digitiser retrieved pulses from the preamplifier at a rate of 100MHz (10 ns) with 14 bit resolution and fed to the V1495 trigger logic card. The trigger output signals from each of the six V1724 channels were fed into one of the 6 channels of a V1495 digital logic clock. This card was programmed to validate and write-out any event that meet the criteria specified by the user. Data could be written out from all the channels including a single channel of the coaxial detector, or only the channels which trigger the system. Signal outputs from V1724 that matched user criteria were transferred to a computer using a CAEN V2718 VME to PCI Optical Link Bridge for data reprocessing by the Multi-Instance Data Acquisition System (MIDAS) [81] software at a later time. For data acquisition with the digitisers, all the strips could not be connected because the V1724 could only provide 48 channels. A previous characterisation of Si(Li) detector [43] showed that strip DC01 was not active, and thus was not used. In addition, strips AC13 and DC13 were also not used as their loss would not significantly affect the performance due to their relatively small size and location at the edge of the detector.

The trigger could either be in single or coincidence modes depending on the

requirements of the experiments. For the singles mode, triggering occurred for an interaction in either the scatterer or absorber detectors exceeding the digital Constant Fraction Discriminator (CFD) threshold on any strip, as monitored by the V1495 card. For the coincidence mode, two assumptions for triggers to occur were (a) that the gamma-ray underwent Compton interactions first in the scatterer detector before undergoing photoelectric absorption in the absorber detector (b) true events would arise from interactions in both detectors which happened within a time span known as the 'coincidence window'. Compton camera measurements required that interactions occurred in both detectors [88] and as such coincidence mode was utilised in this work. The coincidence window was set to 325 ns to maximise event rate whilst minimising false coincidences.

The coaxial detector was not utilised in triggering as the information required for reconstruction of the Compton cone were obtained from the interactions in both scatterer and absorber detectors. The detector helps to improve the efficiency of the system, mostly at the high gamma-ray energies.

8.1.3 Digital Signal Processing

For the image reconstruction of the gamma-ray source, the output signals from the system detector preamplifiers were digitised, analysed and formatted into a text file to be input into an image reconstruction algorithm. The MWD [34] algorithm calculated the pulse height from each gamma-ray interaction in the detectors. The process started by removing the long decay tail from the digitised preamplifier signal to obtain a step function that preserved the pulse height. The resulting signal was then differentiated to produce a square pulse, and by applying a moving averaging window, a trapezoidal signal with reduced noise and a height proportional to the energy deposited in the detectors was obtained.

8.2 GRI+ imaging of a Radioactive Waste Drum

The Compton camera imaging of a radioactive waste drum is required to distinguish radionuclides by their energies, intensities and locations. Localisation of hotspots in a waste drum is very crucial in waste management as the information obtained will be vital in waste classification and possibly, choice of storage methods which have a cost implication.

With the detectors and associated electronics system mounted in a cart, a 500 litre standard waste drum, as presented in Figure A.3 of Appendix A.1, was positioned 20 cm away from the face of the scatterer cryostat. The drum was positioned in such a way to have the central axis aligned with the centre of the

scatterer crystal. However, the size of the drum and its position on the trolley made it difficult getting the central axis of the detectors to align with the central axis of the drum and may have introduced positional error on the locations of the radioactive sources.

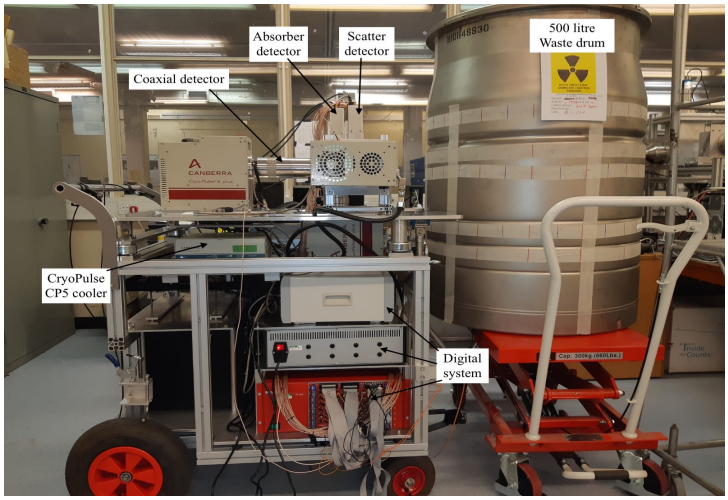

Figure 8.4: Schematic of the GRI+ imaging system positioned 20 cm from a 500 litres standard stainless steel radioactive waste drum.

Considering a Compton camera system for radioactive waste imaging shown in Figure 8.4, consisting of two DSSDs, the element closest to the gamma-ray sources inside the drum is regarded as the scatterer whilst the one behind the scatterer is designated as the absorber. A sequence of gamma-ray interactions within these detectors is referred to as events. This sequence of events leading to the computation of the Compton scattering angle, θ, involves a proportion of the incident gamma-rays undergoing Compton scatter within the scatterer and subsequently, a proportion of these scattered gamma-rays experience photoelectric absorption within the absorber. With the energy of the incident gamma-ray, E_γ, given as the addition of the energy deposited in the scatterer, E_1, and the energy deposited in the absorber, E_2, the Compton scatter angle θ as shown in Equation 8.1, can be calculated by rearranging the Compton scattering equation, Equation 3.4

$$\cos\,\theta = 1 - m_0c^2\left(\frac{1}{E_2} - \frac{1}{E_1 + E_2}\right). \tag{8.1}$$

The radioactive source position is therefore located somewhere at an angle, θ, from the interaction point in the scatterer. Given that the direction of the incident gamma-ray is not known the radioactive source could probably be anywhere on the cone's surface subtending a semi-angle θ. A number of cones will be generated by multiple events and an image is produced by taking a slice perpendicular

to the z-axis. The location of the source is identified as the region with most cone overlaps and high intensity.

The ability of the GRI+ system to identify radioactive source locations and their relative intensities inside a standard stainless steel waste drum was investigated using two ^{137}Cs sources of different positions and activities represented by S1 and S2. These sources, S1 and S2 of activity 230 kBq and 223 kBq respectively, were placed 10 cm and 20 cm respectively to either side of the drum's central axis along the z-direction as shown in Figure 8.5. This made the distance of separation of the two sources as 30 cm and the activity percentage difference 1.54 %. The drum trolley was adjusted such that these sources were 60 cm high from the bottom of the drum. As there was difficulty encountered in aligning the drum central axis to the centre of the detectors, this will impose an uncertainty of approximately ±5 mm error in the relative positions of the sources.

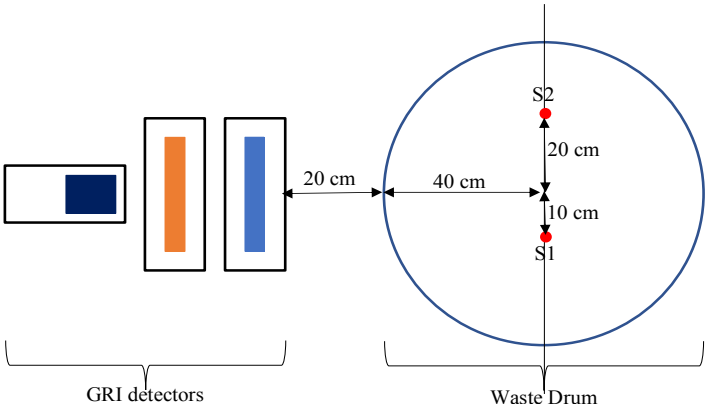

Figure 8.5: Plan view of two ^{137}Cs sources inside a radioactive waste drum relative to the front of the detectors.

Data were acquired for 12 days. This long time of data of acquisition is due to the low level activity of the radioactive sources, their distances from the scatterer detector and the attenuation effects on the gamma-rays by the stainless steel drum wall whose thickness is 7 mm. The length of time was required to collect enough events for image reconstruction. These events collected are classified based on the number of channels in which the charge was registered. The number of channels on a detector face upon which the real charge was registered is called the fold. Therefore, coincidence data from 2-tier events can be represented by F(1,1,1,1,n) where the first four numbers represent the scatterer AC, the scatterer DC, the absorber AC, and the absorber DC. n represents events from the coaxial detector. Figure 8.6 is a spectrum of a coincidence data taken by the GRI+ for two ^{137}Cs point sources depositing energy in F(1,1,1,1,0) events.

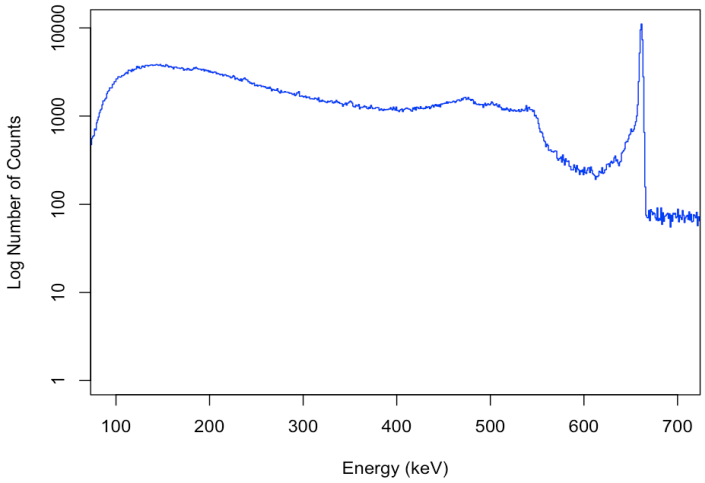

Figure 8.6: Energy spectrum from imaging two ^{137}Cs sources in a radioactive waste drum for coincidence two-tier F(1,1,1,1,0).

8.3 Image Reconstruction

Two forms of image reconstructions in Compton camera are analytical and iterative. The image reconstruction technique utilised in this work was the analytical filtered back projection algorithm. In the analytical algorithm, a back projection is generated using Compton kinematics as described by Equation 8.1. The analytical image reconstruction algorithm developed at the University of Liverpool [50] uses energy and position data to back project a Compton cone into imaging space for each event. The cones, as seen in Figure 8.7, begin in the scatterer detector and are projected outwards onto x-y planes, known as slices. The geometry of each Compton cone was calculated using the discretised input data. The coordinate

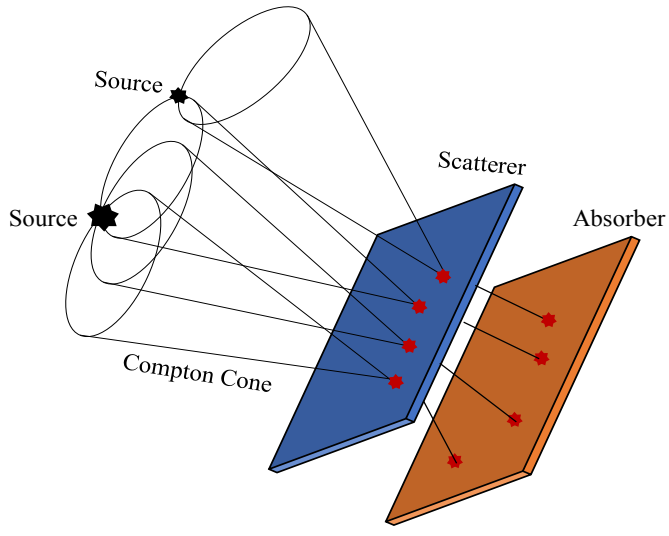

Figure 8.7: Illustration of Compton imaging of two sources.

system for the image projection is such that the centre of the Si(Li) crystal served as the origin of the horizontal (x) and vertical (y) axes, whilst the back of the absorber crystal was relative to the z-position. This coordinate setting, therefore, requires the knowledge of the separation of the detector cryostats and the position of detector crystals within the aluminium casings and any adjustment on the separation will have impact on the reconstructed image.

Three cones in principle are sufficient to reconstruct the image of the point sources. However, due to uncertainties in measurement and the incomplete absorption of gamma-rays, a relatively large number of reconstructed cones are required for accurate localisation of the sources as illustrated in Figure 8.8.

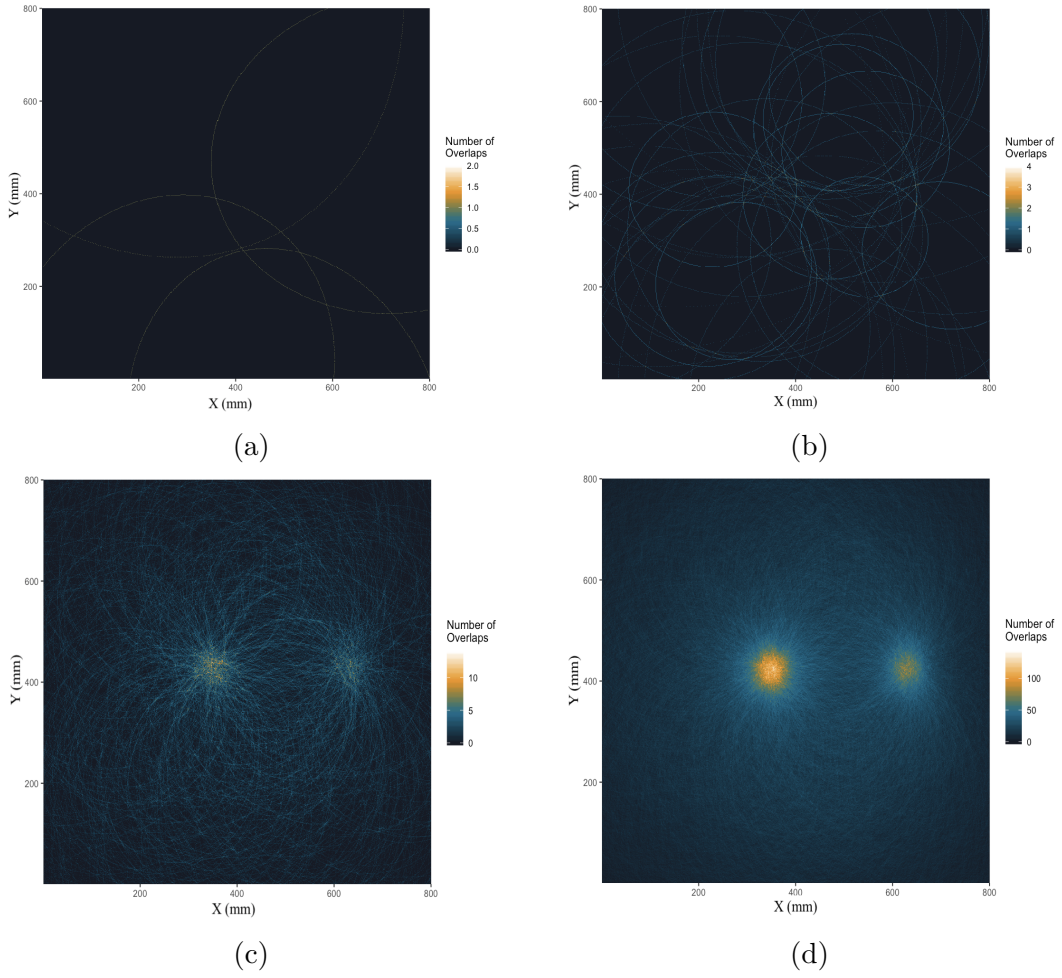

Figure 8.8: Localisation of point sources through cone overlap (a) reconstruction of 5 cones, (b) reconstruction of 50 cones, (a) reconstruction of 1000 cones, and (a) reconstruction of 20000 cones.

It can be seen from the Figure 8.8 that the number of overlaps increases with the number of reconstructed cones. This clearly enhances the probability of localising the point sources.

A multiple number of reconstructed cones projected onto a two dimensional imaging slice (plane) produces a cone overlap intensity map or reconstructed image as represented in Figure 8.9a. The image produced in Figure 8.9a indicates that both sources are distributed across a wider area, and this distribution is attributed to the increase in number of back scatter events as a result of low energy threshold in both the scatterer and absorber. By applying an energy gate, as represented in Table 8.1, events were selected by removing the influence of the Compton continuum and back scattered events, thus enabling the formation of clearer image as illustrated in Figure 8.9b. The energy gating comes with reduced number of events available for reconstruction as illustrated in Table 8.1, where the 41725 events used for energy gating 656 to 668 keV represents 3.6% of the events for the energy gating 0 to 2000 keV.

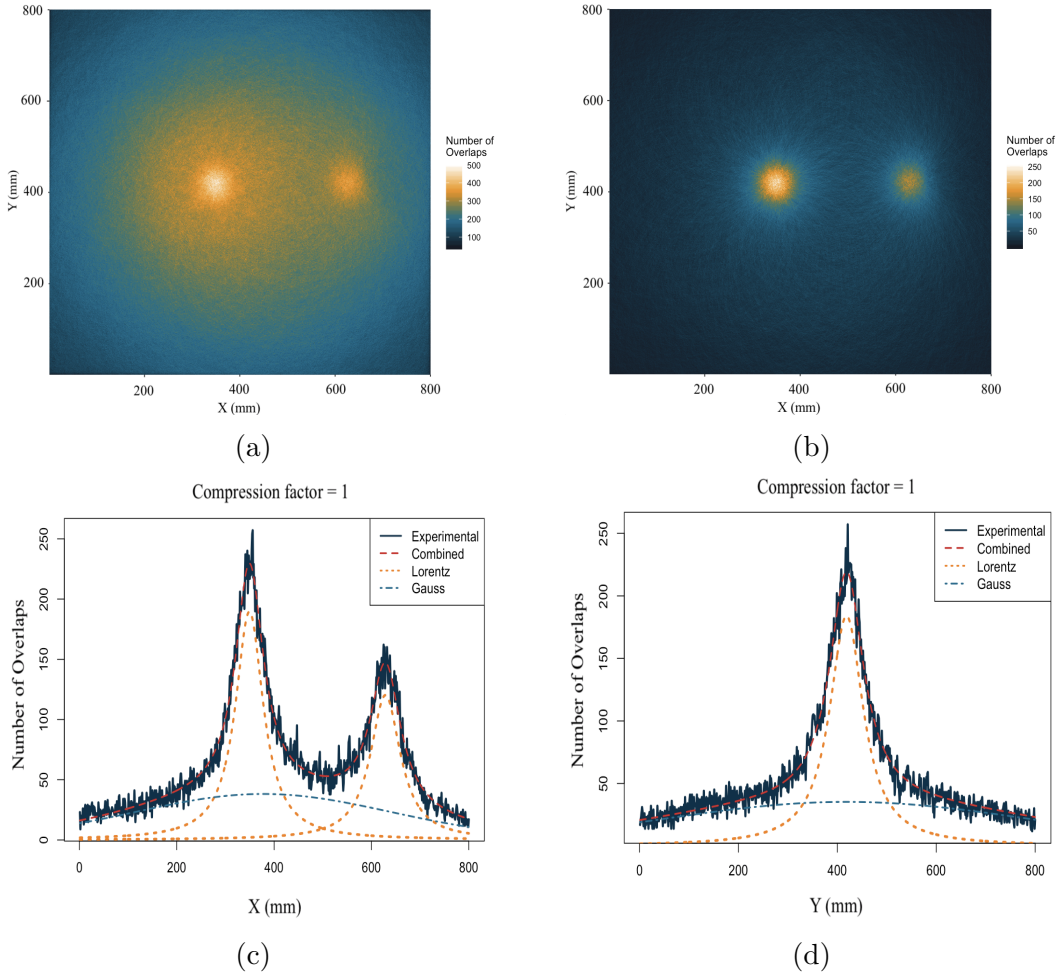

Figure 8.9: Reconstructed image slice with compression factor = 1 and the slice through Z = 421. (a) No energy gate applied (b) Energy gate of 656 keV to 668 keV is applied. (c) and (d) are FWHM fitted from the row and column respectively, with the maximum number of Compton overlaps.

The image, reconstructed by gating on the 661.67 keV photopeak of the two ^{137}Cs sources, clearly shows that the sources were well separated. The image also shows unequal intensities for the two sources. This is an indication that the source activity on the left is greater than the source activity on the right.

Table 8.1: The effect of an energy gate on the number of events available for image reconstruction.

Energy Gate (keV)	**Number of Events Ran**	**% of original Events**
0 to 2000	1068204	100.0
0 to 1000	1055466	98.8
100 to 2000	1022941	95.8
500 to 1000	158909	14.9
600 to 800	70275	6.6
656 to 668	41725	3.9

To obtain a high quality image, the following options can be adjusted by the user when running the Compton imaging algorithm:

- Energy gate for the radioactive sources. The energy gate for the ^{137}Cs source was 656 keV to 668 keV.
- Image space size onto which the cones are projected. For all reconstructions in this work, an 800 $\times$ 800 mm^2 image space size was used.
- Image space compression: this is the number of millimetres per pixel in the reconstructed image.
- The number of events from the imaging file to be run. This number of events varied with each reconstruction.
- Points per degree: this represents the number of points to be drawn per angular degree of cone. The number of points per degree used was 3.

The quality of the reconstructed image can be checked by cutting through the X axis at the maximum number of conic overlaps, the FWHM of the image can then be produced as shown in Figure 8.9c. Carrying out a fit using Lorentzian and Gaussian functions, the FWHM measurement parameters utilised in assessing the image quality are obtained and presented in Table 8.2.

As can be clearly seen from Figure 8.9c, the two photopeaks are well separated, showing the ability of the GRI+ to distinguish radioactive sources at different points. The distance of separation was estimated to be 283.6 $\pm$ 5.9 mm, a percentage difference of 5.47 % between the reconstructed positions of the two

sources to the actual positions of the two sources. For peak S1, the reconstructed image position was 342.2 ± 3.1 mm, while the actual position was 300.0 ± 1.1 mm, a percentage difference of 14.1 %. For peak S2, the reconstructed image position was 625.8 ± 5.1 mm whilst, the actual source position was 600.0 ± 1.4 mm, being a percentage difference of 4.3 %. This disparity between the actual position and reconstructed position could be attributed to the difficulty in aligning the drum central axis to the centre of the scatterer detector. Moreover, the distances of both sources from the scatterer cryostat are not the same. While peak S1 is approximately 608.3 mm from the face of scatterer, peak S2 is 632.5 mm from the same point, making a percentage difference of 1.96 %. As shown in Table 8.2, peak S1 amplitude is greater than that of peak S2 with percentage ratio of 68.5 %. For the same

Table 8.2: Fit parameters for the image reconstruction. Row selected = 421, compression factor = 1 and the number of events ran = 41725.

Fitting Parameters	**Peak S1**	**Error**	**Peak S2**	**Error**
FWHM (mm)	69.47	1.50	74.98	2.77
FWHM (degrees)	6.74	0.15	7.27	0.15
Amplitude (mm)	20684.00	542.40	14162.00	693.10
Position (mm)	342.20	3.04	625.80	5.05

reason as stated above, the variation in amplitude intensities for the two sources is a combination of two factors such as non uniform activities and difference in source to scatterer detector for the two sources.
Figure 8.9d shows the FWHM of the reconstructed image by cutting through the Y axis at the maximum number of overlaps for each of the sources.

The attenuation of the gamma-ray by the drum wall and the relatively high source to detector distance results in reduction in the number of cones overlaping for image reconstruction. The statistical noise seen on the FWHM of the image reconstruction for X and Y slices (see figs. 8.9c and 8.9d) is an indication of these effects on the quality of the reconstructed image. By increasing the compression factor to 2, clearly reconstructed and fitted images were obtained as illustrated in Figure 8.10. However, there was a large uncertainty on the location of sources positions and the FWHM parameters as presented in Table 8.3. Further increase of the compression factor to 3, produced a sharper reconstructed image (see Figure 8.11), but the uncertainty on the sources position increased with more deviations of the reconstructed positions from the actual positions as illustrated in Table 8.4.

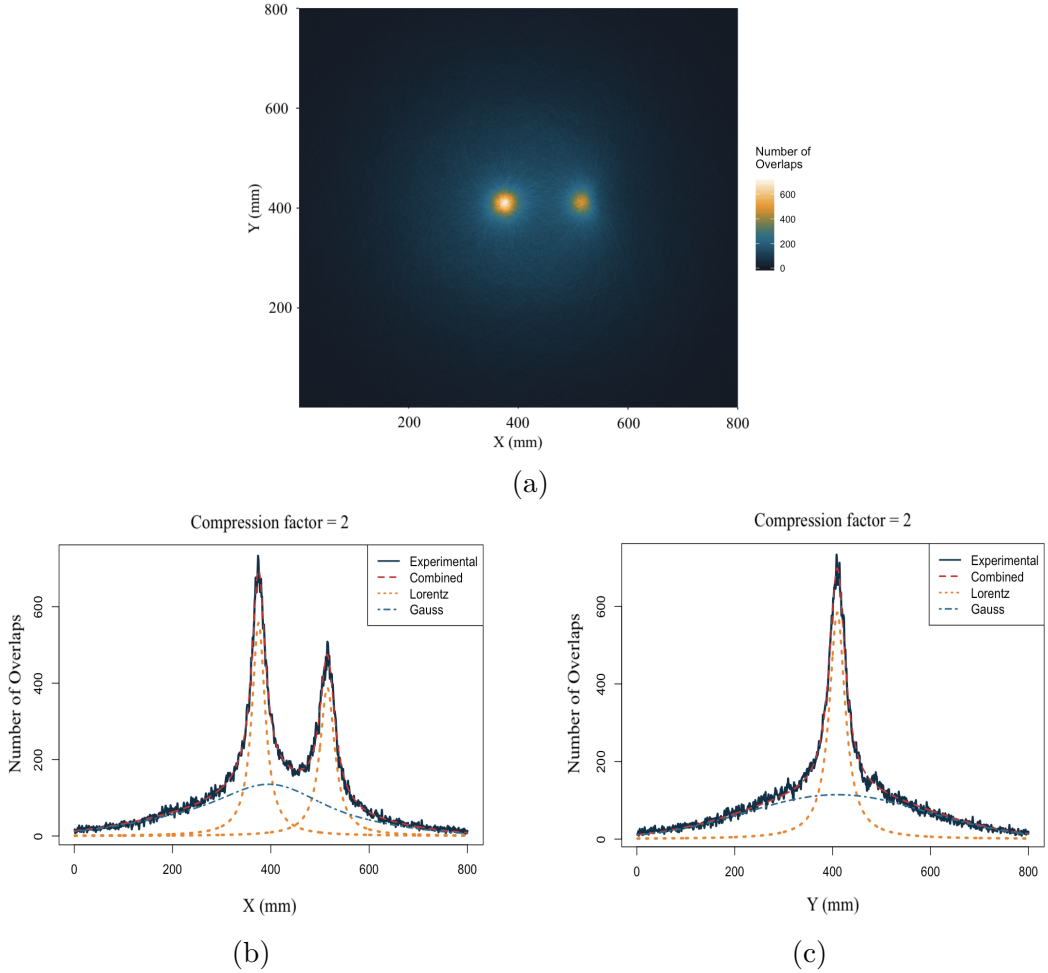

Figure 8.10: Reconstructed image slice generated from the analytical image reconstruction algorithm. (a) with compression factor = 2 mm. (b) and (c) are cross sections through X and Y axis respectively, showing the Lorentzian and Gaussian fits to the data.

From the comparison of the compression factors, it could be seen that increasing the compression results in clearer and sharper reconstructed image. The image quality can therefore be improved by increasing the image compression factor. However, this imposes an uncertainty in determining the position of the source.

Table 8.3: Fit parameters for the image reconstruction. Row selected = 408, compression factor = 2 and the number of events run = 41725.

Fitting Parameters	**Peak S1**	**Error**	**Peak S2**	**Error**
FWHM (mm)	65.48	0.98	73.70	1.41
FWHM (degrees)	6.35	0.10	7.15	0.10
Amplitude (mm)	28682.00	558.20	22451.00	555.40
Position (mm)	375.00	9.22	514.90	14.01

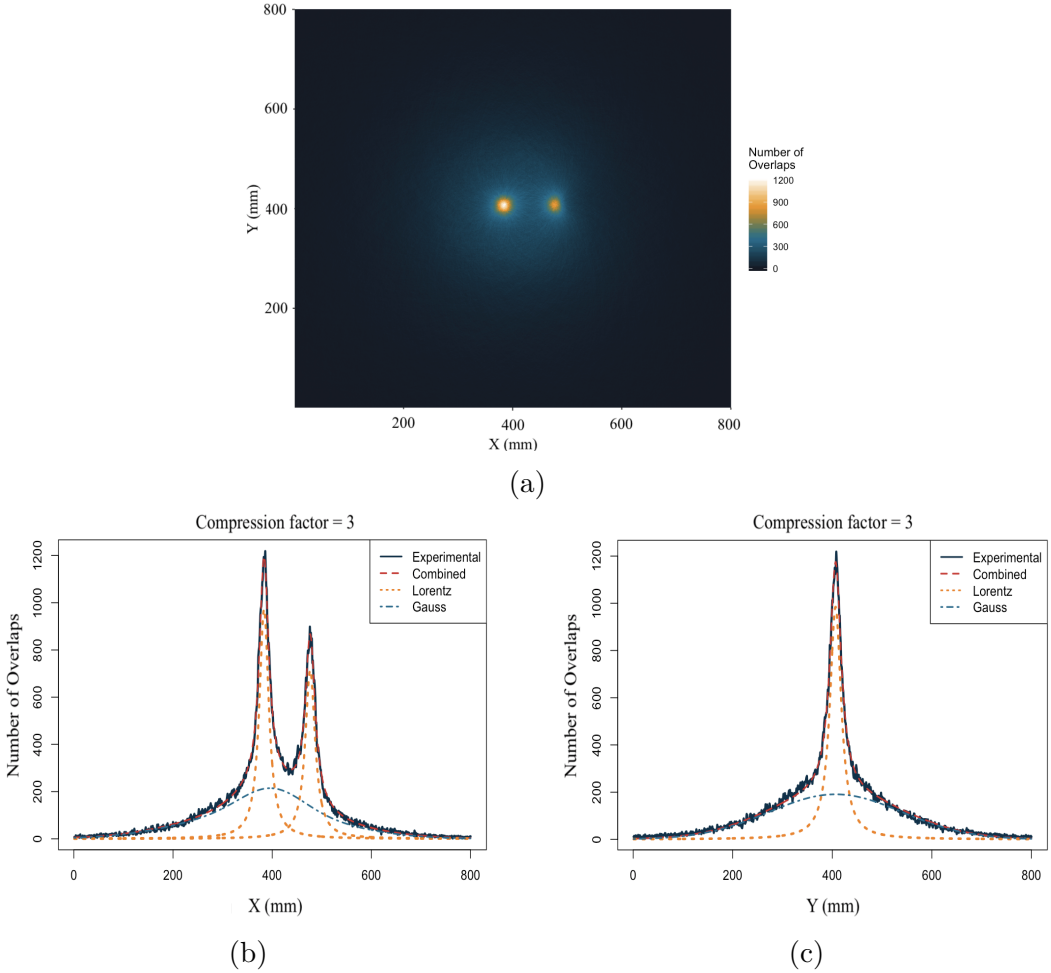

(a)

(b)

(c)

Figure 8.11: Reconstructed image slice generated from the analytical image reconstruction algorithm. (a) with compression factor = 3 mm. (b) and (c) are cross sections through X and Y axis respectively, showing the Lorentzian and Gaussian fits to the data.

Table 8.4: Fit parameters for the image reconstruction. Row selected = 408, compression factor = 3 and the number of events run = 41725.

Fitting Parameters	**Peak S1**	**Error**	**Peak S2**	**Error**
FWHM (mm)	68.63	0.74	72.04	1.07
FWHM (degrees)	6.66	0.07	6.99	0.07
Amplitude (mm)	34993.00	436.10	26982.00	470.70
Position (mm)	383.6	5.43	476.60	7.51

Compared to iterative image reconstruction techniques shown in Figure 8.12, analytical image reconstruction, of the same compression factor (see Figure 8.9b), produced poorer quality images due to a number of artefacts from conic projections being retained by the simple back projection. However, analytical image reconstruction is computationally efficient allowing fast reconstruction of the im-

age. The time for the image reconstruction of a typical analytical reconstruction algorithm is illustrated in Figure 8.13.

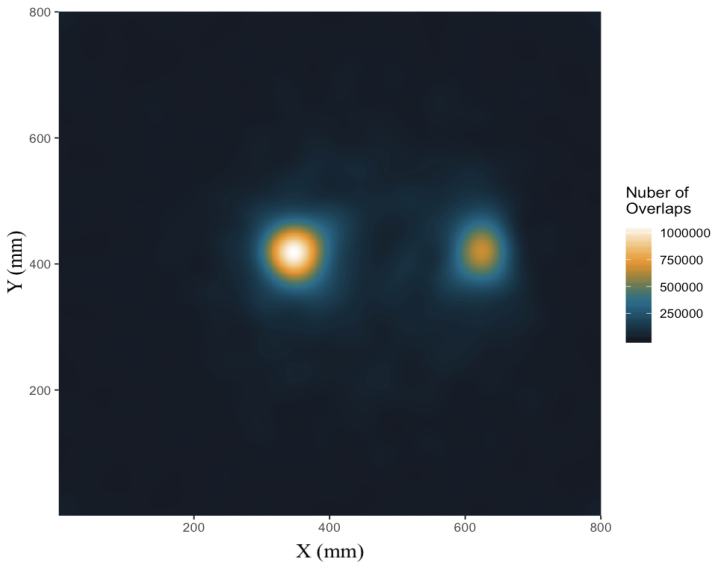

Figure 8.12: Image reconstruction for 41275 events using iterative image reconstruction with compression factor of 1.

From the Figure 8.13, an average time taken for the reconstruction of 41725 being the number of the events for the energy gate utilised in all reconstructions done in this work, as illustrated in Table 8.1, is approximately 0.67 seconds for analytical and 0.86 seconds for iterative.

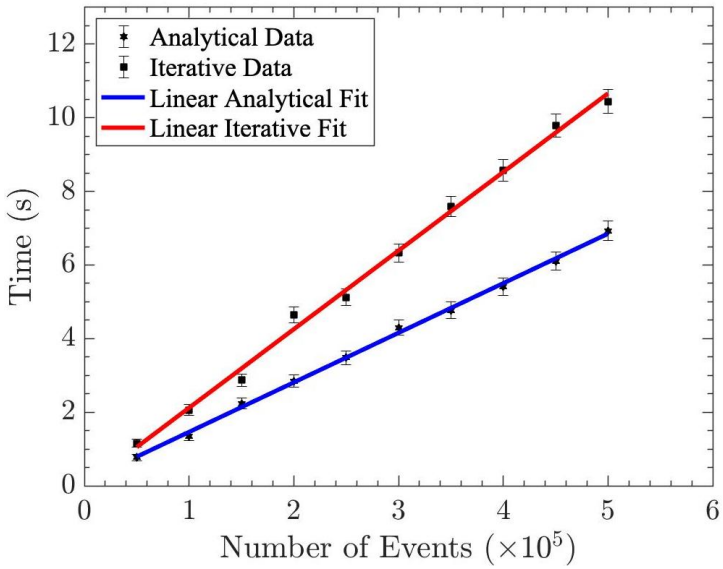

Figure 8.13: Typical time taken to reconstruct number of events using the analytical and iterative reconstruction algorithms.

8.4 Image Filtering

One possible remedy to the poor image resolution of the analytical reconstruction algorithm is the use of image filtering. As discussed in Section 3.6.2.2, one of the basic functions of image filtering is to reduce star artefacts in reconstructed images. One such filter is the high pass filter (HPF), which removes the low-frequency component of the reconstructed images. To improve the resolution of the reconstructed images, a high pass filter was applied to the experimental data. One important parameter to be carefully considered when applying a high pass filter is the cut-off frequency, which measures the extent of influence the high pass filter exerts on the image noise and resolution. A wrong optimisation of the cut-off frequency could therefore lead to formation of ringing artefacts in the image slice. An illustration of the improvement of resolution by the high pass filter on a reconstructed image is presented in Figure 8.14.

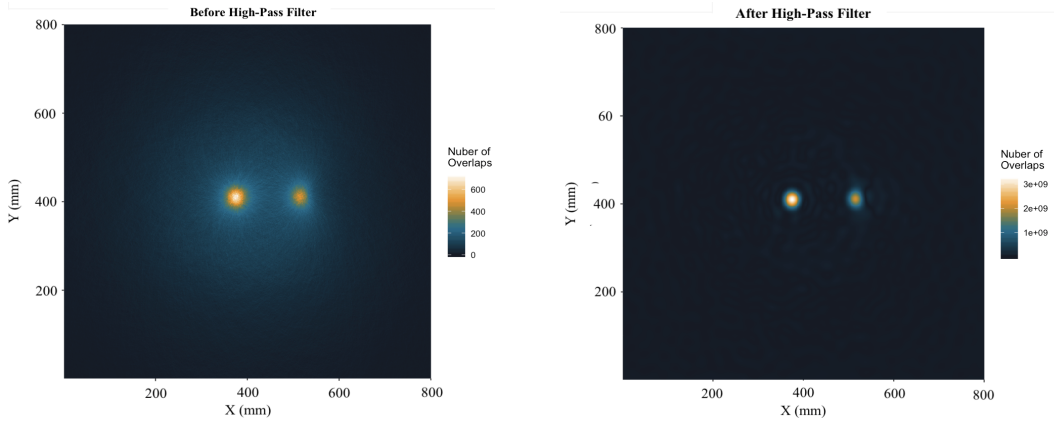

(a) (b)

Figure 8.14: Reconstructed images generated by the analytical algorithm. (a) No filter applied (b) the application of high-pass filter with a cut-off frequency of 25 Hz.

The intensities of the cross section through X and Y slices of the filtered image are shown in Figure 8.15.

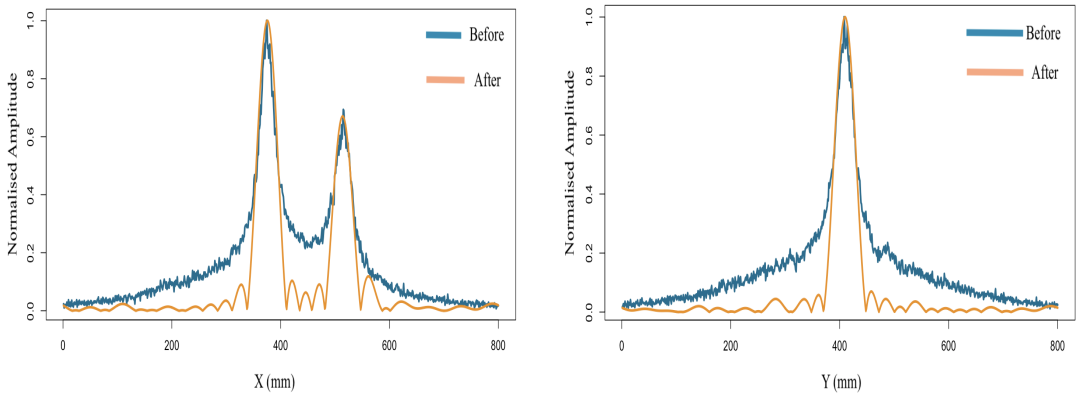

(a) (b)

Figure 8.15: Intensity profiles for the filtered image (a) X slice (b) Y slice.

It can be seen that the high-pass filter improves the resolution of the reconstructed images.

8.5 Uncertainties in Compton Cameras

The three main contributors to the uncertainties in the images produced by a Compton camera are the energy resolution of the detectors utilised, detector spatial resolution and the Doppler broadening in the Compton energy spectrum of scatterer detector.

Computation of the scattering angle, θ, of the gamma-ray depends on the energy resolution of the detector as energy deposited in the detectors is utilised in estimating the value of θ. It therefore reflects that any uncertainties in E_1 and E_2 due to poor energy resolution will be propagated through Equation 8.1 into uncertainty in determining the value of θ as shown in Equation 8.2.

$$\sigma^2_{\theta.E} = \frac{m_e c^2}{\sin\,\theta} \cdot (\Delta E)^2 \cdot \left\{ \frac{1}{E_\gamma^4} + \frac{1}{E_\gamma^4}(1 - (1 + \frac{E_\gamma}{m_e c^2}(1 - \cos\,\theta))^2)^2 \right\}. \tag{8.2}$$

The resulting image with this angle will have greater uncertainty. For identification or localisation of radioactive sources in a waste drum, which this work intends to investigate, the detector performance requirements of high energy resolution for the scatterer and absorber detectors limit the choice of detector material selection to silicon and germanium detectors, for which energy resolutions of 2.1 and 1.9 keV FWHM, respectively, were measured for a 662 keV photopeak [105].

The assumption in Equation 8.1 that the atomic scattering electron is stationary or unbound is another major contribution to uncertainty in θ. In reality, the atomic scattering electron is bound to an atom and moves round the nucleus in an

orbital with a finite momentum [65]. The equation that accounts for the energy and momentum of the electron is given by Equation 8.3 [73].

$$p_z = -m_e c \frac{E_0 - E_1 - E_0 E_1 (1 - \cos\theta)/mc^2}{\sqrt{E_0^2 + E_1^2 - 2E_0 E_0 \cos\theta}}. \tag{8.3}$$

where p_z is the momentum of the electron before the collision, E_0 is the initial gamma-ray energy, E_1 is the scatter energy and m_e is the electron mass.
This momentum will impose an uncertainty, whose magnitude is presented in Equation 8.4 on the measurement of the energy deposited as the kinetic energy of the recoil electron will be at variance to the energy of the gamma-ray.

$$\sigma^2_{\theta.\mathrm{DP}} = \left\{ \frac{1}{E_\gamma} \left(1 + \frac{E_\gamma (1 - \cos\,\theta)}{m_e c^2} \right) \right\}^4 (m_e c^2)^2 \frac{1}{1 - \cos^2\theta} (\Delta E'_{\gamma.\mathrm{DP}})^2. \tag{8.4}$$

This effect had been shown to contribute significantly to the angular uncertainty of a Compton camera [97, 63], especially at low gamma-ray energies [86]. The effect of Doppler broadening on the angular resolution could be minimised by using a low Z material as the scatterer detector. This effect, however, decreases with increasing gamma-ray energy and at the gamma-ray energy of 662 keV being studied for this work, the effect is considered negligible in the analysis [65].

Another source of uncertainty to the cone projection is the detector spatial resolution which in effect is determined by its geometry. Spatial resolution of the interaction points within the detectors is important to the location of cone axis. In the case of the segmented detector used in the work, the size of the charge cloud produced by the interactions, whether completely contained in a single voxel or spread across several voxels, determines the fundamental limit of the spatial resolution. Thus, this voxel size imposes an uncertainty (see Equation 8.5) on the interaction point which affects the angular resolution. The consequences of these uncertainties is the overlapping of the Compton cones over a large volume of imaging space resulting in the reconstructed image occupying larger space compared to the space occupied by the sources. The spatial resolution of an interaction point could be improved by using highly segmented detectors for both scatterer and absorber [57, 65].

$$\sigma^2_{\theta.\mathrm{S}} = \frac{\cos^4\theta}{(z_1 - z_2)^2} \{ (L_1^2 + L_2^2) + \tan^2\theta (\Delta z_1^2 + \Delta z_2^2) \}. \tag{8.5}$$

Where L_1 is the distance of the source from the interaction position in the scatterer detector, L_2 is the distance between the interaction positions in the scatterer

and absorber detectors, Δz is the resolution vector and θ is the scattering angle. The scatterer and absorber detectors utilised in this work had been shown to meet these requirements for the energy and spatial resolutions as both are made of DSSD silicon and DSSD germanium, capable for the Compton camera applications [43].
The uncertainty in the Compton scattering angle is primarily caused by the uncertainties in the detector energy resolution and Doppler broadening. The choice of detector material and type of radionuclides greatly influenced these parameters. The uncertainty in the spatial resolution depends on the interaction point within the detectors and detector layout. The uncertainty in the Compton camera can be computed by adding the three uncertainties in quadrature as in Equation 8.6 [88].

$$\sigma^2_{\theta.T} = \sigma^2_{\theta.E} + \sigma^2_{\theta.DP} + \sigma^2_{\theta.S} \tag{8.6}$$

8.6 Summary of the GRI+ measurements

The reconstructed images show the ability of the Compton camera to passively interrogate a radioactive waste drum. The most remarkable achievements of the GRI+ system are:

- Identification of the positions of the radioactive sources. The estimated positions of the sources are 342.20 ± 3.04 mm and 625.80 ± 5.05 mm as against the actual source positions of 300.00 ± 2.30 mm and 600.00 ± 3.45 mm. The disparity is due to difficulty in aligning the drum central axis to the mid point of the detectors.

- Estimation of the distance of separation between the two sources to be 283.60 ± 5.89 being 5.5% difference from the actual separation.

- Identification of the variations in the intensities of the radioactive sources. The significance of this observation is the ability to locate hotspots in a real radioactive waste scenario. The significant variation in intensities and amplitude despite small percentage difference of 1.54 % in activity is a combination of the non uniform activities of the sources and the difference in the distance of each source to the scatterer detector. Gamma-rays from S2 which is 20 cm from the drum central axis will scatter through a higher angle than those from S1.

- The estimation of the FWHM of the reconstructed image for both X and Y slices. For the X-slice, the FWHM for the peaks are 69.47 ± 1.50 mm and

74.98 ± 2.77 mm, while for the FWHM of the reconstructed image for the Y slice is 82.22 ± 0.61 mm.

The results obtained show that Compton imaging is a reliable alternative in terms of source localisation for imaging of radioactive waste drum. Industrial applications obviously will not take as long a time as in this work given that the 500 litres standard drum used in the work are basically for ILW with activity thresholds of 12 GBq of gamma-rays which is a factor of more than 50,000 to the maximum source activity used in these measurements. When compared to the existing commercial system discussed in Section 1.3, GRI+ does not require mechanical collimators indicating that its sensitivity is not limited by any collimator. Similarly, the resolution of GRI+ was not affected by the noise induced vibration resulting from the movement of detector-scanning platform as found in the existing system.

The effectiveness of the Compton camera for imaging radioactive waste drums of LLW and ILW wastes can be improved by proper calibration of the drum. This will address the difficulty in getting the drum central axis aligned to the mid point of the detectors, hence improving the uncertainty associating with computation of the source positions. The technique is therefore recommended for industrial application as it can offer reliable and effective means of waste characterisation.

Chapter 9

Conclusions and Future Work

9.1 Conclusions

The characterisation of radioactive waste is the process of determining the physical, chemical and radiological properties of the waste in order to establish the most acceptable means of handling, treatment, processing, storage and disposal of the waste samples. This characterisation, as a legal requirement, is performed at every stage of the waste processes. The most critical part of the process is the radiological characterisation as it involves the knowledge of the presence of radionuclides, their locations and activity distributions. Identification and quantification of these radionuclides present in a waste drum requires high resolution gamma-based non-destructive assay instrumentation suitable for measuring more complex mixtures of radionuclides. The most common form of such gamma-based non-destructive assay instrumentation is the high purity germanium (HPGe) detector.

This work is therefore, partly to evaluate the responses of a broad energy germanium (BEGe) detector for radiometric interrogation of radioactive waste drums and also, to investigate the suitability of hotspot localisation using Gamma-Ray Imager plus (GRI+). The early stage of this work was dedicated to characterisation and collimator optimisation of the BEGe detector in order to establish its suitability for waste system assay. The experimental efficiency of the BEGe detector obtained, validated by the MCNP simulated efficiency, showed the effectiveness of the detector for waste drum interrogation. The full width at half maximum (FWHM), which is the measure of the detector energy resolution, was found to be in agreement with the values published by the manufacturer.

The essential part of the measurement procedure is the calibration of the experimental system which intends to establish the response of the measuring system to the radioactive sources. The dynamic of this calibration depends on the radioac-

tive source present in the waste, and the geometrical situation of the waste drum or container. The experimental procedure involved the use of a BEGe detector to scan 500 litre standard waste drum used mostly for intermediate level waste.

The most desirable method of efficiency calibration of a radioactive waste drum in a real measurement entails collecting radioactive waste samples. However, this approach, apart from being demanding in terms of the need for the storage and disposal of the used radioactive waste sample, also requires regulatory licensing for the radioactive waste to be transported to the laboratory for measurements. Therefore, the procedure adopted in this work was to position radioactive source(s) at different points inside the drum and the radiometric responses from BEGe detector recorded. A two way efficiency calibration performed to investigate the detector efficiency response to radioactive sources at different positions inside the waste drum were (a) detector to source distance of 17 cm, and (b) detector to source distance of 55 cm. Photoelectric absorption of the low energy gamma-ray shown by sharp rise in efficiency from 59.54 keV to 121.78 keV was observed for both measurements.

This measurement procedure for the actual interrogation of the drum to locate the hotspot positions was achieved by segmenting the drum axis into segments and by performing vertical, radial and angular scanning of the drum. Detector responses were obtained and recorded as projections. These projections were typically the count rate for each segment of the measurement. The processing of projections from multiple scanning steps created three dimensional images of the drum contents. The location and size of the radioactive source was subsequently visualised through image reconstruction using the filtered back projection (FBP) function in MATLAB.

9.1.1 Tomographic Scanning of the Drum

It has been demonstrated through the results of image reconstruction obtained from the tomographic scanning of the radioactive waste drum that,

- BEGe detectors can efficiently be utilised for localisation and quantification of radioactive hotspots at different points inside the waste drum. The is based on the excellent efficiency and superior energy resolution of the BEGe detector for the gamma-ray energy range considered.

- A well collimated BEGe detector can localise two or more hotspots of non-uniform activity or intensity. This result is vitally important given that radioactive wastes constitute essentially non homogeneous source distributions and that proper localisation of the each hotspot will not only help in

limiting the concentration of radionuclides in the wastes, but to a larger extent help in waste management.

- An extended radioactive source of non-uniform intensity/activity distribution can be reconstructed to get the approximate dimensions and intensity variation of the original source. A ^{137}Cs source of 15 cm length and 1.5 cm in diameter inside the waste drum was measured using the collimated BEGe detector and an estimated source length of 14.9 ± 1.7 cm was obtained from the reconstructed image. The percentage difference of 5.65 % between the two ends of the extended source clearly showed the evidence of non-uniform intensity/activity distribution of the source at both ends.

- There was an increase in uncertainties in estimating the source activity for non-axial source positions to the axial source positions. This was shown by the higher percentage deviation of calculated to true activities of ^{133}Ba (15.16 %), ^{22}Na (13.69 %), and ^{137}Cs (9.78 %), all non-axial position sources as against the ^{60}Co (6.22 %), an axial source position.

9.1.2 MCNP Simulations for Validation of Activity Computation

Detailed MCNP simulations were carried out to examine the effect of the drum wall and matrices on the activity of the radioactive sources. The flexibility of the MCNP modelling allowed for fast computation of the BEGe detector responses for any type of drum packages, source positions and detector measurement positions. It was possible to demonstrate through this work that MCNP can be utilised to obtain good results for modelling the responses of BEGe detectors and radioactive source(s) inside the waste drum. Notable among the conclusions from the MCNP modelling include are:

- An improved simulated activity for both axial (^{60}Co), and non-axial (^{133}Ba, ^{22}Na, and ^{137}Cs) source positions as presented in Table 9.1.

- A computation of the gamma-ray transmission factor and % attenuation for four matrices. Gamma-ray energy, density and elemental composition of the matrix as well as the source to detector distance are important factors on which the transmission and attenuation of gamma-ray through matrix depend.

Table 9.1: % improvement of the simulated activity to the calculated activity of radionuclides.

Radionuclides Reference	**Energy (keV)**	**Simulated (kBq)**	**Calculated Activity (kBq)**	**Improvement (%)**
^{133}Ba	80.99	638.39 ± 28.48	634.58 ± 39.34	0.60
^{137}Cs	661.67	414.36 ± 18.01	408.74 ± 22.98	1.39
^{22}Na	1274.47	100.90 ± 10.67	99.26 ± 19.85	1.65
^{60}Co	1173.28	229.13 ± 16.72	227.90 ± 29.46	0.54
^{60}Co	1332.50	233.20 ± 19.12	231.60 ± 34.57	0.69

It is shown from the simulated results that an accurate utilisation of Monte Carlo N-Particle (MCNP) modelling technique can be applied to validate the detector efficiency, activity quantification and attenuation effects of matrices on the radioactive waste drum.

9.1.3 GRI+ System for Waste Drum Measurement

The reliance of the passive gamma-ray detection techniques on mechanical collimation for hotspot localisation not only introduces complex geometrical corrections but also, poses difficulty in an on-site application such as nuclear site characterisation and facility decomissioning.
The most remarkable achievements by the GRI+ system are:

- Localisation of the positions of the radioactive sources. The Compton camera system was able to estimate positions of the sources as 342.20 ± 3.04 mm and 625.80 ± 5.05 mm compared the actual source positions of 300.00 ± 2.30 mm and 600.00 ± 3.45 mm. The disparity (about 14.1 %) is due to difficulty in aligning the drum central axis to the mid point of the detectors which may have introduced uncertainties on the positions of the sources.

- Calculation of the distance of separation between the two sources to be 283.60 ± 5.89 being 5.5 % difference from the actual separation.

- Clear identification of the variations in the intensities and activities of the radioactive sources. The importance of this observation is the ability of GRI+ to localise hotspots in a real radioactive waste samples. The remarkable variation in intensities and amplitude despite small percentage difference of 1.54 % in activity is a combination of the non uniform activities of the sources and the difference in the distance of each source to the scatterer detector.

- The estimation of the FWHM of the reconstructed image for both X and Y slices. For the X-slice, the FWHM for the peaks are 69.47 ± 1.50 mm and

74.98 ± 2.77 mm for S1 and S2 sources respectively, whilst the FWHM of the reconstructed image for the Y slice is 82.22 ± 0.61 mm.

Compared to the BEGe detector system, the GRI+ exhibits good quality resolution as shown in Table 9.2. The loss in energy resolution for the BEGe detector was due to vibrations caused by the movement of the detector system platform during segmented gamma scanning as explained in Section 1.3.1. This loss has detrimental effect on the image resolution of the BEGe system.

Table 9.2: Comparison of the image resolution measured using peaks from the two ^{137}Cs. point sources for BEGe detector and GRI+.

Sources	**Source Activity (kBq)**	**BEGe FWHM (mm)**	**GRI+ FWHM (mm)**
^{137}Cs	223	125 ± 6	69.47 ± 1.50
^{137}Cs	230	170 ± 8	74.98 ± 2.77

The performance of the GRI+ system shows that Compton cameras could reliably offer an alternative waste sample imaging technique to heavily collimated segmented gamma scanning in terms of source localisation for radioactive waste drum. In an industrial application data collection times will be significantly shorter as the activity of the waste will be higher than the laboratory sources used in this work. For ILW the activity threshold is 12 GBq per tonne for beta particles or gamma-rays. This technique, which has not previously been used for imaging of the 500 litre standard stainless steel waste drum, is therefore recommended for industrial applications as it offers reliable and effective methods of waste characterisation for intermediate level waste (ILW).

9.2 Future Work

The work presented in this thesis improves the quantification and localisation of radioactive sources in a typical waste drum. This was achieved through processes of segmented gamma scanning of the drum and simulations in order to evaluate the efficiency and effectiveness of BEGe detector to waste characterisation. Further work is still needed to be carried out in order to develop a system that can offer high degree of accuracy and precision in measurements.

A number of factors such as self absorption not considered in this research work could impose uncertainty to the results of a real waste sample, and consequently limit the accuracy of the measurements. As this research work considered the use of radioactive sources in place of real waste samples, due to the fact that regulatory licensing is required for both the use of the radioactive waste samples in

the laboratory and disposal of the used samples, it will be necessary to perform a radiological characterisation of a real waste drum to estimate the contributions and effects of self absorption to the efficiency of the measurements. The will help to greatly improve the accuracy and precision of radioactive waste assay.

The effect of matrix attenuation on the gamma-ray signals was estimated using simulations. Further experimental investigation could be performed to calculate this effect using transmission sources (external radioactive sources). The transmitted factor can then be determined by calculating the ratios of the transmitted count rate to those obtained through an empty sample drum.

The mobility of the GRI+ is such that it can be moved for an on-site measurements. Many nuclear power facilities and sites being decommissioned require radiological characterisation. We therefore recommend that the GRI+ system could be applied to characterisation of these facilities and sites as well as interrogation of waste packages from these decommissioned sites.

Appendices

Appendix A

Standard Waste Drum

A.1 Standard Waste Drum for Low/Intermediate Level

The waste drum is a standard 500 litre drum waste container of dimensions 1200 mm by 800 mm and wall thickness of 7 mm. The drum is fabricated from stainless steel and is suitable for the packaging of low heat generating waste. The table below shows the elemental composition of the drum wall which is made of stainless steel.

Table A.1: Material compositions of 500 litre standard waste drum wall.

Material	Composition	Z	Weight Fraction	Density (g/cm^3)
Stainless Steel (316L)	Carbon	6	0.000300	8.00
	Silicon	14	0.010000	
	Phosphorus	15	0.000450	
	Sulphur	16	0.000300	
	Chromium	24	0.170000	
	Manganese	25	0.020000	
	Iron	26	0.653950	
	Nickel	28	0.120000	
	Molybdenum	42	0.025000	

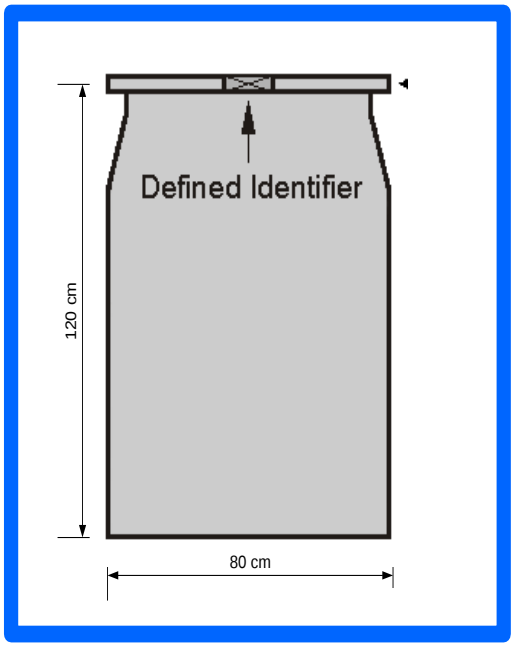

Figure A.1: A 500 litre standard waste drum for low heat generating packaging showing dimensions. Wall thickness is 7 mm

Figure A.2: The physical form of 500 litre standard waste drum for low heat generating packaging.

A.2 Material choice for the Drum Wall

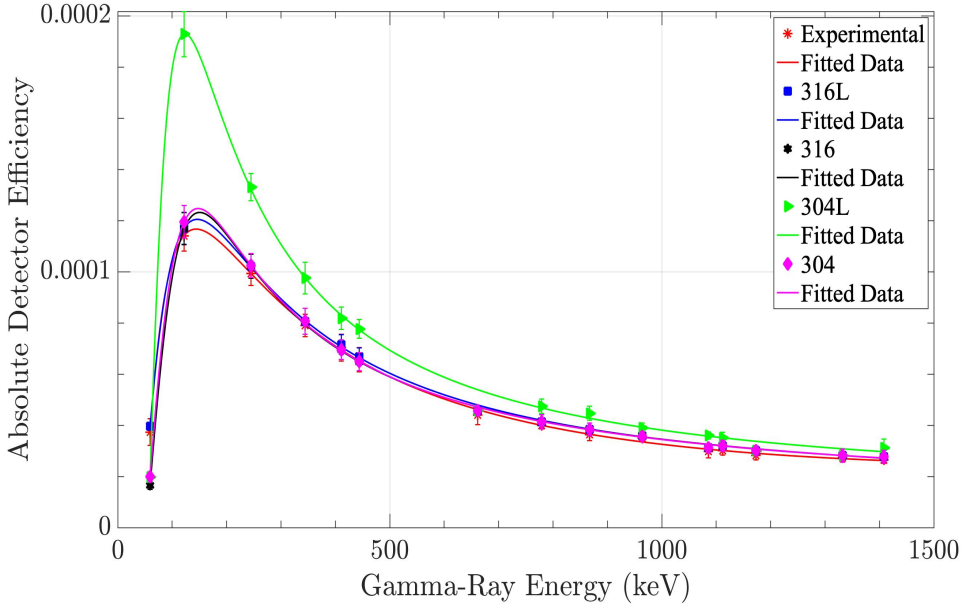

Figure A.3: Efficiency comparison for different drum wall material.

Appendix B

Attenuation Matrices

B.1 Matrices

Four attenuating materials (matrices) used for gamma attenuation/absorptions are Concrete (Los Alamos), Bitumen (Asphalt), Polymer (Epoxy resin) and a composite of polymer concrete material. The gamma attenuation/absorption power of these materials depends on their elemental compositions and densities as shown in the table below obtained from [62] for concrete and bitumen, whilst the density and elemental composition of epoxy resin was obtained from [5].

Table B.1: Material compositions of gamma attenuating matrices inside the waste drum.

Matrix	**Content**	**Z**	**Weight Fraction**	**Density (g/cm^3)**
Air	Carbon	6	0.000124	0.001205
	Nitrogen	7	0.755268	
	Oxygen	8	0.231781	
	Argon	18	0.012827	
Concrete	Hydrogen	1	0.004530	2.25
(Los Alamos)	Oxygen	8	0.512600	
	Sodium	11	0.015270	
	Aluminum	13	0.035550	
	Silicon	14	0.360360	
	Calcium	20	0.057910	
	Iron	26	0.013780	
Bitumen	Hydrogen	1	0.103725	1.30
(Asphalt)	Carbon	6	0.848050	
	Nitrogen	7	0.006050	
	Oxygen	8	0.004050	
	Sulphur	16	0.037700	
	Vanadium	23	0.000393	
	Nickel	28	0.000034	
Polymer	Hydrogen	1	0.76300	1.25
(Epoxy Resin)	Carbon	6	0.06700	
	Oxygen	8	0.170000	

B.1.1 Polymer Concrete Composite (PCC)

As concrete, bitumen and polymer have been used extensively for immobilisation of radioactive waste, this work investigated the effects of polymer (epoxy resin) in strengthening the gamma-ray shielding properties of concrete. The density of the composites, ρ_{pcc}, was calculated by mix proportion based on the elemental weight fractions using Equation B.1 [3].

$$\rho_{\mathrm{pcc}} = \frac{1}{\sum_{1}^{\mathrm{n}}(\omega_{\mathrm{i}}/\rho_{\mathrm{i}})}. \tag{B.1}$$

where ρ_i and ω_i are respectively the density and weight fraction of the ith component of concrete and epoxy resin in the composites.
The weight fractions, density and calculated elemental compositions based on the weight fraction are presented in Table B.2.

Table B.2: PCC elemental composite by changing the % concentration of Epoxy resin (ER) and Concrete (Con).

Weight Fractions	**Density** ($\mathbf{gcm^{-3}}$)	**Elemental Compositons**							
		H	**C**	**O**	**Na**	**Al**	**Si**	**Ca**	**Fe**
50 wt % ER : 50 wt % Con	1.607	0.383765	0.033500	0.341300	0.007635	0.017775	0.180180	0.028955	0.006890
40 wt % ER : 60 wt % Con	1.705	0.307918	0.026800	0.375560	0.009162	0.021330	0.216216	0.034746	0.008268
30 wt % ER : 70 wt % Con	1.815	0.232071	0.020100	0.409820	0.010689	0.024885	0.252252	0.040537	0.009646
20 wt % ER : 80 wt % Con	1.940	0.156224	0.013400	0.444080	0.012216	0.028440	0.288288	0.046328	0.011024
10 wt % ER : 90 wt % Con	2.083	0.080377	0.006700	0.478340	0.013743	0.031995	0.324324	0.052119	0.012402
60 wt % ER : 40 wt % Con	1.520	0.459612	0.040200	0.307040	0.006108	0.014220	0.144144	0.023164	0.005512
70 wt % ER : 30 wt % Con	1.442	0.535459	0.046900	0.272780	0.004581	0.010665	0.108108	0.017373	0.004134
80 wt % ER : 20 wt % Con	1.372	0.611306	0.053600	0.238520	0.003054	0.007110	0.072072	0.011582	0.002756
90 wt % ER : 10 wt % Con	1.308	0.687153	0.060300	0.204260	0.001527	0.003555	0.036036	0.005791	0.001378

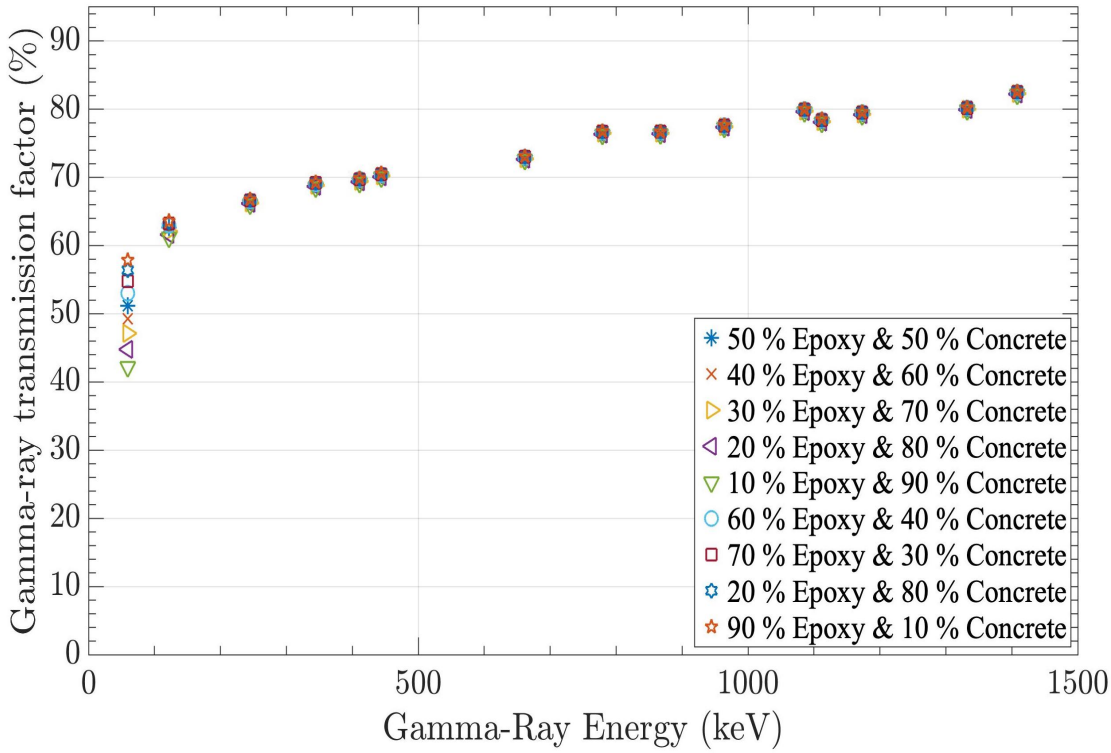

Figure B.1: Comparison of the simulated transmission factor for the change in % composition of epoxy resin and concrete.

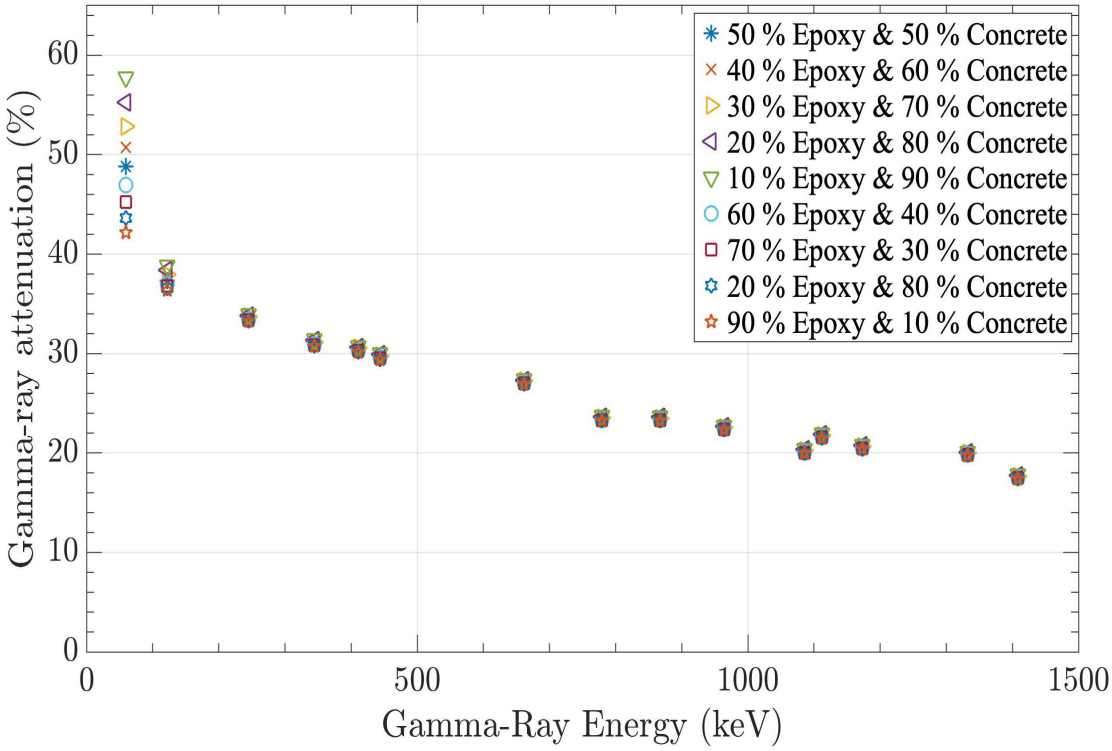

Figure B.2: Comparison of the simulated % attenuation for the change in % composition of epoxy resin and concrete.

Appendix C

MCNP Simulation Files

C.1 Detector Collimator Optimisation

The following file is one of the code for the detector collimator optimisation used to validate the experimental measurements as described in Chapter 5. The file can be rerun in a text format.

MCNP Code for the Optimisation of Collimated BEGe detector
C
C ################## Material Densities ##################
C Ge = -5.35 Al = -2.7 Cu = -8.92 Natural carbon = -1.42
C
C ################## Define Cells ##################
C
1 1 -5.35 -41 4 -5 #(-1 3 -5) #(21 -22 -23 2) imp:p 1 $Detector
11 1 -5.35 -1 2 -5 #(-1 3 -5) #(-41 4 -5) #(21 -22 -23 2) imp:p 1 $Lateral & back dead layer
111 1 -5.35 -1 3 -5 imp:p 1 $Front Dead layer
2 2 -2.7 -14 18 -17 #(-15 18 -16) #(-19 -20 16) #(-19 20 -17) #(-11 13 -3) imp:p 1 $Al cap
3 0 -15 18 -16 #(-1 2 -5) #(-11 13 -3) #(-9 8 -7) #(-19 -20 16) #(-19 20 -17) imp:p 1 $Vacuum between Al cap and cu holder
4 4 -1.42 -19 20 -17 imp:p 1 $Carbon Epoxy window
5 0 -19 -20 16 imp:p 1 $Vacuum below the carbon window
6 3 -8.92 -11 13 -3 #(-10 12 -3) imp:p 1 $Cu cylinder
61 0 -10 12 -3 #(-1 2 -5) #(-1 3 -5) imp:p 1 $Vacuum between detector and cu shell
62 3 -8.92 -9 8 -7 #(-11 8 -7) imp:p 1 $Cu first notch cylinder

63 0 21 -22 -23 2 imp:p 1 $First groove
64 5 -11.34 -24 -25 26 #(-1 2 -5) #(-1 3 -5) #(-9 8 -7) #(-11 13 -3) #(-27 17 -25) #(-14 18 -17) imp:p 1 $Lead collimator
65 0 -27 17 -25 imp:p 1 $Lead collimator aperture
7 0 100 imp:p 0 $Define world
71 0 -100 #(-1 2 -5) #(-1 3 -5) #(-9 8 -7) #(-11 13 -3) #(-14 18 -17) #(-24 -25 26) #(-27 17 -25) imp:p 1 $Define world

C ################## Define Surfaces ##################
C
1 cx 4.575 $Radius of the Ge detector (Active Diameter=91.5 mm)
2 px 0 $Near end of the Ge detector
3 px 3.15 $Far end of the Ge detector
4 px 0.0004 $Bottom Dead layer (0.004 mm)
41 cx 4.5746 $Define lateral Dead layer (0.004 mm)
5 px 3.1504 $Front Dead layer depth (4um)
C 6 px 3.15 $Upper limit of cu shell
7 px 3.00 $Upper limit of first notch in the Cu shell
8 px 2.25 $Lower surface of the first notch
9 cx 4.835 $First notch cylinder (outside thickness is 1 mm)
10 cx 4.585 $Internal Cu Cap
11 cx 4.685 $Outer Cu cap (Thickness is 1 mm)
12 px -1.30 $Lower limit of Cu Shell (inner surface)
13 px -1.40 $Lower limit of Cu Shell (Outer surface)
14 cx 5.715 $Outer Al cap (Diameter = 114.3 mm)
15 cx 5.555 $Internal Al cap (Al thickness = 1.6 mm)
16 px 3.65 $Upper Al shell (inner surface)
17 px 3.81 $Al shell thickness (1.6 mm)
18 px -2.60 $Lower limit of Al Shell
19 sx 4.0 4.915 $Carbon window defined as a sphere
20 px 3.75 $Carbon Epoxy thickness (0.6 mm)
21 cx 0.675 $Radius of P+ contact (Internal diameter = 13.5 mm)
22 cx 1.1 $Outer radius (OD = 22 mm to separate the P+ from n+)
23 px 0.25 $Groove depth = 2.5mm
24 cx 7.715 $Collimator radius
25 px 6.81 $near limit of the lead collimator
26 px -4.81 $far limit of the lead collimator
27 cx 0.1 $Lead collimator aperture

```
100 so 150 $Define World
C

mode p $photon transport
C
C ################### Define Source ###################
C Cs-137 (x-rays)
C
sdef pos=28.81 0 0 erg=d1
SI1 l 31.817e-3 32.194e-3 36.357e-3 37.450e-3 661.660e-3
SP1 d 0.0205 0.0377 0.0104 0.00264 0.8521
C
C ################### Define Tallies ###################
C
f8:P 1
e8 1.72e-3 8190I 2.43734 $0.297 keV bin size
ft8 geb 6.997e-4 2.869e-4 6.967e-4 $Ge detector coefs
C
C ################### Define Materials ###################
C
m1 32000 1.0 $GE detector
m2 13000 1.0 $Aluminium
m3 29000 1.0 $Copper
m4 6000 0.834 8016 0.093 1001 0.073 $Carbon Epoxy
m5 82000 1 $Lead
C
C ################### Define Run Time ###################
C
PRDMP 0 0 1 1 0
nps 1000000000
```

C.2 Validation of Radioactive Waste Drum Counting System

The following file is one of the codes for the assay of radioactive waste drum using BEGe detector. This code was used to validate the experimental measurements as described in Chapter 6. The file can be rerun in a text format.

```
MCNP code for radioactive waste assay with BEGe detector
C
C ################ Material Densities ################
C Ge = -5.35 Al = -2.7 Cu = -8.92 Natural carbon = -1.42
C
C ################## Define Cells ###################
C
1 1 -5.35 -41 4 -5 #(-1 3 -5) #(21 -22 -23 2) imp:p 1 $Detector
11 1 -5.35 -1 2 -5 #(-1 3 -5) #(-41 4 -5) #(21 -22 -23 2) imp:p 1 $Lateral & back
dead layer
111 1 -5.35 -1 3 -5 imp:p 1 $Front Dead layer 2 2 -2.7 -14 18 -17 #(-15 18 -16)
#(-19 16 -20) #(-19 20 -17) #(-11 13 -3) imp:p 1 $Al cap
3 0 -15 18 -16 #(-1 2 -5) #(-11 13 -3) #(-9 8 -7) #(-19 16 -20) #(-19 20 -17)
imp:p 1 $Vacuum between Al cap and cu holder
4 4 -1.42 -19 20 -17 imp:p 1 $Carbon Epoxy window
5 0 -19 -20 16 imp:p 1 $Vacuum above the carbon window
6 3 -8.92 -11 13 -3 #(-10 12 -3) imp:p 1 $Cu cylinder
61 0 -10 12 -3 #(-1 2 -5) #(-1 3 -5) imp:p 1 $Vacuum between detector and cu
shell
62 3 -8.92 -9 8 -7 #(-11 8 -7) imp:p 1 $Cu first notch cylinder
63 0 21 -22 -23 2 imp:p 1 $First groove
64 5 -11.34 24 -25 26 -27 28 -29 imp:p 1 $Lead collimator
65 5 -11.34 24 -25 26 -27 -30 31 imp:p 1
66 6 -8.000 -51 50 imp:p 1 $Radioactive waste drum
67 7 -0.001205 -50 imp:p 1 $Air
68 6 -8.00 -53 52 imp:p 1 $Radioactive waste drum
69 7 -0.001205 -52 imp:p 1 $Air
70 6 -8.00 -55 54 imp:p 1 $Drum
72 7 -0.001205 -54 imp:p 1 $Air
7 0 100 imp:p 0 $Define world
71 0 -100 #(-1 2 -5) #(-1 3 -5) #(-9 8 -7) #(-11 13 -3) #(-14 18 -17) #(24 -25 26
-27 28 -29) #(24 -25 26 -27 -30 31) #(-51 50) #(-50) #(-53 52) #(-52) #(-55 54)
#(-54) #(-50:-52:-54) imp:p 1 $Define world

C ################## Define Surfaces ##################
C
1 cx 4.575 $Radius of the Ge detector (Active Diameter=91.5 mm)
2 px 0 $Near end of the Ge detector
```

3 px 3.15 $Far end of the Ge detector
4 px 0.0001 $Bottom Dead layer (0.004 mm)
41 cx 4.5749 $Define lateral Dead layer (0.004 mm) 5 px 3.1504 $Front Dead layer depth (4um)
C 6 px 3.15 $Upper limit of cu shell
7 px 3.00 $Upper limit of first notch in the Cu shell
8 px 2.25 $Lower surface of the first notch
9 cx 4.835 $First notch cylinder (outside thickness is 1 mm)
10 cx 4.585 $Internal Cu Cap
11 cx 4.685 $Outer Cu cap (Thickness is 1 mm)
12 px -1.30 $Lower limit of Cu Shell (inner surface)
13 px -1.40 $Lower limit of Cu Shell (Outer surface)
14 cx 5.715 $Outer Al cap (Diameter = 114.3 mm)
15 cx 5.555 $Internal Al cap (Al thickness = 1.6 mm)
16 px 3.65 $Upper Al shell (inner surface)
17 px 3.81 $Al shell thickness (1.6 mm)
18 px -2.60 $Lower limit of Al Shell
19 sx 4.0 4.915 $Carbon window defined as a sphere
20 px 3.71 $Carbon Epoxy thickness (0.6 mm)
21 cx 0.675 $Radius of P+ contact (Internal diameter = 13.5 mm)
22 cx 1.1 $Outer radius (OD = 22 mm to separate the P+ from n+) 23 px 0.25 $Groove depth = 2.5mm
24 px 3.82 $Collimator
25 px 11.32 $near limit of the lead collimator
26 py -7.5 $lead collimator length
27 py 7.5 $Lead Collimator length
28 pz 0.5 $Lead collimator width 29 pz 7.5 $Lead collimator width
30 pz -0.5
31 pz -7.5
50 RCC 58.82 0 -59.85 0 0 85.85 39.85 $Drum inner
51 RCC 58.82 0 -60 0 0 86 40 $Drum outer
52 RCC 58.82 0 43 0 0 17 34.85
53 RCC 58.82 0 43 0 0 17 35
54 TRC 58.82 0 26 0 0 17 39.85 34.85. $Truncated part
55 TRC 58.82 0 26 0 0 17 40 35 $Truncated part
100 so 200 $Define World
C

```
mode p $photon transport
C
C ################## Define Source ##################
C Multi Energy gamma-rays
C
sdef pos=58.82 0 0 erg=d1
si1 l 121.7758e-3 244.6923e-3 344.286e-3 411.122e-3 443.890e-3
778.920e-3 867.348e-3 964.110e-3 1085.885e-3 1112.075e-3 1408.002e-3
sp1 d 0.287 0.0758 0.265 0.0223 0.0282 0.1298 0.0421 0.146 0.102 0.136 0.208
C
C ################## Define Tallies ##################
C
f8:P 1
e8 0 8190I 1.5 $0.297 keV bin size
ft8 geb 6.997e-4 2.869e-4 6.967e-4 $Ge detector coefs
C
fmesh14:p geom= xyz origin= -10 -40 -60
imesh= 100 iints= 200
jmesh= 40 jints= 100
kmesh= 60 kints= 100
C
C ################## Define Materials ##################
C
m1 32000 1.0 $GE detector
m2 13000 1.0 $Aluminium
m3 29000 1.0 $Copper
m4 6000 0.834 8016 0.093 1001 0.073 $Carbon Epoxy
m5 82000 1 $Lead
m6 6000 -0.000300 $Carbon weight fractions
14000 -0.010000 $Silicon weight fractions
15000 -0.000450 $Phosphorus weight fractions
16000 -0.000300 $Sulphur weight fractions
24000 -0.170000 $Chromium weight fractions
25000 -0.020000 $Manganese weight fractions
26000 -0.653950 $Iron weight fractions
28000 -0.120000 $Nickel weight fractions
42000 -0.025000 $Molybdenum weight fractions
m7 6000 -0.000124 $Carbon
```

```
7000 -0.755268 $Nitrogen
8000 -0.231781 $Oxygen
18000 -0.012827 $Argon
m8 1000 -0.143716 6000 -0.856284 $Polythene
C
C ################ Define Run Time ################
C
nps 1000000000
```

Bibliography

[1] ISO 19017:2015. *Guidance for gamma spectrometry measurement of radioactive waste.*

[2] *2019 UK Radioactive Waste Inventory*. Cumbria: Nuclear Decommissioning Authority, 2019.

[3] B. D Agarwal and L. J Broutman. *Analysis and Performance of Fiber Composites*. second. New York: John Wiley and Sons, 1990.

[4] A Andreotti et al. "Determination of dead-layer variation in HPGe detectors." In: *Applied Radiation and Isotopes* 87 (2013), pp. 331–335.

[5] A. F Avery and H. F Locke. *Neacrp Comparison of codes for the radiation protection assessment of transport packages solutions to problems 1 - 4*. 1992.

[6] Y.F Bai et al. "An improved method for the non-destructive characterisation of waste by gamma scanning". In: *Applied Radiation and Isotopes* 67.10 (2009), pp. 1897–1903.

[7] K Binder and D.W Heermann. *Monte Carlo Simulation in Statistical Physics: An Introduction*. Springer-Verlag Berlin Heidelberg., 2010.

[8] *Broad Energy Germanium Detectors*. Non-series Publications. MIRION Technology, 2016. URL: https://www.mirion.com/products/bege-broad-energy-germanium-detectors.

[9] F.L Bronson. "Validation of the accuracy of the LabSOCS software for Mathematical Efficiency Calibration of Ge detectors for typical Laboratory Samples." In: *Journal of Radioanalytical and Nuclear Chemistry* 255.01 (2003), pp. 137–141.

[10] P.P Bruyant. "Analytic and iterative reconstruction algorithms in SPECT". In: *Journal of Nuclear Medicine* 45 (2002), pp. 1343–1358.

[11] L. Caballero et al. "Gamma-ray imaging system for real-time measurements in nuclear waste characterisation". In: *Journal of Instrumentation* 13.03 (2018), P03016–P03016. DOI: 10.1088/1748-0221/13/03/p03016.

[12] CAEN. *CAEN V1724 Digitiser Information site*. URL: https://www.caen.it/products/v1724.

[13] CANBERRA. *HPGe EGPS* 60 × 60 × 20-*12X-12Y Operating Manual, OC 174915*. 2015.

[14] CANBERRA. *Silicon 13X-13Y Strip Planar Detector, ESLXS 3500-8 13X-13Y Operating Manual*.

[15] S.R Cherry, J.A Sorenson, and M.E Phelps. *Physics in Nuclear Medicine*. Saunders Philadelphia Pa, USA, 3rd edition, 2003.

[16] E Chham et al. "Monte Carlo analysis of the influence of germanium dead layer thickness of the HPGe gamma detector experimental efficiency measured by use of extended sources." In: *Applied Radiation and Isotopes* 95 (2015), pp. 30–35.

[17] K.S Chuang et al. "A maximum likelihood expectation maximization algorithm with thresholding." In: *Computerized Medical Imaging and Graphics* 29.7 (2005), pp. 571–578.

[18] *Classification of Radioactive Waste*. General Safety Guides GSG–1. Vienna: INTERNATIONAL ATOMIC ENERGY AGENCY, 2009. ISBN: 978-92-0-109209.0. URL: https://www.iaea.org/publications/8154/classification-of-radioactive-waste.

[19] M.J Cree and P.J Bones. "Towards direct reconstruction from a gamma camera based on Compton scattering". In: *IEEE Transactions on Medical Imaging* 13.2 (1994), pp. 398–407.

[20] *Cryo-Pulse® Plus Electrically Refrigerated Cryostat*. MIRION Technology. URL: https://www.mirion.com/products/cryo-pulse-5-plus-electrically-refrigerated-cryostat.

[21] L Dinescu et al. "On the efficiency calibration of a drum waste assay system". In: *Nuclear Instruments and Methods in Physics Research A* 487 (2002), pp. 661–666.

[22] H Domenech. *Radiation Safety: Management and Programs*. Switzerland: Springer, 2017.

[23] J Dorman et al. "Environmental Compton camera development: imaging radionuclides transport in soils and geomaterials". In: *Proceedings of the International Conference on Position Sensitive Detectors, ID 83*. Surrey, UK, 2014.

[24] T.Q Dung. “Calculation of the systematic error and correction factors in gamma waste assay system.” In: *Annals of Nuclear Energy* 24.1 (1997), pp. 33–37.

[25] T.Q Dung et al. “Evaluation of a gamma technique for the assay of radioactive waste drums using two measurements from opposing directions”. In: *Applied Radiation and Isotopes* 67.1 (2009), pp. 164–169.

[26] S Dziri et al. “Simulation approach to coincidence summing in γ-ray spectrometry.” In: *Applied Radiation and Isotopes* 70 (2012), pp. 1141–1144.

[27] C. L Epstein. *Introduction to the Mathematics of Medical Imaging*. Philadelphia: Society for Industrial and Applied Mathematics, 2008.

[28] T.G Feeman. *The Mathematics of Medical Imaging*. Springer, 2010. ISBN: 9780486462417.

[29] P Filß. “Relation between the activity of a high-density waste drum and its gamma count rate measured with an unshielded Ge-detector”. In: *Applied Radiation and Isotopes* 46.8 (1995), pp. 805–812.

[30] O Gal et al. “Operation of the CARTHOGRAM portable gamma camera in a photon-counting mode”. In: *IEEE Transactions on Nuclear Science* 48.4 (2001), pp. 1198–1204.

[31] O Gal et al. “The CARTHOGRAM portable gamma imaging system”. In: *IEEE Transactions on Nuclear Science* 47.3 (2000), pp. 952–956.

[32] S Gallardo et al. “Uncertainty analysis in environmental radioactivity measurements using the Monte Carlo code MCNP5.” In: *Radiation Physics and Chemistry* 116 (2015), pp. 214–218.

[33] *Geological Disposal: Waste Package Specification for 500 litre drum waste packages*. Cumbria: Nuclear Decommissioning Authority, 2013.

[34] A Georgiev and W Gast. “Digital Pulse Processing in High Resolution, High Throughput Gamma-Ray Spectroscopy”. In: *IEEE Transactions on Nuclear Science* 40.4 (1993), pp. 770–779.

[35] Gordon Gilmore and John Hemingway. *Practical Gamma-ray Spectrometry*. John Wiley & Sons, Inc., 2008.

[36] M Gmar et al. “Development of Coded-Aperture Imaging with a Compact Gamma Camera”. In: *IEEE Transactions on Nuclear Science* 51.4 (2004), pp. 1682–1687.

[37] T. Goorley et al. “Features of MCNP6”. In: *Annals of Nuclear Energy (Oxford)* 87 (Jan. 2016), pp. 772–783.

[38] M.W Groch and W.D Erwin. "SPECT in the year 2000: basic principles." In: *Journal of Nuclear Medicine Technology* 28 (2000), pp. 233–244.

[39] Claus Grupen and Irene Buvat. *Handbook of Particle Detection and Imaging*. Springer, Jan. 2012. DOI: 10.1007/978-3-642-13271-1.

[40] S. C. J Guembou et al. "Monte Carlo Method for gamma spectrometry based on GEANT4 toolkit: Efficiency calculation of BE6530 detector." In: *Journal of Environmental Radioactivity* 189 (2018), pp. 109–119.

[41] ISO/IEC Guide98-3. *Evaluation of measurement data-guide to the expression of uncertainty in measurement.* 2008.

[42] D Gurau and O Sima. "Simulation studies of the response function of a radioactive waste." In: *Applied Radiation and Isotopes* 70 (2012), pp. 305–308.

[43] L. J Harkness et al. "Characterisation of a Si(Li) orthogonal-strip detector." In: *Nuclear Instrumentations and Methods in Physics Research Section A* 726 (2013), pp. 52–59.

[44] R.G Helmer and van der Leun. "Recommended standards for γ-ray energy calibration (1999)." In: *Nuclear Instrumentations and Methods in Physics Research Section A* 450 (2000), pp. 35–70.

[45] R.G Helmer et al. "The use of Monte Carlo calculations in the determination of a Ge detector efficiency curve." In: *Nuclear Instrumentations and Methods in Physics Research Section A* 511 (2003), pp. 360–381.

[46] C Herbach et al. "Concept study of a two-plane Compton camera deigned for location and Nuclide identification of remote radiation sources". In: *IEEE Transactions on Nuclear Science Symposium Conference Record* (2009), pp. 909–911.

[47] J. H Hubbell. "Photon Mass Attenuation and Energy-absorption coefficients from 1 keV to 20 MeV." In: *International Journal of Applied Radiation and Isotopes* 33.11 (1982), pp. 1269–1290.

[48] J.H Hubbell and S.M Seltzer. *Tables of X-Ray Mass Attenuation Coefficients and Mass Energy-Absorption Coefficient from 1 keV to 20 MeV for Elements Z = 1 to 92 and 48 Additional Substances of Dosimetric Interest.* Gaithersburg, MD:NIST, 2004. URL: http://www.nist.gov/pml/data/xraycoef.

[49] IAEA. *Application of ion exchange processes for the treatment of radioactive waste and management of spent ion exchangers*. Technical Reports Series No. 408. Vienna: INTERNATIONAL ATOMIC ENERGY AGENCY, 2002.

[50] D. S Judson et al. *A novel, computationally lightweight, Compton imaging algorithm*. JINST, Awaiting publication.

[51] MM-Editor Khalil, ed. *Basic Sciences of Nuclear Medicine*. Berlin, Germany: Springer, 2010.

[52] Glenn F Knoll. *Radiation detection and measurement*. John Wiley & Sons, Inc., 2010.

[53] T Krings and E Mauerhofer. "Reconstruction of the activity of point source for the accurate characterisation of nuclear waste drum by segmented gamma scanning." In: *Applied Radiation and Isotopes* 69 (2011), pp. 880–889.

[54] T Krings and E Mauerhofer. "Reconstruction of the isotope activity content of heterogeneous nuclear waste drums." In: *Applied Radiation and Isotopes* 70 (2012), pp. 1100–1103.

[55] *LabSOCS Calibration Software*. Non-series Publications. MIRION Technology, 2017. URL: https://www.mirion.com/products/labsocs-calibration-software.

[56] N. P Laverov et al. "Confinement Matrices for Low- and Intermediate-Level Radioactive Waste." In: *Geology of Ora Deposits* 54.1 (2012), pp. 1–16.

[57] J. H Lee and C. S Lee. "Studies on sensitivity, resolution, and Doppler broadening in gamma-ray imaging with pixellated semiconductor detectors." In: *Nuclear Physics A* 746 (2004), pp. 639c–642c.

[58] T Lepy M.C.and Altzitzouglou et al. "Intercomparison of efficiency transfer software for gamma-ray spectrometry". In: *Applied Radiation and Isotopes* 55.4 ((2001)), pp. 493–503.

[59] V. Lj Ljubenov and P. M Marinkovic. "Applicability of Compton Imaging in Nuclear Decommissioning Activities." In: *Proceedings of International Yugoslav Nuclear Society Conference (YUNSC-2000)*. Institute of Nuclear Sciences VINCA, Belgrade, Yugoslavia, 2002.

[60] M Lyra and A Ploussi. "Filtering in SPECT Image Reconstruction." In: *International Journal of Biomedical Imaging* 28 (2011), pp. 1–14.

[61] E. R Martin, D. F Jones, and J. L Parker. *Gamma-ray Measurements with the Segmented Gamma Scan, LA-7059-M*. Los Alamos National Laboratory, 1977.

[62] R.J McConn et al. *Compendium of Material Composition Data for Radiation Transport Modelling*. Pacific Northwest National Laboratory, 2011. DOI: 10.2172/1023125.

[63] L Mihailescu et al. "SPEIR: A Ge Compton camera." In: *Nuclear Instrumentations and Methods in Physics Research Section A* 570 (2007), pp. 89–100.

[64] MIRION. *Waste Management Solutions*. 2018. URL: https://www.mirion.com/products/gamma-waste-assay-systems.

[65] D. W Mundy and M. G Herman. "Uncertainty analysis of a Compton camera imaging system for radiation therapy dose reconstruction." In: *Medical Physics* 37.5 (2010), pp. 2341–2350.

[66] S Nagasaki and S Nakayama, eds. *Radioactive Waste Engineering and Management*. Tokyo, Japan: Springer, 2015.

[67] Yasushi Nagata, ed. *Stereotactic Body Radiation Therapy Principles and Practices*. Tokyo, Japan: Springer, 2015.

[68] T Niedermayr et al. "Gamma-ray imaging with a coaxial HPGe detector". In: *IEEE Transcation on Nuclear Science* 553.3 (2005), pp. 501–511.

[69] Cavendish Nuclear. *Cavendish DrumScan® Plus Segmented Gamma-ray Scanner*. 2019. URL: https://www.cavendishnuclear.com/wp-content/uploads/2019/10/DrumScan-SGS-Plus-Products-and-Services-2019_10.pdf.

[70] OECD. *Radioactive Waste in Perspective*. Paris: OECD PUBLISHING, 2010. ISBN: 978-92-64-09261-7. URL: https://www.oecd-ilibrary.org/content/publication/9789264092624-en.

[71] M. I Ojovan, ed. *Handbook of advanced radioactive waste conditioning technologies*. Cambridge, United Kingdom: Woodhead Publishing Limited, 2011.

[72] M. I Ojovan and W. E Lee. *An Introduction to Nuclear Waste Immobilisation*. Second. London, United Kingdom: Elsevier, 2014.

[73] Caesar Ordonez, A Bolozdynya, and Wei Chang. "Doppler broadening of energy spectra in Compton cameras". In: vol. 2. IEEE, Dec. 1997, pp. 1361–1365. ISBN: 0-7803-4258-5. DOI: 10.1109/NSSMIC.1997.670574.

[74] ORTEC. *Comparison of Gamma-Ray Nondestructive Assay Measurement Techniques*. URL: https://www.antech-inc.com/wpcms/wp-content/uploads/DS.G320-340.SGS_.3.4.A4.pdf?x85945.

[75] ORTEC. *MAESTRO-32 MCA Emulator for Microsoft Windows 2000 Professional and XP Professional.* URL: https://www.ortec-online.com/-/media/ametekortec/manuals/a65-mnl.pdf?dmc=1&la=en.

[76] ORTEC. *Preamplifier Introduction, charge sensitive preamplifier.* URL: https://www.ortec-online.com/products/application-software/maestro-mca.

[77] J. L Parker. *A correction for gamma ray self-attenuation in regular heterogeneous materials, LA-UR-87-3954.* Los Alamos National Laboratory, 1987.

[78] D.B Editor Pelowitz, ed. *MCNPX User's Manual. LA-CP-07-1473, version 2.6.0.* Los Alamos National Laboratory, New Mexico, 2008.

[79] G.W Phillips. "Gamma-ray imaging with Compton camera". In: *Nuclear Instruments and Methods in Physics Research B* 99.1–4 (1995), pp. 674–677.

[80] *Predisposal Management of Radioactive Waste.* General Safety Requirements GSR Part 5. Vienna: INTERNATIONAL ATOMIC ENERGY AGENCY, 2009. ISBN: 978-92-0-111508-9. URL: https://www.iaea.org/publications/8004/predisposal-management-of-radioactive-waste.

[81] V. F. E Pucknell. *The midas multi instance data acquisition system.* 1995.

[82] *Radioactive Waste Management Status and Trends.* IAEA/WMDB/ST/4. Vienna: INTERNATIONAL ATOMIC ENERGY AGENCY, 2005.

[83] G.J Royle and R.D Speller. "Design of a Compton camera for imaging 662 keV radionuclide distributions." In: *Nuclear Instrumentations and Methods in Physics Research Section A* 348 (1994), pp. 623–626.

[84] ASE Santo, FG Wasserman, and CC Conti. "HPGe well detector calibration procedure by MCNP5 Monte Carlo computer code." In: *Annals of Nuclear Energy* 46 (2012), pp. 213–217.

[85] V Schonfelder, A Hirner, and K Schneider. "A Telescope for soft gamma-ray Astronomy". In: *Nuclear Instrumentations and Methods* 107.2 (1974), pp. 385–394.

[86] S. H Seo et al. "Effect of detector parameters on the image quality of Compton camera for ^{99m}Tc." In: *Nuclear Instrumentations and Methods in Physics Research Section A* 571 (2007), pp. 251–254.

[87] O Sima et al. “Efficiency calibration of high volume samples using the GESPECOR software.” In: *Applied Radiation and Isotopes* 61 (2004), pp. 123–127.

[88] M Singh and D Doria. “An electronically collimated gamma camera for single photon emission computed tomography. Part II: Image reconstruction and preliminary experimental measurements.” In: *Medical Physics* 10.4 (1983), pp. 428–435.

[89] Helmuth Spieler. *Semiconductor Detector Systems*. Series on Semiconductor Science and Technology. Oxford: Oxford University Press, 2005. ISBN: 97801915223656. URL: https://books.google.co.uk/books?!d=yy_ymccPL8C.

[90] D Stanga, D Radu, and O Sima. “A new model calculation of the peak efficiency for HPGe detectors used in assays of radioactive waste drums”. In: *Applied Radiation and Isotopes* 68.7–8 (2010), pp. 1418–1422.

[91] *Status and Trends in Spent Fuel and Radioactive Waste Management*. IAEA Nuclear Energy Series NW-T-1.14. Vienna: INTERNATIONAL ATOMIC ENERGY AGENCY, 2018.

[92] *Strategy and Methodology for Radioactive Waste Characterisation*. IAEA-TECDOC-1537. Vienna: INTERNATIONAL ATOMIC ENERGY AGENCY, 2007. ISBN: 92-0-100207-6.

[93] D Tattam and L Keightley. *Radiometric Non-destructive Assay*. Measurement Good Practice Guide. 34. Teddington, Middlesex: NATIONAL PHYSICAL LABORATORY, 2012.

[94] T.T Thanh et al. “A prototype of radioactive waste drum monitor by non-destructive assays using gamma spectrometry.” In: *Applied Radiation and Isotopes* 109 (2016), pp. 544–546.

[95] R.W Todd, J.M Nightinghale, and D.B Everett. “A proposed gamma camera”. In: *Nature* 251 (1973), pp. 132–134.

[96] M Toma et al. “Characterization studies of radioactive waste drums using high resolution gamma spectrometric systems”. In: *AIP Conference Proceedings* 1203 (2010), pp. 35–39.

[97] C. Z Uche, W. H Round, and M. J Cree. “Effects of energy threshold and dead time on Compton camera performance.” In: *Nuclear Instrumentations and Methods in Physics Research Section A* 641 (2011), pp. 114–120.

[98] C. Z Uche, W. H Round, and M. J Cree. "MCNP5 modelling of HPGe detectors for efficiency evaluation in $\gamma - ray$ spectrometry." In: *Nuclear Instrumentations and Methods in Physics Research Section A* 641 (2011), pp. 114–120.

[99] Y Ueno et al. "Spectroscopic gamma camera for use in high dose environments". In: *Nuclear Instruments and Methods in Physics Research A* 822.1 (2016), pp. 48–56.

[100] *Update of X Ray and Gamma Ray Decay Data Standards for Detector Calibration and Other Applications*. Non-serial Publications. Vienna: INTERNATIONAL ATOMIC ENERGY AGENCY, 2007. URL: https://www.iaea.org/publications/7551/update-of-x-ray-and-gamma-ray-decay-data-standards-for-detector-calibration-and-other-applications.

[101] S Vandenberghe et al. "Iterative reconstruction algorithms in nuclear medicine." In: *Computerized Medical Imaging and Graphics* 25.2 (2001), pp. 105–111.

[102] M.J Vargas, N.C Diaz, and D.P Sanchez. "Efficiency transfer in the calibration of a coaxial p-type HPGe detector using the Monte Carlo method." In: *Applied Radiation and Isotopes* 58 (2003), pp. 707–712.

[103] R Venkataraman et al. "IAn integrated Tomographic Gamma Scanning system for non-destructive assay of radioactive waste". In: *Nuclear Instruments and Methods in Physics Research A* 579 (2007), pp. 375–379.

[104] R Venkataraman et al. "Improved detector response characterisation method in ISOCS and LabSOCS." In: *Journal of Radioanalytical and Nuclear Chemistry* 264.01 (2005), pp. 213–219.

[105] K. M Vetter et al. "High-sensitivity Compton imaging with position-sensitive Si and Ge detectors." In: *Nuclear Instrumentations and Methods in Physics Research Section A* 579.1 (2007), pp. 363–366.

[106] T Vidmar et al. "An intercomparison of Monte Carlo codes used in gamma-ray spectrometry." In: *Allied Radiation and Isotopes* 66 (2008), pp. 764–768.

[107] Z Wang et al. "Image quality assessment: from error visibility to structural similarity". In: *IEEE Transactions on Image Processing* 13.4 (2004), pp. 600–612.

[108] P.K Wattal. "Indian Programme on Radioactive waste management". In: *Sadhana* 38.5 (2013), pp. 849–857.

[109] C.J Editor Werner, ed. *MCNP Users Manual - Code Version 6.2, LA-UR-17-29981.* Los Alamos National Laboratory, New Mexico, 2017.

[110] M Woodering et al. "Advanced multi-dimensional imaging of gamma-ray radiation". In: *Nuclear Instruments and Methods in Physics Research A* 505.1–2 (2003), pp. 415–419.

[111] S Yamamoto et al. "Three-layer GSO depth-of-interaction detector for high-energy gamma camera". In: *Nuclear Instruments and Methods in Physics Research A* 743.1 (2014), pp. 124–129.

[112] B Zaffora et al. "Uncertainty quantification applied to the radiological characterisation of radioactive waste." In: *Applied Radiation and Isotopes* 127 (2017), pp. 142–149.

[113] G.L Zeng. "image reconstruction - a tutorial." In: *Computerized Medical Imaging and Graphics* 25 (2001), pp. 97–103.

[114] K.P Ziock et al. "Large Area imaging detector for long-range passive detection of fissile materials". In: *IEEE Transactions on Nuclear Science* 51.5 (2004), pp. 2238–2244.